A statistical study of travelling ionospheric disturbances over the African-European and American sectors

Golekamang Piet Thaganyana

RHODES UNIVERSITY
Where leaders learn

A thesis submitted in fulfilment of the requirements for the degree of
Doctor of Philosophy
in the Department of Physics and Electronics
Rhodes University
Makhanda, South Africa
ORCID ID : https://orcid.org/0000-0001-8622-3771
August 2022

Abstract

This research presents a long-term statistical study of travelling ionospheric disturbances (TIDs) of low- and high-latitude origin over the American and African-European sectors between 2010 and 2018. The TIDs of low latitude origin (hereafter known as poleward TIDs) were studied in both quiet and disturbed conditions, whereas the equatorward TIDs were only studied during quiet conditions. The $\mathrm{Kp} > 4$ and $\mathrm{Dst} \leq -50$ nT was used as a criterion for geomagnetic disturbed conditions, while the four geomagnetically quiet days were selected each month based on $\mathrm{Kp} < 3$. Observations of TIDs are made using Global Navigational Satellite Systems (GNSS) total electron content derived data. During quiet conditions, seven and two transhemispheric TIDs were identified over the African-European and American sectors, respectively. The observed TIDs originated from the wintertime hemisphere and propagated into the summertime hemisphere. The horizontal velocity, periods, and horizontal wavelengths of TIDs are in range of $c_H =$ 120-274 m/s, 48-80 min and $\lambda_H =$ 379-1104 km, respectively. These quiet-time equatorward TIDs have been associated with tertiary gravity waves (GWs) from the dissipation of secondary GWs which are in turn generated from the dissipation of mountain waves (MWs) as a result of excited orographic forcing.

The poleward TIDs during geomagnetically quiet conditions over the African and American sectors occur mainly during local daytime. Poleward TIDs were observed mostly in the African-European sector than the American sector. Their horizontal propagation velocities and periods range between 129-280 m/s and 39-70 min over African-European and American sectors. Although the mechanisms responsible for launching quiet-time poleward TIDs have not been established in this study, lower atmospheric processes such as convection systems, sudden stratospheric warming and cold weather fronts may have a role in their generation. During geomagnetic storms in the African sector, almost all poleward TIDs (with the exception of two cases) during the main phase were large-scale with horizontal velocities and periods ranging from 250-503 m/s and 30 min to 2 hours. During recovery phase, poleward TIDs fall under the category of medium scale. In the American sector, the majority of poleward TIDs occurred during the storm's main phase, as opposed to the African-European sector, which experienced a significant number of poleward TIDs during the recovery phase. The periods and horizontal velocities of TIDs range from 45 min-1.5 h and 180-296 m/s during main phase. During the recovery phase, the horizontal velocity and period range from 177-271 m/s and 40-1.5 h, respectively. Overall, it has been shown that statistically, changes in equatorial electrodynamics related to enhanced eastward electric field and hence increased equatorial electrojet (vertical E×B drift) correlates highly with the reported poleward TIDs.

Publication from this thesis

Thaganyana, G. P., Habarulema, J. B., Ngwira, C. and Azeem, I. 2022. Equatorward large-scale travelling ionospheric disturbances of high latitude origin during quiet conditions. Journal of Geophysical Research: Space Physics, 127, e2021JA029558. `https://doi.org/10.1029/2021JA029558`

Habarulema, J. B., Thaganyana, G. P., Katamzi-Joseph, Z. T., Yizengaw, E., Moldwin, M. B. and Ngwira, C. M. 2022. A statistical study of poleward traveling ionospheric disturbances over the African and American sectors during geomagnetic storms. Journal of Geophysical Research: Space Physics, 127, e2021JA030162. `doi:https://doi.org/10.1029/2021JA030162`

Acknowledgement

I would like to express my sincere gratitude to my supervisor Dr John Bosco Habarulema for continuous support during my study, for his patience, motivation, and immense knowledge. His guidance helped me in my research and the writing of this thesis.

A special thanks to the South African National Space Agency (SANSA) for awarding me a bursary to obtain my PhD's degree. Many thanks to my friends, family, and students and staff at SANSA Space Science for their support, encouragement and love. I give thanks to God who gave me the strength to finish this study.

Declaration

This thesis is dedicated to my parents, Mr M.A Thaganyana and Mrs M.L Thaganyana.

Contents

List of Figures

List of Tables

Abbreviations and Acronyms

AE: Auroral electrojet
AGWs: Atmospheric gravity waves
AIRS: Atmospheric Infrared Sounder
ATOVS: Advanced TRIOS Operational Vertical Sounder
BPSK: Binary phase-shift keying
BT: Brightness temperature
C/A: Code/acquisition
CIRs: Corotating interaction regions
CME: Coronal mass ejections
CEJ: Counter electrojet
CWT: Continuous wavelet transform
Dst: Disturbance storm time
EEJ: Equatorial electrojet
EIA: Equatorial ionization anomaly
EOS: Earth Observing System
EUV: Extreme ultraviolet
GNSS: Global Navigational Satellite Systems
GPS: Global Positioning System
IEF: Interplanetary electric field
IMF (Bz): Interplanetary magnetic field
IGS: International GNSS Service
IPP: Ionospheric piercing point
MAD: Median absolute deviations
MIT: Main ionospheric trough
MWs: Mountain waves
PPEF: Prompt penetrating electric fields
PPS: Precise positioning service
PRE: Prereversal enhancement
PRN: Pseudo-random noise
SEPs: solar energetic particles
STEC: Slant total electron content
SPS: Standard positioning service
TEC: Total electron content
TIDs: Travelling ionospheric disturbances
UNAVCO: University NAVSTAR Consortium
USDoD: United States Department of Defense

Chapter 1

Introduction

For decades, atmospheric gravity waves (AGWs)/travelling ionospheric disturbances (TIDs) have been well reported (e.g. Hines, 1960; Hunsucker, 1982; Hocke and Schlegel, 1996; Vadas, 2007; Vadas *et al.*, 2018; Balthazor and Moffett, 1997; Afraimovich *et al.*, 2008; Bruinsma and Forbes, 2008; Ngwira *et al.*, 2012; Habarulema *et al.*, 2016; Katamzi-Joseph *et al.*, 2019). AGWs are vital in transporting energy and momentum (horizontally and vertically) in the different atmospheric layers. It has been well established that TIDs are a signature in the ionosphere of propagating AGWs. TIDs are wave-like perturbations in the ionospheric measurements, such as plasma density, ion and electron temperature and wind (Hunsucker, 1982; Hocke and Schlegel, 1996; Nicolls *et al.*, 2012; Habarulema *et al.*, 2018; Katamzi-Joseph *et al.*, 2019). It is essential to understand the sources and characteristics of these TIDs. The existing literature indicates that TIDs are usually generated by Joule heating, the auroral electrojet, the equatorial electrojet, particle precipitation, the solar terminator and tropospheric/stratospheric processes (Hunsucker, 1982; Hocke and Schlegel, 1996; Afraimovich *et al.*, 2008, 2009*a*; Habarulema *et al.*, 2015, 2016; Ngwira *et al.*, 2019; Katamzi-Joseph *et al.*, 2019). This study presents the statistical observation of poleward and equatorward TIDs that originate in both the low- and the high-latitudes during geomagnetically quiet and disturbed conditions.

Poleward TIDs that originate in the low-latitude have not been as extensively studied as their equatorward counterparts, commonly observed during geomagnetic storms. Knudsen (1969) and Chimonas (1969) suggested the possible existence of TIDs of equatorial origin that propagate poleward during disturbed conditions. Both highlighted that should the auroral electrojet (AE) generate TIDs, the possibility exists that the equatorial electrojet (EEJ) would act similarly. Knudsen (1969) pointed out that the amplitude of AGWs generated by EEJ dynamics is smaller than that which emerges as a result of changes in the AE. As a result, it is difficult to observe and track the AGWs which originate from the low or equatorial latitudes. However, numerous studies have recently reported on poleward TIDs of equatorial origin during disturbed conditions (e.g. Ding *et al.*, 2013; Habarulema *et al.*, 2015, 2016; Jonah *et al.*, 2018; Ngwira *et al.*, 2019). Ding *et al.* (2013) reported two cases of large-scale poleward TIDs during the recovery phase of geomagnetic storm between 27 May and 1 June 2011 in southern China's low-latitude region. According to Ding *et al.* (2013), large-scale TIDs generated during the dissipation of some primary medium-scale TIDs from the lower atmosphere could be a possible mechanism for poleward TIDs. Since then, a few articles have reported cases of poleward TIDs of equatorial origin during the main and recovery phase of the geomagnetic storm (e.g. Habarulema *et al.*, 2015, 2016; Jonah *et al.*, 2018; Ngwira *et al.*, 2019, and references therein). The source mechanisms of poleward TIDs are still under investigation; some studies suggest that poleward TIDs could result from increased Lorentz coupling due to prompt penetration of the electric field (Habarulema *et al.*, 2015, 2016). The Lorentz force (due to the EEJ) can be enhanced, leading to a stronger coupling between neutral particles and ions at the equatorial origin. The ions convey energy to the neutral particles and generate poleward propagating TIDs. According to Jonah *et al.* (2018), deep convection-induced AGWs play an important role in the poleward propagation of medium-scale TIDs during geomagnetically quiet days (26-27 May 2017) and during the storm's recovery phase (28 May 2017). The TIDs of equatorial origin are partly studied on an event-to-event basis (looking at geomagnetic storm periods separately). There is a need to study long-term statistical observations of poleward TIDs during geomagnetically disturbed and quiet conditions. This study was done to determine how frequently poleward TIDs occur and to determine their source mechanisms.

The equatorward and near-equatorward TIDs have been extensively studied, particularly during geomagnetically disturbed conditions (Hunsucker, 1982; Hajkowicz and Hunsucker, 1987; Hocke and Schlegel, 1996; Balthazor and Moffett, 1997; Lei *et al.*, 2008; Ding *et al.*, 2007; Katamzi and Habarulema, 2014; Habarulema *et al.*, 2018; Ngwira *et al.*, 2019). Equatorward TIDs of high-latitude origin are generally linked to auroral region Joule heating, particle precipitation and Lorentz coupling processes during geomagnetically disturbed conditions (Hines, 1960; Davis, 1971; Hunsucker, 1982; Hocke and Schlegel, 1996; Balthazor and Moffett, 1997; Lei *et al.*, 2008; Borries *et al.*, 2016; Katamzi-Joseph *et al.*, 2019, and references therein). The fluctuations in energy within the auroral regions caused by geomagnetic storm-related processes significantly influence the thermospheric composition by contributing to equatorward propagating TIDs (Hunsucker, 1982; Hocke and Schlegel, 1996; Balthazor and Moffett, 1997). However, numerous papers report AGWs and TIDs during geomagnetically quiet conditions (Hedin and Mayr, 1987; Mayr *et al.*, 1990; Vadas and Crowley, 2010; Vadas and Liu, 2009, 2013; Vadas *et al.*, 2019; Vadas and Becker, 2019; Becker and Vadas, 2020; Frissell *et al.*, 2016). For instance, some studies reported secondary AGWs from tropospheric-stratospheric processes, such as deep convections during geomagnetically quiet conditions (e.g. Vadas and Liu, 2013; Vadas *et al.*, 2014). Modelling results have shown that TIDs could probably be launched by tertiary gravity waves (GWs) which were created by the dissipation of secondary GWs excited by the local body force created from mountain waves (MW) breaking in the stratopause region (Vadas and Becker, 2019; Vadas *et al.*, 2019; Becker and Vadas, 2020). Despite numerous observations, there has been no detailed investigation of equatorward TIDs originating from the high-latitudes and crossing the geomagnetic equator into the opposite hemisphere during quiet conditions. There is a need to investigate the source mechanisms of equatorward TIDs during quiet conditions. This study also presents the statistical observations of equatorward TIDs of high-latitude origin, as observed across different hemispheres during quiet conditions.

This study covers the period from 2010 to 2018 for geomagnetically quiet and disturbed conditions. The $Kp > 4$ and $Dst \leq -50$ nT were used as criteria for geomagnetic disturbance conditions. For each month during the study period, the four quietest days (maximum $Kp < 3$) were obtained from the World Data Center for Geomagnetism, Kyoto. The observations of TIDs are based on Global Navigational Satellite Systems (GNSS) data for the

African-European and American sectors.

1.1 Objectives of this research

The main objectives of this research were to:

- Investigate the long-term statistical contribution of low-latitude electrodynamics to atmospheric gravity waves over the African-European and American sectors during disturbed and quiet conditions for the period 2010-2018.
- To study the long-term statistical observations of equatorward TIDs over the American and African-European sectors during quiet conditions for the period 2010-2018.

1.2 Overview of the project

This thesis consists of 7 chapters:

Chapter 1 provides a brief introduction to the research and explains the objectives of the research.

Chapter 2 provides the theoretical background for the study of the Earth's atmosphere, ionosphere and geomagnetic storms.

Chapter 3 offers the theory behind atmospheric gravity waves and travelling ionospheric disturbances.

Chapter 4 presents the broad overview of data sources and methodology, and describes how magnetometer, the hyperspectral infrared sounder and GPS data were obtained and derived.

Chapter 5 presents the results that were obtained and discusses the equatorward medium- to large-scale TIDs originating from high latitudes, and propagating across the equator into the opposite hemisphere in the African-European and American sector, during geomagnetically quiet conditions.

Chapter 6 presents the results that were obtained and discusses the poleward TIDs of low-latitude origin during quiet and disturbed conditions.

Chapter 7 presents the conclusion and a summary of the thesis.

Chapter 2

Theoretical background

This chapter provides an introduction to Earth's atmosphere, as well as theoretical background of the ionosphere and geomagnetic storms.

2.1 Earth's Atmosphere

The Earth's atmosphere consists of a mixture of ideal gases: molecular Nitrogen (N_2, 78.11%), Oxygen (O_2, 20.95%), Argon (Ar, 0.93%), Neon (Ne, 18.18 x 10^{-4} %) and Helium (He, 5.24 x 10^{-4}%). Other minor constituents are water (H_2O, 0-7%), Carbon dioxide (CO_2, 0.01-0.1%) and Ozone (0_3, 0-00001%) (Saha, 2008; Zolesi and Cander, 2014). The Earth's atmosphere is divided into different layers based on temperature, density and pressure (Rishbeth and Garriott, 1969; Davies, 1990; Hargreaves, 1992; Moldwin, 2008; Saha, 2008; Zolesi and Cander, 2014). These layers are the troposphere, stratosphere, mesosphere, thermosphere, and exosphere. These layers protect our planet by absorbing harmful radiation from the Sun. Figure 2.1 shows different layers of the Earth's atmosphere based on temperature. The troposphere extends up to 12 km from the surface of Earth, the stratosphere ranges from 12 to 50 km, the mesosphere lies between 50 and 80 km, the thermosphere between 80 and 700 km and the exosphere stretches from 700 km to outer space, around 10,000 km (Rishbeth and Garriott, 1969; McNamara, 1991; Moldwin, 2008; Atiq, 2018).

The tropospheric temperature decreases with altitude at the rate of about 6.5°C per km until a minimum value of about -60°C is reached at a level known as the tropopause. The tropospheric temperature distribution is maintained by convective and turbulent heat transfer due to the absorption of solar radiation from the Earth's surface by the atmosphere (Rishbeth and Garriott, 1969; Hargreaves, 1992; Saha, 2008; Zolesi and Cander, 2014). The stratospheric temperature increases with altitude to reach a maximum of about 0°C at an altitude of about 50 km, limited by the stratopause. The increase in temperature in this layer is due to the existence of a layer of ozone, a tri-atomic molecule of oxygen that absorbs the extreme ultraviolet (EUV) radiation from the Sun and acts as a source of heat for the atmosphere (Rishbeth and Garriott, 1969; Moldwin, 2008; Saha, 2008; Zolesi and Cander, 2014). In the mesosphere, temperature decreases and reaches a minimum of about -100°C at an altitude of about 80 km. Above the mesopause lies the thermosphere, where temperature varies throughout solar activity, with a value of about 2000 K during solar maximum and 500 K during solar minimum (Rishbeth and Garriott, 1969; Saha, 2008; Zolesi and Cander, 2014). The increase in temperature is due to the absorption of EUV and nitrogen in this layer. The thermosphere plays a vital role in intercepting the highly-charged solar rays from space and the EUV radiation from the Sun, both harmful to life at the Earth's surface (Saha, 2008). This ionised layer is essential for reflecting high-frequency radio waves to help global telecommunication (Moldwin, 2008; Saha, 2008). The ionosphere is part of the Earth's atmosphere, starting from the mesosphere to the exosphere. The ionosphere is a highly ionized layer in the Earth's atmosphere (Rishbeth and Garriott, 1969; Hargreaves, 1992; McNamara, 1991; Moldwin, 2008; Zolesi and Cander, 2014; Atiq, 2018).

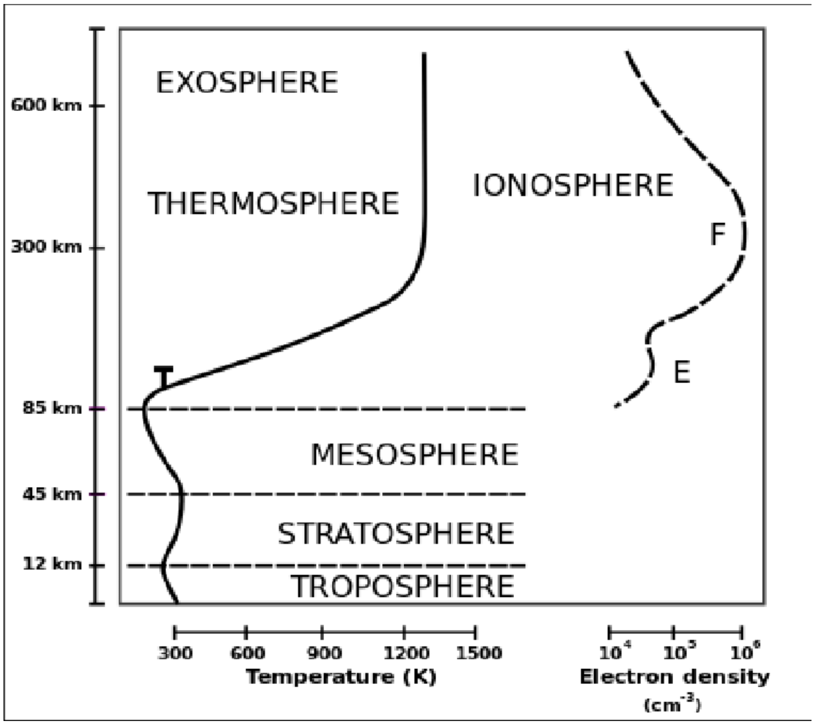

Figure 2.1: Layers of the Earth's atmosphere: troposphere, stratosphere, mesosphere, thermosphere and exosphere (Hargreaves, 1992; Atiq, 2018).

2.2 Formation of the ionosphere

The ionosphere is a layer of the Earth's atmosphere that contains a high concentration of ions and free electrons. The ionosphere lies at an altitude of about 50-1000 km, covering the mesosphere, thermosphere, and exosphere (Rishbeth and Garriott, 1969; Hargreaves, 1992; McNamara, 1991; Zolesi and Cander, 2014). The term ionosphere came into use in 1932, and was proposed by R. A. Watson-Watt (Rishbeth and Garriott, 1969). This layer is created when extreme ultraviolet light and x-rays from the Sun strip electrons from the neutral atoms of the Earth's atmosphere (Rishbeth and Garriott, 1969; Hargreaves, 1992; Hunsucker and Hargreaves, 2007; Moldwin, 2008; Zolesi and Cander, 2014; Thompson *et al.*, 2017). For example, when EUV photons hit a neutral atom such as an oxygen atom, an electron can escape and move freely and cause the atom to become positively charged (positive ion). This process is known as photoionisation. The chemical formula for this process is as follow

(McNamara, 1991; Zolesi and Cander, 2014):

$$A + hv \rightarrow A^+ + e^- \tag{2.1}$$

where A is an atom, hv is the energy of photons, A^+ is an ion, and e^- is an electron. It is worth noting that photoionisation occurs only during the daytime when the Sun is above the horizon. There is a reverse process of photoionisation, which is called recombination. Recombination happens when free electrons recombine with the positive ions to form neutral atoms. There are two types of recombination: radiative and dissociative. Radiative recombination is less vital than dissociative recombination, which is more efficient. In radiative recombination, the electrons combine directly with the positive ion to produce a neutral atom or molecule plus excess energy (E) (McNamara, 1991; Zolesi and Cander, 2014):

$$A^+ + e^- \rightarrow A + E \tag{2.2}$$

In dissociative recombination, positively charged ions are generally lost through a two-stage process. In the first stage, positive ions originating from the photoionisation interact with the numerous neutral molecules (such as oxygen and nitrogen), according to the following equation (McNamara, 1991; Zolesi and Cander, 2014):

$$X^+ + A_2 \rightarrow AX^+ + A \tag{2.3}$$

where X^+ is a positive ion formed by photoionisation. In the second stage, the free electrons combine with positive molecules (AX^+) to produce two neutral atoms:

$$AX^+ + e^- \rightarrow A + X \tag{2.4}$$

These two types of recombination occur during the nighttime at ionospheric altitudes. However, this process is not entirely effective in the ionosphere; some free electrons survive until sunrise when their numbers rapidly increase. The electron density in the ionosphere varies with solar activity, seasons and geomagnetic activity (McNamara, 1991; Hunsucker and Hargreaves, 2007; Zolesi and Cander, 2014).

2.2.1 Ionospheric regions

The ionosphere is divided into three regions, namely D, E and F. Due to certain solar-terrestrial conditions, the F region is split into F1 and F2, during the day. Figure 2.2 shows typical daytime and nighttime electron density profiles of the ionospheric regions during solar maximum (sunspot maximum). During the daytime, all ionospheric regions are present due to photoionisation. At nighttime, the F1 and F2 regions merge to form one region (F-region), the D-region almost disappears, and the E-region sometimes remains. The ionospheric regions play an important and active role in high-frequency radio communication.

2.2.2 The D-region

The D-region is the lowest ionospheric layer that ranges from 50-90 km above the surface of the Earth. It has electron density values in the order of about $10^2 - 10^3 cm^{-3}$. This region comprises neutral components such as N_2, O_2, Ar, CO_2, He and a highly variable quantity of O_3 and H_2O (Zolesi and Cander, 2014). The ionisation source in this region is

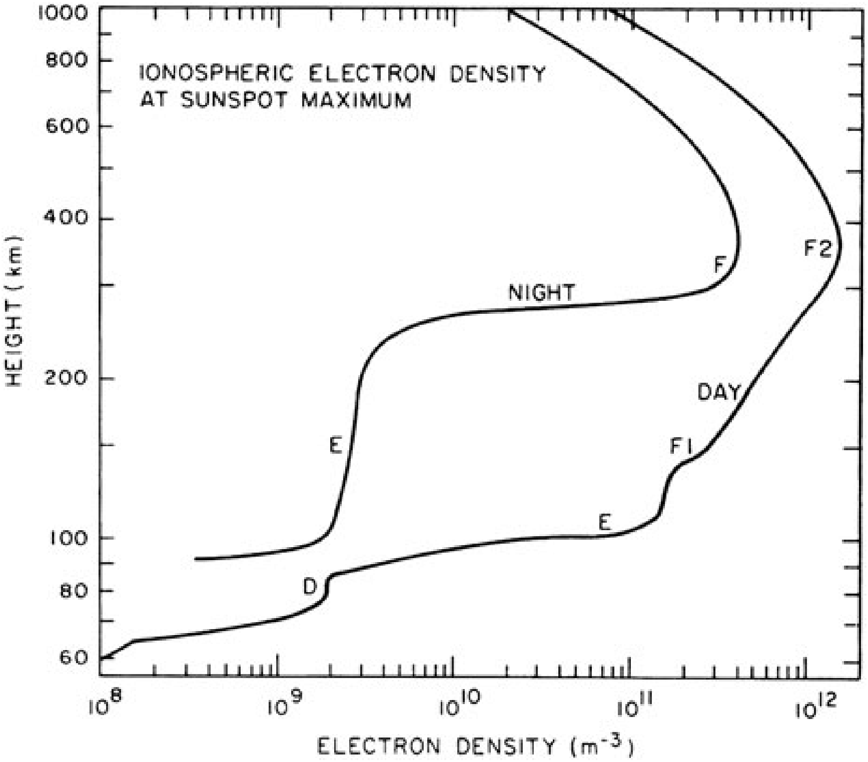

Figure 2.2: The daytime and nighttime vertical profiles of the electron density (Thompson *et al.*, 2017)

solar Lyman-α which ionises nitric oxide (NO), O and N molecules (Thomas, 1996; Rishbeth and Garriott, 1969; Zolesi and Cander, 2014). In addition, galactic cosmic rays are vital in producing ionisation in this region during solar minimum (associated with decreasing sunspot numbers), when the number of galactic cosmic ray particles reaching the Earth's atmosphere is higher. This is due to the weakening of the ambient solar wind and its magnetic field, allowing galactic cosmic ray particles to penetrate the solar system (Hargreaves, 1992; Moldwin, 2008). The ionisation in the D-region is lower than in other ionospheric regions. During the geomagnetic storm, large amounts of x-rays are emitted, which causes a rapid increase in ionisation (sudden ionospheric disturbances) in this region (Moldwin, 2008). This region is only present during the daytime (though galactic cosmic rays give rise to a residual ionisation level at nighttime). At nighttime, it almost disappears due to the recombination process, where negatively charged electrons and positively charged ions combine to produce neutral atoms. The electron density is higher during the daytime because photoionisation is at its greatest. The electron density is much less than the atomic molecular density in this region (Davies, 1990; Moldwin, 2008; Schunk and Nagy, 2009; Zolesi and Cander, 2014).

Under normal conditions, the solar x-rays are too small to be an important cause of ionization in the D region (McRae and Thomson, 2004). However, when solar flares occur, the flux of X-rays from the Sun increases sharply. The x-rays with wavelengths well below 1 nm are transmitted to the height of the D region, which significantly increases the ionisation rate and electron density (Mitra, 1974; McRae and Thomson, 2004). The enhancement in electron density leads to an increase in HF radio waves attenuation in this region due to collision between electrons and neutral particles (Mitra, 1974; Handzo *et al.*, 2014; Bland *et al.*, 2018). The D-region plays a vital role in high-frequency radio communication because it absorbs radio waves, which causes degradation of long-distance high-frequency communication (Moldwin, 2008; McNamara, 1991).

2.2.3 The E-region

The E-region, also previously known as the Kennelly-Heaviside layer, is an ionospheric region that generally extends from 90-140 km above the Earth's surface. It has an electron density of about 10^{11} m^{-3} and 5 x 10^{9} m^{-3} during the daytime and nighttime, respectively (Hunsucker and Hargreaves, 2007; Rishbeth and Garriott, 1969; Zolesi and Cander, 2014). This region does not entirely disappear at nighttime, but remains weakly ionised. The primary sources of ionisation in the E-region are x-rays and solar ultraviolet, producing the NO^{+}, O_2^{+} and secondary O^{+}, N_2^{+} ion components (Rishbeth and Garriott, 1969; Hargreaves, 1992; Hunsucker and Hargreaves, 2007; Moldwin, 2008; Zolesi and Cander, 2014). Particle precipitation is also a source of ionisation in this region, especially during the night when there is no photoionisation (Hunsucker and Hargreaves, 2007; Moldwin, 2008).

Additionally, there are short-lived sources of ionisation at E-region altitudes, such as complex dynamics, which result from the effects of the neutral atmosphere motion, auroral electric fields and meteors entering the upper atmosphere. The latter burn up and influence the surrounding neutral gas with adequate energy to form an ionised trail (Rishbeth and Garriott, 1969; Hunsucker and Hargreaves, 2007; Moldwin, 2008; Zolesi and Cander, 2014). These sources form a narrow, short-lived region of highly dense ionisation at E-region heights, generally known as sporadic E (Rishbeth and Garriott, 1969; Moldwin, 2008). The sporadic E has a higher critical frequency than the usual E-region (Hargreaves, 1992; Hunsucker and Hargreaves, 2007). Sporadic E usually depends on the latitude, occurs randomly and can last for a few minutes to several hours. This highly dense ionisation reflects the high-frequency radio waves for long-distance communication (Rishbeth and Garriott, 1969; Moldwin, 2008).

2.2.4 The F region

The F-region of the ionosphere lies at an altitude of about 140-600 km. Its electron density that ranges between 10^{11}-10^{12} m^{-3} (Hunsucker and Hargreaves, 2007; Zolesi and Cander, 2014). The F-region splits into two separate regions during the daytime, called F1 and F2. The density of the F2 peak is greater than that of the F1 peak. The F1 region lies between 140 and 210 km in altitude. The maximum electron density reaches approximately 2 x 10^{11} m^{-3} (McNamara, 1991; Hargreaves, 1992). The major source of ionisation in the F1 region is EUV solar radiation. The major ions are NO^{+} and O_2^{+}. The F1 region varies with hour of the day, solar activity, season, and geomagnetic activity. This region is observed only during the daytime and is more prominent during summer than in winter, consistently vanishing during the nighttime and sometimes in winter, even during the day (Rishbeth and Garriott, 1969; McNamara, 1991; Hargreaves, 1992; Moldwin, 2008; Zolesi and Cander, 2014).

The F2 region is an ionospheric region that generally extends from 210-600 km above the surface of the Earth. During local noon, the F2 region peaks at an altitude of approximately 300 km. The F2 region is always present under all solar-terrestrial conditions. It has a maximum electron density of between 10^{10} and 8 x 10^{12} m^{-3} (Zolesi and Cander, 2014). This region has a higher concentration of free electrons. The main source of ionisation in this region is the EUV radiation ionising atomic oxygen (Rishbeth and Garriott, 1969; McNamara, 1991; Moldwin, 2008; Zolesi and Cander, 2014). The ionisation decreases at nighttime in this region, but not as much as in the D and E regions because, at this altitude, recombination rates are lower. This is due to the fact that atomic ions have much lower recombination rates, and this region consists of atomic oxygen (Moldwin, 2008). The F2 region plays a vital role in high-frequency communication as it is always present (Davies, 1990; McNamara, 1991; Zolesi and Cander, 2014). This region reflects high-frequency radio waves with a frequency of up to 35 MHz.

2.2.5 Ionospheric variability

The ionosphere displays significant diurnal, seasonal and solar cycle variations.

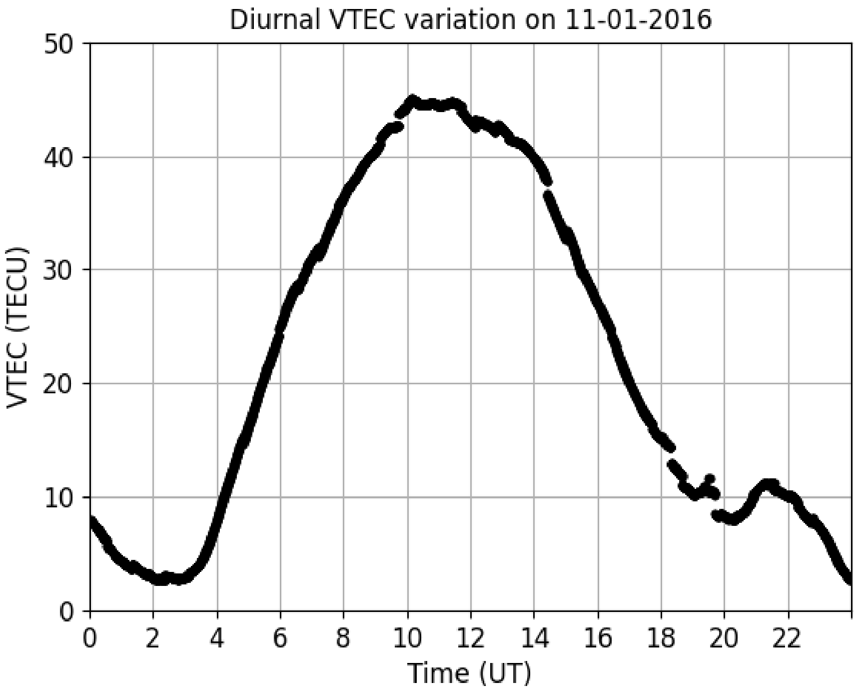

Figure 2.3: An graph illustrating the diurnal variation of VTEC on 11 January 2016 over Addis Ababa (9.04°N, 38.77°E), Ethiopia.

Diurnal Variations

The ionospheric electron density varies throughout the day and night. According to Hofmann-Wellenhof *et al.* (1992), TEC depends on electron density, which depends on solar radiation, the main source of photoionisation. The TEC is determined by integrating the electron density with respect to the altitude (Hofmann-Wellenhof *et al.*, 1992; Zolesi and Cander, 2014). TEC variability is highly influenced by changes in the intensity of the daily solar radiation. TEC reaches its maximum values during the local midday when the solar zenith angle is almost zero. The zenith angle is the angle between the Sun's rays and the vertical direction. When the solar zenith is zero, the Sun is overhead, and photoionisation is at its greatest.

During the night, TEC reaches its minimum values due to the loss of electrons during the recombination process. Figure 2.3 represents, as an example, the diurnal variability of VTEC on 11 January 2016, over Addis Ababa station (9.04°N, 38.77°E). VTEC reached its lowest around 03:00 UT (05:35 LT) in the morning, while peak in VTEC reached its peak between 10:00 UT (12:35 LT) and 12:00 UT (14:35 LT) in the afternoon.

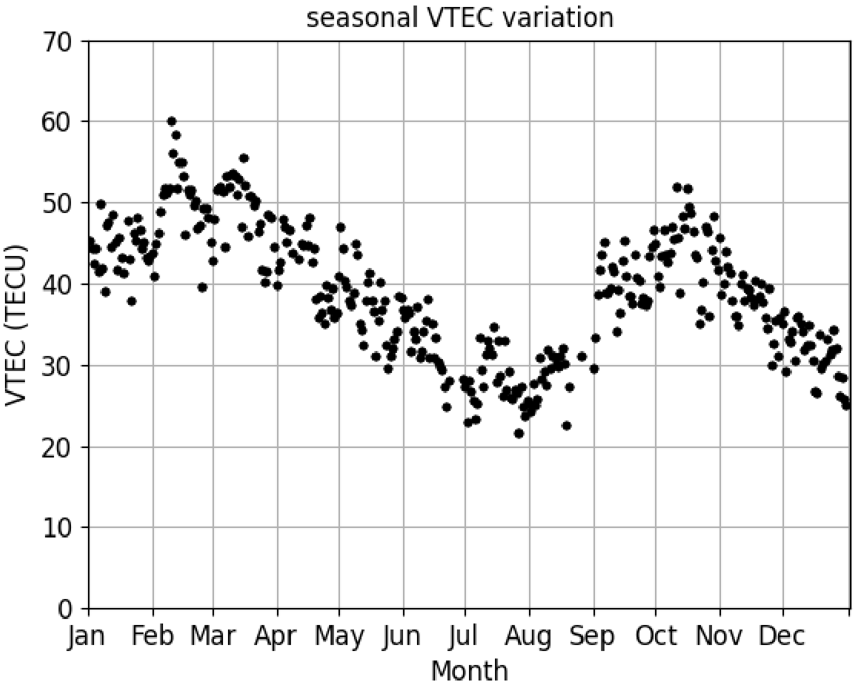

Figure 2.4: Seasonal variation of VTEC during the year 2016, over Addis Ababa (9.04°N, 38.77°E), Ethiopia at 10:00 UT.

Seasonal Variations

The ionosphere displays significant seasonal variation, partly due to the solar zenith angle, which varies throughout the year. The ionosphere is formed in the neutral atmosphere that changes depending on the solar zenith angle. During midday in winter, the solar zenith angle is always greater than during the midday in summer (McNamara, 1991). The ionisation rate in the ionosphere during summer is higher than during winter. The electron density in the ionosphere exhibits significant seasonal variation (Davies, 1990; McNamara, 1991; Zolesi and Cander, 2014). Maximum TEC values are generally observed during the equinox months (March to May and September to November) and in summer, while the lowest values of TEC are generally observed in winter (Davies, 1990; Rishbeth and Garriott, 1969; McNamara, 1991; Mukherjee *et al.*, 2010; Patel *et al.*, 2017). Figure 2.4 shows, as an example, the variation of VTEC values for the year 2016 at 10:00 UT (12:35 LT) over Addis Ababa, Ethiopia. The graph shows that VTEC values were much greater during the equinox months and in summer than in winter. According to Chapman's ionisation theory, the ionospheric electron density must behave to be controlled by the solar zenith angle. For seasonal variation, electron density should be greater in summer than during the equinoxes, and minimal in winter (Davies, 1990; Schunk and Nagy, 2009; McNamara, 1991; Kelley, 2009; Mukherjee *et al.*, 2010). However, earlier studies revealed some interesting "anomalous" features (e.g. Torr and Torr, 1973; Rishbeth *et al.*, 2000; Balan *et al.*, 2000; Zhang *et al.*, 2005; Liu *et al.*, 2009, and references therein), which are radically different from those predicted by Chapman's ionisation theory. Historically, when the behaviour of the F2 layer deviates significantly from the dependence on the solar zenith angle as predicted by Chapman's ionisation theory, these deviations were called "anomalies". Typical anomalies in the F2 layer electron density are seasonal anomalies, when the average ionospheric electron density is higher during the winter solstice than during the summer solstice (e.g. Rishbeth *et al.*, 2000; Liu *et al.*, 2009; Azpilicueta *et al.*, 2012, and references therein).

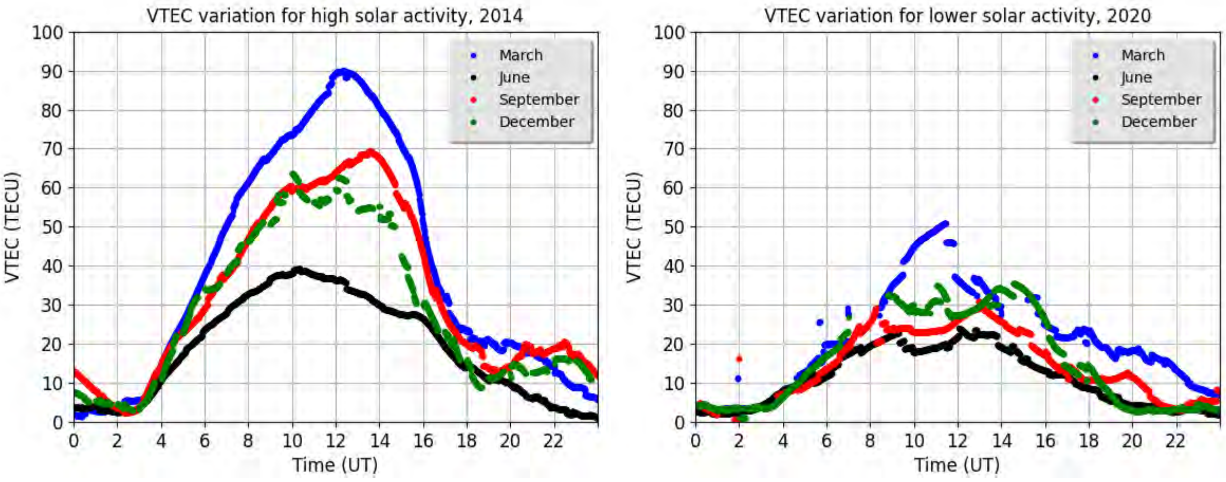

Figure 2.5: (a) VTEC variation for the 20 March 2014 and 23 September 2014 equinoxes, and for solstice days 21 June 2014 and 22 December 2014, over Addis Ababa (9.04°N, 38.77°E), Ethiopia. (b) illustrates the VTEC variation during the equinoxes of 20 March 2020 and 22 September 2020, and during solstice days on 20 June 2020 and 21 December 2020.

Solar Cycle Variations

The Sun's magnetic field tends to follow 11-year solar cycles. The solar cycle describes the level of solar activity and variability. The sunspot number is used as a good indicator of solar activity. The number of sunspots decreases and then increases over a period of approximately 11 years. During the solar maximum period, solar activity is higher and lower during the solar minimum period (Davies, 1990; Moldwin, 2008). The solar x-rays and EUV radiation vary throughout the solar cycle. The x-ray and EUV radiation levels are greater during the solar maximum than the solar minimum period. As such, the production of electrons in the ionosphere is higher during the solar maximum (McNamara, 1991; Hargreaves, 1992; Zolesi and Cander, 2014). Figure 2.5 represents, as an example, the solar cycle variability of VTEC during the March and September equinoxes and during the solstices of June and December during a period of high (2014) and low (2020) solar activity over Addis Ababa station (9.04°N, 38.77°E). High TEC values during high solar activity are the results of a higher photoionisation rate. Solar flares occur more frequently during periods of high solar activity, and are the main cause of high levels of ionisation in the ionosphere (Davies, 1990; Saha, 2008; Zolesi and Cander, 2014). Variations in the neutral density and temperature, neutral wind, ion and electron densities and temperature, and electric fields are due to changes in the solar activity in the ionosphere (Mukherjee *et al.*, 2010; Liu *et al.*, 2011).

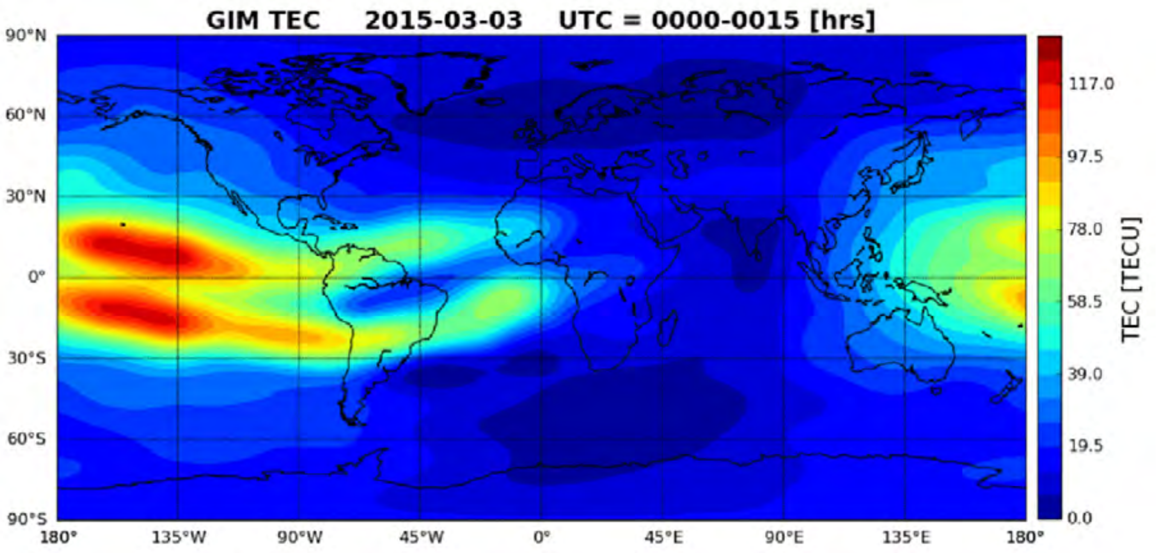

Figure 2.6: Global ionospheric TEC map (GIM) generated at Jet Propulsion Laboratory (JPL) using GNSS data for 00:15 UTC on 3 March 2015 (Pi *et al.*, 2021).

2.2.6 Low-Latitude Ionosphere

The low-latitudinal ionospheric geomagnetic latitude ranges from 0°-20° on each side of the geomagnetic equator (Zolesi and Cander, 2014; Saha, 2008). This region is affected by a broader range of peculiar behaviours than regions at other latitudes. This is mainly due to the fact that the Sun is directly above and the Earth's magnetic field is horizontal at the geomagnetic equator, which increases the influence of the electric field and increases the vertical ionisation drift (Hargreaves, 1992; Moldwin, 2008; Zolesi and Cander, 2014). Therefore, the equatorial ionosphere is higher in altitude than at the mid-latitudes, with the electron density dropping to a minimum near the magnetic equatorial, and reaching a maximum at 15°-20° latitude on either side of the geomagnetic equator (Kelley, 2009; Zolesi and Cander, 2014). This phenomenon is called the equatorial ionisation anomaly (EIA). The EIA occurs at about 10:00 LT in the morning, lasts far beyond sunset, and covers about half of the global area in 24 hours (Balan, Liu and Le, 2018). The location of the crests and the ratio of crest-to-trough depends on the geophysical conditions (Kelley *et al.*, 2004; Kelley, 2009). Local regions of the EIA can become unstable at night, especially in the evening when only the high-altitude F region ionosphere persists (Eastes *et al.*, 2019). The EIA is the result of an eastward electric field along the equator during the day (Appleton, 1946; Kelley, 2009). Fluctuations in the electric fields and neutral winds cause changes in the position and intensity of the two crests of the EIA (Kelley *et al.*, 2004; Kelley, 2009). The most dramatic change in EIA occurs shortly after sunset when prereversal enhancement (PRE) increases the plasma drift velocity. Due to the tilt, offset, and distortion of the Earth's magnetic field and atmospheric tides (Lin *et al.*, 2005; Immel *et al.*, 2006; Kelley, 2009; Eastes *et al.*, 2019), EIA is subject to additional dependencies due to geographic location and seasonal changes (Kelley, 2009; Eastes *et al.*, 2019). During the main phase of super geomagnetic storms, the plasma fountain becomes a super fountain (Kelley *et al.*, 2004; Balan *et al.*, 2009), and the

EIA becomes more vigorous with more than 1000 % increase in density at the crests that shift up to ±30° latitude (Mannucci *et al.*, 2005; Balan, Liu and Le, 2018). It has been suggested that such strong EIA is caused by strong eastward prompt penetration electric fields (PPEFs) (Kelley *et al.*, 2004), but later studies based on models show that PPEF alone is unlikely to produce strong EIA (Balan *et al.*, 2009; Balan, Liu and Le, 2018). Strong EIA has been explained by the combined effect of strong eastward PPEF and fast storm-time equatorial winds (Lin *et al.*, 2005; Balan *et al.*, 2010; Balan, Souza and Bailey, 2018). Figure 2.6 shows the global ionospheric TEC map at 00:15 UTC on 3 March 2015. High TEC values exist in the EIA within a latitudinal coverage of about ±20°. Farther from the EIA, the TEC gradually decreases with increasing latitude.

Several highly variable electrodynamics processes affect the low-latitude ionosphere (e.g. increased dynamo currents and enhanced vertical drift). The electrodynamic processes mostly emerge from changes in the wind dynamo current system in the E-region ionosphere on solar quiet days, due to differential heating of the Earth's atmosphere (Richmond, 1973; Richmond and Thayer, 2000; Wei *et al.*, 2015). The changes in the wind dynamo current system and Earth's magnetic field in the equatorial regions result in the Lorentz force. The latitudinal distribution of plasma in low-latitude ionosphere is due to the Lorentz force (Anderson, 1973; Sastri, 1990; Kelley, 2009). The source of low-latitude perturbation electric fields results from the dynamo action of disturbance winds driven by enhanced energy and momentum deposition into the high-latitude ionosphere by Joule heating and particle precipitation (Blanc and Richmond, 1980; Fejer, 1991, 2011, 1997; Richmond and Thayer, 2000). Low-latitude electrodynamics are driven by the equatorial vertical drift and dynamo electric field in the E- and F-regions of the ionosphere (Heelis *et al.*, 1974; Fejer, 1991; Richmond and Thayer, 2000; Kelley, 2009). These electrodynamic processes and their ionospheric effects exhibit a wide range of temporal and spatial variation during both geomagnetically quiet and disturbed conditions (Fejer, 1991, 2011; Richmond and Thayer, 2000; Habarulema *et al.*, 2019). The variability of low-latitude electrodynamics has been studied with ionosondes, magnetometers, space receiver techniques, and coherent and incoherent scatter radars (Fejer, 1997, 2011; Kelley, 2009; Habarulema *et al.*, 2019).

Additional electric fields arising from penetration and the disturbance dynamo contribution drastically alter the conventional understanding of low-latitude electrodynamics during disturbed conditions. The penetration electric field is the result of the interaction of the solar wind with Earth's magnetosphere or ionosphere (Fejer, 1991; Fejer and Scherliess, 1998; Fejer, 2011; Wei *et al.*, 2015). At low-latitude, the penetration electric field during the southward turning of the interplanetary magnetic field (Bz) usually enhances the eastward electric field during daytime (leading to increased vertical drift) and the westward electric field during nighttime, causing downward vertical drift (Fuller-Rowell *et al.*, 1997; Fejer, 2011; Habarulema *et al.*, 2015, 2019). During quiet conditions, the vertical ExB drifts are mostly upward and downward during daytime and nighttime, respectively (Sastri, 1995; Fejer, 2011; Dubazane and Habarulema, 2018; Habarulema *et al.*, 2019). The short-period variations in a vertical drift near the dip equator may be due to electric fields associated with the gravity waves during evening hours (Sastri, 1995; Balan *et al.*, 1992). The medium-scale gravity waves are the source of shorter period (<1 h) variation of vertical drift in the evening hours in the low-latitudes (Nair *et al.*, 1992; Subbarao and Murthy, 1994). The E-region electric field associated with the counter electrojet pushes the vertical drift downwards during the daytime (Alex *et al.*, 1987). The counter electrojet event refers to the reversal of the equatorial electrojet current from eastward to westward during local daytime (Marriott *et al.*, 1979; Habarulema *et al.*, 2019). The probability of occurrence of the counter electrojet is lower around noon, very large in the evening and early in the morning (Rastogi, 1975; Marriott *et al.*, 1979; Zhou *et al.*, 2018; Habarulema *et al.*, 2019).

2.2.7 Mid-Latitude Ionosphere

The mid-latitudinal ionospheric geomagnetic latitude ranges from 30°-60° on each side of the geomagnetic equator. The mid-latitudinal ionosphere is less complex than other regions under normal solar-terrestrial conditions and is characterised by a relatively small, slowly changing spatial gradient (Zolesi and Cander, 2014). At mid-latitudes the length of magnetic field lines containing high-density plasma is much shorter, gravity acts parallel to the magnetic field, and wind effects are at least as important as electric field (Hunsucker and Hargreaves, 2007; Kelley, 2009; Zolesi and Cander, 2014). The magnetospheric electric field does not significantly affect the mid-latitude quiescent ionosphere due to the shielding effect of the Alfvén layer (Huba *et al.*, 2005; Kelley, 2009). Under geomagnetically quiet conditions, the mid-latitude ionosphere is quiescent plasma, but there is still an irregularity in the plasma density produced by both the plasma and neutral processes (Titheridge, 1995; Tsugawa *et al.*, 2004). The irregularity of the ionosphere during the geomagnetic storms at mid-latitudes is strong enough to cause fluctuations in signal power, known as ionospheric scintillation (e.g., Basu *et al.*, 2001, 2002; Xiong *et al.*, 2016, and references therein). These irregularities scatter radio waves and cause amplitude and phase scintillation, affecting satellite communications and GPS navigation systems (Basu *et al.*, 2001, 2002; Mishin *et al.*, 2003). Mid-latitude scintillation reaches its maximum during the solar maximum, the ionisation density in the F-region increases, and anomalies appear against the background of the increase in ionisation density (Basu *et al.*, 2002; Heelis, 2004; Kelley, 2009). The occurrence rate of scintillation in the mid-latitude ionosphere is generally lower than in the low- and high-latitude ionospheres (Basu *et al.*, 1988, 2002; Kuai *et al.*, 2022). Ionospheric scintillation is a common phenomenon in low latitudes during sunset and evening hours (Abdu *et al.*, 1985; Muella *et al.*, 2010; Liu *et al.*, 2015), and it is also observed frequently in high latitudes (Kersley *et al.*, 1988; Secan *et al.*, 1997; Jiao *et al.*, 2013). During disturbed geomagnetic storm conditions, the auroral region expands toward the equator and shrinks in size in the mid-latitude region (Zolesi and Cander, 2014). The mid-latitude ionosphere exhibits strong daytime, seasonal, and solar cycle fluctuations, because the main ionisation source and energy of the ionosphere is photoionisation (Rishbeth and Garriott, 1969; Saha, 2008; Heelis, 2004; Kelley, 2009; Schunk and Nagy, 2009; Zolesi and Cander, 2014).

2.2.8 High-Latitude Ionosphere

The high latitude ionosphere geomagnetic latitude ranges from 60°-90° on each side of the geomagnetic equator (Schunk and Nagy, 2009; Zolesi and Cander, 2014). High-latitude is subjected to the highest variability of all the regions due to its connection via the field lines to the outer magnetosphere and interplanetary medium. It is strongly influenced by the various processes that occur within it and the nature of the geophysical environment. The magnetosphere electric field gives rise to a large-scale motion of the high-latitude ionosphere, affecting the electron density morphology. When the plasma drifts through the neutral particles, the ion temperature rises due to ion-neutral frictional heating (Rishbeth and Garriott, 1969; Schunk and Nagy, 2009; Zolesi and Cander, 2014). As the ion temperature rises, the chemical kinetics of the ions, topside plasma scale heights, and ion composition change. In addition, the deposition of particles in the auroral oval increases the ionisation rate and raises the electron temperature. This affects the density and temperature of ions and electrons. These ionospheric changes, in turn, have a significant impact on the structure, circulation, and composition of the thermosphere (Kelley, 2009; Schunk and Nagy, 2009; Zolesi and Cander, 2014).

Due to the low elevation of the Sun, ion generation from solar EUV and X-rays is relatively weak, and high-energy charged particles contribute mainly to ion generation at high-latitudes (Saha, 2008; Schunk and Nagy, 2009). The polar ionosphere at geomagnetic latitudes above about 75° is also the region where solar wind energy dissipates, which often dominates the entire upper atmospheric energy balance. Energy is distributed by heat and cold, wind and waves (Schunk and Nagy, 2009; Kelley, 2009). An important feature of the high-latitudes is the main ionospheric trough (MIT) found in the electron density in the F-region at night. Presenting as an ionised latitudinal patch in the afternoon sector at about 70° magnetic latitude, it is the natural boundary between the mid-latitudes and the auroral ionosphere (Taylor Jr *et al.*, 1975; Collis and Häggström, 1988; Zolesi and Cander, 2014). The MIT can also be observed at mid-latitudes, where it is referred to as the mid-latitude ionospheric trough (Moffett and Quegan, 1983; Lubyk *et al.*, 2022). The MIT is the most important structural feature of the subauroral ionosphere, as it is very likely to occur under winter night conditions. 90-95% of the MIT observations have been during periods of high solar activity (Karpachev and Afonin, 1998; Karpachev *et al.*, 2016). The higher the illumination of the high-latitude ionosphere, the lower the probability of a daytime MIT (Karpachev *et al.*, 2022). The location of the MIT depends on local time, longitude, and magnetic activity (Ahmed *et al.*, 1979; Karpachev and Afonin, 1998). With strong geomagnetic disturbances, the dynamics of the MIT are very complex. During a moderate geomagnetic storm, MIT slowly shifts to about 57° around midnight local time, reaching latitudes above about 10° as local time advances (Collis and Häggström, 1988; Zolesi and Cander, 2014). The density ratio inside and outside the trough may vary from less than 0.1 to nearly 1 (Zolesi and Cander, 2014).

Various mechanisms explain the formation tactics of the MIT, such as the stagnation mechanism. It states that the minimum value of the trough is due to the fact that corotation with the Earth and polar convection remain in the dark region, where they counteract each other (Knudsen, 1974). The plasma density decays withinside the quasi-stagnation location because of extended recombination withinside the dark sectors lacking photoionisation (e.g. Knudsen, 1974; Collis and Häggström, 1988; Aa *et al.*, 2020, and references therein). Second, an increased recombination rate due to an increase in ion temperature: large poleward electric fields associated with the subauroral ion drift (Spiro *et al.*, 1979) or subauroral polarisation currents can increase ion temperature by ion-neutral friction heating and accelerate the nonlinear ion loss process (e.g., Taylor Jr *et al.*, 1975; Foster and Burke, 2002; Voiculescu *et al.*, 2016, and references therein). Third, field-aligned plasma upflow, may result from stronger frictional heating and growth withinside the subauroral ion drift/subauroral polarisation streams region or because of substantial ion-neutral relative speed related to large meridional neutral winds (e.g. Anderson *et al.*, 1991; Rodger *et al.*, 1992; Ishida *et al.*, 2014;

Aa *et al.*, 2020, and references therein). The plasma flows westward of the equator of the subauroral ion drift and becomes more westward as the fixed latitude increases. Poleward of the subauroral ion drift, the evening stream averages the entire auroral zone to the west and turns east at midnight (Anderson *et al.*, 1991). The poleward edges of the trough are less clearly defined at higher altitudes and are often defined only by sharp ionisation peaks that extend several degrees within the auroral zone (Ahmed *et al.*, 1979). Lastly, the poleward wall of the trough is formed primarily by precipitation of auroral particles or partially by high-density plasma transport across the polar cap from the dayside, that is, boundary blobs (Rodger *et al.*, 1986, 1992). Boundary blobs are regions of enhanced plasma density located either inside or on the equatorward edge of the auroral oval (Schunk and Nagy, 2009). The boundary blobs are polar cap patches that have converted through the nightside auroral oval and around toward dusk (Schunk and Nagy, 2009; Kelley, 2009). The equatorial wall of the trough is formed by the replenishment of plasma from the plasmasphere at night (Yizengaw and Moldwin, 2005), and by co-rotational sunlit plasma (Voiculescu *et al.*, 2010). The high-latitude trough located at the equatorward edge of the peak gradually decreases in amplitude as altitude increases (Ahmed *et al.*, 1979; Anderson *et al.*, 1991).

2.3 Geomagnetic Storms

Geomagnetic storms are major disturbances in the Earth's magnetosphere that occur when there is a highly efficient energy exchange between the solar wind and the Earth's surrounding space environment (Tsurutani *et al.*, 1997, 2006; Campbell, 1997). These storms cause major changes in the current, plasma, and magnetic fields of the Earth's magnetosphere due to fluctuations in the solar wind (Tsurutani *et al.*, 1997; Hargreaves, 1992; Tsurutani *et al.*, 2006; Campbell, 1997; Saha, 2008; Moldwin, 2008). The increase in solar wind pressure compresses the magnetosphere. The solar wind interacts with the Earth's magnetic field and transfers increased energy into the magnetosphere when interplanetary magnetic field Bz component is southward for a prolonged period of time (Tsurutani *et al.*, 1997; Parkinson, 1983). Both interactions cause an increase in the electric field (ring current) in the magnetosphere (Tsurutani *et al.*, 1997). The increase in ring current is observed as a decrease in the horizontal component (H) of the Earth's magnetic field. This decrease in the H component is due to an increased number of trapped magnetospheric particles and can be monitored by the Disturbance storm time (Dst) index (Gonzalez *et al.*, 1994). H component is used to compute Dst (Kamide and Maltsev, 2007). The Dst is used as an indicator of a geomagnetic storm, its intensity and duration.

2.3.1 Causes of Geomagnetic Storms

Geomagnetic storms are usually caused by coronal mass ejections (CMEs) and the associated interplanetary shock, and by the corotating interaction regions (CIR) that result from interactions between slow and fast solar wind speed streams (Hargreaves, 1992; Moldwin, 2008; Tsurutani *et al.*, 2006). CMEs are associated with solar events, such as solar flares and eruptive prominences (Crooker *et al.*, 1997; Moldwin, 2008). The highly energetic, fast CMEs set up shock waves in front of them as they stream away from the Sun (Moldwin, 2008; Crooker *et al.*, 1997). The shock waves play a critical role in accelerating solar energetic particles (SEPs) (Crooker *et al.*, 1997). The transit time of a CME from the Sun to the Earth is about one to five days and depends on the CME's initial velocity, mass, size, as well as on the conditions and coupling processes with the ambient solar wind flow in interplanetary space (Crooker *et al.*, 1997; Moldwin, 2008; Temmer, 2016). The CMEs have stronger magnetic fields than the ambient solar wind, resulting in a compressed magnetosphere. If the magnetic field of a CME is opposite to the Earth's magnetic field, it transmits a significant amount of the energy into the magnetosphere by magnetic reconnection (Akasofu, 1981; Crooker *et al.*, 1997; Hargreaves, 1992; Moldwin, 2008). This energy may cause a geomagnetic storm, resulting in a visible aurora and enhancements to the Van Allen radiation belts (Moldwin, 2008). CMEs that affect the Earth's magnetosphere can cause intense geomagnetic storms that can lead to ionospheric disturbances (Gopalswamy, 2006). CMEs occur primarily during the solar maximum and are the main source of large magnetic storms with social impacts that are more harmful than those caused by CIR storms (Webb, 1991; Turner *et al.*, 2009).

The corotating interaction regions are the leading cause of moderate geomagnetic storms and occur when they impinge on the magnetosphere (Tsurutani *et al.*, 2006). CIR-driven storms are generated in response to the interaction between the fast solar wind emitted from the coronal hole and the slow solar wind of the interplanetary medium (Moldwin, 2008; Tsurutani *et al.*, 2006; Turner *et al.*, 2009; Richardson, 2018). When the fast and slow solar winds interact, the plasma is compressed at the boundary, increasing the density of the slow solar wind region. The kinetic energy of the plasma of the fast solar wind is converted into thermal energy, which leads to heating and a decrease in plasma density (Akasofu, 1981; Balogh *et al.*, 2000; Turner *et al.*, 2009; Richardson, 2018). Many CIR storms occur during the decline of the solar cycle, and occur every 27 days (solar rotation period) (Borovsky and Denton, 2006; Richardson, 2018).

2.3.2 Geomagnetic Storm Indices

The most commonly used storm time indices are the Dst and the Kp.

Figure 2.7: An example of SYM-H and Dst indices for 16-19 March 2015 .

Disturbance Storm-Time Index

The Disturbance storm time (Dst) index measures the strength of the Earth's equatorial magnetic field due to particle injection into the magnetosphere (Tsurutani *et al.*, 1997; Echer *et al.*, 2011). During the main phase of a geomagnetic storm, particles are injected into the magnetosphere and ring current increase. As the ring current increases, Dst decreases. The ring current around the Earth produces a magnetic field that is the exact opposite of the Earth's magnetic field, resulting in a weakening of the Earth's magnetic field (Davies, 1990; Tsurutani, 2001; Parkinson, 1983; Campbell, 2001). The Dst index is expressed in nanotesla (nT) and four near-equatorial geomagnetic observatories are used to measure hourly average values of the horizontal component of the Earth's magnetic field Campbell (1997). The Dst index only describes the average disturbance of the zonal, not its spatial dependency. The Dst index is defined by the following formula

$$Dst(t) = \frac{1}{N}\sum_{n=1}^{N}\frac{\Delta H - H_q}{cos\lambda} \tag{2.5}$$

where λ denotes the geomagnetic latitude of the station, ΔH and H_q are the horizontal components of the magnetic field disturbance on the quietest day at a particular station and N is the total number of stations. The $cos\lambda$ coefficient aims to normalise magnetic disturbances to the values at the equator at various latitudes (Kamide and Maltsev, 2007). The Dst index is calculated from four ground-based magnetic stations: Hermanus (33.3°S, 80.3° in magnetic dipole latitude and longitude), Kakioka (26.0°N, 206.0°), Honolulu (21.0°N, 266.4°), and San Juan (29.9°N, 3.2°). These four observatories were chosen because they are close enough to the magnetic equator and they are thus less affected by the auroral current system. Secondly, they are so far away from the magnetic equator that they are less influenced by the equatorial electrojet current flowing through the ionosphere (Wanliss and Showalter, 2006).

Geomagnetic storms are categorised as weak, moderate, strong, severe and great storms based on their Dst values. For example, a storm with a Dst value of between -30 nT and -50 nT is considered weak, of between -50 nT and -100 nT moderate, of between -100 nT and -200 nT strong, of between -200 nT and -350 nT severe, and < -350 nT great (Loewe and Prölss, 1997). A Dst range of between -20 and 20 nT is the criterion for geomagnetically quiet conditions (Walker *et al.*, 2013). Both Dst and SYM-H were developed to measure the intensity of the ring current during storms. The calculation of the SYM-H index is based on the data from six ground-based magnetic stations. The procedure for calculation is as follows (Iyemori, 1990; Wanliss and Showalter, 2006): (1) The average effect of the ionospheric dynamo current (Sq) is subtracted using the data for the five quiet days of the month; that is, the average Sq pattern for the quiet five days is subtracted. (2) For the horizontal component (H), the Sugiura's derived Dst index (Sugiura and Poros, 1971; Sugiura and Kamei, 1991) is used to deduct the effects of ring current on five quiet days to determine the baseline. (3) The background field is then subtracted to obtain the monthly disturbance field at 1-min intervals. These calculations are followed by a coordinate transformation to a magnetic dipole system. The implicit assumption is that the ring current flows parallel to the dipole equatorial plane (Iyemori, 1990; Wanliss and Showalter, 2006). (4) Then the six-station average of the longitudinal symmetrical magnetic field component is calculated from the average value of the perturbation component every minute. Finally, do a latitudinal correction, as was done in calculating Dst. The final calculation involves division by the average value of the cosines of the dipole latitude (Wanliss and Showalter, 2006). Figure 2.7 illustrates the SYM-H and Dst indices for 16-19 March 2015. The main difference between the 1-minute SYM-H and the hourly Dst index is the time resolution, and the effects of changes in solar wind pressure can be seen more clearly on the SYM-H than on the hourly Dst index (Iyemori, 1990; Wanliss and Showalter, 2006). The effects of substorms are clearly observed in the Dst, but there is no large resolution. This is due to the fact that the time scale of the substorm is usually about 1 hour, so most of its higher frequency fluctuations are averaged in the Dst index calculation (Iyemori and Rao, 1996; Wanliss and Showalter, 2006).

Kp Index

The Kp index measures the variability of the Earth's magnetic field at the mid-latitudes. The Kp index is derived from the standardized K index of the network of geomagnetic observatories. The K index is based on the more disturbed observed horizontal magnetic field component after eliminating the daily quiet variations (Bartels *et al.*, 1939; Menvielle and Berthelier, 1991). After removing local time and seasonal effects, concurrent values from all 13 subauroral ground-based magnetometer stations are used to create the global Kp index (Bartels *et al.*, 1939; Elliott *et al.*, 2013). The Kp index is constructed by first normalising the observatory's K index to the Ks value (standardized K index). Each observatory compiles a table that creates a uniform distribution of Ks values for each observatory every 3 hours for each season. The table for each observatory converts the integral K value (0-9) into 28 fractional Ks values in units of 0, $\frac{1}{3}$, $\frac{2}{3}$, 1,...,9. Therefore, Kp is the arithmetic average of the 3-hour standardized K indices for the 13 mid-latitude observatories presented in Table

2.1 and Figure 2.8. Figure 2.8 shows the locations of the 13 observatories involved in the computation of the Kp index. The Kp index ranges from 0 to 9, where Kp = 0 indicates no magnetic activity, Kp = 5 implies a minor activity, and Kp = 9 indicates extreme magnetic activity. For more information about the computation of Kp, readers are referred to Bartels *et al.* (1939), Maynard and Chen (1975) and Matzka *et al.* (2021). Kp is vital for physics-based geospace models, e.g. the Wideband Ionospheric Scintillation Model (Secan *et al.*, 1997; Matzka *et al.*, 2021). The Kp is used to describe and forecast the intensity, latitude and local time of irregularities and scintillation in global navigational system signals (Secan *et al.*, 1997; Xiong *et al.*, 2016, 2018). Kp also plays a vital role in low-Earth orbit space safety and operational space traffic management systems (Horne *et al.*, 2013; Berger *et al.*, 2020).

Table 2.1: Geographic (GLat & GLon) and geomagnetic (GMLat & GMLon) coordinates of 13 observatories that contribute to the calculation of the Kp index

Code	Name	Country	GLat	GLon	GMLat	GMLon
ESK	Eskdalemuir	Scotland	55.32	356.80	57.90	83.90
LER	Lerwick	Scotland	60.13	358.82	62.00	89.20
WNG	Wingst	Germany	53.75	9.07	54.10	95.10
NGK	Niemegk	Germany	52.07	12.68	51.90	97.70
HAD	Hartland	England	50.97	355.52	54.00	80.20
MEA	Meanook	Canada	54.62	246.67	61.70	305.70
OTT	Ottawa	Canada	45.40	284.45	55.80	355.00
SIT	Sitka	Alaska	57.05	224.67	60.40	279.80
UPS	Uppsala	Sweden	59.90	17.35	58.50	106.40
BFE	Brorfelde	Denmark	55.62	11.66	55.40	98.60
EYR	Eyrewell	New Zealand	-42.58	172.35	-47.20	253.80
FRD	Fredericksburg	USA	38.20	282.63	48.60	353.10
CNB	Canberra	Australia	-34.70	149.00	-42.90	226.80

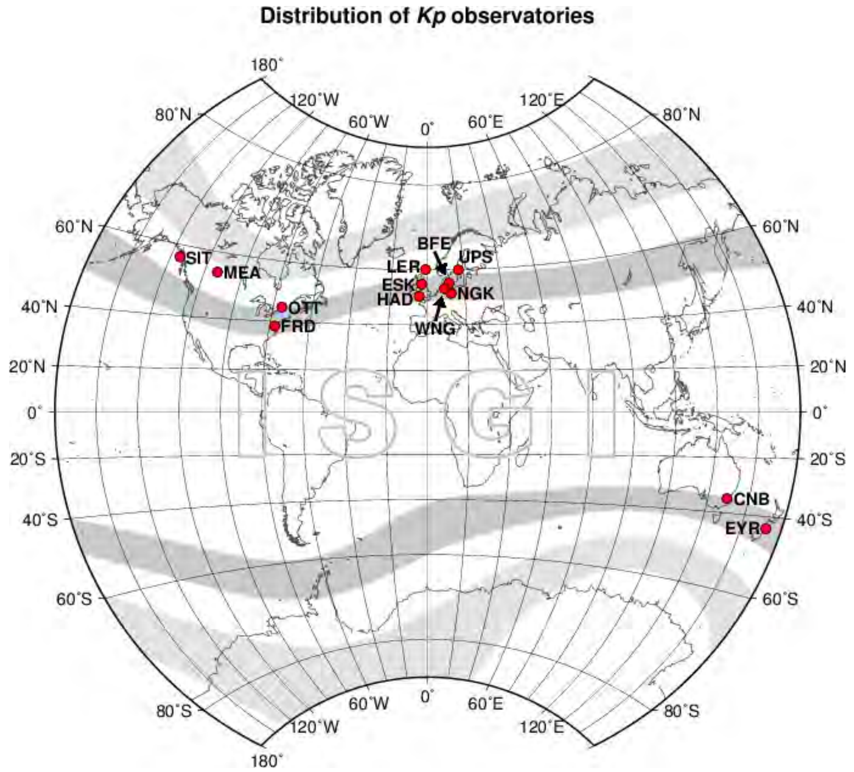

Figure 2.8: A map showing the network of magnetometers that are used to derive the Kp index (`http://isgi.unistra.fr/index.php`).

Auroral Electrojet (AE) Index

The Aurora Electrojet (AE) index is designed to provide a global, quantitative measure of the magnetic activity of the auroral zone, generated by the increase in ionospheric current flowing below and inside the auroral oval (Davies, 1990; Nakamura *et al.*, 2015). The AE index is based on measurements from selected stations in the auroral and slightly subauroral zones with the purpose of providing evenly spaced coverage around the auroral zone (Rostoker, 1972; Davies, 1990). Table 2.2 shows the 12 stations used to calculate the AE index. AE is derived from the horizontal (H) component at an observatory at latitudes near the auroral zone. The AU and AL indices are defined by the maximum and minimum values of the data, respectively (Nakamura *et al.*, 2015). As a function of universal time, the symbols AU and AL represent the values that form the upper and lower envelopes of the superimposed plots of all the data from these stations (Davies, 1990; Nakamura *et al.*, 2015). The AU and AL indices represent the maximum intensities of the eastward and westward electrojet currents in the auroral ionosphere, respectively (Davis and Sugiura, 1966; Davies, 1990; Nakamura *et al.*, 2015). Hence, the AE index is described by the following formula

$$AE = AU - AL, \tag{2.6}$$

while the AO index, defined as

$$AO = \frac{AU + AL}{2}, \tag{2.7}$$

provides a measure of the equivalent zonal current (Davis and Sugiura, 1966; Davies, 1990). The AE index represents the sum of the maximum current intensities of two opposing currents at two different moments in local time and is commonly used as an index of global auroral activity (Nakamura *et al.*, 2015). Figure 2.9 shows the AE, AU, AL and AO indices for 14-17 May 2005.

Table 2.2: The 12 observatories that are used to construct the AE index (`https://wdc.kugi.kyoto-u.ac.jp/aedir/ae2/AEObs.html`).

Observatory	Code	GLat (°N)	GLon (°E)	GMLat(°N)	GMLon (°E)
Abisko	ABK	68.36	18.82	66.04	115.08
Dixon Island	DIK	73.55	80.57	63.02	161.57
Cape Chelyuskin	CCS	77.72	104.28	66.26	176.46
Tixie Bay	TIK	71.58	129.00	60.44	191.41
Cape Wellen	CWE	66.17	190.17	61.79	237.10
Barrow	BRW	71.30	203.25	68.54	241.15
College	CMO	64.87	212.17	64.63	256.52
Yellowknife	YKC	62.40	245.60	69.00	292.80
Fort Churchill	FCC	58.80	265.90	68.70	322.77
Poste-de-la-Baleine	PBQ	55.27	282.22	66.58	347.36
Narsarsuaq	NAQ	61.20	314.16	71.21	36.79
Leirvogur	LRV	64.18	338.30	70.22	71.04

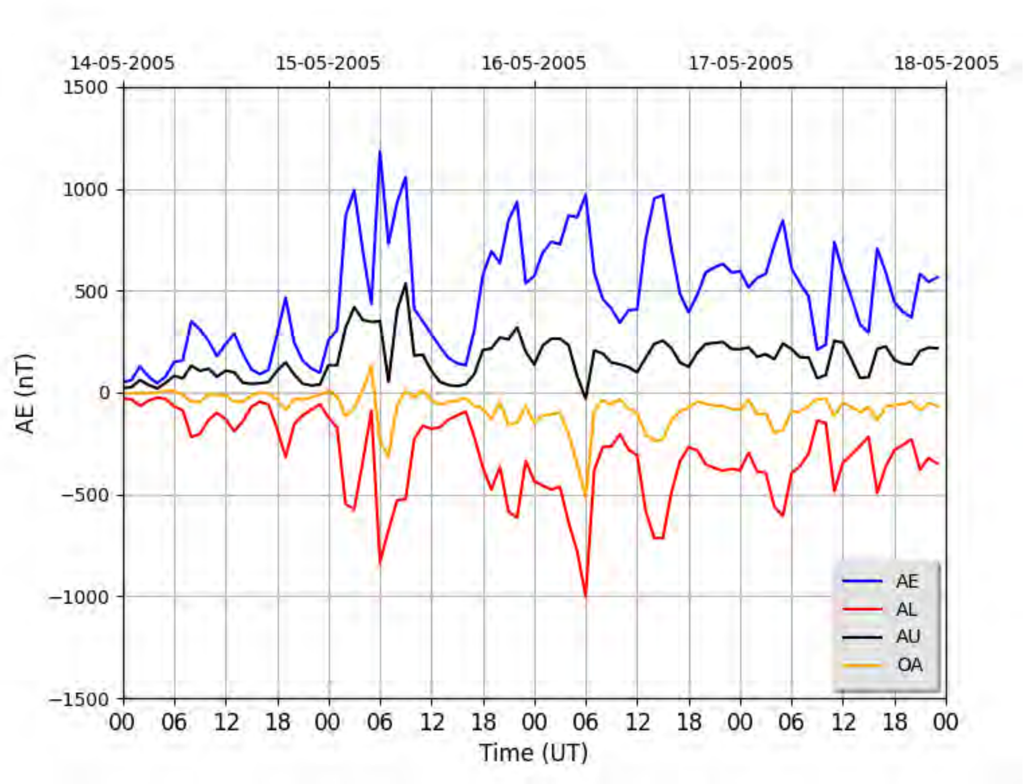

Figure 2.9: The AE, AU, AL and AO indices for 14-17 May 2005 .

Polar Cap (PC)

The PC index is a characteristic of the polar cap's magnetic activity produced by the solar wind acting on the Earth's magnetosphere. The northern and southern polar cap indices (PCN and PCS), are derived from magnetic data of only two stations, namely Thule and Vostok, which are located in the northern and southern near-pole regions (Troshichev *et al.*, 1988, 2006; Borries *et al.*, 2016; Stauning, 2020). The convection of the plasma and magnetic field across the poles (noon to midnight) is driven by the interaction of the solar wind and the magnetosphere creating electric (Hall) currents in the upper atmosphere. These currents then cause magnetic fluctuations near the ground (Troshichev *et al.*, 1988, 2006; Stauning, 2020). To derive the PC index from the recorded horizontal magnetic field vector series, F, the horizontal magnetic variations,

$$\Delta F = F - F_{RL}, \tag{2.8}$$

for the non-perturbative reference level (RL), F_{RL}, are projected in the spatial direction, which is supposed to be perpendicular to the current associated with transpolar convection, in order to focus on the effects of the solar wind (Stauning, 2013, 2020). The best direction is characterised through its angle, φ , to the E-W direction. Next, the ΔF_{PROJ} value is then scaled so that the PC index averages equal to the solar wind merging electric field E_m,

$$E_m = V_{SW}(B_Z^2 + B_Y^2)^{\frac{1}{2}} sin^2(\frac{\varphi}{2}), \tag{2.9}$$

and is calculated for each month and UT hour (Kan and Lee, 1979; Troshichev *et al.*, 2006; Stauning, 2020), where V_{SW} is velocity of the solar wind, B_Z and B_Y are the components of the interplanetary magnetic field (IMF), and φ is the angle between the IMF transverse component and the geomagnetic dipole (Troshichev *et al.*, 2006). Thus,

$$PC = (\Delta F_{PROJ} - \beta)\alpha \approx \xi E_m, \tag{2.10}$$

where ξ is just a scale coefficient ($\xi = 1\text{m/mV}$). The optimum angle φ and propagation delay τ between the reference position of the solar wind data and the position of the relevant effect in the polar cap are both estimated from the search for the optimum correlation between E_M and ΔF_{PROJ}. The calibration constant, slope α and intercept β are determined by a linear regression between ΔF_{PROJ} and E_M over the extended epoch of past data (Stauning, 2013, 2020). Figure 2.10 illustrates the PCN and PCS indices for 07-08 April 2021.

In 2013 the International Association of Geomagnetism and Aeronomy recommended that the international scientific community use the PC index. The procedure adopted by the National Space Institute, Technical University of Denmark (DTU) and Arctic and Antarctic Research Institute (AARI, Russian Federation) provides online calculation of the PCS and PCN indices, corresponding to geoeffective interplanetary electric field values, irrespective of the time, season and solar cycle (Borries *et al.*, 2016; Stauning, 2020).

This thesis made use of the Dst and Kp indices to identify the geomagnetically quiet and disturbed days. The NASA Goddard Space Flight Center calculates AE and Dst (`https://omniweb.gsfc.nasa.gov/`).

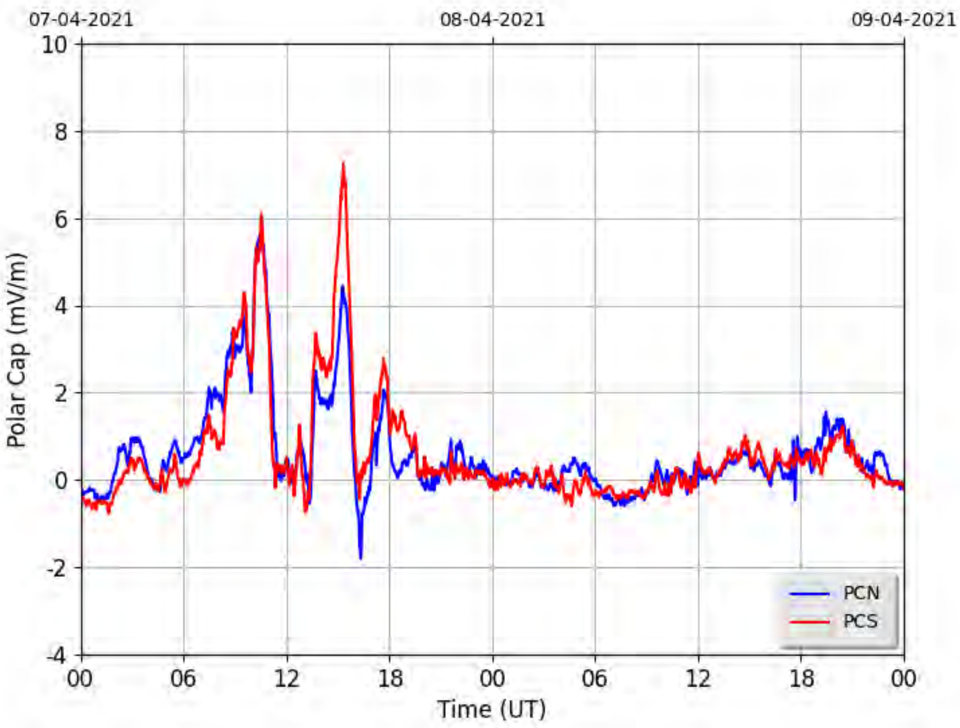

Figure 2.10: PCN and PCS indices for 07-08 April 2021 .

2.3.3 Phases of Geomagnetic Storms

The geomagnetic storm usually has three phases: initial phase, main phase, and recovery phase. Figure 2.11 shows the three phases of the geomagnetic storms that occurred on 14-17 May 2005 and 02-11 January 2008. It is worth noting that not all geomagnetic storms have three phases. The initial phase of a geomagnetic storm is characterized by a positive increase in the Dst index. The sudden change in the Dst index is due to the intense current at the magnetosphere interface caused by the rise in the dynamic pressure of the solar wind. This initiates a magnetohydrodynamic wave that later propagates into the magnetosphere (Tsurutani *et al.*, 1997). During the main phase of the geomagnetic storm, the Dst decreases until it reaches its minimum value. During main phase of the storm a ring current belt of energetic particles is formed that surrounds the Earth (Tsurutani *et al.*, 1997; Moldwin, 2008). The duration of the main phase of a CME-driven storm can last only a few hours, and in exceptional cases, up to one day (Borovsky and Denton, 2006; Matamba and Habarulema, 2018). The main phase of the CIR-driven storm can last about a day and is weak to moderate (-30 nT $>$ Dst > -75 nT) in intensity. The recovery phase of the storm is characterised by a slow increase from the minimum Dst value towards normal, around zero. This phase can last from a few hours to a week or more (Moldwin, 2008; Davies, 1990; Campbell, 2001; Matamba and Habarulema, 2018). The geomagnetic storm recovery period is longer for CIR-driven storms than for CME-driven storms. The recovery phase of a CME storm can last a day or two (Tsurutani *et al.*, 1997; Borovsky and Denton, 2006). CME-driven storms are characterised by a large maximum energy input, but relatively short duration. The CIR-driven storms, on the other hand, have a relatively small maximum energy input, but their duration is significantly longer (Borovsky and Denton, 2006; Chen *et al.*, 2014). Storms caused by CIR and CME are classified according to proton temperature, solar wind velocity, magnetic field, and proton density (Richardson and Cane, 2010; Richardson, 2018; Borovsky and Denton, 2006). CME-induced storms have stronger magnetic fields, increased solar wind velocities, lower proton temperatures, and higher proportions of alpha particles and protons (Gonzalez *et al.*, 1999; Huttunen *et al.*, 2002; Borovsky and Denton, 2006; Matamba and Habarulema, 2018).

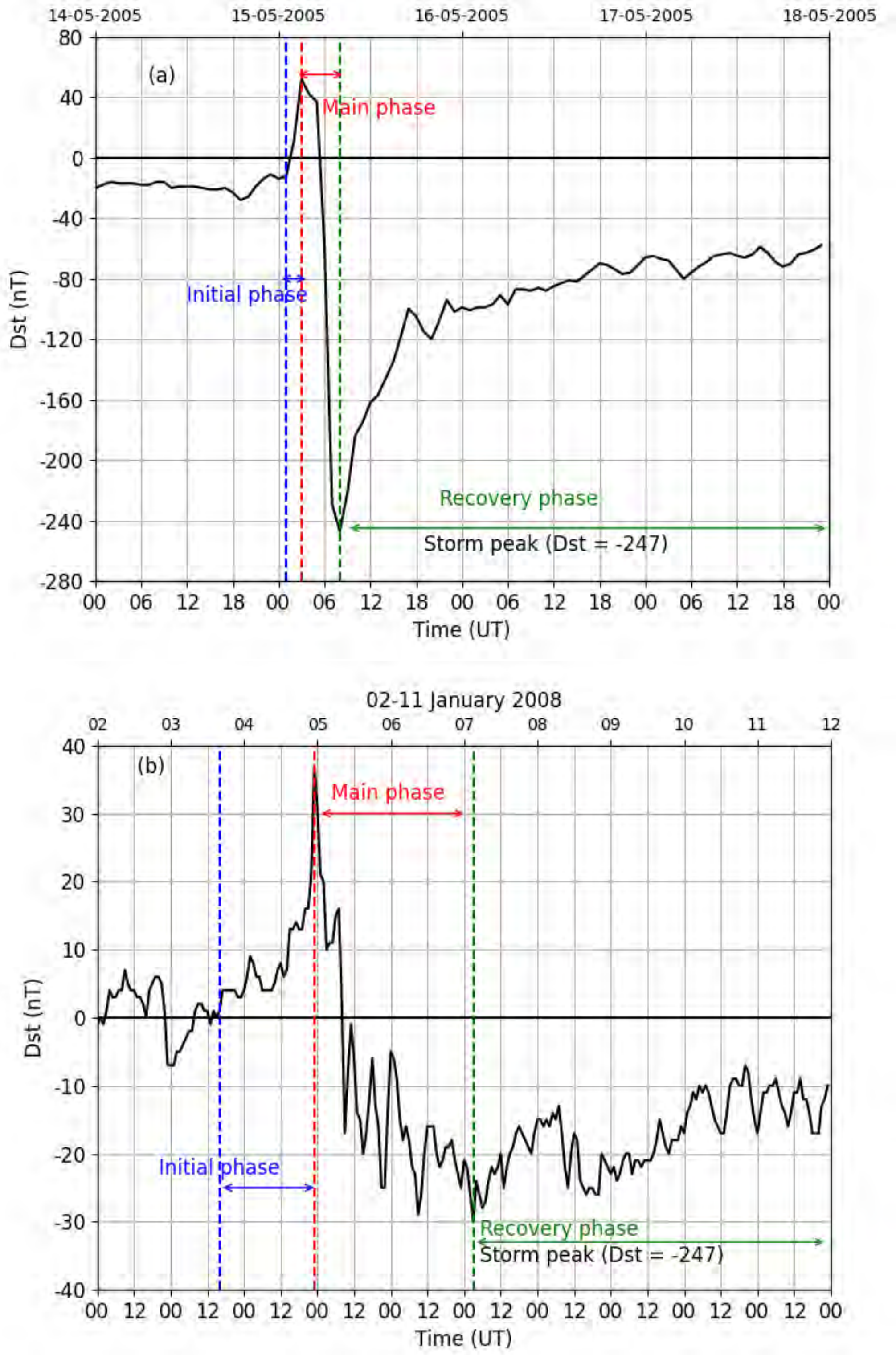

Figure 2.11: (a) CME-driven storm during 14-17 May 2005 and (b) CIR-driven storm during 02-11 January 2008, measured by Dst index.

Chapter 3

Atmospheric Gravity Waves

This chapter describes the atmospheric conditions required for the propagation of atmospheric gravity waves. In addition, the derivation of dispersion relations of gravity waves to show the difference between atmospheric gravity waves and acoustic waves. Possible source mechanisms and modes of propagation of atmospheric gravity waves are discussed. The manifestation of travelling ionospheric disturbance (TIDs) by atmospheric gravity waves are discussed.

3.1 Introduction

Atmospheric gravity waves are buoyancy oscillations in a stably stratified fluid where the restoring force is gravity (Holton *et al.*, 2003; Rauber and Ramamurthy, 2015). The restoring force causes the parcel to move back into its neutral position, overshoot due to its inertia, and oscillate around its neutral position if viscous forces are sufficiently weak. Due to the local displacement of the fluid, this oscillation spreads throughout the region as a transverse waves, commonly referred to as atmospheric gravity waves (Hines, 1960; Beer, 1974; Hunsucker, 1982; Nappo, 2013). The AGWs are oscillations that cause perturbations in the atmospheric wind, temperature, density, and pressure fields (Alexander, 2003; Holton *et al.*, 2003; Nappo, 2013). AGWs can be detected directly/indirectly using arrays of pressure sensors, satellite, radar, and rocket soundings (Hunsucker, 1982; Waldock and Jones, 1986; Hocke and Schlegel, 1996; Afraimovich *et al.*, 2003; Nicolls and Heinselman, 2007; Otsuka *et al.*, 2011; Nappo, 2013; Atilaw *et al.*, 2021; Habarulema *et al.*, 2018; Katamzi-Joseph *et al.*, 2019). The AGWs have some crucial effects on the general circulation of the Earth's atmosphere. They can spontaneously accelerate the flow, causing phenomena like quasi-biennial and semiannual oscillations of the tropical middle atmosphere (Holton *et al.*, 2003; Dunkerton, 2015). AGWs also slow down the flow and the speed of the polar night jet in winter, the mesosphere jet in summer, and the upper part of the tropospheric jet stream (Holton *et al.*, 2003; Dunkerton, 2015). The AGWs propagate energy horizontally and vertically within a stably stratified fluid (Alexander, 2003; Fritts and Vanzandt, 1993; Fritts, 2015; Dunkerton, 2015). Depending on their properties, the AGWs generated in the lower atmosphere can propagate to the ionosphere. As they propagate from the lower to the upper atmosphere, they transfer energy and momentum from their origin to the ionosphere (Yiğit *et al.*, 2016). The amplitude of the AGWs generally increases with height due to the decreases in density so that a small perturbation in the middle and upper atmosphere becomes large (Fritts, 2015; Dunkerton, 2015). Small-amplitude waves in the lower atmosphere can have a massive impact at high altitudes (Alexander, 2003). Momentum irreversibly deposits in areas where waves reach large amplitudes, become locally unstable, and break via convective or shear instability (Holton *et al.*, 2003; Dunkerton, 2015). The breaking AGWs produce heating of the mean flow and induce a downward sensible heat flux (Yiğit and Medvedev, 2009; Dunkerton, 2015).

3.1.1 Atmospheric Hydrostatic Equilibrium

The atmosphere is considered a hydrostatic equilibrium fluid consisting of a mixture of gases. Even in this case, the ideal gas law applies to a reasonable approximation (Beer, 1974; Zolesi and Cander, 2014; Nappo, 2013):

$$PV = nRT \tag{3.1}$$

where P is the pressure, V is the volume, R is the universal gas constant, T is the absolute temperature and n is the number of moles of gas. Use $n = \frac{m}{M}$, where M is molecular mass and m is the total mass. Then substitute $\frac{m}{M}$ in Equation 3.1 to obtain:

$$PV = \frac{m}{M}RT, \tag{3.2}$$

and rearrange the formula to get

$$\frac{P}{RT} = \frac{m}{MV}. \tag{3.3}$$

Now, recall that density is equal to total mass divided by volume:

$$\rho = \frac{m}{V}. \tag{3.4}$$

From Equation 3.3 the term $\frac{m}{V}$ appears on right-hand side. Equations 3.4 is then substituted in the Equation 3.3 to get

$$\frac{P}{RT} = \frac{\rho}{M}. \tag{3.5}$$

Rearrange equation 3.5 in terms of P to get the following

$$P = \frac{\rho RT}{M} \tag{3.6}$$

and hence

$$P = \rho R_s T, \tag{3.7}$$

where $R_s \equiv \frac{R}{M}$ is the constant per unit mass. The value of R depends on the exact composition of the air sample under consideration (Nappo, 2013). Equation 3.7 is important to characterise the relationship between the gas's pressure, density, and temperature. With no vertical motion, the atmosphere is almost in hydrostatic equilibrium. This means there is a balance between the upward-directed pressure force and the force of gravity (Beer, 1974; Andrews, 2010; Nappo, 2013). This can be expressed as

$$dp = -\rho g dz, \tag{3.8}$$

where z is the height and g is the Earth's gravity, given by 9.8 m/s^2. The minus sign occurs because the gravitational acceleration is downward while the altitude is measured upward (Beer, 1974). Equation 3.9 can be written as

$$\frac{dp}{dz} = -\rho g, \tag{3.9}$$

and is generally known as the hydrostatic equation. Substituting Equation 3.7 into Equation 3.9 leads to

$$\frac{dp}{dz} = -\frac{pg}{R_sT}. \tag{3.10}$$

This equation can be rearranged to get

$$\frac{1}{p}\frac{dp}{dz} = -\frac{g}{R_sT}. \tag{3.11}$$

Perform the integration from the surface, where $p = p_0$ and $z = 0$, this way

$$\int_{p_0}^{p} \frac{1}{p} dp = -\frac{g}{R_sT}\int_{0}^{z} dz, \tag{3.12}$$

leads to

$$\ln\left(\frac{p}{p_0}\right) = -\frac{gz}{R_sT}. \tag{3.13}$$

Then exponentiate each side of the equation and use $e^{lnx}= x$, to obtain

$$p = p_0 e^{(-\frac{gz}{R_sT})}, \tag{3.14}$$

where p_0 is the atmospheric pressure at the ground surface. $H = \frac{R_sT}{g}$ is defined as the isothermal scale height of the atmosphere. This leads to equation 3.14 to as follow

$$p = p_0 e^{(-\frac{z}{H})}. \tag{3.15}$$

The above equation demonstrates the exponential dependence of pressure on height, which means the pressure falls by a factor of e over the height. For an isothermal atmosphere with temperature of 260 K, H is about 7.6 km (Andrews, 2010; Nappo, 2013).

3.1.2 Isothermal Buoyancy Angular Frequency

The effect of buoyancy, the driving force of atmospheric gravity waves, can be understood by considering the stable displacement of air particles in the Earth's atmosphere. Restoring force acts when the particles are displaced vertically in a stable atmosphere. Consider air particles in a stable atmosphere with a height z. Its density (ρ_0) is the same as the density (ρ) of the surroundings. Hydrostatic equilibrium is disturbed as the parcel shifts from z to $z + \Delta z$. According to Beer (1974), if the displacement is adiabatic, then the density is given by

$$\Delta\rho_a = \frac{\Delta p}{c^2} \tag{3.16}$$

where c is the speed of sound. When the environment is in hydrostatic equilibrium, then from equation 3.8, change in pressure (Δp) can be expressed by

$$\Delta p = -\rho g \Delta z. \tag{3.17}$$

Change in density (Δp) due to altitude of the surrounding atmosphere is given by

$$\frac{d\rho_0}{dz}, \tag{3.18}$$

and the displacement (Δz) and the change in density can be expressed as:

$$\Delta \rho_b = \frac{d\rho_0}{dz}\Delta z. \tag{3.19}$$

At the height $z + \Delta z$ (from equation 3.16 and 3.19), the mass density of the parcel will not be equal to the mass density of the background. The mass and density of an air parcel is expressed by the following formula:

$$\rho_0 + \Delta \rho_a = \rho_0 + \frac{d\rho_0}{dz}\Delta z. \tag{3.20}$$

Then, the restoring force acting on the fluid parcel is

$$F_b = g(\Delta \rho_b - \Delta \rho_a), \tag{3.21}$$

where (F_b) is buoyancy force (Nappo, 2013). From Newton's second law of motion it follows that

$$\rho_0 \frac{d^2 \Delta z}{dt^2} = g(\frac{d\rho_0}{dz} + \frac{\rho_0 g}{c^2})\Delta z. \tag{3.22}$$

The equation above is for simple harmonic motion in the vertical direction (Beer, 1974; Nappo, 2013). If the parcel of air is displaced vertically and is released, its motion is described as follows:

$$\Delta z(t) = Ae^{i\omega t} + Be^{-i\omega t}, \tag{3.23}$$

where A and B are constants, ω is an oscillation frequency and $i = \sqrt{-1}$. The second-order derivative of the above equation is

$$\frac{d^2 \Delta z}{dt^2} = -\omega \Delta z. \tag{3.24}$$

Equation 3.24 is then substituted in Equation 3.22 to get

$$\omega = -\frac{g}{\rho_0}(\frac{d\rho_0}{dz} + \frac{\rho_0 g}{c^2}). \tag{3.25}$$

The oscillation frequency (ω) of air parcel is sometimes called the Brunt-Väisälä frequency. The speed of adiabatic sound is described by

$$c = \sqrt{\frac{\partial p_0}{\partial \rho_0}}. \tag{3.26}$$

Assuming that air is an ideal gas, the relationship between pressure and density in the adiabatic process is defined by the following relation

$$\frac{p}{p_0} = (\frac{\rho}{\rho_0})^{\gamma}. \tag{3.27}$$

From equation 3.26 for speed of sound the following expression is derived:

$$c^2 = \frac{\gamma p_0}{\rho_0} = \gamma g H, \tag{3.28}$$

where γ is ratio of thermal capacities (specific heat) for air in the presence of constant pressure and volume (Hines, 1960; Kelley, 2009; Kirtskhalia, 2012). It can be written as

$$\gamma^2 = \frac{c_p}{c_v}. \tag{3.29}$$

Therefore, equation 3.25 can be written as

$$\omega^2 = -\frac{g}{\rho_0}\frac{d\rho_0}{dz} - \frac{g^2}{c^2}. \tag{3.30}$$

Substitution of equation 3.28 into equation 3.30 leads to

$$\omega^2 = -\frac{g}{\rho_0}(\frac{d}{dz}\frac{\gamma p}{c^2}) - \frac{g^2}{c^2}. \tag{3.31}$$

The application of the quotient rule of differentiation in the above equation leads to

$$\omega^2 = \frac{\gamma g}{\rho_0}[\frac{1}{c^2}\frac{dp_0}{dz} + \frac{p_0}{c^4}\frac{dc^2}{dz}] - \frac{g^2}{c^2}. \tag{3.32}$$

Since the atmosphere is considered to be an isothermal ideal gas, equation 3.1 and 3.28 are used in equation 3.32 to get

$$\omega^2 = \frac{\gamma gRT}{c^2 H} + \frac{g}{c^2}\frac{dc^2}{dz} - \frac{g^2}{c^2}. \tag{3.33}$$

Substitution of equation 3.28 in equation 3.33. Then, after grouping the terms, and for a perfect gas the Brunt-Väisälä frequency becomes

$$\omega^2 = \frac{g(\gamma - 1)}{c^2} + \frac{g}{c^2}\frac{dc^2}{dz} \equiv \omega_g^2 + \frac{g}{c^2}\frac{dc^2}{dz} \tag{3.34}$$

where ωg^2 is the isothermal Brunt-Väisälä frequency. If the background is isothermal, the Brunt Vaisala frequency usually uses the symbol ω_g instead of ω (Beer, 1974). This buoyantly disturbed air parcel in the atmosphere is known as an AGW and later appears as a TID in the ionosphere (Hines, 1960; Beer, 1974; Hocke and Schlegel, 1996)

3.1.3 Dispersion Relation for AGWs

The dispersion relation of gravity waves can provide insight into some of the wave characteristics, and so the derivation is outlined here. The dispersion relation of acoustic gravity waves was first derived from the hydrodynamic equations of the atmosphere by Hines (1960). Molecule viscosity and thermal conductivity cause wave energy dissipation and affect wave propagation (Hines, 1960). Only first-order perturbations are considered when passing through the AGW in a stable, stationary atmosphere (Hines, 1960; Beer, 1974; Kelley, 2009). Therefore, the relationship between the velocity, pressure, and density of the perturbed atmosphere are described by the following equations

$$p = p_0 + p_1, \tag{3.35}$$

$$\rho = \rho_0 + \rho_1 \tag{3.36}$$

and

$$U = U_0 + U_1 \tag{3.37}$$

where ρ_0 and p_0 are the unperturbed density and pressure, ρ and p the perturbed density and pressure, and U is the velocity perturbation (Beer, 1974). The first order perturbation velocity (U) has directional components x, y, z, which can be expressed as U_1x, U_1y, and U_1z. The perturbation of each parameter ($p1$, ρ_1, U_1x, U_1y, U_1z) is assumed to be proportional to $e^{i(\omega t - K_x x - K_y y - K_z z)}$, i.e.

$$p1, \rho_1, U_1x, U_1y, U_1z \propto e^{i(\omega t - K_x x - K_y y - K_z z)}, \tag{3.38}$$

where U_1x and U_1y are horizontal components. U_1z is a component of perturbation, and ω is the AGW frequency. The K_x, K_y are horizontal wave numbers of complex form, while K_z is a vertical wave number of complex form; this means that the wave can be attenuated or amplified (Hines, 1960; Beer, 1974; Nappo, 2013). For a two-dimensional wave, U_1y and K_y are set to be zero (Beer, 1974). In addition, all air movements are considered adiabatic. The Coriolis force is negligible because the Earth's rotation period is much larger than the wave period (less than 4 hours) (Beer, 1974). Under these approximations, atmospheric oscillations are governed by these three equations (Hines, 1960):

$$\rho_0 \frac{\partial U_1 z}{\partial t} = \rho g - \nabla p \tag{3.39}$$

$$\frac{\partial p}{\partial t} + U_1 z \bullet \nabla p_0 = c^2 [\frac{\partial \rho}{\partial t} + U_1 z \bullet \nabla \rho_0] \tag{3.40}$$

$$\frac{\partial p}{\partial t} + U_1 z \bullet \nabla \rho_0 + \rho_0 \nabla U_1 z = 0. \tag{3.41}$$

These are the equations for hydrostatic equilibrium, adiabatic state, and the law of conservation of mass, respectively. The solutions to these three equations have complex wavenumbers K_x and K_z associated with the solution's circular frequency through dispersion relation:

$$\omega^4 - \omega^2 c^2 (K_x^2 + K_z^2) + (\gamma - 1) g^2 K_x^2 + i \gamma g \omega^2 K_z = 0. \tag{3.42}$$

Further constraints are given by the polarization equations of pressure change, density change, horizontal and vertical motion, respectively,

$$P = \gamma \omega^2 K_z - i \gamma g \frac{\omega^2}{c^2}, \tag{3.43}$$

$$R = \omega^2 K_z + i(\gamma - 1) g K_x^2 - i \gamma g \frac{\omega^2}{c^2}, \tag{3.44}$$

$$X = \omega K_x K_z c^2 - i g \omega K_x, \tag{3.45}$$

$$Z = \omega^3 - \omega K_x^2 c^2. \tag{3.46}$$

Assuming that the wave propagates at the speed of light (c) in any direction, entirely dependent on the x-axis, then gravitational acceleration (g) is assumed to be zero. Then equation 3.42 is reduced to the equation governing sound propagation:

$$\omega^2 = (K_x^2 + K_z^2) c^2. \tag{3.47}$$

However, in the case of gravity, an examination of equation 3.42 reveals that both K_x and K_z may not have real and nonzero values in the solution. For zonal propagation, K_x must be real and is expressed as $K_x = k_x$. This is because complex or imaginary horizontal wavenumbers cause the amplitude to decay exponentially with horizontal distance. Allow the vertical amplitude to be attenuation or growth, $K_z = k_z + ik'_z$, where k'_z and k_z are real. Equating the imaginary coefficients in equation 3.42 yields:

$$-\omega^2 c^2 k_z k'_z + \gamma g \omega^2 k_z = 0. \tag{3.48}$$

Therefore, the vertical wavenumber of the wave is

$$\begin{aligned} K_z &= k_z + \frac{i\gamma g}{2c^2} \\ &= k_z + \frac{i}{2H}. \end{aligned} \tag{3.49}$$

These waves can propagate vertically. The substitution of equation 3.49 into equation 3.42 to gives the dispersion relation for internal waves:

$$\omega^4 - \omega^2 c^2 (K_x^2 + K_z^2) + (\gamma - 1) g^2 K_x^2 - \omega^2 \frac{\gamma^2 g^2}{4c^2} = 0. \tag{3.50}$$

When k_z is made the subject of the formula, equation 3.50 is written as

$$K_z^2 = (\frac{\omega_g^2 - \omega^2}{\omega^2}) K_x^2 + (\frac{\omega^2 - \omega_a^2}{c^2}), \tag{3.51}$$

where ω_a is the acoustic cut-off frequency for an isothermal atmosphere. ω_g was introduced in equation 3.34, and

$$\omega_a^2 \equiv \frac{\gamma g}{2c} \tag{3.52}$$

or a frequency lower than the isothermal Brunt-Väisälä frequency,

$$\omega_c \equiv (\gamma - 1)\frac{g}{c}. \tag{3.53}$$

for all gases $1 < \gamma < 2$, and $\omega_c < \omega_a$. No internal waves can propagate with frequencies $\omega_c < \omega < \omega_a$. The waves propagate longitudinally when the frequencies are higher than the acoustic frequency. The waves are transverse when the frequencies are below ω_c. These internal waves are atmospheric gravity waves.

3.1.4 Effects of AGWs on the Ionosphere

The continuity equation of electron density is the basis for understanding the fluctuations of the ionosphere. It represents the rate of change of electron density at each altitude as

$$\frac{dN_e}{dt} = P_e - L_e - \nabla \bullet (N_e V_e), \tag{3.54}$$

where N_e is the electron density, V_e is the velocity of electrons, and P_e and L_e, the electron production and loss rates (as explained in Section 2.2), respectively (Hooke, 1970; Beer, 1974; Kelley, 2009). The passage of gravity waves disturbs the electron density, and the electron density is divided into two parts, the background (N_{e0}) and the disturbed N'_e (Hooke, 1970). The electron density is expressed as

$$N_e = N_{e0} + N'_e. \tag{3.55}$$

Similarly, the electron velocity is expressed as

$$V_e = V_{e0} + V'_e. \tag{3.56}$$

Assuming that the perturbations of the production and loss coefficients in equation 3.54 are negligible and that the background ionosphere is windless, the perturbations are as follows

$$\frac{dN_{e1}}{dt} = -\nabla \bullet (N_{e0}V'_e). \tag{3.57}$$

The AGW-induced velocity (V'_e) can be associated with the perturbation velocity of the neutral gas (U_n) through the balance between the Lorentz force and ion drag (Beer, 1974; Kelley, 2009):

$$M_e V_d(V'_e - U_n) + e^-(V'_e \times B) = 0, \tag{3.58}$$

where B is the geomagnetic field, M_e is the electron mass, and V_d represents the electron-neutral collision frequency. The solution of equation 3.58 is described by Macleod (1966) as

$$V'_e = \frac{1}{1+r^2}[r^2 U_n + r(U_n \times b) + (U_n \times b)b], \tag{3.59}$$

where r is the ratio of ion-neutral frequency to the electron gyro-frequency, and b is a unit vector in the direction of the geomagnetic field. According to Macleod (1966), at altitudes greater than 170 km $r << 1$, and leads to

$$V'_e = (U_n \times b)b. \tag{3.60}$$

Suppose the perturbed electron density is of the following form:

$$N_{e1} \propto e^{i(\omega t + k_x x + k_y y)}. \tag{3.61}$$

According to Hooke (1970), the perturbed electron density in equation 3.57 can be expressed as

$$N_{e1} = -\frac{1}{i\omega}\nabla \bullet [N_{e0}(U_n \bullet b)b]. \tag{3.62}$$

Equation 3.62 shows that the electron density fluctuations caused by these AGWs propagate in the atmosphere. They are called travelling ionospheric disturbances in the ionosphere (Hines, 1960; Hooke, 1970; Hocke and Schlegel, 1996).

3.1.5 Modes of AGWs Propagation

Figure 3.1 shows a schematic representation of the four modes of propagation (modes 1, 2, 3 and 4) that assume propagation of AGWs in the atmosphere (Mayr *et al.*, 1991, 2013). Mode (1) is a direct gravity wave propagating quasi-horizontally in the thermosphere. These waves travel a long distance from the source at high speeds and have a long wavelength. These waves appear to propagate equatorward from either the high- or mid-latitudes (Mayr *et al.*, 1991, 2013; Hocke and Schlegel, 1996). The second upper gravity wave mode (2) propagates diagonally from the thermosphere. These waves (mode 2) have shorter vertical wavelengths (as compared to mode 1), and they attenuate as they move to the upper atmosphere due to high viscosity and thermal conduction in higher atmospheric regions (Hines, 1960; Mayr *et al.*, 1991; Hocke and Schlegel, 1996; Kelley, 2009).

AGW modes of propagation 3 and 4 propagate at a speed less than the speed of sound in the lower atmosphere. These modes (3 and 4) correspond to two TID observations classes in the ionosphere, namely medium- and large-scale TIDs (Hocke and Schlegel, 1996; Mayr *et al.*, 2013). These waves occurs randomly and have little to do with any particular atmospheric process (Beer, 1974; Mayr *et al.*, 1991; Hunsucker, 1982). Mode 3 represents wave propagation between the surface of the Earth and the lower thermosphere. Due to the low viscosity and thermal conduction of the lower atmosphere, this wave can travel long distances. Mode 4 represents a wave that bounces off the surface of the Earth and propagates into the thermosphere (Mayr *et al.*, 1991, 2013; Hocke and Schlegel, 1996).

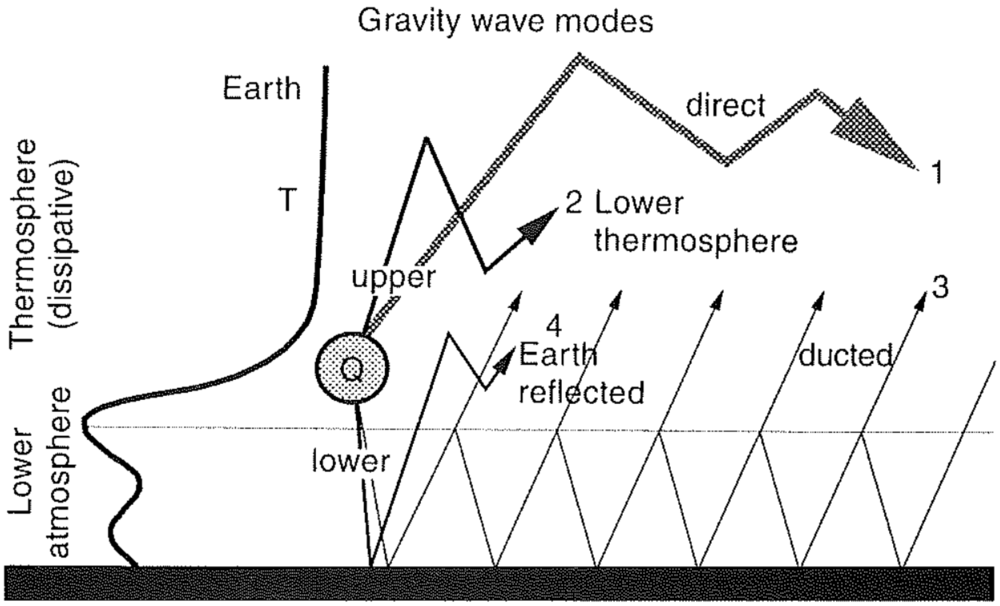

Figure 3.1: Schematic representation of the four modes of AGW propagation in the lower and upper atmosphere (Mayr *et al.*, 1991).

3.1.6 Sources of AGWs

The AGWs in the thermosphere and ionosphere can have local or distant sources, such as the presence of a geomagnetic storm, auroral activity, wind shear, large-scale convective system, solar eclipse, solar terminator, meteorological processes in the lower atmosphere and man-made nuclear explosions (Hines, 1967; Mayr *et al.*, 1984; Hajkowicz and Hunsucker, 1987; Hunsucker, 1982; Afraimovich *et al.*, 2008, 2009*a*; Vadas, 2007; Vadas and Becker, 2018; Vadas *et al.*, 2019; Hoffmann *et al.*, 2017; Katamzi-Joseph *et al.*, 2019). The boundary between day and night is known as the solar terminator. On this boundary, the rapid changes in energy input caused by solar radiation, result in a steep gradient in the Earth's atmospheric and ionospheric parameters, such as density, temperature, and pressure (Somsikov and Ganguly, 1995). A sharp gradient produces the instability and fluctuations in ionospheric plasma (Hines, 1960; Francis, 1974; Somsikov and Ganguly, 1995). As a result, the gravity response to these perturbation causes AGWs to move in the same direction as the solar terminator (Somsikov and Trotskii, 1975). Of all the sources of gravity waves, moving solar terminators have a special status because their characteristics are well-known and predictable phenomena. If the solar terminator is considered a stable and repetitive source of AGWs, information about atmospheric conditions can be derived from the medium's response to this input (Afraimovich *et al.*, 2009*a*). Afraimovich *et al.* (2003, 2009*a*,*b*) found that the solar terminator passage is associated with the generation of certain types of medium-scale ionospheric perturbations. This is the wave packet that appears as a narrowband oscillation of the TEC. MacDougall *et al.* (2009) found that solar terminators were responsible for some of the observed TIDs. Recent research has succeeded in linking TIDs to the solar terminator (Somsikov and Trotskii, 1975; Somsikov and Ganguly, 1995; Somsikov, 2011; Afraimovich *et al.*, 2003; Hernández-Pajares *et al.*, 2006; Afraimovich *et al.*, 2009*a*,*b*; MacDougall *et al.*, 2009). AGWs are also caused by natural geological hazards such as earthquakes, tsunami and volcanic eruptions (e.g., Hocke and Schlegel, 1996; Boška and Šauli, 2001; Ibrahim *et al.*, 2010; Chen *et al.*, 2017; Savastano *et al.*, 2017; Bravo *et al.*, 2022; Themens *et al.*, 2022, and references therein).

A pressure gradient is created throughout the mountain when air flows over the mountain, requiring the exchange of momentum and energy between the overlying fluid and the ground (Beer, 1974; Nappo, 2013; Charron and Brunet, 1999). Pressure is usually high on the upwind side of the mountain and low on the downwind side. Therefore, the air exerts a net force on the ground and, conversely, the drag is felt through the flow (Charron and Brunet, 1999). The rise of surface winds flowing over the terrain results in the generation of quasi-stationary waves that propagate to the upper atmosphere Nappo (2013); Heale *et al.* (2020). A unique characteristic of a mountain wave (MW) is that it can only exist in the presence of the mean background wind. When the MW reaches the zero wind region, the layer acts as a critical level and filters the wave into the mean flow (Booker and Bretherton, 1967; Heale *et al.*, 2020). As the MW approaches the critical level, it breaks down into minor vertical scales. A small vertical scale creates a large vertical gradient in the wind and temperature structure of the wave with large amplitude, which can break a MW. Breaking waves generate secondary atmospheric gravity waves (Bacmeister and Schoeberl, 1989; Satomura and Sato, 1999; Vadas and Becker, 2018, 2019; Heale *et al.*, 2020). Figure 3.2 shows a sketch of the multistep vertical coupling mechanism that links extreme mountain wave events to the tertiary gravity wave (GW) of the thermosphere (Vadas and Becker, 2019). The mountain waves (MWs) propagated to $z \sim$50–70 km before breaking and creating local body forces (horizontal black arrows). These local body forces generated secondary GWs. The secondary GWs produced tertiary GWs when they broke/attenuated in the mesosphere and thermosphere to generate a local body force at $z \sim$80–130 km. The tertiary GWs propagated to higher altitudes in the upper mesosphere and thermosphere before they dissipated (Vadas and Becker, 2019). The hotspots fir MWs are over the South American Andes, the European Alps, Greenland and the Scandinavian mountains, New Zealand, and Antarctica (Leutbecher and Volkert, 2000; Doyle *et al.*, 2005; Hoffmann *et al.*, 2013; Vadas and Becker, 2019; Vadas *et al.*, 2019; Kivi *et al.*, 2020; Heale *et al.*, 2020).

Various studies have shown that energy fluctuations in the auroral region caused by processes associated with geomagnetic storms contribute significantly to the thermospheric composition by generating atmospheric gravity waves (Hunsucker, 1982; Hocke and Schlegel, 1996; Balthazor and Moffett, 1997). Momentum transfer by the Lorentz force and heating, and particle deposition by Joule heat are two mechanisms by which equatorward AGWs are generated (Hajkowicz and Hunsucker, 1987; Hocke and Schlegel, 1996; Balthazor and Moffett, 1997; Afraimovich *et al.*, 2008; Habarulema *et al.*, 2016).

Chimonas (1970) studied the equatorial electrojet as a possible source of gravity waves during disturbed conditions. He concluded that the Lorentz force (due to the equatorial electrojet) can be enhanced, and lead to stronger coupling between neutral particles and ions in the equatorial region. The ions convey energy to the neutral particles through this process and poleward travelling gravity waves are generated. The equatorial electrojet coupling is less productive in terms of the generation of gravity waves that resulting into travelling ionospheric disturbances than the auroral electrojet (Chimonas, 1969, 1970; Knudsen, 1969).

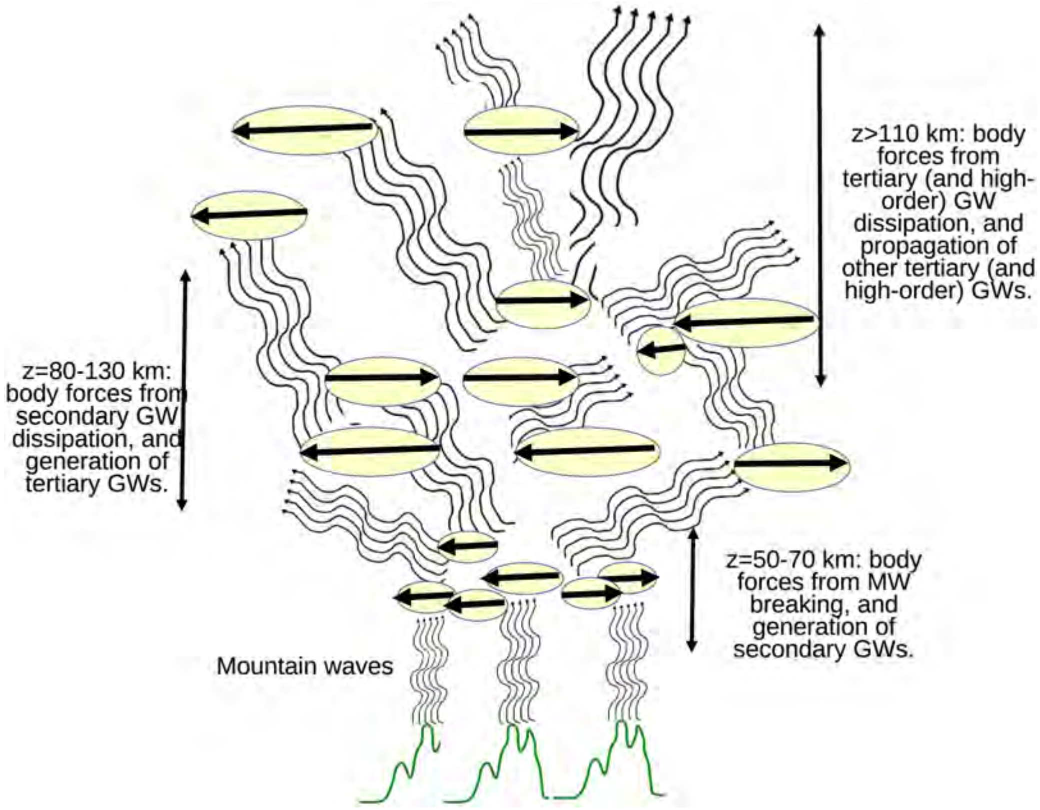

Figure 3.2: Schematic diagram of a vertical multi-level coupling mechanism linking intense mountain wave events to the tertiary GW of the thermosphere (Vadas and Becker, 2019).

3.2 Traveling Ionospheric Disturbances

TIDs are wave-like motions of the ionosphere, resulting from waves passing through the neutral atmosphere and the coupling between the ionosphere and the neutral atmosphere (McNamara, 1991). TIDs play a vital role in the dynamics of the thermosphere and ionosphere. The direction and occurrence of the TIDs show significant diurnal and seasonal variation. In general, the characteristics of the signature of TIDs are highly dependent on the ionospheric parameterisation that was used. TIDs can be divided into large-scale and medium-scale groups based on their horizontal velocity, wavelength, and period.

Medium-Scale TIDs

Medium-scale TIDs have horizontal propagation velocities of 100-250 m/s, periods of 15-60 minutes and wavelengths of approximately 100-1000 km (Mayr *et al.*, 1984; Hocke and Schlegel, 1996; Kotake *et al.*, 2007; Katamzi-Joseph *et al.*, 2019; Vadas and Becker, 2019). Over the years, medium-scale TIDs were observed by the airglow imager (Otsuka *et al.*, 2004; Shiokawa *et al.*, 2009; Vadas *et al.*, 2009; Fukushima *et al.*, 2012), incoherent scatter radar (Nicolls and Heinselman, 2007; Nishioka *et al.*, 2009; Panasenko *et al.*, 2019), ionosonde (Bowman, 1990; Kozlovsky *et al.*, 2013), HF Doppler (Waldock and Jones, 1986; Grocott *et al.*, 2013), and the total electron content technique (Afraimovich *et al.*, 2003, 2009*a*; Kotake *et al.*, 2007). The medium-scale TIDs reported by these authors were observed both during the day and at night. Medium-scale TIDs have vary by temporal and spatial characteristics. The Medium-scale TIDs occur more frequently. The incidence of medium-scale TIDs is generally higher during winter daytimes and summer nighttimes (Shiokawa *et al.*, 2009; Kotake *et al.*, 2007; Ding *et al.*, 2014; Oinats *et al.*, 2015). The observed occurrence of nighttime medium-scale TIDs decrease with a decrease in solar activity (Fukushima *et al.*, 2012). Medium-scale TIDs propagate in any direction, depending on the background tropospheric conditions of the source and the season. Chum *et al.* (2012) found that medium-scale TIDs propagate equatorward in winter, and poleward during summer. The nocturnal medium-scale TIDs occur in summer and propagate southwestward in the northern hemisphere and northeastward in the southern hemisphere (Pimenta *et al.*, 2008; Otsuka *et al.*, 2013).

It is known that the source of medium-scale TIDs may be natural processes of different origin: geomagnetic storms, auroral phenomena, tsunamis, tropospheric turbulence and jet currents, severe earthquakes, volcanic eruptions, the solar terminator, vortices, cold fronts, deep convective plume, and artificial nuclear explosions (e.g., Hines, 1960; Richmond, 1978; Hunsucker, 1982; Hocke and Schlegel, 1996; Wan *et al.*, 1998; Boška and Šauli, 2001; Afraimovich *et al.*, 2003, 2009*a*; Vadas *et al.*, 2009; Ibrahim *et al.*, 2010; Chum *et al.*, 2012; Grocott *et al.*, 2013; Otsuka *et al.*, 2011, and references therein). Medium-scale TIDs are much more susceptible to neutral winds than large-scale TIDs with long periods and high propagation speeds. Chum *et al.* (2012) found that medium-scale TIDs speeds are higher in winter than in summer. The average horizontal wavelength of nighttime medium-scale TIDs increased with decreasing solar activity (Fukushima *et al.*, 2012).

Large-Scale TIDs

Large-scale TIDs have periods that range between 30 minutes and 3 hours, horizontal phase speeds greater than 250 m/s, wavelengths of more than 1000 km, and generally propagate equatorward from both hemispheres (Hocke and Schlegel, 1996; Katamzi-Joseph *et al.*, 2019). The equatorward large-scale TIDs are associated with auroral region joule heating, particle precipitation and Lorentz-coupling processes during geomagnetically disturbed conditions (Hunsucker, 1982; Hocke and Schlegel, 1996; Balthazor and Moffett, 1997; Bruinsma and Forbes, 2008). During a geomagnetic storm, a large amount of energy is injected into the thermospheric-ionospheric system at high latitudes, resulting in increased thermospheric winds, sudden changes in neutral composition due to Joule heating, and/or particle precipitation, and leading to amplification of equatorward large-scale TIDs (Hunsucker, 1982; Richmond *et al.*, 1992; Fuller-Rowell *et al.*, 1994; Hocke and Schlegel, 1996; Balthazor and Moffett, 1997; Habarulema *et al.*, 2013). Ding *et al.* (2013) and Habarulema *et al.* (2015, 2016) reported on poleward large-scale TIDs of equatorial origin during the disturbed conditions. Habarulema *et al.* (2015, 2016) have shown that poleward large-scale TIDs could be a result of enhanced EEJ during local daytime.

Numerous studies have reported on large-scale TIDs during quiet conditions (e.g. Vadas and Liu, 2009; Vadas *et al.*, 2018; Vadas and Becker, 2019; Vadas *et al.*, 2019; Becker and Vadas, 2020). Several authors have reported on large-scale secondary AGWs due to deep convection (e.g. Vadas and Liu, 2009, 2013; Vadas *et al.*, 2014). Becker and Vadas (2020), Vadas and Becker (2019) and Vadas *et al.* (2019) suggested that large-scale TIDs during geomagnetically quiet conditions were probably launched by the tertiary GWs due to the dissipation of the secondary GWs, which are generated from the dissipation of mountain waves as a result of the excited orographic forcing. The large-scale TIDs can also be produced by rare events such as volcanic eruptions, earthquakes, rocket launches or nuclear explosions (Davies, 1990; Afraimovich *et al.*, 1992; Themens *et al.*, 2022)

Chapter 4

Data sources

This chapter describes the data sources and instruments that were used to conduct the research for this thesis. A brief introduction is given to GPS and its segments, and a description of how TEC is derived from GPS measurements. The magnetometer and Atmospheric Infrared Sounder (AIRS) observations are described.

4.1 GPS overview

The Global Positioning System (GPS) is a satellite-based navigation system developed by the United States Department of Defense (USDOD) in the early 1970s. The satellites are operated and maintained by the USDOD to accurately determine their position, speed, and time. GPS was originally developed as a military system to meet the needs of the United States military. However, it was later made available to civilians and is now a dual-use system accessible to both military and civilian users (Hofmann-Wellenhof *et al.*, 1992; Ferguson, 1997; Kumar and Moore, 2002; Misra and Enge, 2006; El-Rabbany, 2002; Mulla *et al.*, 2015). However, to maintain a military advantage, the USDOD offers two levels of service in terms of GPS positioning and timing: Precise Positioning Service (PPS) and Standard Positioning Service (SPS). It uses the precision code (P-code), one of the transmitted GPS codes. The expected position accuracy of the PPS is 16 m for the horizontal component and 23 m for the vertical component (95% confidence level) (Farrell and Barth, 1999; El-Rabbany, 2002). SPS is less accurate than PPS. SPS is a coarse acquisition (C/A) code-only positioning and timing service that is directly available to all GPS users worldwide for free. This level of service is provided on the L1 frequency, which includes C/A codes and navigation data messages (Farrell and Barth, 1999). Initially, SPS provided a positioning accuracy of 100 m for horizontal components and 156 m for vertical components (95% confidence level) (El-Rabbany, 2002). Any user with a GPS receiver near the Earth's surface can get exact continuous location, timing, and speed information from the GPS satellite. GPS is a one-way-ranging system because it serves an unlimited number of users and is used for security purposes, i.e. the user can only receive satellite signals (Ferguson, 1997; Misra and Enge, 2006; El-Rabbany, 2002).

4.1.1 GPS segments

GPS consists of three segments: space segment, control segment, and user segment (Figure 4.1). The space segment consists of at least 24 satellites (Kumar and Moore, 2002; Misra and Enge, 2006; Mulla *et al.*, 2015). Each GPS satellite broadcasts a signal consisting of two sine waves, two digital codes, and several components of the navigation message (El-Rabbany, 2002; Kumar and Moore, 2002). Code and navigation messages are added to the carrier as binary two-phase modulation. Carriers and codes are primarily used to determine the distance from a user's receiver to GPS satellites. Navigation messages include satellite coordinates (positions) as a function of time, among other information. The transmitted signal is controlled by a high-precision atomic clock mounted on the satellite (Hofmann-Wellenhof *et al.*, 1992; Ferguson, 1997; El-Rabbany, 2002).

Space Segment

The GPS consists of a constellation of at least 24 satellites orbiting the Earth at an altitude of approximately 20,000 km (Hofmann-Wellenhof *et al.*, 1992; Kumar and Moore, 2002; Misra and Enge, 2006; Mulla *et al.*, 2015). GPS satellites orbit the Earth at a tilt angle of 55° to the equator. The corresponding GPS orbital period is about 12 sidereal hours (Kumar and Moore, 2002; Leick *et al.*, 2015). These satellites are placed in space to provide the fastest and most accurate information about the Earth 24 hours a day. For continuous coverage of the world, four GPS satellites are placed in each of the six orbital planes. Figure 4.2 depicts the satellite constellation. Each satellite orbits the earth twice a day (Hofmann-Wellenhof *et al.*, 1992; Misra and Enge, 2006; El-Rabbany, 2002; Leick *et al.*, 2015).

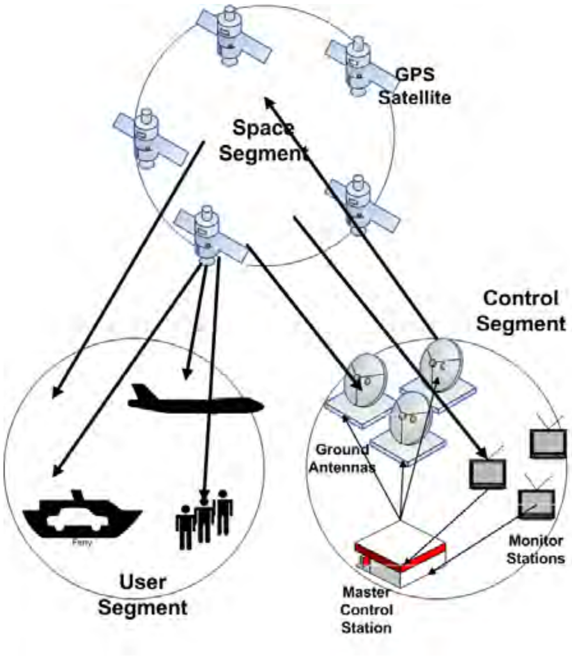

Figure 4.1: Overview of the GPS segments (U.S.Army, 1996).

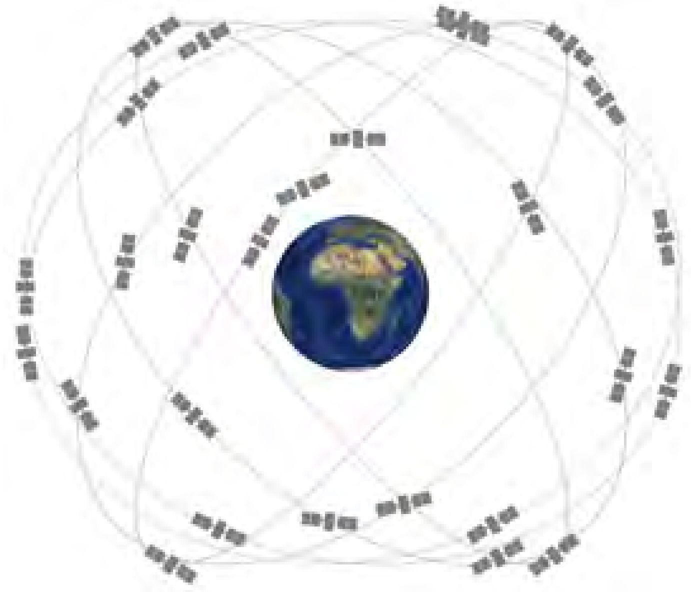

Figure 4.2: GPS constellation (`https://www.gps.gov/systems/gps/`).

Control Segment

The control segment of the GPS system consists of a worldwide network of tracking stations with a master control station in Colorado Springs, Colorado, USA. The primary responsibility of the operational control segment is to track GPS satellites to determine and predict satellite position, system integrity, satellite atomic clock operation, atmospheric data, satellite almanac, and other considerations (Hofmann-Wellenhof *et al.*, 1992; Ferguson, 1997; El-Rabbany, 2002). Figure 4.3 shows the location of the GPS control segment. There is one master control station, an alternate master control station, 11 command and control antennas, and 16 monitoring sites. Signals transmitted by GPS satellites are received through the antenna and decoded by the receiver processor. The receiver processor specifies the user's position and speed, as well as accurate time information (Hofmann-Wellenhof *et al.*, 1992; El-Rabbany, 2002; Mulla *et al.*, 2015).

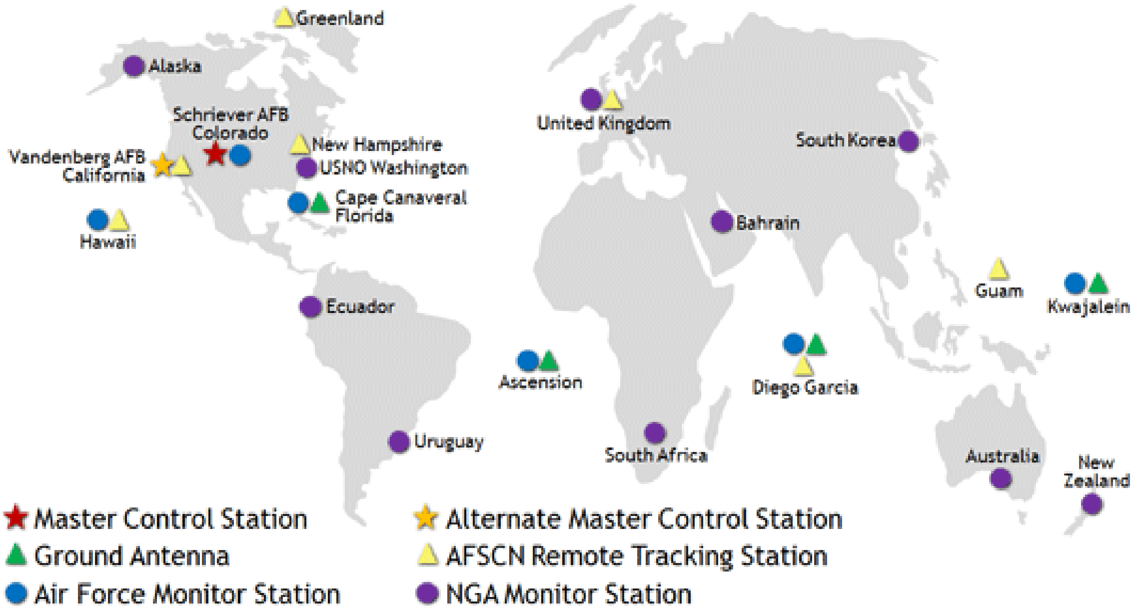

Figure 4.3: Global network of ground facilities that track the GPS satellites.

User Segment

The user segment includes all military and civilian users. Equipped with a GPS receiver and antenna, both military and civilian users can receive broadcast GPS signals. In addition, the user's location can be determined anywhere near the surface of the Earth at any time. It is important to note that the GPS system is a line-of-sight system. If the route between the receiver and the satellite is blocked, no satellite signal will be received (Farrell and Barth, 1999; Hofmann-Wellenhof *et al.*, 1992; El-Rabbany, 2002; Mulla *et al.*, 2015).

4.1.2 GPS Signal

Each GPS satellite is equipped with a caesium and/or rubidium atomic clock to provide time information for signals broadcast by the satellites. Internal clock correction is provided for each satellite clock (Farrell and Barth, 1999). Each GPS satellite transmits continuously using two L-band radio frequencies called Link 1 (L1) and Link 2 (L2) (Kumar and Moore, 2002; Misra and Enge, 2006; Mulla *et al.*, 2015; Xu and Xu, 2016). The L band covers frequencies from 1 GHz to 2 GHz. The two carrier frequencies are generated at $f_1 = 1575.42$ MHz (L1) and $f_2 = 1227.60$ MHz (L2) (Saito *et al.*, 1998; Farrell and Barth, 1999; El-Rabbany, 2002; Mulla *et al.*, 2015). These two frequencies are derived from the fundamental frequency $f_o =$ 10.23 MHz:

$$\begin{aligned} f_1 &= 154.f_0 = 1575.42MHz, \\ f_2 &= 120.f_0 = 1227.60MHz \end{aligned} \tag{4.1}$$

The L1 signal from each satellite uses binary phase-shift keying (BPSK), which is quadrature modulated by two pseudo-random noise (PRN) codes called C/A code and P-code (El-Rabbany, 2002; Misra and Enge, 2006). The C/A code is modulated on the L1 carrier only. Each satellite has a different C/A PRN code, and each C/A PRN code is approximately orthogonal to all other C/A PRN codes. The L2 signal from each satellite is BPSK modulated only by P-code (Ferguson, 1997; Farrell and Barth, 1999). P-code is a very long 10.23 MHz PRN code. In the anti-spoofing mode of operation, the P-code is encrypted into the Y-code (Farrell and Barth, 1999; El-Rabbany, 2002). The encrypted Y-code can only be used by authorized users with an encryption key. This requires anti-spoofing modules sorted by receiver channel (Farrell and Barth, 1999; Misra and Enge, 2006). The navigation message is modulated into both L1 and L2 carriers. Navigation messages are 50 bits per second (b.p.s) signals and consist of bits of data that the GPS receiver decode into satellite orbits, clock corrections, and other system parameters (Farrell and Barth, 1999).

4.1.3 Code Pseudorange Measurements

The pseudorange is a measure of the distance between a GPS receiver and a GPS satellite. Distance is measured by measuring the transmission time of GPS signals from the satellite to the antenna of the GPS receiver (Farrell and Barth, 1999; Misra and Enge, 2006; El-Rabbany, 2002). The states of the satellite clock at the time of transmission and the receiver clock at the time of signal reception are shown by t_s and t_r, respectively. The clock delay with respect to GPS system time is indicated by δ_s and δ_r. The difference in clock readings corresponds to the time-shifted Δt that aligns the satellite and reference signals during the receiver's code correlation process (Hofmann-Wellenhof *et al.*, 1992). Thus,

$$\begin{aligned} \Delta t &= t_r - t_s \\ &= [t_r(GPS) - \delta_r] - [t_s(GPS) - \delta_s] \\ &= t_r(GPS) - t_s(GPS) - \delta_s - \delta_r \\ &= \Delta t(GPS) + \Delta\delta \end{aligned} \tag{4.2}$$

where $\Delta t(GPS) = t_r(GPS)$ - $t_s(GPS)$ and $\Delta\delta = \delta_s$ - δ_r. The satellite clock bias δ_s can be modelled by a polynomial and the coefficients are transmitted in the first subframe of the navigation message. Assuming δ_s corrections are applied, $\Delta\delta$ is equal to the negative receiver clock delay (Hofmann-Wellenhof *et al.*, 1992). Multiply equation 4.2 by the speed of light (c = 3 x 10^8 m/s) to get the pseudorange (R):

$$R = c\Delta t(GPS) + c\Delta\delta. \tag{4.3}$$

The TEC can be derived from GPS pseudorange measurements. The pseudorange measurements, P_1 and P_2 at L1 and L2 are expressed (Gao *et al.*, 2002; Choi *et al.*, 2011; Sabzehee *et al.*, 2018) by

$$P_1 = \rho + c(dt - dT) + d_{orb} + d_{trop} + I_1 + b^s_{p_1} - B^r_{p_1} + \varepsilon(P_1) \tag{4.4}$$

$$P_2 = \rho + c(dt - dT) + d_{orb} + d_{trop} + I_2 + b^s_{p_2} - B^r_{p_2} + \varepsilon(P_2) \tag{4.5}$$

where ρ is the true geometric range (m) between receiver and satellite, c is the speed of light (m/s), dt is the satellite clock error with respect to GPS time (s), dT is the receiver clock error with respect to GPS time (s), d_{trop} is the tropospheric error (m), d_{orb} is the orbital error (m), I_1 and I_2 are pseudorange ionospheric delays (m) at L1 and L2, respectively, $b^s_{p_1}$ and $b^s_{p_2}$ are pseudorange satellite delays (m) at L1 and L2, respectively, $B^r_{p_1}$ and $B^r_{p_2}$ are pseudorange receiver delays (m) at L1 and L2, respectively, $\varepsilon(P_1)$ and $\varepsilon(P_2)$ are pseudorange measurement noises which include multipath errors (m). Ignoring thermal noise and multipath errors and subtracting equation 4.4 from equation 4.5, pseudorange measurements eliminate geometric range, orbital error, clock errors and tropospheric delay, resulting in a geometry-free linear combination, i.e.

$$\begin{aligned} P_2 - P_1 &= I_2 - I_1 + (b^s_{p_2} - b^s_{p_1}) + (B^r_{p_2} - B^r_{p_1}) \\ P_2 - P_1 &= I + b^s_p + B^r_p \end{aligned} \tag{4.6}$$

where $b_p = b^s_{p_2}$ - $b^s_{p_1}$ is the differential satellite delay, $B^r_p = B^r_{p_2}$ - $B^r_{p_1}$ is the differential receiver delay between frequencies L1 and L2, and $I = I_1$ - I_2 is the ionospheric delay. Hofmann-Wellenhof *et al.* (1992) defines the ionospheric delay as

$$I = \frac{40.30}{f^2} TEC, \tag{4.7}$$

where 40.30 is the constant coefficient. Then, substitute equation 4.7 into equation 4.6 to obtain:

$$P_2 - P_1 = 40.30 TEC(\frac{1}{f_2^2} - \frac{1}{f_1^2}) + b^s_p + B^r_p. \tag{4.8}$$

Solving the TEC for pseudorange measurements at two frequencies yields

$$TEC = \frac{1}{40.30}(\frac{f_1^2 f_2^2}{f_1^2 - f_2^2})[(P_2 - P_1) - (b^s_p + B^r_p)]. \tag{4.9}$$

Then, the expression of TEC derived from the pseudorange measurements is

$$TEC = 9.524[(P_2 - P_1) - (b^s_p + B^r_p)]. \tag{4.10}$$

By ignoring the bias term in above equation, TEC can be expressed in its units (TECU) as follows:

$$TEC = 9.524(P_2 - P_1), \tag{4.11}$$

where 1 TECU is equivalent to 10^{16} electrons/m^2. TEC derived from code pseudorange measurements is unambiguous, but with relatively much noise and inaccurate (Araujo-Pradere, 2005).

4.1.4 Carrier Phase Pseudorange

The carrier phase pseudorange is a measurement of the phase difference between the carrier signal generated by the receiver‘s internal oscillator and the carrier signal transmitted by the satellite (Farrell and Barth, 1999; Hofmann-Wellenhof *et al.*, 1992; El-Rabbany, 2002; Misra and Enge, 2006). The phase term is usually the unit of the cycle associated with a complete carrier wave. By shifting the phase generated by the receiver to match the received phase, the range is the total number of complete carrier cycles and fractional cycles at the receiver multiplied by the carrier wavelength (El-Rabbany, 2002; Misra and Enge, 2006). The fractional carrier phase can be measured by electronics with an accuracy greater than 1 % of the wavelength, which corresponds to millimetre precision (Xu and Xu, 2016). This is why phase measurements are more accurate than code pseudorange. Due to the ambiguity of the initial carrier phase, it is not possible to determine the total number of complete carrier cycles between the receiver and the satellite (Hofmann-Wellenhof *et al.*, 1992; El-Rabbany, 2002; Xu and Xu, 2016). Therefore, measuring the carrier phase is the same as counting the complete carrier waves and the received fractional phase (El-Rabbany, 2002; Misra and Enge, 2006; Xu and Xu, 2016). The measured carrier phase at L1 and L2 frequencies can be represented (Gao *et al.*, 2002; Choi *et al.*, 2011; Sabzehee *et al.*, 2018) by

$$\phi_1 = \rho + c(dt - dT) + d_{orb} + d_{trop} + \lambda_1 N_1 - I_1 + b^s_{\phi_1} - B^r_{\phi_1} + \varepsilon(\phi_1) \tag{4.12}$$

$$\phi_2 = \rho + c(dt - dT) + d_{orb} + d_{trop} + \lambda_2 N_2 - I_2 + b^s_{\phi_2} - B^r_{\phi_2} + \varepsilon(\phi_2) \tag{4.13}$$

where λ_1 and λ_2 are carrier signal wavelengths at L1 and L2 frequencies respectively, N_1 and N_2 are carrier phase integer ambiguities, I_1 and I_2 are carrier phase ionospheric delays, $b^s_{\phi_1}$ and $b^s_{\phi_1}$ are carrier phase satellite delays or interfrequency biases (m), $B^r_{\phi_1}$ and $B^r_{\phi_1}$ are carrier phase receiver delays (m), $\varepsilon(\phi_1)$ and $\varepsilon(\phi_2)$ include the carrier phase measurement noises with multipath errors (m). Like the code pseudorange measurements, the TEC can be extracted from the carrier phase measurement by means of the following equation:

$$TEC = \frac{1}{40.30}\left(\frac{f_1^2 f_2^2}{f_1^2 - f_2^2}\right)[(\phi_2 - \phi_1) - (b^s_p + B^r_p)]. \tag{4.14}$$

Thus the expression of TEC derived from the carrier phase measurements is

$$TEC = 9.524[(\phi_2 - \phi_1) - (b^s_p + B^r_p)]. \tag{4.15}$$

Solving for a TEC value independent of ambiguities and biases gives

$$TEC = 9.524(\phi_2 - \phi_1), \tag{4.16}$$

which is ambiguous but precise (Araujo-Pradere, 2005)

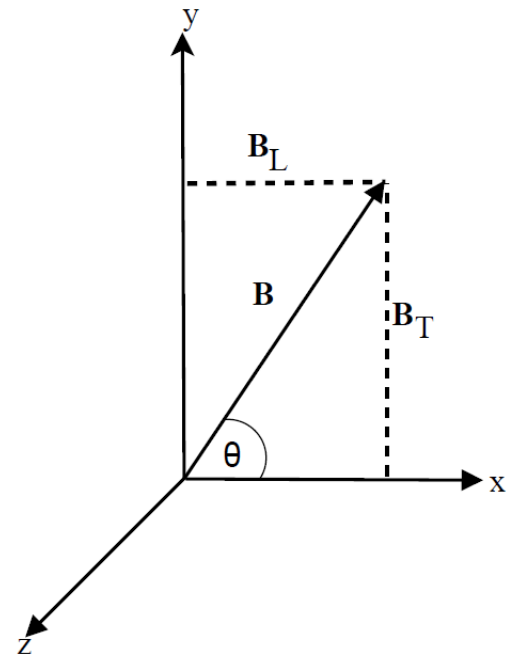

Figure 4.4: A schematic illustration of the system of orthogonal axes (Davies, 1990).

4.2 The effects of the ionosphere on GPS

GPS satellites generate signals that reach the GPS receiver through the ionosphere. These emitted signals pass through the ionosphere at the speed of light (Misra and Enge, 2006). As GPS signals propagate through the ionosphere, they bend according to Fermat's principle. Fermat's principle states that "of all the paths that electromagnetic waves follow, GPS signals, radio waves, or light waves that travel from one point to another follow the path in the shortest amount of time" (Hofmann-Wellenhof *et al.*, 1992). In the ionosphere, the propagation of radio waves in the Earth's magnetic field, is expressed by Appleton Lassen's equation (Rishbeth and Garriott, 1969). This equation expresses the refractive index μ as follows (Rishbeth and Garriott, 1969):

$$\mu^2 = 1 - \frac{X(1-X)}{(1-X) - \frac{1}{2}Y_T^2 \pm [\frac{1}{4}Y_T^2 + (1-X)^2 Y_L^2]^{\frac{1}{2}}}. \tag{4.17}$$

The above equation is also known as Appleton-Hartree formula (Zolesi and Cander, 2014), where

$$\begin{aligned} X &= \frac{N_e e^2}{m_e \omega^2 \epsilon_0} = \frac{\omega_p^2}{\omega^2} \\ Y_L &= \frac{eB_L}{M_e \omega} = \frac{\omega_{ce}}{\omega} \\ Y_T &= \frac{eB_T}{m_e \omega} \\ Z &= \frac{v}{\omega}, \end{aligned}$$

and B is the geomagnetic field strength, N_e is the electron density, e is the electron charge (-1.602 $\times$ 10^{-19} C), ϵ_0 (8.854 $\times$ 10^{-12} Fm^{-1}) is the electric permittivity of free space, m_e (9.11 $\times$ 10^{-31} kg) is the mass of the electron, ω is the angular wave frequency, ω_p is angular plasma frequency and v is the collision frequency of electrons with heavy particles, $Y_L = Y \cos\theta$ and $Y_T = Y \sin\theta$, where the two subscripts L and T refer to the longitudinal and transverse components of the imposed magnetic field, and θ is the angle between the direction of propagation of the radio waves and the Earth's magnetic field, as schematically illustrated in Figure 4.4 (Rishbeth and Garriott, 1969; Davies, 1990). Figure 4.4 shows a schematic illustration of the system of orthogonal axes (Davies, 1990). The plus sign refers to the ordinary wave and the minus sign refers to the extra-ordinary wave (Rishbeth and Garriott, 1969). Ignoring the magnetic field assumption for Y = 0, equation 4.17 can be reduced to

$$\begin{aligned} \mu^2 &= 1 - \frac{X(1-X)}{1-X} \\ &= 1 - X. \end{aligned} \tag{4.18}$$

Solving equation 4.18 by expansion, results in

$$\mu = 1 - \frac{1}{2}X + \frac{\frac{1}{2}(\frac{1}{2}-1)}{2!}X^2 + ... \tag{4.19}$$

The higher order powers are ignored, since their contribution generally is much smaller than the first order term at higher frequencies in the ionosphere. The refractive index may be approximated as:

$$\begin{aligned} \mu &\approx 1 - \frac{1}{2}X \\ &= 1 - \frac{1}{2}\frac{\omega_p^2}{\omega^2}, \end{aligned} \tag{4.20}$$

where

$$\begin{aligned} \omega_p^2 &= 2\pi f_p \\ \omega^2 &= 2\pi f, \end{aligned} \tag{4.21}$$

f_p is the plasma frequency (Hz), and f is the signal carrier frequency (Hz). Then, substitute 4.21 into equation 4.20 to obtain

$$\begin{aligned} \mu &\approx 1 - \frac{1}{2}(\frac{2\pi f_p}{2\pi f})^2 \\ &\approx 1 - \frac{1}{2}\frac{f_p^2}{f^2}. \end{aligned} \tag{4.22}$$

According to Rishbeth and Garriott (1969) plasma frequency is expressed as

$$f_p^2 = \frac{N_e e^2}{4\pi^2 m_e \epsilon_0}, \tag{4.23}$$

and then, becomes

$$\begin{aligned} f_p^2 &= \frac{(-1.602 \times 10^{-19}C)^2}{4\pi^2(9.11 \times 10^{-31}kg)(8.854 \times 10^{-}12Fm^{-1})}N_e \\ &= 80.594N_e. \end{aligned} \tag{4.24}$$

Substitute equation 4.24 into equation 4.22 to get

$$\begin{aligned} \mu &\approx 1 - \frac{1}{2}\frac{80.594N_e}{f^2} \\ \mu_\phi &\approx 1 - \frac{40.30N_e}{f^2} \end{aligned} \tag{4.25}$$

Thus, the group refractive index is written in terms of the phase refractive index as (Hofmann-Wellenhof *et al.*, 1992)

$$\mu_g = \mu_\phi + f\frac{d\mu_\phi}{df}. \tag{4.26}$$

The differentiation of the phase refractive index, leads to

$$d\mu_\phi = \frac{40.30N_e}{f^3}df \tag{4.27}$$

Substitute equation 4.25 and equation 4.27 into equation 4.26 to get the group refractive index

$$\mu_g = 1 + \frac{40.30N_e}{f^2}. \tag{4.28}$$

Thus, the phase and group velocity of the wave is expressed as

$$\begin{aligned} v_\phi &= \frac{c}{1 - \frac{40.30N_e}{f^2}} \\ v_g &= \frac{c}{1 + \frac{40.30N_e}{f^2}} \end{aligned} \tag{4.29}$$

where c is the speed of light. Thus, conventionally, the phase and group refractive indices are written as

$$\begin{aligned} n_\phi &= 1 - \frac{40.30N_e}{f^2} \\ n_g &= 1 + \frac{40.30N_e}{f^2} \end{aligned} \tag{4.30}$$

where n_ϕ and n_g are the phase and group refractive indices, respectively. The signal transmitted by GPS satellites is transmitted to the GPS receiver through the ionosphere. Due to the non-uniform composition of the ionosphere, the time it takes for a GPS signal to reach the receiver from a satellite (τ) is longer than the time it takes for the same signal to pass through a vacuum (τ_0) (Hofmann-Wellenhof *et al.*, 1992; Misra and Enge, 2006). The difference between these times, $\Delta\tau = \tau$ - τ_0, is known as the ionospheric time delay. The propagation time of the radio signal from the satellite to the receiver is determined by integrating the index of the refraction profile along the signal path (Misra and Enge, 2006):

$$\tau = \frac{1}{c}\int_S^R n(l)\,dl \tag{4.31}$$

where $n(l)$ represents the refractive index of the medium, c is the speed of light in a vacuum, S represents the satellite and R represents the receiver. If the ionosphere behaves like a vacuum, the time it takes for the signal to travel the same distance is

$$\tau_0 = \frac{1}{c}\int_S^R 1\,dl \tag{4.32}$$

An expression for excessive delay in signal propagation due to refraction may be written as

$$\Delta\tau = \frac{1}{c}\int_S^R [n(l) - 1]\,dl \tag{4.33}$$

while the corresponding delay in path length is expressed by:

$$\Delta\rho = \int_S^R [n(l) - 1]\,dl \tag{4.34}$$

Substituting equation 4.30 into equations 4.33 and 4.34, it follows that the excess phase delay (seconds) experienced by a signal as it propagates through the ionosphere, is

$$\begin{aligned} \Delta\tau_\phi &= -\frac{1}{c}\int_S^R \frac{40.30N_e(l)}{f^2}\,dl \\ &= -\frac{40.30}{cf^2}TEC \\ I_\Phi &= c\Delta\tau_\phi \\ &= -\frac{40.30}{f^2}TEC. \end{aligned} \tag{4.35}$$

Similarly, group delay is expressed in seconds and in meters as follows:

$$\begin{aligned} \Delta\tau_g &= \frac{40.30}{cf^2} TEC \\ I_\rho &= \frac{40.30}{f^2} TEC \end{aligned} \tag{4.36}$$

where TEC is defined as the total number of electrons integrated along the path from the receiver to each GPS (Hofmann-Wellenhof *et al.*, 1992; Misra and Enge, 2006). Mathematically, TEC is represented by

$$TEC = \int_S^R N_e \, dl \tag{4.37}$$

where N_e is the electron density (Hofmann-Wellenhof *et al.*, 1992; Araujo-Pradere, 2005; Misra and Enge, 2006). TEC as an indicator of ionospheric variation and is derived from free electron modified GPS signals (Hofmann-Wellenhof *et al.*, 1992). TEC measured along the signal path from the satellite to the receiver is called the Slant Total Electron Content (STEC). STEC depends on the raypath geometry through the ionosphere whereby an equivalent vertical value of TEC (VTEC), which is independent of the elevation of the raypath, is calculated (Hofmann-Wellenhof *et al.*, 1992; Silwal *et al.*, 2021). VTEC is calculated by projecting diagonally and vertically by means of a thin shell model and assuming an altitude of 350 km, according to the method of Klobuchar (1987). Figure 4.5 shows the geometry for the projection of STEC measured along the satellite line of sight onto a VTEC measurement at the ionospheric piercing point (IPP). The IPP is the intersection of the GPS signal and the ionospheric shell (Hofmann-Wellenhof *et al.*, 1992). The conversion of STEC into VTEC is expressed (Hofmann-Wellenhof *et al.*, 1992; Silwal *et al.*, 2021) by

$$VTEC = STEC \times \cos\chi \tag{4.38}$$

where

$$\begin{aligned} \sin\chi &= \frac{R_E}{R_E + h} \cos\theta \\ \cos\chi &= \sqrt{1 - (\frac{R_E}{R_E + h} cos\theta)^2}. \end{aligned} \tag{4.39}$$

Thus,

$$VTEC = STEC \times \cos[sin^{-1}(\frac{R_E}{R_E + h})] \tag{4.40}$$

where R_E (∼6,371 km) is the Earth's radius, θ is the elevation angle of the satellite (degrees), χ is the zenith angle (degrees), h is the assumed height of the ionosphere, usually assigned a value of 350 km.

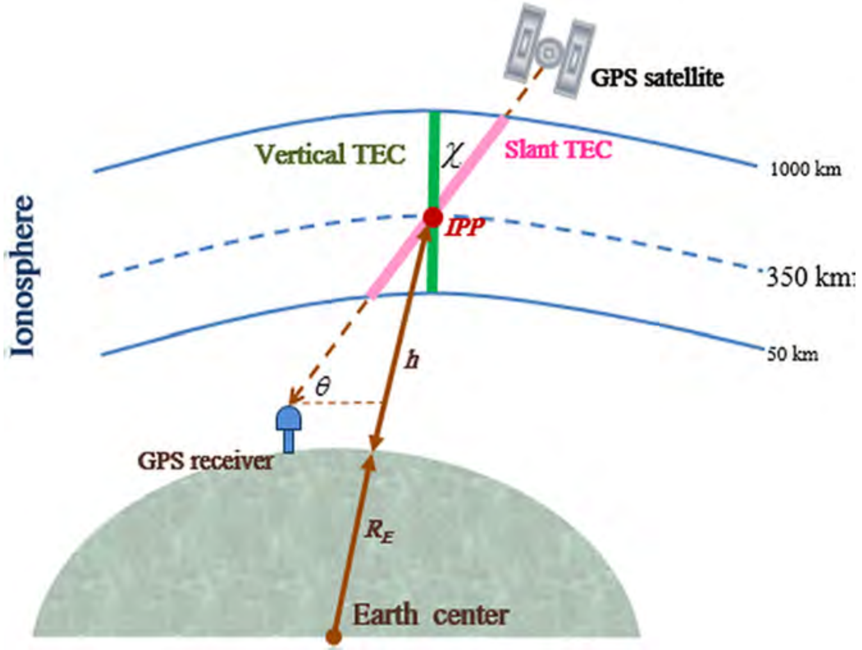

Figure 4.5: The VTEC value obtained from STEC (Silwal *et al.*, 2021).

4.2.1 GPS Data Processing

Global Navigational Satellite Systems (GNSS) derived TEC data over the African-European and American sectors was used. The GNSS data was downloaded from Trignet (`ftp://ftp.trignet.co.za/`), the University NAVSTAR Consortium (UNAVCO: `www.unavco.org/`), and the International GNSS Service (IGS) network (`https://igs.org/`). Figure 4.6 shows the geographical location of the GNSS stations, mostly within the IGS network. The GNSS data was obtained within the longitudinal ranges of 20°-40°E and 50°-70°W over the African-European and American sectors, respectively. The GPS TEC software developed at Boston College was used to derive VTEC from receiver independent exchange records (Seemala and Valladares, 2011; Uwamahoro *et al.*, 2018). The software reads the raw GPS data from the RINEX files and calculates the phase and code TEC values along with the azimuth and elevation of the corresponding satellite (Uwamahoro *et al.*, 2018). This software uses the differential satellite biases published by the University of Bern and the receiver biases that are calculated by minimizing the TEC variation between 02:00 and 06:00 LT (Seemala and Valladares, 2011; Uwamahoro *et al.*, 2018). Assuming a thin shell model, the equivalent VTEC is calculated at an IPP altitude of 350km (Uwamahoro *et al.*, 2018). To reduce the effects of multipath, a cutoff satellite elevation angle of 20° was taken into account during data processing and only TEC values corresponding to elevation angles above 20° were used. The TEC outliers were removed by using the median together with median absolute deviations (MAD). According to Huber (1981) the median and MAD have a 50% breakpoint, and thus both can be used for removing outliers in VTEC observations. Huber (1981) defines MAD as follows:

$$MAD = bM(\mid x - M(x)\mid) \tag{4.41}$$

where $b = 1.4826$ is a constant for normally distributed observations (Huber, 1981). M represents the median value for the absolute deviation of the observations, and x represents the time series observations (Rousseeuw and Croux, 1993; Miller, 1991; Leys *et al.*, 2013;

Dubazane and Habarulema, 2018; Pignalberi *et al.*, 2019). The criterion for the elimination of outliers was used as follows (Leys *et al.*, 2013; Dubazane and Habarulema, 2018):

$$M - 2.5 \times MAD < VTEC < M + 2.5 \times MAD \tag{4.42}$$

The median and MAD filtering technique are used as best method for outlier detection (Leys *et al.*, 2013; Dubazane and Habarulema, 2018; Pignalberi *et al.*, 2019). Figure 4.7 shows an example of this method using data recorded at Kiev (GLSV) GPS station (PRN = 23) on 15 February 2017. After removing the outliers by means of the median and MAD filtering technique, 2.56% of the outliers in VTEC were removed.

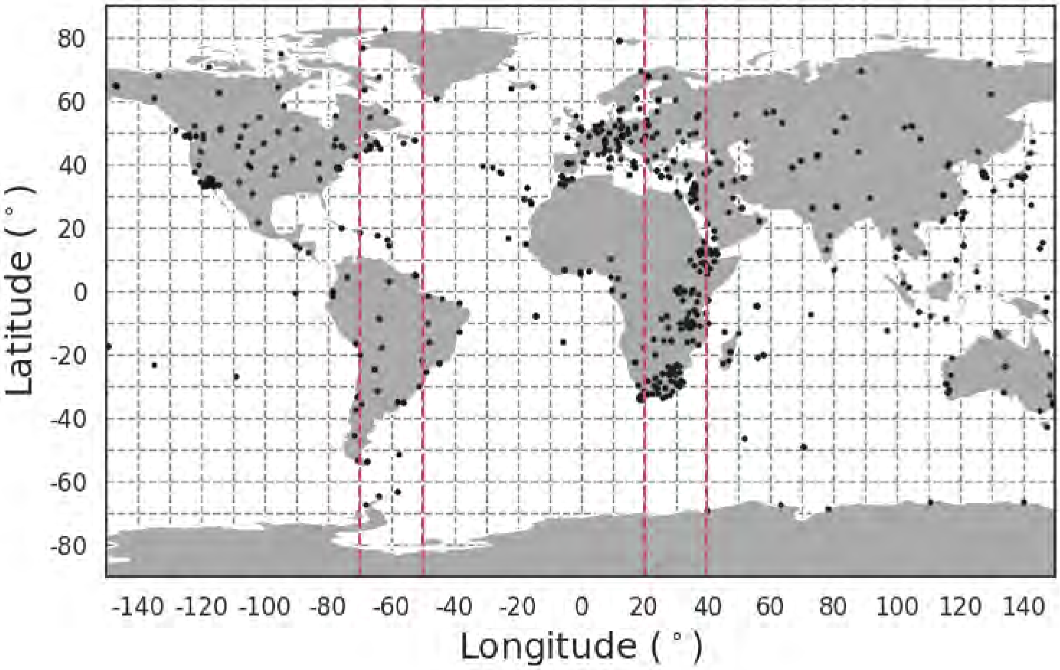

Figure 4.6: GNSS receiver stations (black dots) (`https://igs.org/` and `ftp://ftp.trignet.co.za/`). The vertical dash lines (red) represents the location of GNSS receivers used in this study. Some receiver stations are not shown as they were obtained from different data sources, for example, the South American sector.

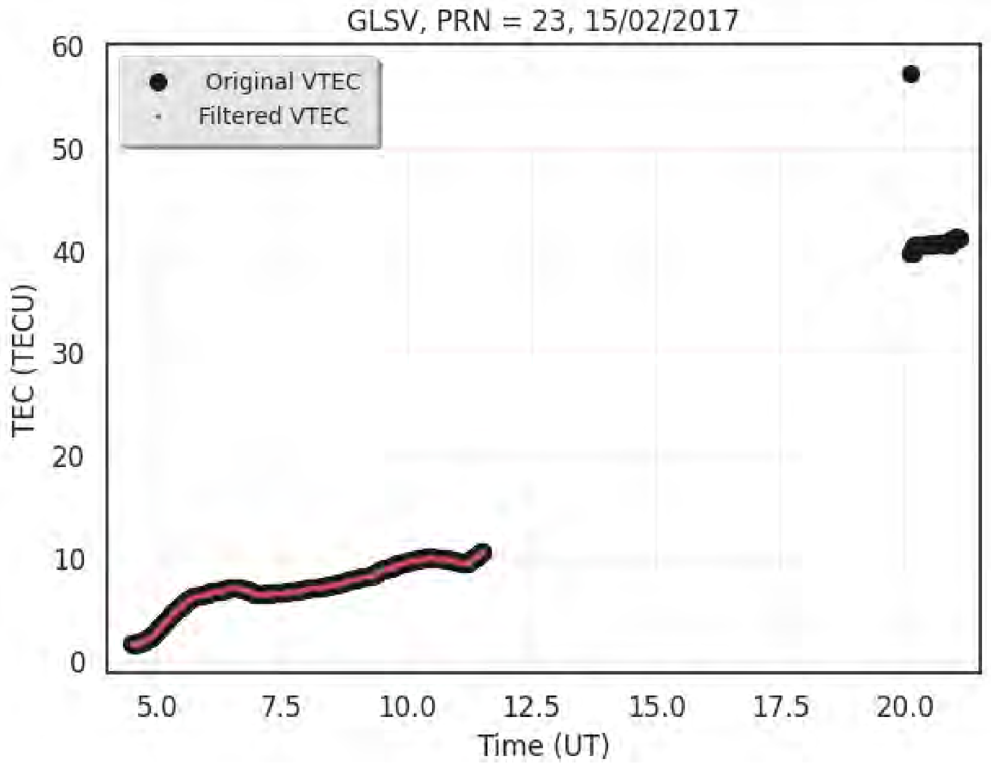

Figure 4.7: GPS VTEC before (black dotted) and after removing outliers by means of the median and MAD filtering technique (red dotted) for data recorded on 15 February 2017 over GLSV (50.36°N, 30.50°E).

4.3 Magnetometers

The Earth's magnetic field and its fluctuations are measured by ground-based magnetometers. The magnetic field component is preferably measured by one of two methods, XYZ and HDZ, respectively (Campbell, 1997): (1) three orthogonal component field directions with positive values for geographic northward (X), eastward (Y), and vertically into the Earth (Z, negative values for the opposite directions) or (2) the horizontal magnitude (H), the eastward angular deviation of the magnetic horizontal component from geographic northward (D), and the downward vertical component (Z) shown in Figure 4.8. Figure 4.8 shows components of the Earth's geomagnetic field in the geographic coordinate system. Using Figure 4.8, the conversion of X and Y to H and D is done as follows:

$$\begin{aligned} H &= \sqrt{X^2 + Y^2} \\ D &= \tan^{-1}\left(\frac{Y}{X}\right) \end{aligned} \tag{4.43}$$

or, equivalently

$$\begin{aligned} X &= H\cos(D) \\ Y &= H\sin(D) \end{aligned} \tag{4.44}$$

The total geomagnetic field strength is expressed by the F-component and is mathematically expressed by the following formula:

$$\begin{aligned} F =& \sqrt{X^2 + Y^2 + Z^2} \\ =& \sqrt{H^2 + Z^2} \end{aligned} \tag{4.45}$$

The inclination, I-component, which is the angle the F-component with the horizontal plane, can be derived from the F-component:

$$\tan(I) = \frac{Z}{H}. \tag{4.46}$$

The geomagnetic equator is defined by a line along the surface of the earth with an inclination of zero, that is, $I = 0$, thus the inclination is most useful in the geomagnetic dipole equation (Campbell, 1997).

There are also various magnetometers, each with unique characteristics and applications, such as the Optical Zeeman, Classical Variometer, Fluxgate, SQUID, and Proton Magnetometer. The fluxgate magnetometers use well-known techniques, are cheaper than other magnetometers and are therefore preferred by many magnetic stations (Ripka, 1992, 2001; Cruz and Trujillo, 1999). Fluxgate magnetometers are traditional instruments for low frequency measurements in magnetic observatories, usually sampling at 1 Hz or lower (Ripka, 1992, 2001; Phiri, 2013). A fluxgate magnetometer consists of a probe or sensor coupled to a processing electronic circuit. In its simplest form, the probe sensor coil, the core of which is made of a soft ferromagnetic material, has two windings, namely an excitation coil and a pickup coil. The processing electronics supplies an excitation current to the premagnetisation coil and does the pickup's signal processing (Ripka, 1992, 2001; Cruz and Trujillo, 1999). A brief description of the fluxgate magnetometer can be found in Primdahl (1979), Ripka (1992), Cruz and Trujillo (1999) and Phiri (2013).

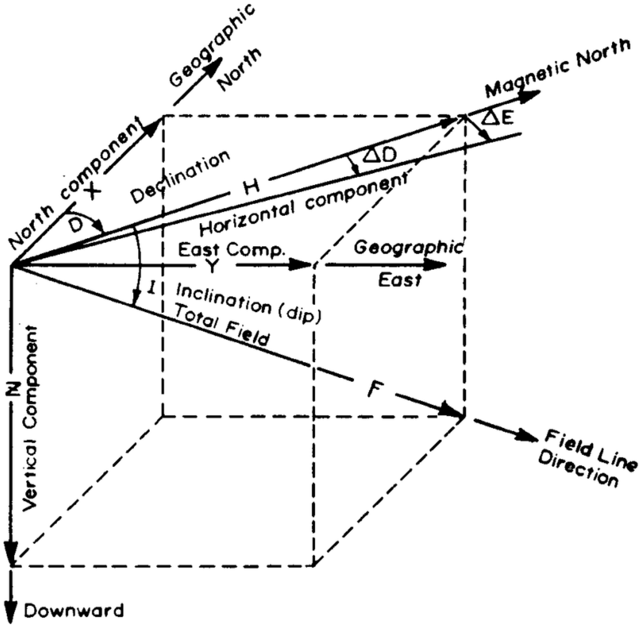

Figure 4.8: Components of the geomagnetic field measurements for a sample northern hemisphere total field vector F inclined into the Earth (Campbell, 1997).

4.3.1 Magnetometer Data Processing

Since the H component of the Earth's magnetic field at the equator reflects changes in the equatorial ionospheric current system, the ground-based magnetometer measurements have been used to infer the electrodynamics of the equatorial ionosphere (Rastogi and Klobuchar, 1990; Anderson *et al.*, 2002; Yizengaw *et al.*, 2012; Habarulema *et al.*, 2015, 2016, 2019; Dugassa *et al.*, 2019). Figure 4.9 shows the geographic location of ground-based magnetometers used in this study. A pair of magnetometers, one near the dip equator and another 6°-9° away, are used for the estimation of the equatorial electrojet (EEJ) current during daytime (Anderson *et al.*, 2002; Yizengaw *et al.*, 2012; Habarulema *et al.*, 2015, 2016, 2019; Dubazane and Habarulema, 2018). Magnetometers provide the magnetic field data for the X, Y and Z components. The horizontal H component was determined by using equation 4.43. Local daily baseline values (H_0) were determined by taking the local midnight (22, 23, 00, 01, 02 hours) average data value for each day.

$$H_0 = \frac{H_{22} + H_{23} + H_{00} + H_{01} + H_{02}}{5} \tag{4.47}$$

where H_{22}, H_{23}, H_{00}, H_{01} and H_{02} are the hourly values of the H component at 22, 23, 00, 01 and 02 hours local time, respectively. To avoid different offset values on the H component, the nightime baseline value (H_0) was subtracted from the corresponding H component data (Yizengaw *et al.*, 2012).

$$\Delta H = H - H_0 \tag{4.48}$$

The contribution of the ring current and Sq dynamo can be removed from ΔH component by subtracting the ΔH component by recorded at the magnetometer $6° - 9°$ latitudes (geomagnetic) from the dip equator, from the ΔH component value measured at the geomagnetic equator (ΔH_{equ}) (Anderson *et al.*, 2002; Yizengaw *et al.*, 2012).

$$\Delta H = \Delta H_{\text{equ}} - \Delta H_{\text{off-equ}} \tag{4.49}$$

This method of estimating EEJ by using magnetometer observations is only reliable during the day. The EEJ is a daytime phenomenon within the E-region ionosphere, which is due to the electric fields driven by the dynamics of neutral winds and geomagnetic field geometry at the geomagnetic equator (Anderson *et al.*, 2002; Yizengaw *et al.*, 2012; Ngwira *et al.*, 2012; Dubazane and Habarulema, 2018; Habarulema *et al.*, 2019). EEJ is a current that flows within about ±3° latitudes from the geomagnetic equator. The direction of the current is usually eastward during the daytime (Anderson *et al.*, 2002; Yizengaw *et al.*, 2012; Ngwira *et al.*, 2012, 2019; Dubazane and Habarulema, 2018; Habarulema *et al.*, 2019). Figure 4.10 shows the daytime ΔH (EEJ) data at 1-minute intervals recorded at the Addis Ababa (AAE) station (0.17°N, 110.47°E geomagnetic) and Adigrat (ETH) station (6.0°N, 111.06°E geomagnetic). In this study, horizontal components of geomagnetic field (H) measurements by the magnetometer stations Alta Floresta, ALTA (9.9°S, 56.1°W, 0.8°N geomagnetic), Cuiaba, CUIB (15.6°S, 56.1°W, 5.9°S geomagnetic), Belem station, BELM (1.45°S, 48.5°W, 1.05°S geomagnetic), Petrolina station, PETR (9.5°S, 40.5°W, 6.95°S geomagnetic), Jicamarca, JICA (11.8°S, 77.2°W; 0.8°N geomagnetic) and Piura, PIUR (5.2°S, 80.6°W; 6.8°N geomagnetic), AEE and ETH were used.

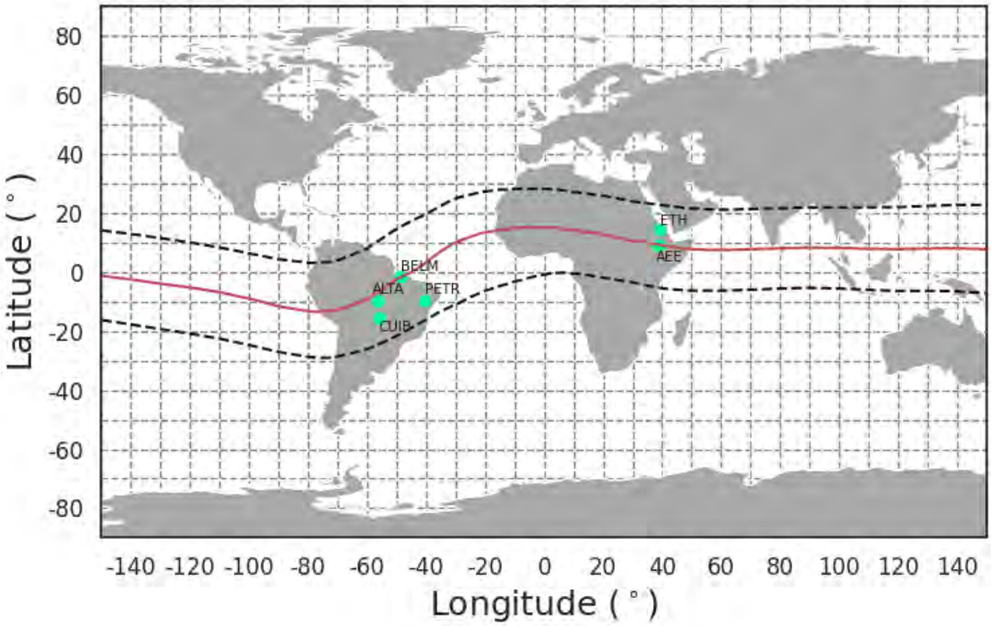

Figure 4.9: Geographic location of the ground-based magnetometers. The horizontal solid line represents the geomagnetic equator and the two dashed lines represent the EEJ region on either side of the geomagnetic equator.

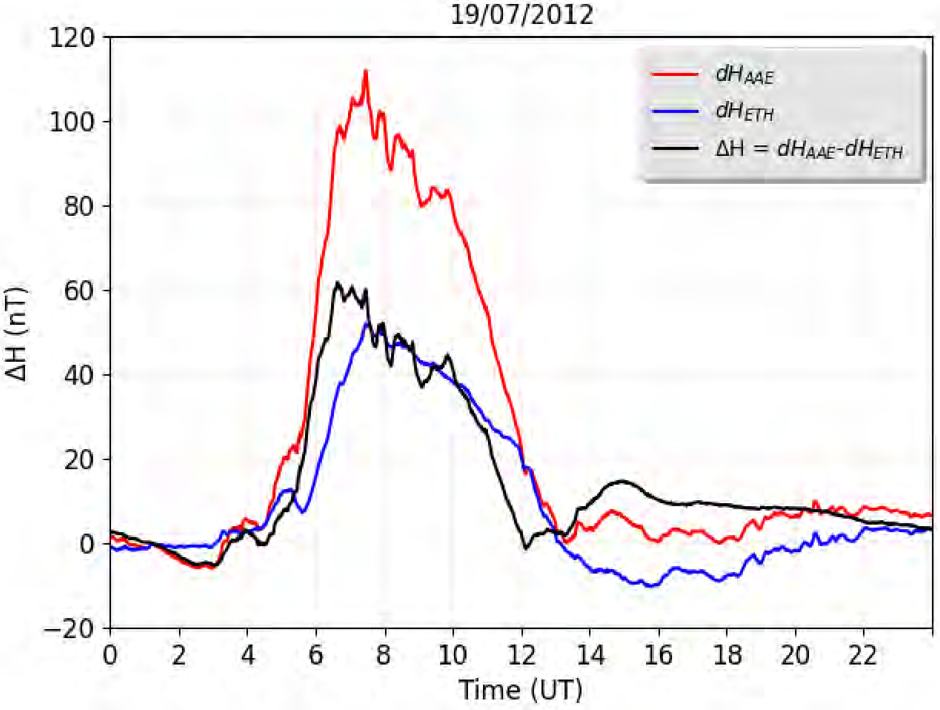

Figure 4.10: Variation of ΔH (nT) for 19 July 2012.

4.4 Atmospheric Hyperspectral Infrared Spectrometer

The Atmospheric Infrared Sounder (AIRS) is the first of a new generation of Hyperspectral Infrared Nadir Sounders designed to replace the Advanced TRIOS Operational Vertical Sounder (ATOVS) system for Numerical Weather Prediction (NWP) (Aumann *et al.*, 2003, 2006; JPL, 2021). The AIRS on NASA's Earth Observing System (EOS) Aqua Spacecraft was launched on May 4, 2002. Six instruments onboard the Aqua spacecraft monitor the state of the Earth's atmosphere globally (Chahine *et al.*, 2006; Hoffmann and Alexander, 2009; Bani Shahabadi *et al.*, 2016). AIRS measures key elements of these propulsion forces, including surface and atmospheric thermal structure, cloud volume and height, outgoing long-wave infrared radiation, atmospheric water vapour distribution, and precipitation (Aumann *et al.*, 2003; Chahine *et al.*, 2006; Hoffmann and Alexander, 2009). AIRS infrared technology creates a three-dimensional map of temperature, water vapor and cloud characteristics (Hoffmann and Alexander, 2009; Hoffmann *et al.*, 2016). In addition, AIRS radiation is sensitive to the concentration of some trace gases, such as methane (CH_4), carbon monoxide (CO) and ozone (O_3). The AIRS has 2378 channels that capture measurements at various wavelengths, such as 3.74-4.61 μm, 6.20-8.22 μm, and 8.8-15.4 μm (Aumann *et al.*, 2003, 2006; Hoffmann *et al.*, 2013, 2016; Bani Shahabadi *et al.*, 2016). AIRS has more than 100 times the spectral resolution of previous infrared sounders and provides more accurate information about the vertical profile of temperature and humidity. The AIRS temperature profile is as accurate as the accuracy achieved by a radiosonde launched from a ground station in the troposphere (Aumann *et al.*, 2003, 2006; JPL, 2021).

AIRS measures the infrared radiance spectra of the Earth's atmosphere by means of the geometry associated with the nadir and sub-limb (Hoffmann *et al.*, 2016). The instrument gazes at the ground with a cross-track rotating mirror that scans between ±49.5° ground coverage, which represents a roughly 1800 km wide swath at 705 km orbital altitude. It produces cross-track scans every 2.67 s with 90 footprints on the ground. The scans are separated by an along-track distance of 18 km. The size of the footprint varies from 14×14 km^2 on the nadir to 21×42 km^2 on extreme scans (Aumann *et al.*, 2003; Hoffmann and Alexander, 2009; Hoffmann *et al.*, 2013, 2016). The orbit period is 98.8 min. The repeating cycle period is 233 orbits (16 days), and the reproducibility of ground orbits is ±20 km (Haridas *et al.*, 2018; JPL, 2021). AIRS views the same area on Earth twice per day; once during a descending pass which occurs at 01:30 LT and once during the ascending pass at 13:30 LT (Aumann *et al.*, 2003; Hoffmann *et al.*, 2016). The geometry of the scans of the atmospheric infrared spectrum AIRS instrument is schematically illustrated in Figure 4.11 (Aumann *et al.*, 2003; Prata, 2017).

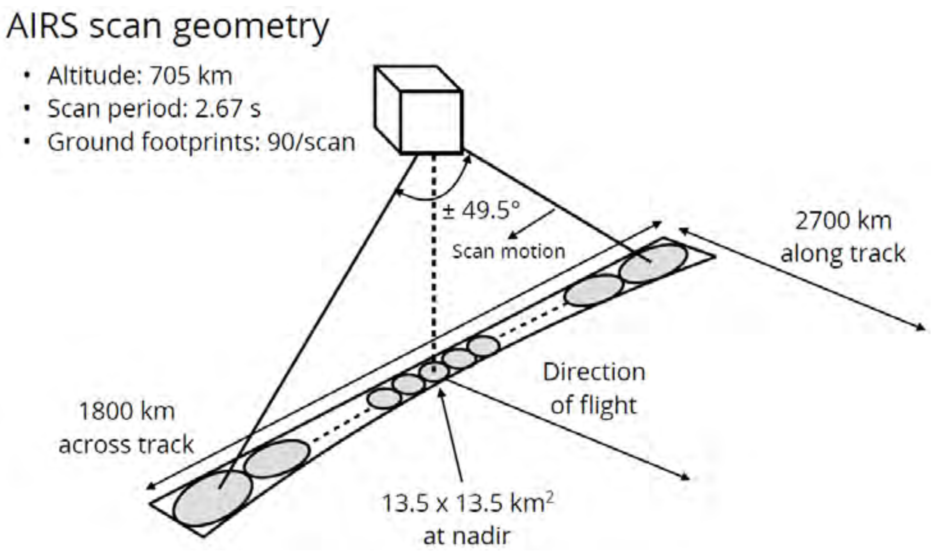

Figure 4.11: Schematic illustration of the geometry of the AIRS instrument (Aumann *et al.*, 2003; Prata, 2017).

4.4.1 AIRS Data Processing

AIRS measurements are used in applications such as AGW detection (Hoffmann *et al.*, 2013; Azeem *et al.*, 2015). The AIRS is a hyperspectral radiometer that measures atmospheric emission of CO_2 with high spectral resolution. The AIRS radiance measurements are converted to brightness temperature. The channel properties file (Aumann *et al.*, 2003; Bani Shahabadi *et al.*, 2016; JPL, 2021) is required to identify and remove unwanted spectral channels and match the channel number to the correct wavenumber. Once each radiance matches the wavenumber, the inverse Planck equation is used to convert the radiance to the brightness temperature. The inverse Planck equation for a given wavenumber is written as follows (Smith *et al.*, 1972; Bani Shahabadi *et al.*, 2016):

$$TB(v) = \frac{c_2 v}{\log(\frac{c_1 v^3}{B(v)} + 1)} \tag{4.50}$$

where $TB(v)$ is the wavenumber (v) dependant brightness temperature, $B(v)$ is the wavenumber dependent radiance, $c_1 = 2hc^2 = 1.19104 \times 10^{-5}$ [W m^{-2} sr cm^{-4}], $c_2 = hc/k = 1.43878$ [K cm], h is Planck's constant, k is Boltzmann's constant and c is the speed of light. Here, c_1 and c_2 are converted to the units of centimeters (cm) and milliwatts (mW). This is because AIRS emissions are expressed in units of mW/m^2/cm^{-1}/ steradian (Smith *et al.*, 1972; Bani Shahabadi *et al.*, 2016; Wright *et al.*, 2016).

The radiance measurements are provided at high horizontal resolution for each satellite footprint. AIRS operational temperature retrievals have degraded horizontal resolution as 3×3 footprints are combined within the cloud clearing process. More information on high resolution AIRS retrieval can be found in Hoffmann and Alexander (2009) and Hoffmann *et al.* (2013). Information on stratospheric gravity wave activity is derived from radiance measurements in the 4.3 μm and 15 μm CO_2 fundamental bands. This analysis is based on the average brightness temperature of 42 AIRS channels in the 4.3 μm CO_2 baseband (2322.6 to 2345.9 cm^{-1} and 2352.5 to 2366.9 cm^{-1}, AIRS channel numbers 2040 to 2065 and 2072 to 2087). The temperature kernel function of the 4.3 μm channel shows the maximum sensitivity of radiance to stratospheric temperatures at altitudes of 30-40 km, with a full width at half maximum of about 25 km (Hoffmann and Alexander, 2009; Hoffmann *et al.*, 2013). Below 18-20 km, the sensitivity of the weight function is below the maximum value of 1%. These channels are unaffected by surface radiation, tropospheric clouds, or reflected sunlight (Hoffmann *et al.*, 2013).

The 4.3 μm brightness temperature (BT) perturbations were calculated through subtracting a fourth-order polynomial match for every across-track scan from the individual BT measurements for every satellite footprint. This method of detrending gets rid of background signals associated with large-scale temperature gradients and planetary waves (Hoffmann and Alexander, 2009; Hoffmann *et al.*, 2013). This limits the amplitude response to 90, 50, and 20 % at across-track wavelengths of 800, 1200, and 1650 km, respectively. The short wavelength limit of the observation is about 30 km, based on the Nyquist theorem, and the sampling distance at the nadir is 14 km (Hoffmann *et al.*, 2013, 2014, 2016). Measurement noise is significantly reduced by averaging the radiance measurements of multiple AIRS channels. The noise of the spectral average TB is about 0.059 K at 250 K scene temperature Hoffmann *et al.* (2014). For example, Figure 4.12 shows the estimated noise of the spectral mean 4.3 μm TB. AIRS data is sensitive only to a portion of the GW spectrum, namely with horizontal wavelengths less than 1,400 km and vertical wavelengths larger than 15 km (Ern *et al.*, 2017). AIRS gravity wave data is provided separately for nighttime (01:30 LT) and daytime (13:30 LT) observations. The AIRS data used in this study is available from the following website: `https://datapub.fz-juelich.de/slcs/airs/gravitywaves/index.htm`.

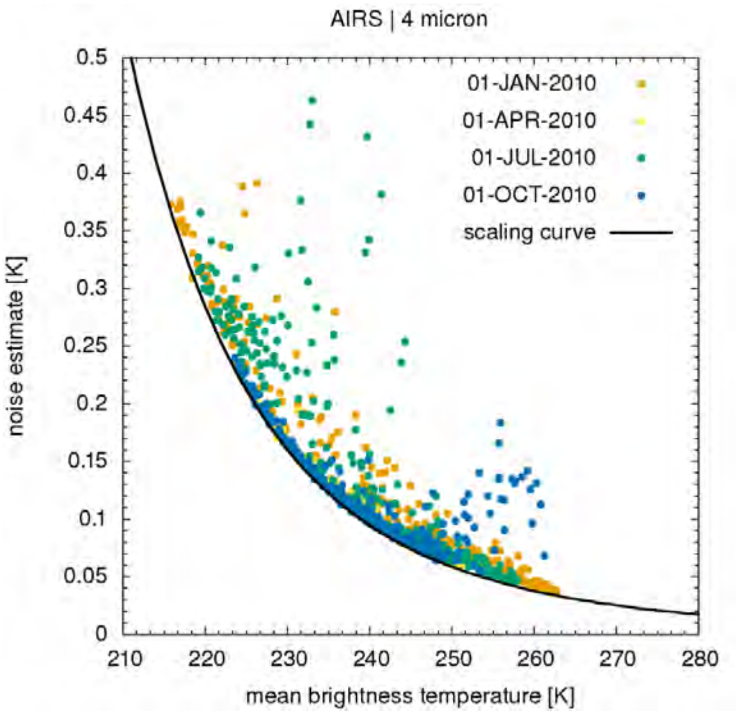

Figure 4.12: Noise estimates for the AIRS 4.3μm TB dataset versus mean background temperature (`https://datapub.fz-juelich.de/slcs/airs/gravity_waves/data/noise.pdf`).

Chapter 5

Trans-hemispheric equatorward TIDs during geomagnetically quiet conditions

5.1 Introduction

This chapter presents observations of medium- to large-scale TIDs that originated from high-latitudes, and propagated across the equator into the opposite hemisphere in the African-European and American sectors during geomagnetically quiet conditions between 2010 and 2018. These are the first observational results showing trans-hemispheric TIDs during quiet conditions, despite having been reported theoretically (Vadas and Becker, 2019; Vadas *et al.*, 2019; Becker and Vadas, 2020). Equatorward TIDs that originate in the high-latitudes have been known to be present during geomagnetic storms (Hunsucker, 1982; Balthazor and Moffett, 1997; Lei *et al.*, 2008; Habarulema *et al.*, 2018; Ngwira *et al.*, 2019). Global Navigation Satellite System (GNSS) data is used for the identification of equatorward TIDs. For this study, geomagnetically quiet days (maximum Kp < 3) were identified by means of Kp index data from the World Data Center for Geomagnetism, Kyoto (`http://wdc.kugi.kyoto-u.ac.jp/qddays/`). During the period of study, four geomagnetically quiet days were selected each month for the period 2010-2018. Most of the results and explanations in this chapter are based on the information presented in a paper published by Thaganyana *et al.* (2022).

5.2 Methodology

5.2.1 Observation of TID from TEC

The procedure focused on the identification of medium- to large-scale TIDs that were launched from the high-latitudes over the African-European and American sectors during geomagnetically quiet conditions, with the unique property of being observable in both hemispheres. Data within the latitudinal and longitudinal areas covered by 90°S-90°N and 20°-40°E, and 90°S-90°N and 50°-70°W of the African-European and American sectors, respectively, was considered. For this analysis, VTEC data was detrended using the polynomial fitting (Valladares *et al.*, 2009; Valladares and Hei, 2012). Data detrending was required to remove other dominant TEC perturbations and leave only the perturbations of interest within the

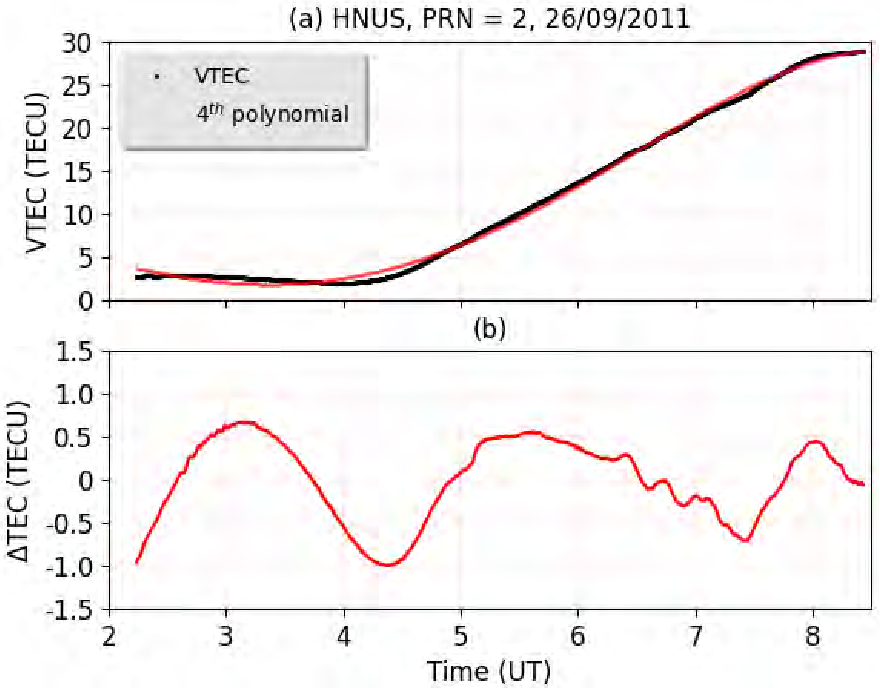

Figure 5.1: Estimation of ΔTEC by means of a fourth-order polynomial fitting for one PRN over Hermanus (HNUS) (34.4°S, 19.2°E) on 26 September 2011.

frequency range of TIDs (Valladares and Hei, 2012; Habarulema *et al.*, 2015). Several detrending methods are available for the estimation of background atmospheric conditions and VTEC perturbation. The most popular methods are polynomial fitting (Valladares *et al.*, 2009; Valladares and Hei, 2012; Katamzi *et al.*, 2012; Habarulema *et al.*, 2015, 2016) and the running average (Kotake *et al.*, 2007; Shiokawa *et al.*, 2009). In this study, VTEC data was fitted by using a fourth-order polynomial. The fitted VTEC was subtracted from the corresponding VTEC to produce a detrended TEC (ΔTEC) time series for each PRN. According to Valladares *et al.* (2009), "this method reflects quite well the variability of the integrated number density due to the transit of large-scale gravity waves". The VTEC time series fitting for each satellite is explained as follows (Habarulema *et al.*, 2016):

$$\begin{cases} vT^f(t)_{i,j} = at^4_{i,j} + bt^3_{i,j} + ct^2_{i,j} + dt_{i,j} + \varepsilon, forj = 1, 2, 3, ..., 31 \\ \Delta TEC(t)_{i,j} = TEC(t)_{i,j} - vT^f(t)_{i,j}, \forall i, j \end{cases} \tag{5.1}$$

where j = 1, 2, 3, ..., 31 represents the number of satellites; i = 1, 2, 3, ..., 140^+ is the number of GNSS receiver locations within the defined longitudinal sectors in this study; the coefficients a, b, c, d are acquired through the least squares method; ε represents the residual error of the fitting process; $vT^f(t)$ and $TEC(t)$ represent the fitted and actual VTEC at time, respectively (Habarulema *et al.*, 2016). A 20° elevation cutoff was considered to minimize multipath-related errors. Figure 5.1 (a) shows the polynomial fitting to VTEC measurements for data from the Hermanus (HNUS) GPS station (PRN = 2) on 26 September 2011. The filtered VTEC time series is shown by ΔTEC (Figure 5.1 (b)) and was obtained by subtracting the polynomial fitted TEC from the corresponding VTEC time series. The same procedure was applied to estimate ΔTEC throughout the day using all PRNs from the Hermanus station, as shown in Figure 5.2.

The same method was used to determine ΔTEC for data from different stations. Estimated ΔTEC made it possible to create a two-dimensional (2-D) map of ΔTEC with respect to the time and latitude of a particular day. To produce the 2-D map, the ΔTEC data was binned within 5 min × 0.5° (time and latitude). The diurnal ΔTEC maps with respect to the selected latitudinal ranges were produced within the corresponding longitudinal sector spanning 20°.

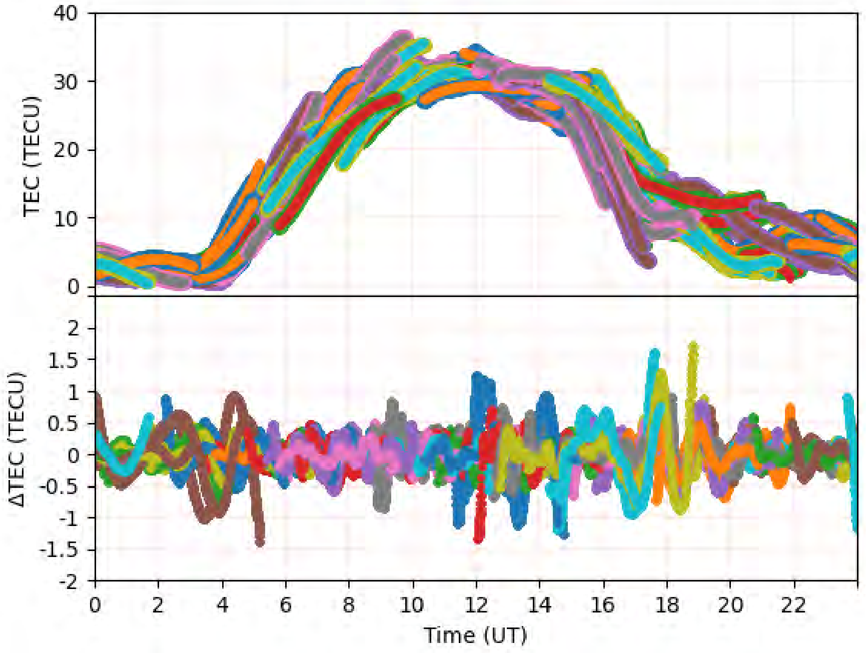

Figure 5.2: Estimation of ΔTEC using a fourth-order polynomial fitting for all PRNs over HNUS on 26 September 2011.

5.2.2 Determination of the Characteristics of TIDs

All the methods for the determination of the characteristics of TIDs are based on information presented in the paper published by Liu *et al.* (2019) and Thaganyana *et al.* (2022).

Velocity and Direction of Propagation of TIDs

In order to estimate the meridional phase velocity and propagation direction, a linear regression method was used (Liu *et al.*, 2019). Figure 5.3 shows Dst and Kp indices and ΔTEC as a function of time within the longitudinal sector of 20°-40°E and latitudinal range of 90°S-90°N for 27 July 2012 and 29 January 2016 over the African-European sector. The Kp and Dst indices data was obtained from the NASA Goddard Space Flight Center (`https://omniweb.gsfc.nasa.gov/`). In both cases (Figure 5.3 (a) and (c)), Kp index values were less than 2, and the Dst ranged between -20 and 20 nT. Walker *et al.* (2013) propose a Dst range of -20 to 20 nT as a criterion for geomagnetically quiet conditions. The longitudinal sector in Figure 5.3 (b) and (d) was chosen for this analysis because of the dense

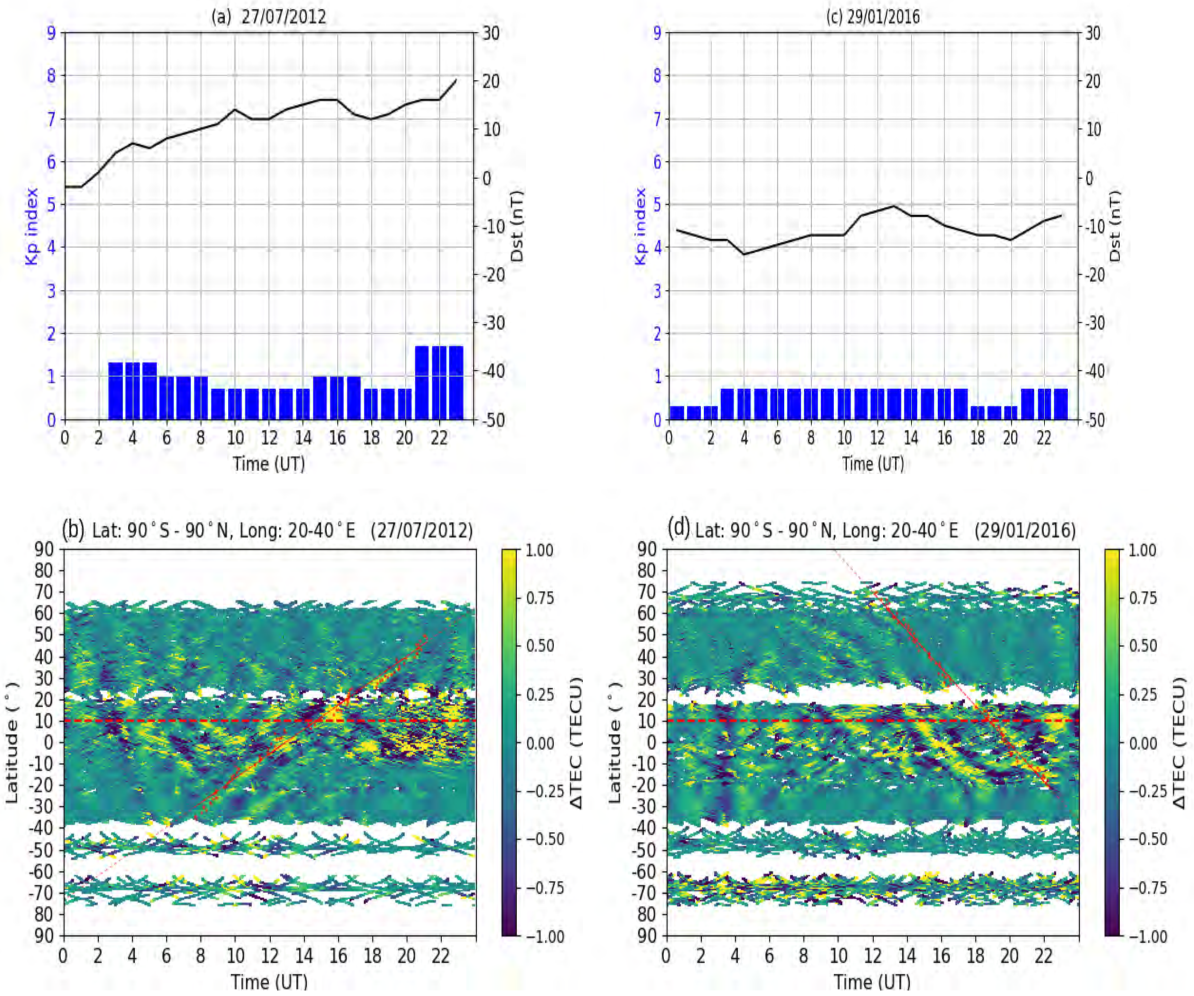

Figure 5.3: (a) and (c) Variation of Kp and Dst indices for the 27 July 2012 and 29 January 2016 (`https://omniweb.gsfc.nasa.gov/`). (b)-(d) An example of the wave linear fitting method. Red dots show the data points for linear fitting, and the horizontal red dotted lines represent the geomagnetic equator at 10°N.

distribution of the GNSS receiver network. This provides a clearly visible TID structure. Habarulema *et al.* (2018) and Figueiredo *et al.* (2017) considered longitudinal ranges covering 40° and 25°, respectively. At about 20°N, 40°S, and 60°S, there is a data gap (white spaces) due to unavailability of the GNSS receiver network. In Figures 5.3 (b) and (d), the dotted lines are fitted along the TID structure and are later used to compute velocities. The horizontal red dotted lines in Figures 5.3 (b) and (d) indicate the estimated geomagnetic equator at 10°N (Habarulema *et al.*, 2018).

In Figures 5.3 (b) and (d) the equatorward TIDs appear to have originated from high-latitudes. These Figures show a detailed example of the linear regression method with the ΔTEC (time and latitude) maps. The linear regression method is used to a fit maximum ΔTEC in a bin interval of 1 degree latitude by 40 min range. Keeping the interval constant, the time was incremented by 10 min. The data points for the linear fitted lines (red dots) are maximum ΔTEC values for each latitude-time bin. The values of the latitudes were converted to distance (km) in order to compute the meridional speed. The meridional velocity of the TIDs were derived in terms of the gradient of the fitted lines. The meridional propagation velocity of TIDs that were estimated from the data points (red dots) in Figures 5.3 (b) and 5.3 (d) were 311 ± 11 m/s and 273 ± 20 m/s for 27 July 2012 and 29 January 2016, respectively. All fitted data points on the ΔTEC maps in Figures 5.3 (b) and (d) comprise of longitude, latitude and time. In order to compute the propagation azimuth, longitude and latitude are required. Therefore, the propagating azimuth of TIDs were estimated by means of these fitted data points (red dots) in Figures 5.3 (b) and (d), namely 44.2° (clockwise from north) and 116.5° (clockwise from north) for 27 July 2012 and 29 January 2016, respectively.

The horizontal phase speed (c_H) was computed as follows (Vadas and Becker, 2018):

$$c_H = \frac{1}{\sqrt{(1/c_x^2 + 1/c_y^2)}} \tag{5.2}$$

where c_x and c_y are the phase velocities of the TID in the x and y directions, respectively. Then the following formula was used:

$$\begin{aligned} c_x &= \omega_r/k \\ c_y &= \omega_r/l \end{aligned} \tag{5.3}$$

where k and l are the zonal and meridional wavenumbers, respectively. By using the following equations:

$$\begin{aligned} k &= k_H \times \sin(\phi) \\ l &= k_H \times \cos(\phi) \end{aligned} \tag{5.4}$$

where $k_H = 2\pi/\lambda_H$ is the horizontal wavenumber, ϕ is the azimuth (clockwise from north) and λ_H is the horizontal wavelength, then equation 5.2 can be written in terms of the meridional propagation velocity and the propagation azimuth. Then equation 5.2 becomes

$$c_H = \frac{c_y}{\sqrt{(1 + (\tan(\phi))^2)}} \tag{5.5}$$

The above equation was used to calculate c_H. The calculated c_H values for 27 July 2012 and 29 January 2016 were 223 m/s and 120 m/s, respectively.

Periods of TIDs

To compute periods, continuous wavelet transform (CWT) was used to reconstruct time series data to the time scale/frequency (period) domain (Torrence and Compo, 1998). The time series is convolved with a scaled wavelet in order to achieve this. A mother wavelet ($\psi(t)$), whether real or complex, is a function that satisfies the equation

$$\int_{-\infty}^{\infty} \psi(t) dt = 0 \tag{5.6}$$

Mother wavelets can be expanded (enlarged or reduced) and time-converted (Torrence and Compo, 1998). The dilation and translation parameters transform $\psi(t)$ to $\psi_{s,\tau}(t)$ by

$$\psi_{s,\tau}(t) = \frac{1}{\sqrt{s}} \psi(\frac{t-\tau}{s}) \tag{5.7}$$

where t is time, s is the scaling parameter representing the frequency and τ is a position parameter which slides the wavelet along the time domain (Mallat, 1999). A convolution integral can be defined as a CWT of a time series, $x(t)$, with respect to the wavelet function, $\psi(t)$:

$$\begin{aligned} CWT(s,\tau) &= \int_{-\infty}^{\infty} x(t)\psi^*(t)dt \\ &= \frac{1}{\sqrt{s}}\int_{-\infty}^{\infty} x(t)\psi^*(\frac{t-\tau}{s})dt \end{aligned} \tag{5.8}$$

where $\psi^*(t)$ is the complex conjugate of the wavelet function analyzed $\psi(t)$ (Mallat, 1999). The periods information leads to the computation of the wavelength by the multiplying the period and speed of the TIDs (Habarulema *et al.*, 2013). In this context, the mother wavelet, Morlet, was used to map time series into frequency-time space. It was chosen because its shape resembles that of several geophysical parameter features (Torrence and Compo, 1998; Materassi and Mitchell, 2007; Katamzi *et al.*, 2012; Habarulema *et al.*, 2013). The Morlet wavelet is defined as

$$\psi_0(t) = \pi^{1/4}e^{i\omega_0 t}e^{-t^2/2} \tag{5.9}$$

where t is time, and ω_0 represents the non-dimensional frequency which is taken to be 6 to satisfy the admissibility condition (Farge, 1992). This method has been used to analyse the amplitudes and periods of TIDs identified in GNSS TEC data (Katamzi *et al.*, 2012; Habarulema *et al.*, 2013). More information about the wavelets and their applications are discussed in Torrence and Compo (1998), Materassi and Mitchell (2007) and Farge (1992). Figure 5.4 (a) presents the 30 min moving averaged ΔTEC for the latitudes $-20° \pm 2°$ and $-10° \pm 2°$ within the longitudinal sector of 20°-40°E for 27 July 2012. Figures 5.4 (b)-(c) show the application of CWT to ΔTEC at $-20° \pm 2°$ and $-10° \pm 2°$ latitude to produce scalegrams. The propagation period of wave modes are $\approx$ 52 min (Figure 5.4 (b)) and $\approx$ 56 min (Figure 5.4 (c)). These values are the average of the maximum and minimum of the intense yellow colour. Figures 5.4 (d)-(f) are similar to Figures 5.4 (a)-(c), but for 29 January 2016. The estimated periods according to the scalegrams are $\approx$ 45 min (Figure 5.4 (e)) and $\approx$ 52 min (Figure 5.4 (f)) at $-20°$ and $-10°$ latitude.

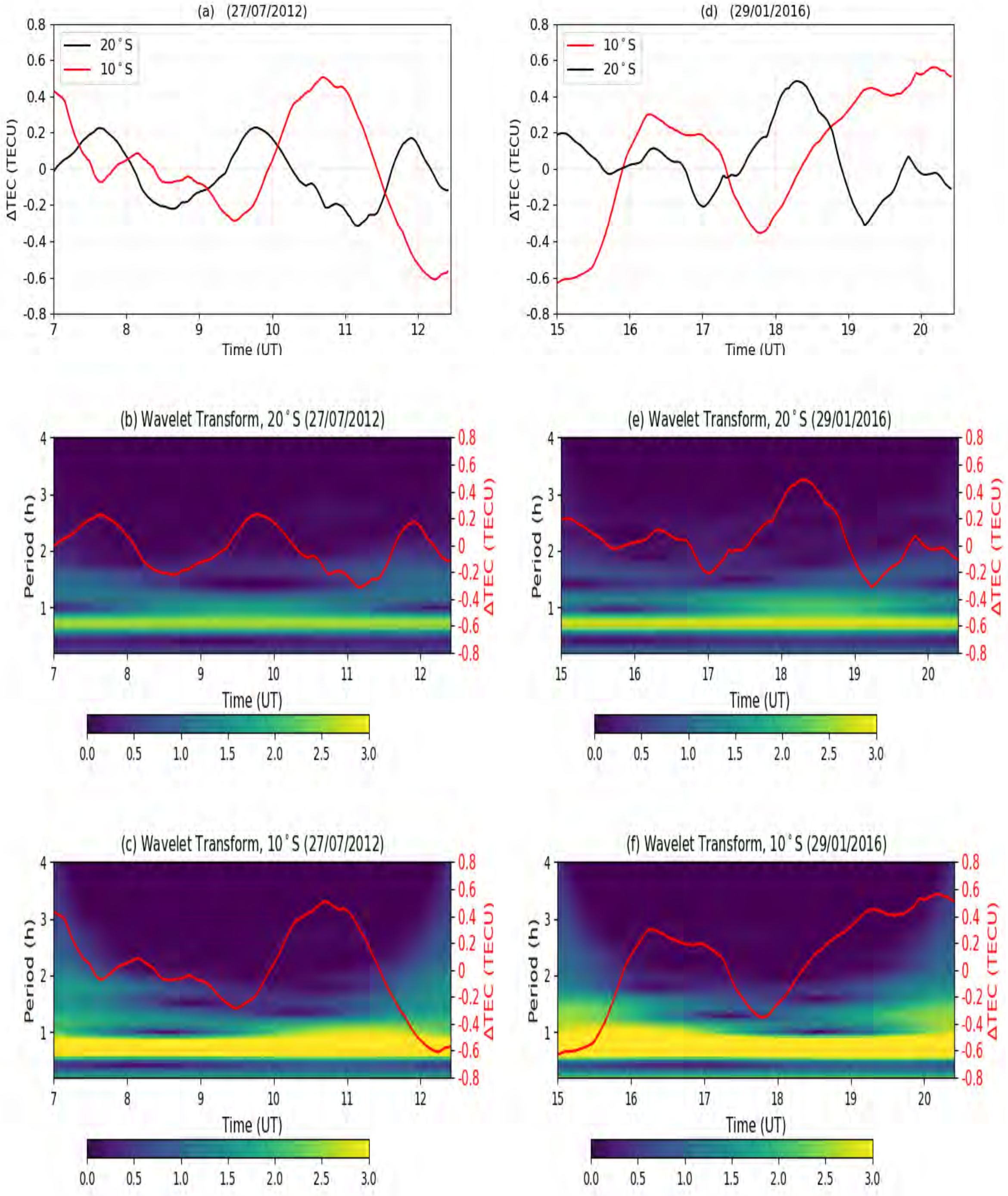

Figure 5.4: Power spectrum of wavelet transform over African-European sector computed for different latitudes (colour) for 27 July 2012 and 29 January 2012. ΔTEC was computed by subtracting TEC from the values of fourth-order fitted polynomial functions and applying the moving average of 30 min for $-20° \pm 2°$ and $-10° \pm 2°$ latitude ((a) and (d)). From averaged ΔTEC, the CWT was applied to each latitude to produce scalegrams ((b)-(c) and (e)-(f)). Estimated periods were ≈ 54 min and ≈ 49 min for 27 July 2012 and 29 January 2016, respectively.

Table 5.1: Geographic latitude and longitude coordinates of the GPS which supplied the data to demonstrate the propagation of TIDs

13 July 2012				16 January 2014			
Southern Hemisphere Stations				Northern Hemisphere Stations			
ID	Name	Latitude	Longitude	ID	Name	Latitude	Longitude
SCOT	Scottsburgh	-30.29	30.75	SVTL	Svetloe	60.53	29.78
ULDI	Ulundi	-28.29	31.42	RIGA	Riga	56.95	24.06
BENI	Benoni	-26.20	28.34	LAMA	Lamkowko	53.01	20.67
SPRT	Steelport	-24.67	30.19	KHAR	Kharkiv	50.01	36.24
SYOG	Syowa	-69.01	39.58				
KERG	Kerguelen Islands	-49.35	70.25				
REUN	Le Tampo	-21.208	55.57				
SEY2	La misere	-4.67	55.47				
Northern Hemisphere Stations				Southern Hemisphere Stations			
ARMI	Arba Minch University	6.06	37.56	ADIS	Addis Ababa University	9.04	38.77
METU	Metu	8.27	35.59	HAWA	Hawassa University	7.05	38.50
ASOS	ASSOSA	10.05	34.55	NEGE	Negele	5.33	39.59
DEBK	Debarek	13.15	37.89	MOIU	Eldoret	0.29	35.29

5.3 Results

5.3.1 African-European Sector

To further illustrate cases where TIDs were observed, two examples are shown, 13 July 2012 and 16 January 2014. Figure 5.5 shows the latitude-time plot for ΔTEC within the longitudinal sector of 20°-40°E. On 13 July 2012 and 16 January 2014, TIDs from the southern and northern winter hemispheres in the mid- and high-latitudes over the African-European sector, respectively, were observed. The presence of TIDs extended to both hemispheres in both cases. Figure 5.5 (a) shows that the equatorward TID structure emerged from the southern hemisphere in winter at the high-latitudes (based on the time estimated from the extrapolated fitted line) around 02:30 (UT) and crossed the geomagnetic equator into the summertime northern hemisphere at around 15:20 (UT). It is worth pointing out that this TID structure was visible in the mid-latitude at about 09:00 (UT). This TID had a period of approximately 80 ± 13 min, and a meridional propagation velocity of 270 ± 22 m/s. The horizontal velocity and wavelength values of this TID were 230 m/s and 1104 km, respectively, which are characteristic of large-scale TIDs (Mayr *et al.*, 1984; Hunsucker, 1982; Hocke and Schlegel, 1996; Vadas and Becker, 2019; Katamzi-Joseph *et al.*, 2019). Figure 5.5 (d) shows the visible TID propagating equatorward from the wintertime northern hemisphere (at about 10:20 UT and assuming the source was in high-latitude) to the summertime southern hemisphere on 16 January 2014. The available data shows the TID structure from around 12:00 UT at 70°N. It was estimated that this TID started at around 10:20 UT in mid- to high-latitudes, with period and meridional propagation velocity values of 63 ± 17 min and 322 ± 12 m/s, respectively. The horizontal velocity and wavelength of the TID were 195 and 737 km, respectively.

The propagation of equatorward medium- to large-scale TIDs was demonstrated by means of several GPS PRNs. The ΔTEC for GPS locations with data for the same satellites (PRNs) for 13 July 2012 and 16 January 2014, was analysed. Table 5.1 shows the GPS receivers that were used within the longitudinal sector of 20°-40°E. A moving average of 15 min was applied to ΔTEC for selected GPS receivers (Figures 5.5 (b)-(c) and (e)-(f)) for the 13 July 2012 and 16 January 2014, respectively. On these days, four stations were selected in both the northern and southern hemispheres to demonstrate TID propagation. From Figures 5.5

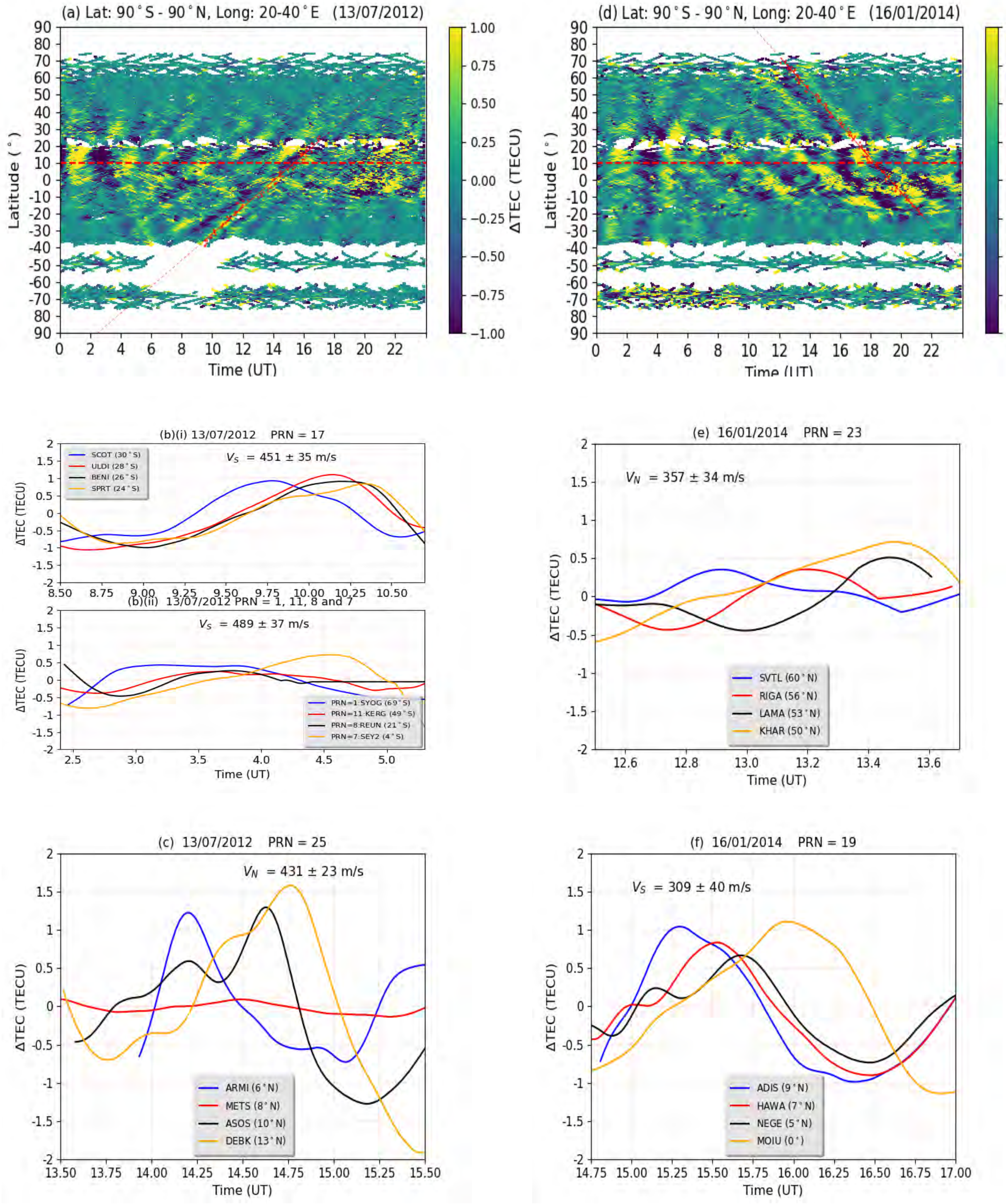

Figure 5.5: Latitude-time plot of TEC perturbations for 13 July 2012 (a) and 16 January 2014 (d). The ΔTEC for satellite PRNs ((b)-(c) and (e)-(f)) at different stations for 13 July 2012 and 16 January 2014, respectively. ΔTEC was computed by subtracting TEC from the values of fourth-order fitted polynomial functions and applying a moving average of 15 min.

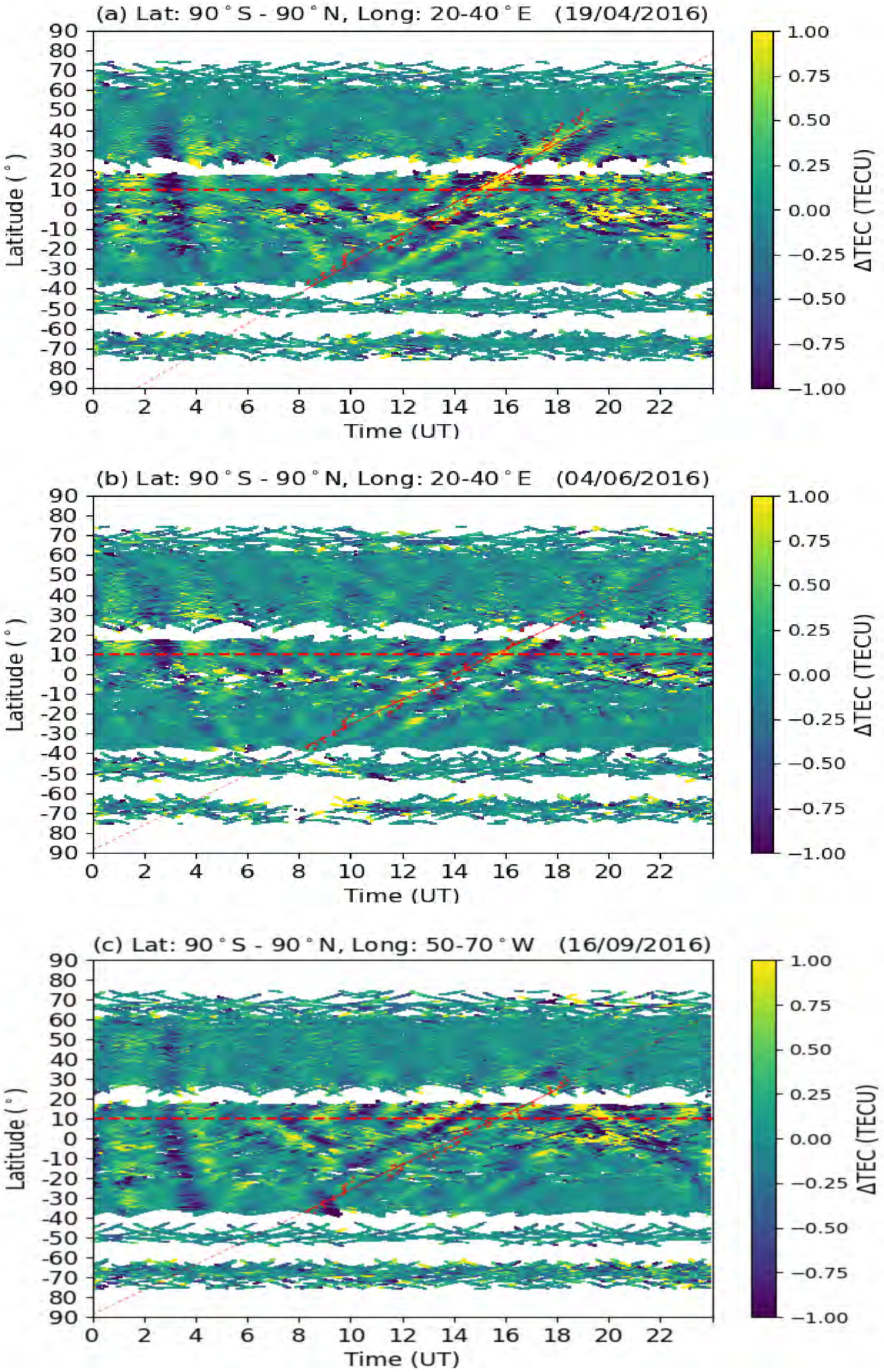

Figure 5.6: Cases of equatorward medium-scale TIDs which appear to have originated from the mid-latitudes during quiet conditions on 19 April 2016, 04 June 2016 and 16 September 2016.

(b(i-ii))-(c) illustrate the presence of wave-like propagation structures in GPS measurements at different stations at different times for a number of PRNs. Figure 5.5 (b (i)) shows that the observation of PRN 17 at mid-latitudes in the southern hemisphere had a TID structure with a meridional velocity of 451 ± 35 m/s. Figure 5.5 (b(ii)) shows the presence of a TID as observed from the time-shift of the ΔTEC, with peaks starting at a high-latitude, namely at SYOG (69.01°S) at 03:19 UT and moving all the way to SEY2 (4.67°S, peak appearing at 04:36 UT) with a meridional velocity of 489 ± 37 m/s. The peaks at KERG (49.35°S) and REUN (21.21°S) occurred at 03:34 UT and 03:49 UT, respectively. Given that the meridional velocities of these observations are comparable even though they are computed at different times and made use of different PRNs observations, it is appropriate to assume that these observations point to the same structure. This supports the assumption of extrapolation of the fitted red line in Figure 5.5 (a). Also, Figure 5.5 (c) is similar to Figure 5.5 (b (i)) for the northern hemisphere, and the meridional velocity of the TID structure observed on 13 July 2012 was 431 ± 23 m/s. These velocities in Figures 5.5 (b (i)) and 5.5 (c) are statistically comparable and are for the same period as the TIDs observed in Figure 5.5 (a). This further confirms the propagation from the southern wintertime hemisphere to the northern summertime hemisphere on 13 July 2012. The propagation velocity that was calculated by means of the linear regression method is slightly lower than the velocity calculated by means of the time shift of the Δ TEC peaks of the PRNs (see Figure 5.5 (a)). This is to be expected, because the time shift method assumes perfect equatorward propagation and thus results in higher propagation velocity values (Ngwira *et al.*, 2012; Habarulema *et al.*, 2013). Figures 5.5 (e)-(f) present the 15 min moving averaged ΔTEC of the GPS measurements by different stations for PRNs 23 and 19 on 16 January 2014. There is a time shift in the ΔTEC peaks of PRNs 23 and 19 for the different stations in the northern and southern hemispheres. The meridional propagation velocities were 357 ± 34 m/s in the northern hemisphere and 309 ± 40 m/s towards the equator. On 13 July 2012 and 16 January 2014, the overall meridional propagation velocities were 457 ± 32 m/s and 333 ± 37 m/s, respectively. The propagation angles were 31.5° and 127.2° were reference to the northward direction, as shown in Figures 5.5 (a) and (d).

The remaining cases of equatorward medium-scale TIDs possibly launched from mid- to high-latitudes in the southern wintertime hemisphere on 19 April 2016, 04 June 2016 and 16 September 2016 are shown in Figures 5.6 (a)-(c). It is worth pointing out that, with respect to universal time (UT), some of the observed equatorward TIDs could possibly have been launched the day before they crossed the geomagnetic equator (e.g. Figures 5.6 (b)-(c)). However, those days were also geomagnetically quiet (maximum kp<3). All the characteristics of these equatorward medium- to large-scale TIDs are presented in Table 5.2. All waves originated in the winter hemisphere. These observations lead to the conclusion that equatorward medium- to large-scale TIDs more often propagated from the southern wintertime hemisphere than from the northern wintertime hemisphere. In the northern hemispheres, equatorward medium- to large-scale TIDs were observed during winter months in the morning hours, while in the southern hemisphere medium- to large-scale TIDs were observed predominantly during winter. The meridional propagation velocities, periods and wavelengths of the TIDs were in the range of 270-322 m/s, 48-80 minutes and 802-1296 km, respectively. The horizontal propagation velocities and horizontal wavelengths were in the range of c_H=120-274 m/s and λ_H=379-1104 km, respectively. These results show that medium- to large-scale TIDs cross the geomagnetic equator during quiet conditions in winter months, although they do not occur frequently.

Table 5.2: Properties of TIDs originating in the high-latitudes and crossing the geomagnetic equator during quiet conditions. 1^{st} column: dates of occurrence of medium- to large-scale TIDs; 2^{nd} column: daily maximum Kp index; 3^{rd} column: progagation direction of the wavefront of medium- to large-scale TIDs (clockwise from north); 4^{th} column: averaged meridional phase velocities (southward and northward) based on the wave least-square fitting method; 5^{th} column: the periods of TIDs; 6^{th} column: meridional wavelength of TIDs; 7^{th} column: horizontal phase velocities c_H; 8^{th} column: horizontal wavelength λ_H.

Date	Maximum Kp index	Prop.direction (°)	Velocity (m/s)	Period (min)	Wavelength (km)	c_H (m/s)	λ_H (km)
13.07.2012	1	31.5	270 ± 22	80 ± 13	1296	230	1104
27.07.2012	2	44.2	311 ± 11	54 ± 9	1007	223	723
16.01.2014	1	127.2	322 ± 12	63 ± 17	1217	195	737
29.01.2016	1	116.5	273 ± 20	49 ± 8.3	802	120	379
19.04.2016	1	31.1	320 ± 47	48 ± 9.7	922	274	789
04.06.2016	1	36.2	251 ± 14	55±10.5	828	203	670
16.09.2016	2	32.1	309 ± 23	53±14.2	984	262	833

5.3.2 American sector

Figure 5.7 is similar to Figure 5.6, but covers the American sector. Figures 5.7 (a)-(b) shows ΔTEC plots as a function of time within the longitudinal sector of 50°-70°W and latitudinal range of 90°S-90°N for both 01 June 2014 and 18 July 2016. Figure 5.7 (a) shows that the equatorward TID structure emerged from the southern hemisphere in winter at high-latitudes (based on the time estimated from the extrapolated fitted line) around 14:00 (UT) and crossed the geomagnetic equator into the summertime northern hemisphere. This TID had an approximate period of 62 ± 13 min and a meridional propagation velocity of 310 ± 22 m/s. The horizontal velocity and wavelength values were 236 m/s and 590 km, respectively, which are typical of medium-scale TIDs (Hocke and Schlegel, 1996; Katamzi-Joseph *et al.*, 2019). Figure 5.7 (b) depicts the visible TID as it propagates equatorward from the wintertime southern hemisphere (at approximately 09:00 UT) to the summertime northern hemisphere. The horizontal propagation velocity and wavelength were 152 m/s and 491 km, respectively. Table 5.3 depicts two cases of equatorward medium-scale TIDs that appear to have originated from the mid- to high-latitude and crossed the geomagnetic equator to the opposite hemisphere over America sector during geomagnetically quiet conditions. These TIDs originated in the winter hemisphere.

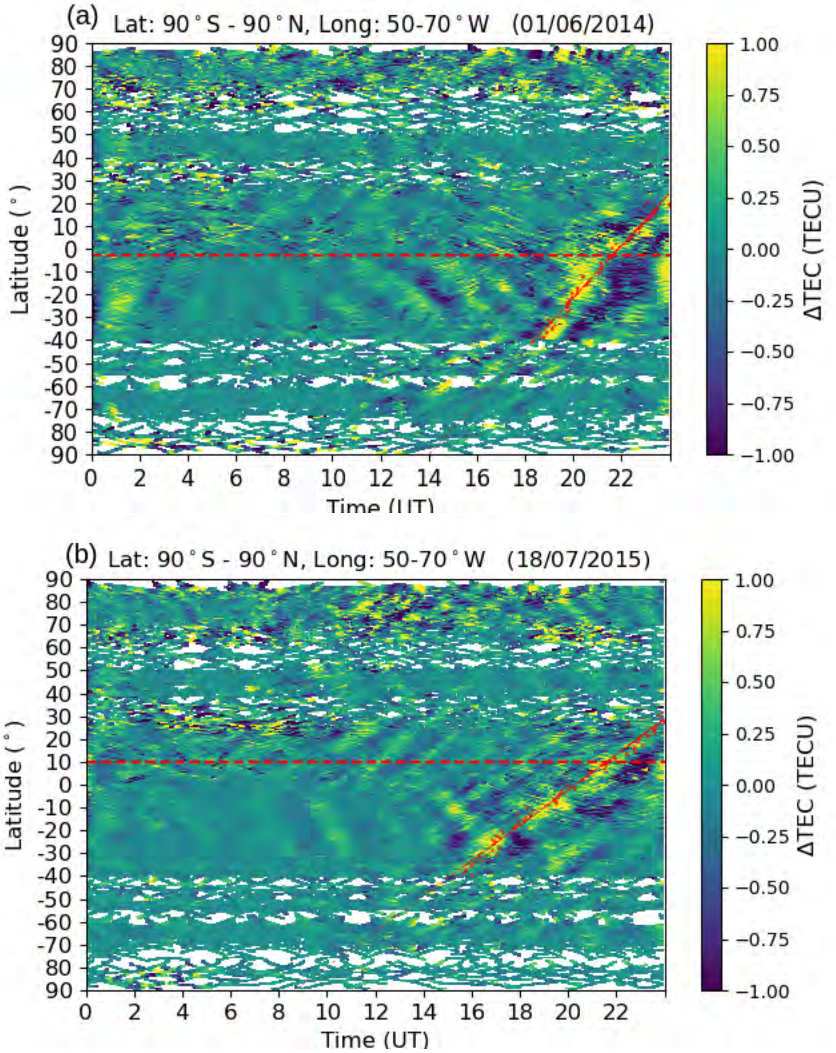

Figure 5.7: Latitude-time plot of ΔTEC within the longitudinal sector of 50°-70°W and latitudinal range of 90°S-90°N.

Table 5.3: Properties of TIDs originating from the high-latitudes and crossing the geomagnetic equator over the American sector during quiet conditions. 1^{st} column: dates of occurrence of medium- to large-scale TIDs; 2^{nd} column: daily maximum Kp index; 3^{rd} column: progagation direction of the wavefront of medium- to large-scale TIDs (clockwise from north); 4^{th} column: averaged meridional phase velocities (southward and northward) based on the wave least-square fitting method; 5^{th} column: the periods of TIDs; 6^{th} column: meridional wavelength of TIDs; 7^{th} column: horizontal phase velocity c_H; 8^{th} column: horizontal wavelength λ_H.

Date	Maximum Kp index	Prop.direction (°)	Velocity (m/s)	Period (min)	Wavelength (km)	c_H (m/s)	λ_H (km)
01.06.2014	1	40.2	310 ± 15	61.5 ± 11	772	236	590
18.07.2015	1	50.4	238 ± 10	54 ± 9	771	152	491

Figure 5.8: Variation of interplanetary magnetic field (Bz [nT]), interplanetary electric field (IEF [mV/m]), AE index (nT), polar cap (PCN and PCS [mV/m]), Dst index and Kp index on 13 July 2012 (`https://omniweb.gsfc.nasa.gov/`).

5.3.3 Possible Sources of TIDs

The aurora electrojet index, solar wind parameters (solar wind velocity, IMF Bz and interplanetary electric field), polar cap index, Kp, and Dst index were examined to identify possible causes of these TIDs. For example, Figure 5.8 shows variations of the polar cap (PCN and PCS [mV/m]), interplanetary magnetic field, Bz (nT), interplanetary electric field, IEF (mV/m), Dst, Kp and AE index on 13 July2012. The IMF Bz was moving southward and northward, ranging from -2.14 nT to 2.95 nT. The maximum solar wind velocity was 398.3 km/s (00:02 UT). The AE index had a maximum value of 266 nT (11:02 UT). The IEF and polar cap (PCN and PCS) varied from -1.05 mV/m to 1.0 mV/m and -0.7 mV/m to 1.3 mV/m, respectively. The Kp values were less than 2, and the Dst ranged between -20 and -8 nT. The typical minimum value of the Dst index during quiet conditions is -20 nT (Walker *et al.*, 2013), while Kp < 3 (Zhang and Holt, 2008; Huang *et al.*, 2020; Cai *et al.*, 2021). The parameters (shown in Figure 5.8) clearly show that it was a geomagnetically quiet day (Zhang and Holt, 2008; Walker *et al.*, 2013; Huang *et al.*, 2020; Cai *et al.*, 2021). This suggests that space weather was not a driver. Results of other cases (not shown) also show no evidence of space weather as a driver of the observed TIDs. The lower atmosphere was

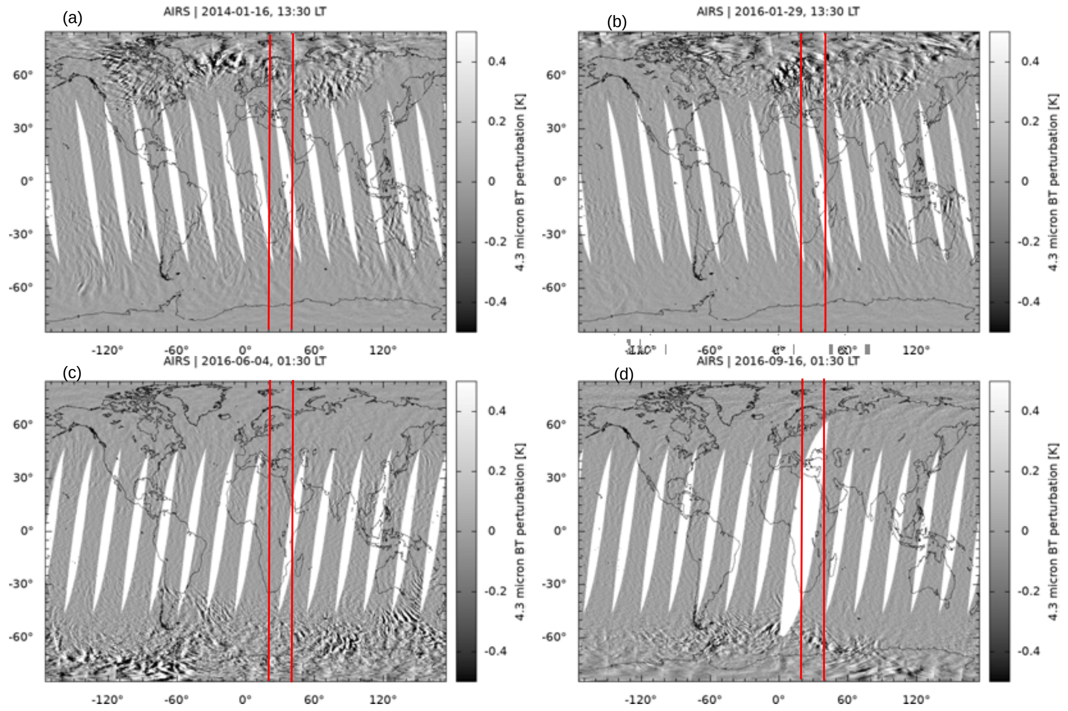

Figure 5.9: Global AIRS derived 4.3 μm brightness temperature perturbations on (a) 16 January 2014, (b) 29 January 2016, (c) 04 June 2016 and (d) 16 September 2016 at the approximate times when TIDs were identified to have originated in the high-latitudes according to GPS data. The red vertical solid lines show the region of the 20°-40°E longitudinal sector for which in GPS data analyses were done.

studied as a possible driver for the observed waves via multi-step vertical coupling. Figure 5.9 shows the 4.3 μm brightness temperature (BT) perturbations derived from the Atmospheric Infrared Sounder (AIRS) (Hoffmann *et al.*, 2013) for four cases and at the approximate times when medium- to large-scale TIDs were thought to have originated from high-latitudes, as identified on the 2D ΔTEC maps for the African-European sector. AIRS gravity wave data was provided separately for nighttime (01:30 LT) and daytime (13:30 LT) observations, as explained in Section 4.4. The red vertical solid lines in Figure 5.9 show the region of 20°-40°E longitudinal sector for which GPS data analyses were done. Figures 5.9 (a)-(b) show the 4.3 μm BT for 16 January 2014 and 29 January 2016 both at 13:30 LT. On these days, TID signatures were observed to have originated from northern hemisphere high-latitudes (see Figures 5.4 (d) and 5.3 (b)) at about 12:00 LT and propagated equatorward. Interestingly, in both cases, the presence of a AGW (a wave-formed ripple) was observed just west of the red vertical line of the AIRS 4.3 μm BT perturbations at high-latitudes in the northern hemisphere. It is noteworthy, in Figure 5.9 (a)-(b), that there were no visible AGWs at high-latitudes in the southern hemisphere. Based on azimuth propagation angles (127.2° (Figures 5.4 (d)) and 116.5° (Figure 5.3 (b)), it is possible that these TIDs were tertiary GWs from the dissipation of secondary GWs excited by the local body force created from mountain waves (MWs) breaking over Greenland and the Alps, respectively. Recent studies show that there was evidence of MWs on Greenland (Leutbecher and Volkert, 2000; Doyle *et al.*, 2005; Olafsson and Agústsson, 2009; Kivi *et al.*, 2020).

Figures 5.9 (c)-(d) show the 4.3 μm BT for 04 June 2016 and 16 September 2016, both at 01:30 LT. These figures show strong MW activity in the Andes and the Antarctic Peninsula, respectively. Assuming the TID in Figures 5.6 (b)-(c) are from high-latitudes, the estimated start time was at approximately 01:00 LT in both cases. From the available data, TID traces could be seen from 08:00 UT in the mid-latitudes of the southern hemisphere. For the sake of clarity, please note that in Figure 5.6 (b), the fitted line along the TID trajectory indicates that the structure started on 03 June 2016 at 23:00 UT (based on the time estimated from the extrapolated fitted line), which is at 01:00 LT on 04 June 2016 along 30°E longitude. This is a similar case to the observation on 16 September 2016. As in the previous case, AGWs were present in the southern hemisphere latitudes during the period when TIDs were detected in GPS observations on 04 June 2016, and 16 September 2016. The conclusion is therefore that the AIRS and GPS observations in both the southern and northern hemispheres are in perfect agreement in terms of AGWs and TIDs representations, respectively. Note that there is evidence of MWs in the AIRS data for the southern Andes and Antarctica (Wu *et al.*, 2006; Alexander and Teitelbaum, 2007, 2011; Eckermann *et al.*, 2009; Hoffmann *et al.*, 2013, 2016; Kogure *et al.*, 2020, and references therein), referring to Figures 5.9 (c)-(d). The modelling results show that these MWs break and dissipate just above the maximization of the stratospheric polar night jet, resulting in secondary GWs that continue to dissipate in the mesosphere and lower thermosphere, giving rise to localised body forces (Vadas and Becker, 2019). In their study, Vadas and Becker (2019) showed that the resulting body forces led to the excitation of medium- and large-scale tertiary GWs, extending to the African region's west coast. For this to happen, the propagation angles were expected to be 30°-40° which agrees with propagation angles of 36° and 32° for 04 June 2016 and 16 September 2016, respectively. Furthermore, Vadas and Becker (2019) reported horizontal phase speeds (c_H) values of 120-420 m/s which agrees with the calculated c_H values for 04 June 2016 and 16 September 2016, which were 203 m/s and 262 m/s, respectively. Based on the propagation angles and AIRS data shown in Figures 5.9 (c)-(d), the sources of the tertiary GWs were likely the MWs over the Southern Andes and Antarctic Peninsula on 04 June 2016, and while on 16 September 2016, the MWs were over the Antarctic Peninsula.

Figures 5.10 (a)-(b) show the 4.3 μm BT for 01 June 2014 and (b) 18 July 2015, both at 01:30 LT. These Figures show a high level of MW activity in the Andes and the Antarctic Peninsula. On these days, TID signatures were observed to have originated from southern hemisphere high-latitudes (see Figures 5.7 (a)-(b)), at around 12:00 UT (09:00 LT) and 11:00 UT (08:00 LT), respectively, and propagated equatorward. AGWs (Figures 5.10 (a)-(b)) were present in the latitudes of the southern hemisphere between 01 June 2014, and 18 July 2015, when TIDs were detected in GPS data. In both cases Figures 5.10 (a)-(b) show no visible signs of AGWs in the high-latitudes of the northern hemisphere.

Based on the calculated horizontal velocities (c_H=230 m/s (Figure 5.5 (a)), c_H=195 m/s (Figure 5.5 (d)) and c_H=152 m/s (Figure 5.7 (b))), it may be possible that these lower atmospheric activities could be direct sources of TIDs. However, the MWs had nearly zero phase velocity: $c_H \sim 0$ (Fritts, 2015), which is clearly inconsistent with results in Table 5.2 and Table 5.3. According to the literature, the AGW in the lower atmosphere can propagate at horizontal velocities slower than the speed of sound (about 307 m/s), and propagate to the upper atmosphere where they dissipate or produce secondary/tertiary waves (Balachandran, 1980; Nastrom and Fritts, 1992; Vadas and Liu, 2009; Tsugawa *et al.*, 2004; Vadas *et al.*, 2018,

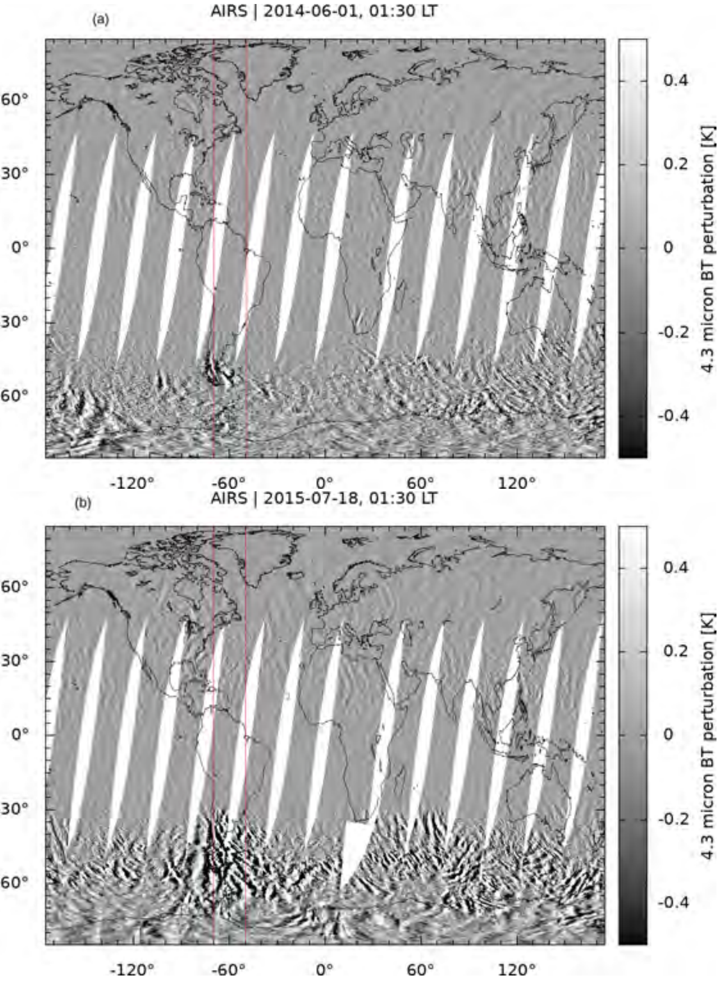

Figure 5.10: Global AIRS derived 4.3 μm brightness temperature perturbations on (a) 01 June 2014 and (b) 18 July 2016 at the approximate times when TIDs originated in the high-latitudes as detected in GPS data. The red vertical solid lines show the region of the 50°-70°W longitudinal sector for which GPS data analyses were done.

and references therein). Vadas and Becker (2019), Vadas *et al.* (2019) and Becker and Vadas (2020) suggested that medium- and large-scale TIDs during geomagnetic quiet conditions were probably generated by tertiary GWs created by the dissipation of secondary GWs and excited by the local body force which is created by the MW breaking in the stratopause region. As the investigation was conducted during geomagnetically quiet conditions, dominant mechanisms which lead to large-scale TIDs such as Lorentz forcing, particle precipitation and Joule heating were excluded as possible sources based on the observations. Regardless of the results presented here, sources of large-scale equatorward TIDs during geomagnetically quiet conditions have generally not been extensively studied as compared to disturbed conditions. However, there research on medium- to large-scale TIDs at high latitudes during quiet conditions is increasing (e.g. Vadas and Liu, 2009, 2013; Vadas *et al.*, 2018; Vadas and Becker, 2019; Vadas *et al.*, 2019; Becker and Vadas, 2020). Since MWs have $c_H \sim 0$, the source of these medium- and large-scale equatorward TIDs could be the tertiary GWs resulting from the dissipation of the secondary GWs formed by MW breaking (Vadas and Becker, 2019; Becker and Vadas, 2020).

5.4 Summary

The study focussed on medium- to large-scale TIDs, possibly originated in the polar region and crossing the geomagnetic equator into the opposite hemisphere over the African-European and American sectors during quiet conditions. Four geomagnetically quiet days were chosen for each month of the eight years studied, based on data from the World Data Center for Geomagnetism in Kyoto. For both African-European and American sectors, 384 days were analysed. The same procedure was used for both the African-European and American sectors. For the American sector, two cases of equatorward propagating medium- to large-scale TIDs were identified. For the African-European sector, seven transhemispheric TIDs were identified, with five originating in the southern and the rest in northern wintertime hemisphere. The meridional phase velocities, periods, and wavelengths of the TIDs were 270-322 m/s, 48-80 min, and 802-1296 km, respectively. The horizontal propagation velocities and horizontal wavelengths were in the range of c_H=120-274 m/s and λ_H=491-1104 km, respectively. These characteristics are in the range of medium- to large-scale TIDs. In the African-European sector, TIDs were more often launched in the high-latitudes southern winter hemisphere than in the high-latitudes northern winter hemisphere. In the American sector, TIDs were only launched in the southern winter hemisphere. The observed TIDs originated from the wintertime hemisphere and propagated into the summertime hemisphere. Previous studies have suggested that background neutral winds blowing from the summer to the winter hemisphere, may drive the production of equatorward TIDs in the region (Titheridge, 1995; Hari and Murthy, 1995; Habarulema *et al.*, 2018). There have been studies that show that when the phase velocity vectors of the TIDs are opposite the direction of the background neutral wind, wind filtering does not occur, resulting in azimuthal preferences in TIDs propagation, and when both the AGWs and background winds are in the same direction, there is wind filtering (Kalikhman, 1980; Waldock and Jones, 1986; Crowley *et al.*, 1987; Azeem, 2021; Katamzi-Joseph *et al.*, 2022). The impact of background neutral winds on TID periods, on the other hand, has not been adequately addressed in the literature. The meridional wind component of the neutral wind may or may not plays a significant role in the equatorward TIDs direction. The 16 April 2016 and 16 September 2016 events over the

African-European were both wintertime events (Liu *et al.*, 2019). In comparison with the results of earlier research (e.g. Vadas and Becker, 2019; Vadas *et al.*, 2019; Becker and Vadas, 2020), it is plausible to suggest that the source of these medium- to large-scale TIDs may be tertiary GWs as a result of the dissipation of secondary GWs and excited by the local body force created by breaking mountain waves.

Chapter 6

Results of the statistical analysis of poleward TIDs during quiet and disturbed conditions

This chapter discusses the statistical analysis of observations of poleward TIDs of equatorial origin over the African-European and American sectors during geomagnetically quiet and disturbed conditions between 2010 and 2018. Poleward TIDs of equatorial origin have received less attention than their equatorward counterparts, which are often seen during geomagnetic storms. These poleward TIDs during geomagnetic storms have only recently gained attention (Ding *et al.*, 2013; Habarulema *et al.*, 2015, 2016; Jonah *et al.*, 2018; Ngwira *et al.*, 2019), despite their existance having been proposed and demonstrated theoretically (Chimonas, 1969; Knudsen, 1969). Poleward TIDs of equatorial origin during geomagnetic storms were researched on a case-by-case basis (Ding *et al.*, 2013; Habarulema *et al.*, 2015, 2016; Jonah *et al.*, 2018; Ngwira *et al.*, 2019). For each month, four geomagnetically quiet days (maximum Kp < 3) were selected, based on data provided by the World Data Center for Geomagnetism, Kyoto. As criteria for geomagnetically disturbed conditions, a Kp$>$4 and Dst$\leq$ -50 nT were selected. Storm-time periods during the years from 2010 to 2018 may also be accessed on the following websites: `https://www.sidc.be/cactus/catalog/LASCO/250/cmelz.txt`, `https://cdaw.gsfc.nasa.gov/CME_list/` and `https://izw1.caltech.edu/ACE/ASC/DATA/level3/icmetable2.htm`. TEC derived data supplied by Global Navigation Satellite Systems (GNSS) was used to identify poleward TIDs.

6.1 Statistical results of poleward TIDs during quiet conditions

The approach described in Section 5.2 to identify medium- to large-scale equatorward TIDs over the American and African-European sectors was also taken to identify poleward TIDs of equatorial origin during quiet conditions. Data was considered within latitude and longitude coverages of 40°S-60°N and 20°-40°E, and 40°S-60°N and 50°-70°W for the African-European and American sectors, respectively. The meridional propagation velocity, period, and wavelength of the TIDs were determined by using the methods described in Section 5.2 and in the papers published by Liu *et al.* (2019) and Thaganyana *et al.* (2022). For example, Figure 6.1 shows the Kp and Dst indices, and latitude-time plots of ΔTEC over the African-European

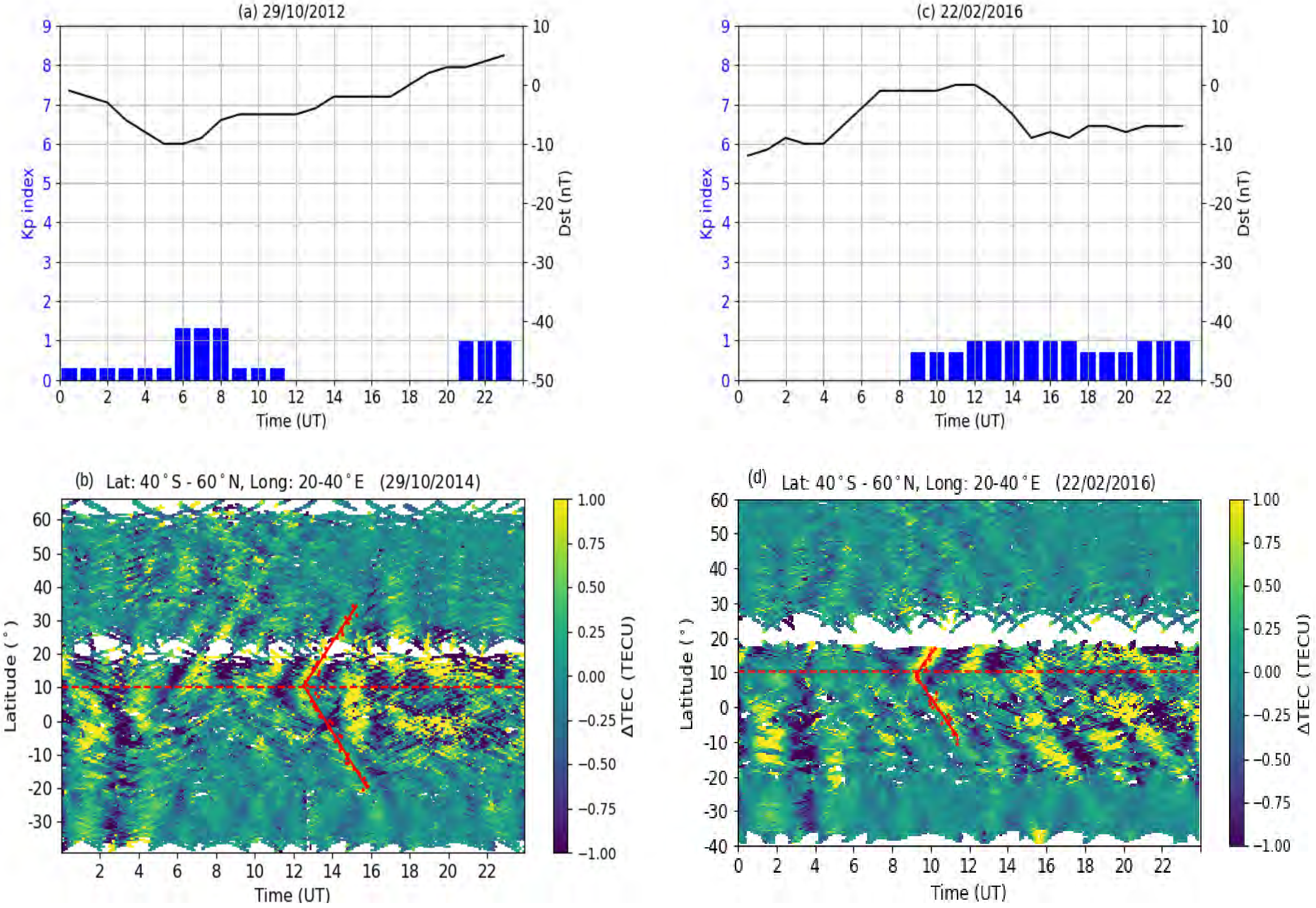

Figure 6.1: (a) and (c) Variation of the Kp and Dst indices on 29 October 2012 and 22 February 2016 (`https://omniweb.gsfc.nasa.gov/`). The blue bar graph represents the Kp index, whereas the black solid line represents the Dst index. (b) and (d) An example of the wave linear fitting method. Red dots show the data points for linear fitting, and the horizontal red dash lines approximate the geomagnetic equator at 10°N geographic latitude.

sector within a longitudinal sector of 20°-40°E for 29 October 2012 and 22 February 2016. The data for the Kp and Dst indices was obtained from the NASA Goddard Space Flight Center website (`https://omniweb.gsfc.nasa.gov/`). In Figure 6.1 (a) and (c), the blue bar graph indicates the Kp index and the black solid line represents the Dst index. The Kp values were less than 2, and the Dst ranged between -15 and 10 nT on both occasions (Figure 6.1 (a) and (c)), indicating typical geomagnetically quiet days (Walker *et al.*, 2013). The averaged meridional propagation velocities (northward and southward) of TIDs estimated from the data points (red dots) in Figures 6.1 (b) and 6.1 (d) were 276 ± 19 m/s and 245 ± 41 m/s on 29 October 2012 and 22 February 2016, respectively. The southward propagating azimuth of TIDs, estimated from the red data points in Figures 6.1 (b) and 6.1 (d) were 131° (clockwise from north) and 140° (clockwise from north) on 29 October 2012 and 22 February 2016, respectively. The periods of the TIDs were 46 ± 18 min and 47 ± 6 min on 29 October 2012 and 22 February 2016, respectively.

6.1.1 Quiet-time poleward TIDs over the African-European sector

Analyses of poleward TIDs were done for the African-European sector for quiet conditions. These were done for the four quiet days of each month of the year between 2010 and 2018. An additional example of a typical scenario of a TID over African-European is shown for 16 July 2011. Figure 6.2 shows variations of polar cap (PCN and PCS [mV/m]), interplanetary magnetic field (IMF Bz [nT], in GSM coordinates), interplanetary electric field (IEF [mV/m]), Dst, Kp and AE index for 16 July 2011. The IEF, Dst, IMF Bz, Kp and AE data was obtained from the NASA Goddard Space Flight Center (`https://omniweb.gsfc.nasa.gov/`), and polar cap data from the Polar Cap Magnetic Index (`https://pcindex.org/`). The IMF Bz was oscillating between southward and northward, ranging from -2.4 nT to 3.65 nT. The maximum value of solar wind velocity was 410 km/s at 02:07 UT. Meanwhile, the AE index had increased to a maximum of 370 nT (07:03 UT). The IEF and polar cap (PCN and PCS) varied from -1.4 mV/m to 1 mV/m and -1.1 mV/m to 1.6 mV/m, respectively. Figure 6.2 (d) shows that the minimum value of the Dst index was -5 at 05:00 UT, while the Kp value was 1.3 (09:00 UT). The typical minimum value of the Dst index during quiet conditions is -20 nT (Walker *et al.*, 2013), while Kp < 3 (Zhang and Holt, 2008; Huang *et al.*, 2020; Cai *et al.*, 2021; Thaganyana *et al.*, 2022). The results in Figure 6.2 clearly show that it was a geomagnetically quiet day (Zhang and Holt, 2008; Walker *et al.*, 2013; Huang *et al.*, 2020; Cai *et al.*, 2021; Thaganyana *et al.*, 2022). For 16 July 2011, TIDs originating from the geomagnetic equator were identified (see Figure 6.3 (a)). Figure 6.3 (a) shows ΔTEC as a function of latitude and time for 16 July 2011, within the latitudinal and longitudinal ranges of 40°S-60°N and 20°-40°E. The red fitted lines depict the poleward TID orientation in both the southern and northern hemispheres. The traces of poleward TIDs begin at around 11:00 UT. The meridional velocities and periods of the TID are 254 ± 27 m/s and 45 ± 14 min, respectively.

While poleward TIDs have not been reported for quiet conditions, studies have associated storm-time poleward TIDs with changes in the electrodynamics of low-latitude (Habarulema *et al.*, 2015, 2016; Ngwira *et al.*, 2019). It have been established that the local electrodynamics are responsible for poleward TIDs that originate from the geomagnetic equator via the Lorentz coupling of the electrojet with the neutral atmosphere, and which is enhanced during geomagnetic storms (Habarulema *et al.*, 2015, 2016; Ngwira *et al.*, 2019). To investigate the role played by changes in electrodynamics in contributing to this poleward TID (Figures 6.3 (a)) during quiet conditions, the variability of equatorial electrojet (EEJ, ΔH (nT)) was analysed with reference to monthly median EEJ values. The EEJ is a current that flows within the range of ± 3° latitude from the geomagnetic equator. The direction of the current is usually eastward during the daytime (Anderson *et al.*, 2002; Yizengaw *et al.*, 2012; Ngwira *et al.*, 2012, 2019; Dubazane and Habarulema, 2018; Habarulema *et al.*, 2019). A pair of magnetometers, one near the dip equator (EEJ region) and another 6°-9° away, can be used to estimate the EEJ current and thus the E×B drift during the daytime (Anderson *et al.*, 2002; Yizengaw *et al.*, 2012; Dubazane and Habarulema, 2018). Details about the differential magnetometer approach may be found in Section 4.3. This method for estimating the EEJ by means of magnetometer observations is only reliable during the local daytime. The EEJ is a daytime phenomenon within the E-region ionosphere, which is caused by the electric fields driven from neutral wind dynamics and geomagnetic field geometry at the geomagnetic equator (Anderson *et al.*, 2002; Yizengaw *et al.*, 2012; Ngwira *et al.*, 2012;

Dubazane and Habarulema, 2018; Habarulema *et al.*, 2019). EEJ was calculated by means of two magnetometers: Addis Ababa (AAE, 0.17°N, 110.47°E, geomagnetic) and Adigrat (ETHI, 6.0°N, 111.06°E, geomagnetic). To suggest that EEJ variability may have an impact on the origin of poleward TIDs, the background ΔH was computed using the monthly median method (Dugassa *et al.*, 2020; Habarulema *et al.*, 2022). Other approaches for calculating a background include the moving average, polynomial fitting, and mean method (Shiokawa *et al.*, 2002; Habarulema *et al.*, 2016; Thaganyana *et al.*, 2022). The median method offers the advantage of being sensitive to the presence of outliers (Leys *et al.*, 2013; Dubazane and Habarulema, 2018; Thaganyana *et al.*, 2022). In order to conclude that EEJ variability may have led to launching of poleward TIDs, the ΔH should be greater than the background ΔH (monthly median EEJ values). There was a clear increase in ΔH between 11:00 and 12:00 UT over the corresponding monthly median ΔH values, as shown by two vertical black lines in Figure 6.3 (b). The ΔH is represented by a blue curve, while the monthly median ΔH is represented by a red curve. The inset in Figure 6.3 (b) displays the zoomed-in fluctuation of ΔH over this time period. The black dot in the inset in Figure 6.3 (b) represents the maximum value of ΔH. Due to insufficient data from the ETH station, the correlation between changes in EEJ and the occurrence of poleward TIDs could not be established. Only three cases had EEJ data available, and the ΔH during the time period of these poleward TIDs was greater than the monthly median EEJ values. The eastward prompt penetration electric field (PPEF), which is associated with geomagnetic storms, could enhance the EEJ and produce the poleward TIDs (Habarulema *et al.*, 2015, 2016; Ngwira *et al.*, 2019). During the period that poleward TIDs were observed (Figure 6.3 (a)), the IMF Bz (Figure 6.2 (a)) was already moving in a northward direction. As shown in Figure 6.2, the AE and IEF indices only showed minor increases during the observation period of poleward TIDs on 16 July 2011, ruling out the possibility of a major PPEF. The enhanced EEJ over the monthly median EEJ could be associated with the forces from the lower atmosphere, such as fronts, convection systems and sudden stratospheric warmings (Kazimirovsky and KoKouRov, 1991; Anderson and Araujo-Pradere, 2010; Goncharenko *et al.*, 2010; Chau *et al.*, 2012; Huang *et al.*, 2020), during geomagnetically quiet conditions. However, the actual causes of an enhanced EEJ over the monthly medium values have not been investigated in detail. TIDs may be caused by tropospheric-stratospheric processes such as fronts, convection systems, vortices, tropospheric turbulence and sudden stratospheric warnings (Hocke and Schlegel, 1996; Wan *et al.*, 1998; Boška and Šauli, 2001; Vadas *et al.*, 2009; Jonah *et al.*, 2018; Bravo *et al.*, 2022).

Table 6.1 shows the results of the statistical analysis of the poleward TIDs, thought to have been launched from the geomagnetic equator over the African-European sector during quiet conditions. The maximum Kp values were obtained from following website: `https://omniweb.gsfc.nasa.gov/`. The meridional and horizontal velocities, periods, and propagation direction of the TIDs were determined by the methods described in Section 5.2 and in the papers published by Liu *et al.* (2019) and Thaganyana *et al.* (2022). The fourth column in Table 6.1 indicates the southward (S) and northward (N) propagation angles of the wavefronts of the TIDs (clockwise from north). The horizontal velocities c_H were computed (Equation 5.5) using the southward propagation angles of TIDs wavefront (clockwise from the north). The majority of poleward TIDs were medium-scale TIDs. The meridional velocity and period were 210-299 m/s and 0.5-1.5 h, respectively. The horizontal velocity varied between 110 m/s and 270 m/s, which are typical of medium-scale TIDs (Hunsucker, 1982;

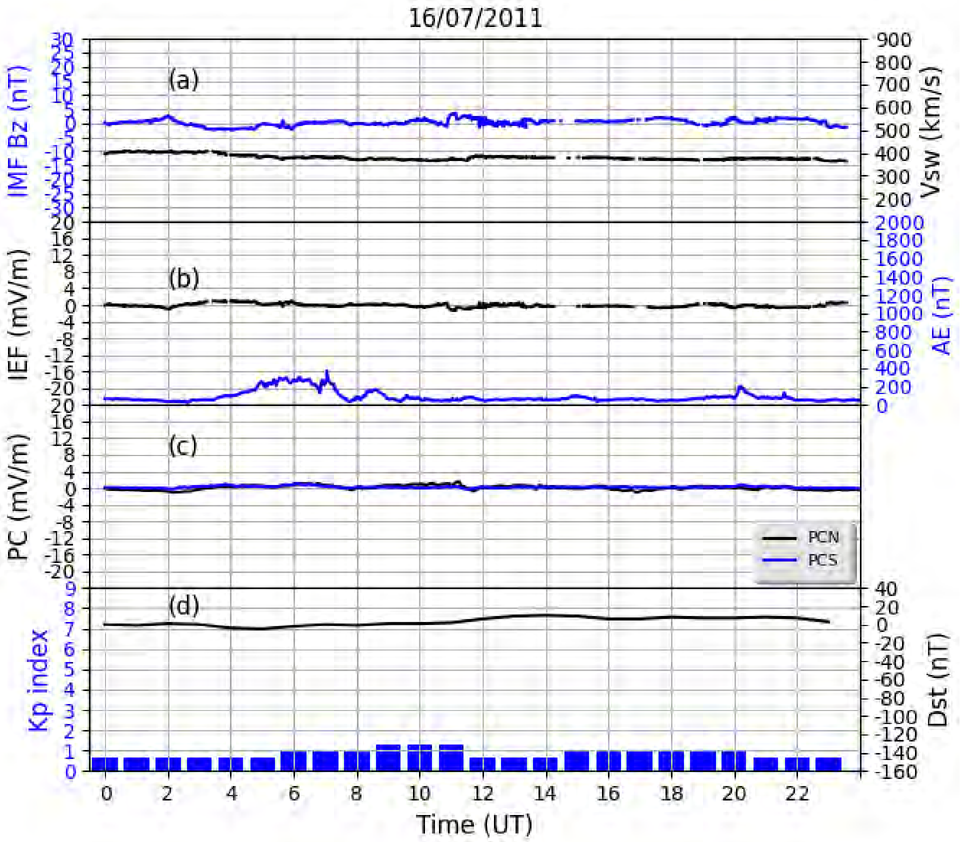

Figure 6.2: Variation of solar wind speed (V_{sw}, km/s), interplanetary magnetic field (Bz [nT]), interplanetary electric field (IEF [mV/m]), polar cap (PCN and PCS [mV/m]), Dst, Kp and AE index (nT) on 16 July 2011 (`https://omniweb.gsfc.nasa.gov/`). The blue curve represents the IMF Bz, AE index, PCS index, whereas the black curve represents the V_{sw}, IEF, PCN and Dst index. The blue bar graph represents the Kp index.

Table 6.1: Statistical observations of poleward TIDs during quiet conditions over African-European Sector. 1^{st} column: dates of occurrence of poleward TIDs; 2^{nd} column: estimated occurrence time of poleward TIDs: 3^{rd} column: daily maximum kp index; 4^{th} column: southward (S) and northward (N) progagation direction of TIDs wavefront (clockwise from north); 5^{th} column: averaged meridional phase velocities (southward and northward) obtained using wave least-square fitting method; 6^{th} column: horizontal phase velocities c_H; 7^{th} column: the periods of TIDs.

Date	Time	Maximum Kp index	Prop. direction S (N)	Velocity (m/s)	c_H (m/s)	period (min)
08.05.2011	06:00-08:00	1.0	140 (38)	292 ± 37	224	62 ± 13
16.07.2011	04:30-05:30	1.3	158 (49)	254 ± 27	235	45 ± 14
17.07.2011	04:00-05:00	1.7	138 (36)	250 ± 20	186	63 ± 17
11.09.2011	05:00-06:00	2.6	130 (34)	210 ± 27	135	49 ± 11
19.06.2012	04:00-06:00	0.7	144 (40)	250 ± 20	202	52 ± 15
05.08.2012	04:00-06:00	2.3	136 (32)	238 ± 32	171	45 ± 9
10.08.2012	04:30-06:00	1.0	140 (44)	259 ± 13	198	48 ± 7
29.10.2012	12:00-14:00	1.3	131 (33)	276 ± 19	181	46 ± 14
05.02.2013	08:00-10:00	1.3	137 (36)	299 ± 14	219	55 ± 12
11.05.2013	07:00-10:00	1.3	145 (42)	233 ± 32	190	39 ± 10
02.07.2013	05:00-06:00	1.3	149 (45)	247 ± 43	212	40 ± 13
08.07.2013	03:30-04:30	1.7	135 (38)	255 ± 21	180	55 ± 15
31.01.2014	17:00-19:00	0.7	134 (36)	227 ± 27	158	46 ± 9
06.05.2014	09:30-10:30	0.7	130 (34)	332 ± 35	213	75 ± 19
13.02.2015	08:00-10:00	1.0	138 (43)	224 ± 15	166	49 ± 10
02.06.2015	04:00-06:00	0.3	140 (42)	273 ± 19	209	51 ± 16
02.07.2015	04:00-06:00	0.7	136 (35)	253 ± 33	182	37 ± 8
25.01.2016	10:00-12:00	0.7	138 (40)	282 ± 15	210	54 ± 13
22.02.2016	09:00-10:0	1.0	140 (35)	245 ± 41	188	47 ± 6
	11:30-12:30		132 (38)	212 ± 35	142	50 ± 8

Hocke and Schlegel, 1996; Katamzi-Joseph *et al.*, 2019). Almost all poleward TIDs occur primarily during the local daytime.

6.1.2 Quiet-time poleward TIDs over the American sector

Analyses of poleward TIDs during quiet conditions were also done for the American sector. Figure 6.4 shows variation of polar cap (PCN and PCS [mV/m]), interplanetary magnetic field (IMF Bz [nT], in GSM coordinates), interplanetary electric field, IEF (mV/m), Dst, Kp and AE index for 19 November 2010. The IMF Bz was moving southward and northward, ranging from -1.85 nT to 3.90 nT. The maximum solar wind velocity was 574.5 km/s (00:27 UT). The AE index had a maximum value of 132 nT (09:03 UT). The IEF and polar cap (PCN and PCS) varied from -1.5 mV/m to 1.3 mV/m and -1.5 mV/m to 1.5 mV/m, respectively. The Kp values were less than 2, and the Dst ranged between -17 and 6 nT. The parameters (given in Figure 6.4) clearly demonstrate that it was a geomagnetically quiet day (Walker *et al.*, 2013; Huang *et al.*, 2020). Figure 6.5 (a) is similar to Figure 6.3 (a), but it depicts results over the American sector during quiet conditions. The latitude-time plot of ΔTEC is shown for 19 November 2010 in Figure 6.5. Poleward TIDs are visible, starting at around 16:30 UT (12:30 LT). Figure 6.5 (b) shows changes in ΔH for 19 November 2010 with monthly median ΔH. When poleward TIDs occur, the ΔH was above the monthly median ΔH, as shown in the insert in Figure 6.5 (b) between vertical solid black lines. It is possible

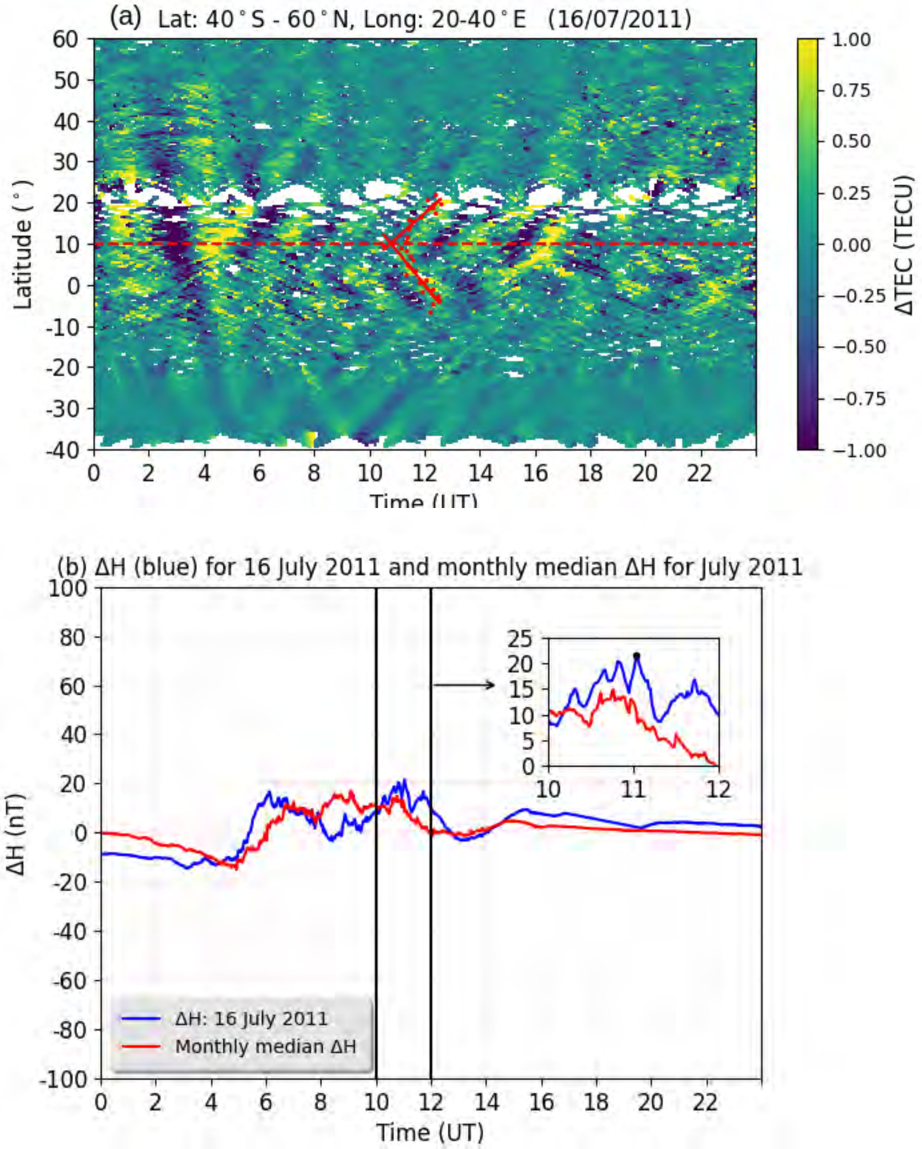

Figure 6.3: An example of poleward TIDs of equatorial origin. (a)-(b) Variation of ΔTEC (TECU) over African-European sector, ΔH (nT) for July 16, 2011 and corresponding monthly median ΔH (nT) for July 2011. The ΔH is represented by a blue curve, while the monthly median ΔH is represented by a red curve.

that EEJ variability has an impact on the origin of this poleward TID. The increase in the ΔH (EEJ) could be attributed to forces from the lower atmosphere such as fronts, convection systems, sudden stratospheric warmings (Kazimirovsky and KoKouRov, 1991; Anderson and Araujo-Pradere, 2010; Goncharenko *et al.*, 2010; Chau *et al.*, 2012; Huang *et al.*, 2020), during geomagnetically quiet conditions.

Table 6.2 shows the results of the statistical analysis poleward TIDs thought to have been launched from the geomagnetic equator over the American sector during quiet conditions. Fewer poleward TIDs were observed in the American sector than in the African-European sector. The reasons for this difference were not established and are to be investigated in the future. Regardless of the results shown here, the sources of poleward TIDs have generally not been as extensively studied for quiet conditions as during disturbed conditions. There is no literature on quiet-time poleward TIDs originating from equatorial region. Overall, during quiet conditions, the electrodynamics associated with an increase in the eastward electric field and thus an increase in the vertical E×B drift may play a critical role in launching AGWs in equatorial latitudes, which may be among the likely sources of the reported poleward TIDs.

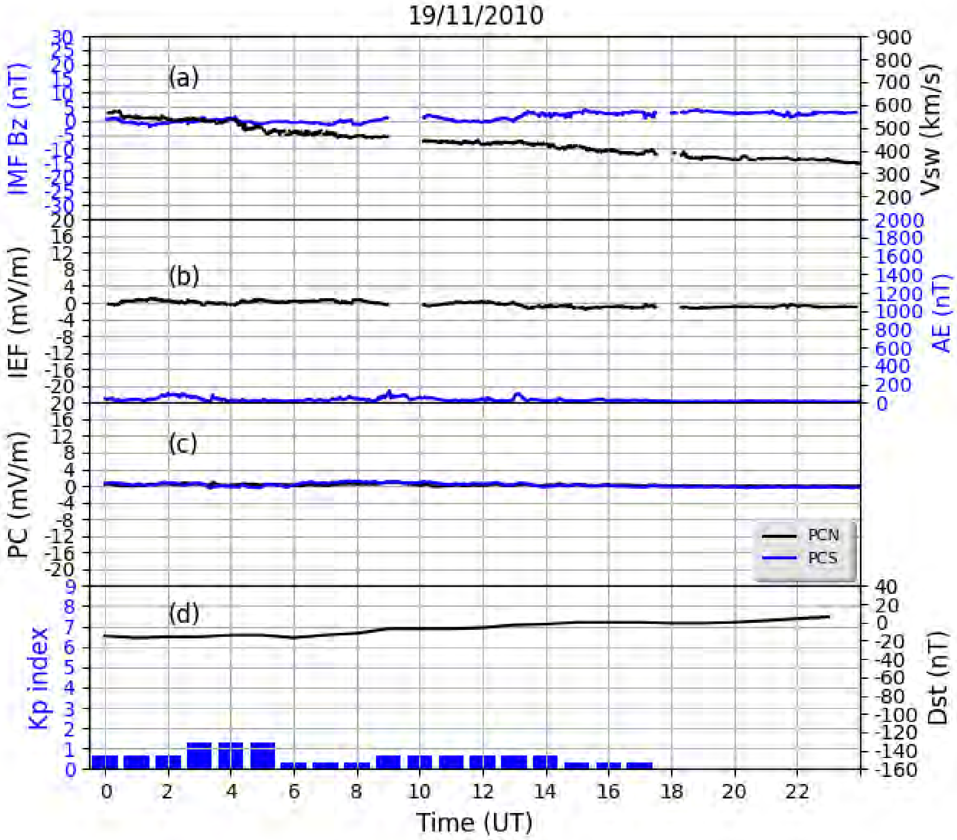

Figure 6.4: Variation of solar wind speed (V_{sw}, km/s), interplanetary magnetic field (Bz [nT]), interplanetary electric field (IEF [mV/m]), polar cap (PCN and PCS [mV/m]), Dst, Kp and AE index (nT) on 19 November 2010. The blue curve represents the IMF Bz, AE index, PCS index, whereas the black curve represents the V_{sw}, IEF, PCN and Dst index. The blue bar graph represents the Kp index.

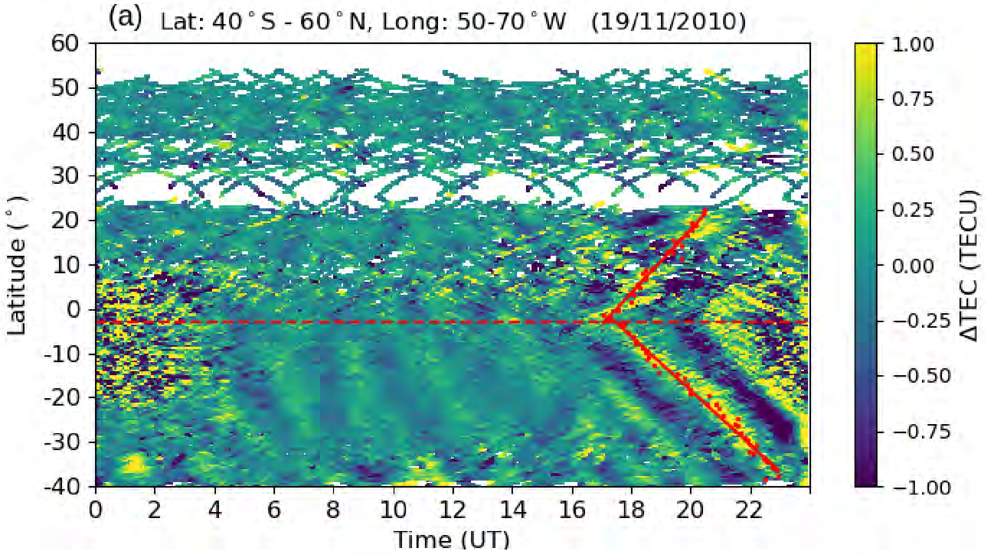
(a) Lat: 40 °S - 60 °N, Long: 50-70 °W (19/11/2010)

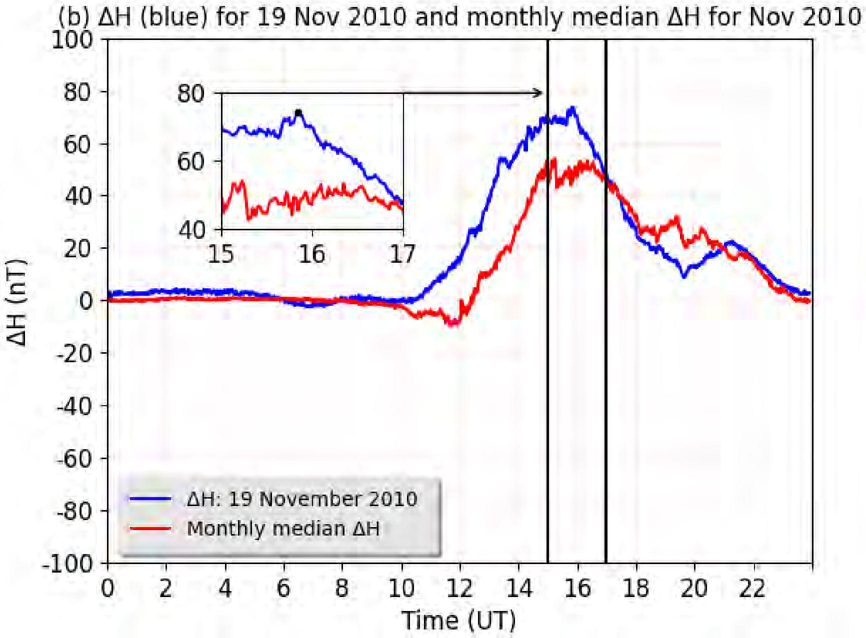
(b) ΔH (blue) for 19 Nov 2010 and monthly median ΔH for Nov 2010

Figure 6.5: Variation of ΔTEC (TECU) over the American sector, ΔH (nT) for 19 November 2010 and corresponding monthly median ΔH (nT) for November 2010. The ΔH is represented by a blue curve, while the monthly median ΔH is represented by a red curve.

Table 6.2: Statistical observations of poleward TIDs during quiet conditions over the American sector. 1st column: dates of occurrence of poleward TIDs; 2nd column: estimated time occurrence of poleward TIDs: 3rd column: daily maximum kp index; 4th column: southward (S) and northward (N) progagation angles of the wavefronts TIDs (clockwise from north); 5th column: averaged meridional phase velocities (southward and northward) calculated by means of the wave least-square fitting method; 6th column: horizontal phase velocities c_H; 7th column: the periods of TIDs.

Date	Time	Maximum Kp index	Prop. direction S (N)	Velocity (m/s)	c_H (m/s)	period (min)
19.11.2010	17:00-18:00	1.3	130 (40)	271 ± 12	174	51 ± 11
19.11.2011	16:00-15:00	0.3	145 (46)	265 ± 25	217	45 ± 27
09.08.2014	12:00-13:00	1.3	138 (45)	279 ± 20	207	70 ± 11
09.09.2014	15:00-16:00	2.3	143 (39)	238 ± 32	190	77 ± 21
14.09.2014	11:00-12:00	0.7	132 (41)	210 ± 27	141	30 ± 9
15.09.2014	16:00-17:00	1.0	145 (43)	250 ± 20	205	49 ± 15
09.04.2016	02:30-06:00	1.0	137 (38)	241 ± 13	176	36 ± 7

6.2 Results of the statistical analysis of poleward TIDs during disturbed conditions

In the past, poleward TIDs of equatorial origin during geomagnetic storms were researched on a case-by-case basis (Ding *et al.*, 2013; Habarulema *et al.*, 2015, 2016; Ngwira *et al.*, 2019). This study presents results of a statistical analysis of TIDs originating near the geomagnetic equator during geomagnetic storms for the period between 2010 and 2018.

6.2.1 Storm-time poleward TIDs over the African-European sector

Analyses of poleward TIDs during disturbed conditions over the African-European sector were done for the period between 2010 and 2018. A Kp > 4 and Dst ≤ -50 nT were used as criteria to define for geomagnetically disturbed conditions. To demonstrate the typical cases identified where poleward TIDs were observed during disturbed conditions over African-European sector, two examples are shown for 03 September 2012 and 16 July 2012. The poleward TID was observed during the main phase of a geomagnetic storm on 03 September 2012. During the period 01-06 September 2012 there was a CME driven geomagnetic storm (Keesee and Scime, 2015; Olifer *et al.*, 2018; Matamba and Habarulema, 2018; Nitta *et al.*, 2021). Figure 6.6 shows variation of the polar cap (PCN and PCS [mV/m]), interplanetary magnetic field, Bz (nT), interplanetary electric field, IEF (mV/m), Dst, Kp and AE index for 01-06 September 2012. The red vertical dash line indicates the arrival of the shock (06:00 UT, 01 September 2012), and the black vertical dash line indicates the end of the main phase (10:00 UT, 03 September 2012) (Keesee and Scime, 2015; Olifer *et al.*, 2018; Nitta *et al.*, 2021). After the shock, the IMF Bz oscillated northward and southward until around 23:00 UT, when it turned southward until the end of the main phase (10:00 UT). The solar wind speed increased from approximately 301 km/s to 333 km/s. The IEF varied between ≈ -2 mV/m and ≈ 3 mV/m (Figure 6.6 (b)). Meanwhile, the AE index abruptly increased to a maximum value of 1191 nT (23:00 UT, 02 September 2012). The polar cap indices varied between ≈ -1 mV/m and ≈ 7 mV/m. The minimum and maximum that the Dst and Kp

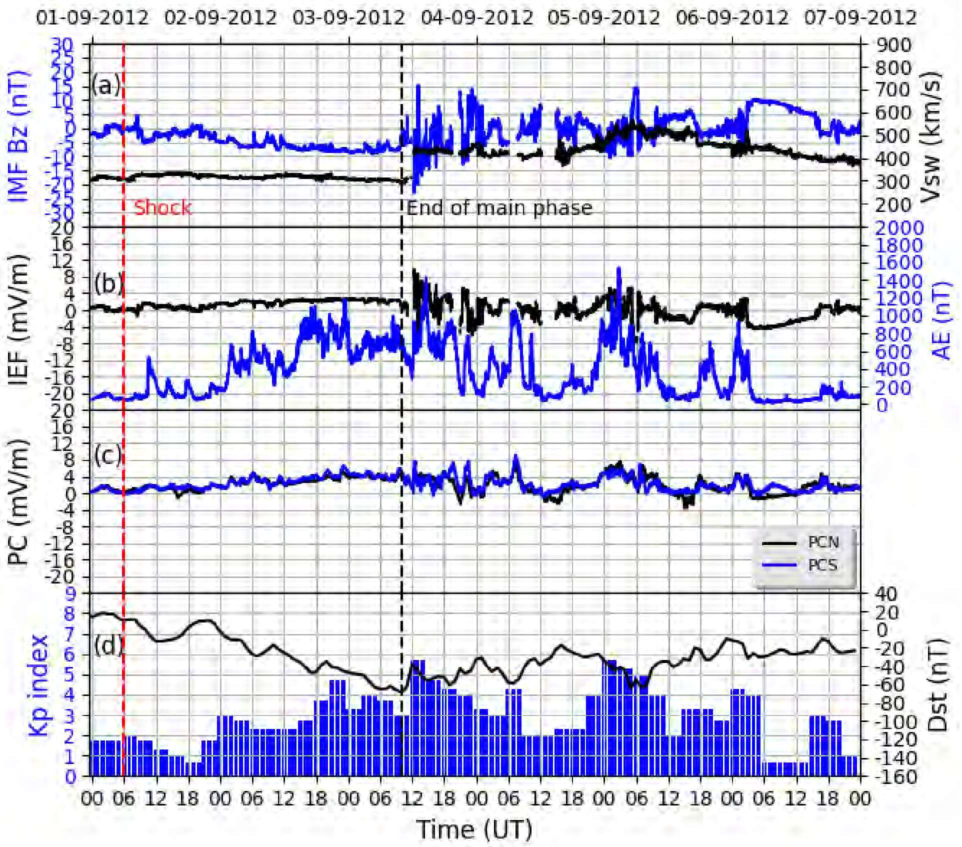

Figure 6.6: Variation of interplanetary magnetic field (Bz [nT]), interplanetary electric field (IEF [mV/m]), polar cap (PCN and PCS [mV/m]), Dst, Kp and AE index (nT) on 01-06 September 2012. The red vertical dash line represents the arrival of the shock, while the black vertical dash line represents the end of the main phase. The IMF Bz, AE index, and PCS index are shown by blue curves, while the V_{sw}, IEF, PCN index, and Dst index are represented by black curves. The Kp index is represented by the blue bar graph.

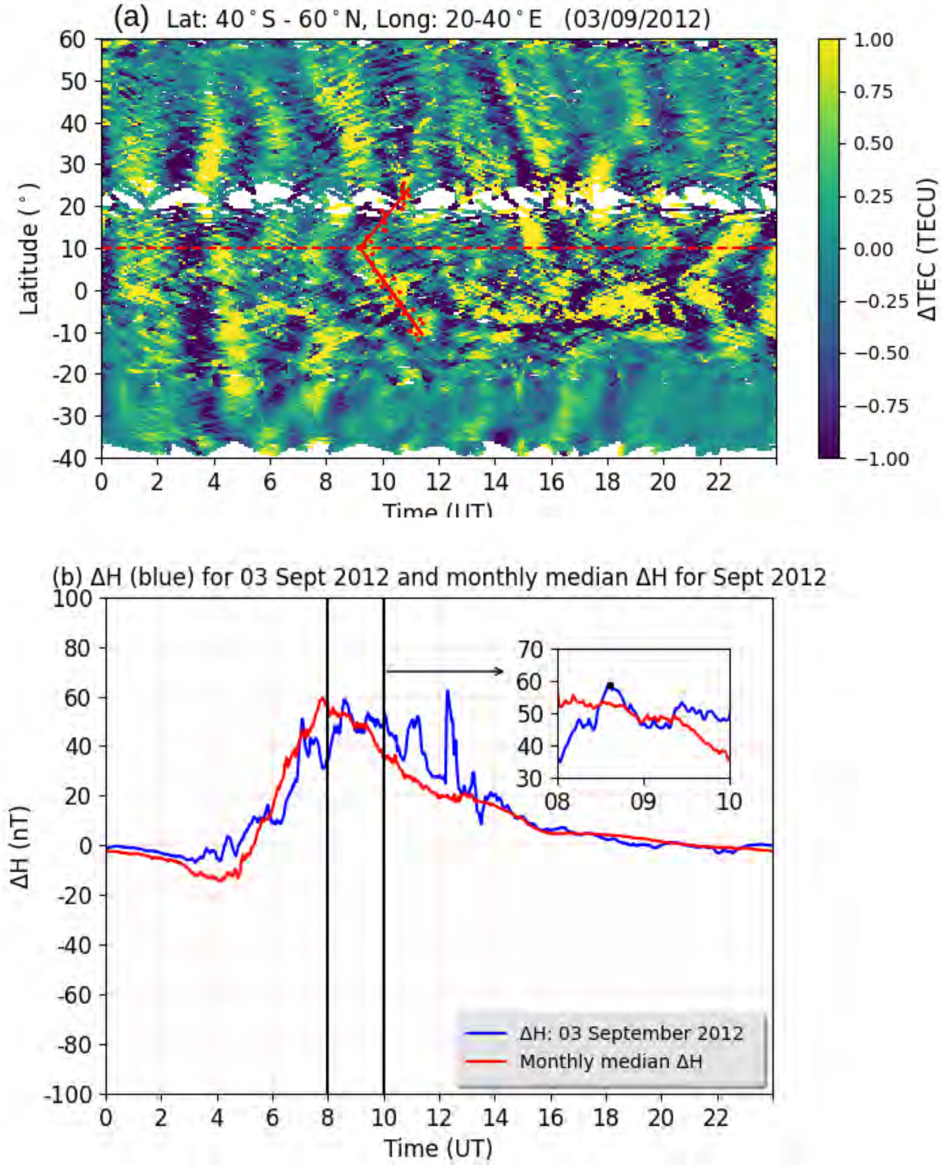

Figure 6.7: Variation of ΔTEC (TECU) over Africa-European sector, ΔH (nT) for 03 September 2012 and corresponding monthly median ΔH (nT) for September 2012. The blue curve represents the ΔH, whereas the red curve represents the monthly median ΔH.

indices reached during this storm period were -67 nT (10:00 UT, 03 September 2012) and 4.7 (12:00 UT), respectively (Figure 6.6 (d)). After the main phase of the storm, there was another interplanetary shock wave (12:00 UT) on 03 September 2012, and was indicated by a significant rise in solar wind speed, AE, IEF, and an abrupt change in the IMF direction (Baker *et al.*, 2013; Olifer *et al.*, 2018).

Figures 6.7 (a) shows ΔTEC as a function of latitude and time for 03 September 2012, within the latitudinal and longitudinal ranges of 40°S-60°N and 20°-40°E. As can be seen in Figure 6.7, a TID structure emerged during the period 08:00-10:00 UT at the geomagnetic equator on the day of the main phase of the storm. The values of the meridional velocity and period were 211.9 ± 40.1 m/s and 23 ± 6 min, respectively. Figures 6.7 (b) shows the variation of ΔH (nT) for 03 September 2012 with the monthly median ΔH (red curve) for September 2012. Both ΔH and the monthly median ΔH began to increase gradually around 05:00 UT, indicating an eastward electric field (EEJ). During the period 08:00-10:00 UT, there was a clear increase in ΔH over the corresponding monthly median ΔH values, as shown by the two vertical black lines. Another trace of poleward TIDs emerged between 06:30 and 07:30 UT on 19 November 2010, coinciding with an increase in the ΔH over the respective monthly median ΔH values. The enhanced EEJ in the magnetometer data for the period between 08:00 and 10:00 UT agrees well with the observed poleward TID, as is seen in Figure 6.7 (a). Thus, the dynamics of the storm led to a substantial increase in ΔH over the monthly median ΔH values. It is a well-known fact that the low-latitude electric field is influenced during disturbed conditions by the prompt penetration electric fields (PPEFs) (Fejer and Scherliess, 1998; Kikuchi *et al.*, 2008; Kikuchi and Hashimoto, 2016; Bagiya *et al.*, 2014, 2011) and disturbance dynamo electric fields (Nishida, 1968; Blanc and Richmond, 1980). The PPEFs are eastward during the local day to dusk sector and westward from the midnight to dawn sector (Fejer, 1991, 1997; Fejer and Scherliess, 1998; Kikuchi *et al.*, 2008). PPEFs over the equatorial latitude increase the ΔH (E×B) during daytime and lead to a decrease at nighttime (Fejer, 1997; Fejer and Scherliess, 1998; Bagiya *et al.*, 2014), whereas disturbance dynamo electric fields cause a decrease and an increase in ΔH (E×B) during the local day and nighttime (Fejer, 1991, 2011; Bagiya *et al.*, 2011, 2014), respectively. PPEFs are typically short-lived, lasting for about an hour (Kuai *et al.*, 2015; Huang, 2013) during the main phase of geomagnetic storms, but can last for 6-8 hours during strong storms (Huang *et al.*, 2005; Huang, 2013). The PPEFs are associated with a southward IMF Bz and caused by other solar wind and magnetospheric processes (Fejer and Scherliess, 1998; Kikuchi *et al.*, 2008; Kikuchi and Hashimoto, 2016; Bagiya *et al.*, 2014, 2011). During the period when the poleward TID appeared (Figures 6.7 (a)), the IMF Bz (Figure 6.6 (a)) was already moving in a southward direction. The increase in ΔH over the monthly median ΔH values between 08:00 UT and 10:00 ΔH, during the main phase, leads to the conclusion that PPEFs may be possible contributors to the eastward electric field, which could lead to the launch of poleward TIDs. The increasing eastward electric field causes an increase in the Lorentz force, which renders neutral-to-ionized component coupling effective for conditions responsible for launching poleward TIDs (Chimonas, 1969; Habarulema *et al.*, 2015, 2016).

Poleward TIDs were also detected on 16 July 2012, during the recovery phase of the geomagnetic storm. The storm lasted from 14 July until 19 July 2012. On 12 July 2012, at approximately 16:45 UT, an earthward coronal mass ejection erupted, along with an X1.4

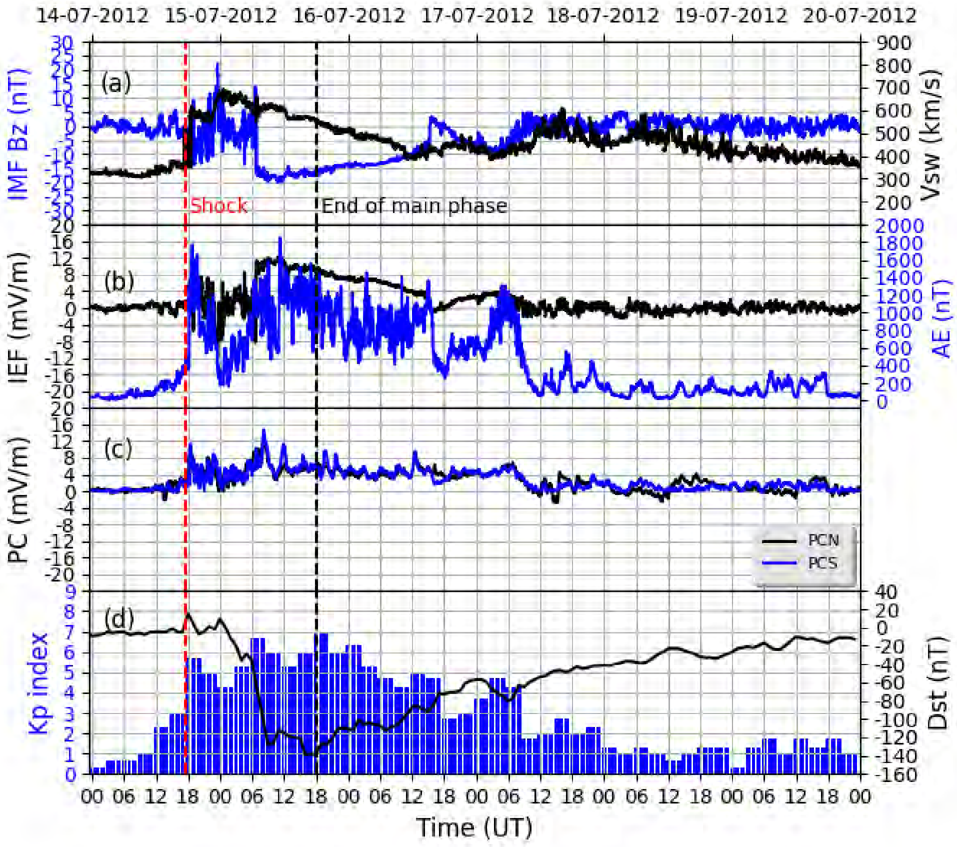

Figure 6.8: Variation of solar wind speed (V_{sw}, km/s), interplanetary magnetic field (Bz [nT]), interplanetary electric field (IEF [mV/m]), polar cap (PCN and PCS [mV/m]), Dst, Kp and AE indices on 14-19 July 2012. The arrival of the shock is indicated by the red vertical dash line, while the end of the main phase is indicated by the black vertical dash line. The IMF Bz, AE index, and PCS index are shown by blue curves, while the V_{sw}, IEF, PCN index, and Dst index are represented by black curves. The Kp index is represented by the blue bar graph.

class solar flare from sunspot AR1520 (Hess and Zhang, 2014; Liu *et al.*, 2014; Kuai *et al.*, 2017). Hess and Zhang (2014), Bagiya *et al.* (2014), Kuai *et al.* (2017), Liu *et al.* (2014) and Gil *et al.* (2020) describe the interplanetary and geomagnetic activity indices for this storm. The Advanced Composition Explorer (ACE) satellite detected a shock arrival at approximately 17:30 UT on 14 July 2012, and the solar wind speed increased from approximately 350 km/s to 630 km/s (Liu *et al.*, 2014; Kuai *et al.*, 2017). Meanwhile, the AE index abruptly increased to a maximum value of 1851 nT (11:17 UT on 15 July), and the Kp index increased to about 5.7 and reached a maximum value of 7.0 (18:00 UT on 15 July) during the storm's main phase. The IEF ranged from -2 mV/m to 2 mV/m prior to the shock, and reached minimum of -13.72 mV/m (23:30 UT on 14 July) and maximum of 12.14 mV/m (10:58 UT on 15 July) after the arrival of the shock. After the arrival of the shock, the IMF Bz oscillated between northward and southward. The major southward turning of IMF Bz occurred around 06:30 UT on 15 July 2012, and is regarded as the start of the storm's main phase. The IMF Bz remained southward for about 30 h below -10 nT (Bagiya *et al.*, 2014; Kuai *et al.*, 2017). The IMF Bz headed southward again on 16 July at 15:57 UT after reaching the recovery for the active period of around 33 hours (Bagiya *et al.*, 2014; Liu *et al.*, 2014; Kuai *et al.*, 2017). The Dst index reached a minimum of -139 nT at 16:00 UT 15 July and then recovered gradually. Figure 6.8 show variations of (a) IMF Bz (blue curve) and V_{sw} (black curve), (b) AE (blue curve) and IEF (black curve), (c) polar cap indices (PCN in black curve line and PCS in blue curve), and (d) Dst (black curve) and Kp (blue bar) indices on 16 July 2012. The red vertical dash line indicates the arrival of the shock, and the black vertical dash line indicates the end of the main phase. The results (as seen in Figure 6.8) clearly show that poleward TIDs emerged during the recovery period.

Figures 6.9 (a) depicts a latitude-time plot of ΔTEC, which shows traces of poleward TIDs beginning around 07:00 UT (09:00 LT) on 16 July 2012. The meridional velocity and period values were 380 ± 33.3 m/s and 32 ± 11 min, respectively, which are characteristic of medium-scale TID (Mayr *et al.*, 1984; Hunsucker, 1982; Hocke and Schlegel, 1996; Vadas and Becker, 2019; Katamzi-Joseph *et al.*, 2019). The ΔH displayed a counter electrojet (CEJ) from 05:30 UT until about 09:00 UT (Figure 6.9 (b)). Despite some missing data, ΔH was mostly negative from 0700 UT to 0800 UT, whereas the monthly median ΔH displayed the EEJ. Due to the data gap, it is impossible to conclude whether there was increased EEJ responsible for this TID. However, a trace of a poleward TID was identified for the period between 08:00 and 10:00 UT on 16 July 2012. During the existence of the poleward TID, the ΔH was above the monthly median ΔH values, as shown by the insert in Figure 6.9 (b). For period that the poleward TIDs were observed (07:00-08:00 UT, Figure 6.9 (a)), the IMF Bz (Figure 6.8 (a)) was already moving southward. A westward electric field (CEJ) can be caused by delayed ionospheric electric field perturbations, which on their part are caused by storm-time disturbance dynamo effects during daytime (Nishida, 1968; Blanc and Richmond, 1980; Bagiya *et al.*, 2014). The disturbance dynamo electric fields generated by the increased energy deposited at high-latitudes may disrupt the equatorial region for one to two days after the main phase of the geomagnetic storm has passed (Bagiya *et al.*, 2011). In general, disturbance dynamo electric fields over the dip equator are westward on the dayside and eastward on the nightside (Nishida, 1968; Liu *et al.*, 2014; Bagiya *et al.*, 2014). The westward electric field between 06:00 UT and 08:00 UT in Figure 6.9 (b) on 16 July indicates the effects of disturbance dynamo electric fields at equatorial latitudes. The increased in ΔH above the monthly median ΔH values, as shown by the insert in Figure 6.9 (b), may been due to eastward PPEFs. Since the IMF Bz was already moving in a southward direction, it is possible that eastward PPEFs from high-latitudes were contributors to the enhanced eastward electric field (EEJ) during local daytime, which could have resulted in the launch of poleward TID between 08:00 and 10:00 UT on 16 July 2012.

The relationship between maximum ΔH and estimated time of occurrence of poleward TIDs (derived fitted red line, e.g. Figure 6.7 (a) and Figure 6.9 (a)) was established. Unfortunately, data from the ETH magnetometer station was only available from 2008 to 2013. The correlation was computed only for the period 2010-2013, when data from AAE-ETH was available. Thus, out of 15 and 25 cases where traces of poleward TIDs were identified during the main and recovery phases, respectively, only 11 cases were found to have data to determine ΔH. Out of 11 cases, 6 and 5 cases of TIDs were evident during the main and recovery phases, respectively. Figure 6.10 depicts the relationship between the time of maximum ΔH and the approximate start time of the TIDs. There is a clear one-to-one relationship between the estimated start of poleward TIDs from the geomagnetic equator and an increase in the ΔH above the monthly median ΔH values (Habarulema, Thaganyana *et al.*, 2022).

Tables 6.3 and 6.4 shows all characteristics of poleward TIDs that launched from the geomagnetic equator over the African-European sector during the main and recovery phases of geomagnetic storms. Storm-time periods, storm drivers, and minimum Dst values were obtained from following websites: `https://www.sidc.be/cactus/catalog/LASCO/250/cmelz.txt`, `https://cdaw.gsfc.nasa.gov/CME_list/`, `https://omniweb.gsfc.nasa.gov/` and `https://izw1.caltech.edu/ACE/ASC/DATA/level3/icmetable2.htm`. The meridional and horizontal velocities, periods, and propagation direction of the TIDs were determined by using the methods described in Section 5.2 and in the papers published by Liu *et al.* (2019) and Thaganyana *et al.* (2022). The fifth column in Tables 6.3 and 6.4 indicates the southward (S) and northward (N) propagation angles of the wavefronts of the TIDs (clockwise from north). The horizontal velocities c_H were computed (Equation 5.5) using the southward propagation angles of the wavefronts of the TIDs (clockwise from the north). The storm-induced poleward TIDs emerging from the equatorial regions are largely constrained within the boundaries 10°N and 25°S around the geomagnetic equator over the African-European sector. It should be noted that the northward propagation range (0° to 10°N) of the TIDs from the geomagnetic equator was determined only from the limited available data, due to data gaps between 10°N and 25°N. Figure 6.11 shows the results of the statistical analysis of the poleward TIDs. Figure 6.11 (a) shows for different years the approximate time which poleward TIDs occurred as a function of the calculated horizontal velocity (c_H). The results are shown for the main (blue dots) and recovery (black crosses) phases, and the red curve represents the monthly sunspot number S_n. The monthly sunspot number S_n data was obtained from the Sunspot Index and Long-term Solar Observations website (`https://www.sidc.be/silso/monthlyssnplot`). These poleward TIDs were mostly observed in data for 2012 and 2015 during period of high solar activity (represented by monthly sunspot number), as shown Figure 6.11 (a). High solar activity is associated with increasing sunspot numbers (Crooker *et al.*, 1997; Campbell, 1997). The majority of poleward TIDs were launched during storms caused by coronal mass ejections (CMEs). Table 6.3 shows that during the main phase of storms, CMEs account for 66.7 % and CIRs for 33.3 % of poleward TIDs. In Table 6.4 CMEs account for 92 % and CIRs for 8 % of poleward TIDs during the

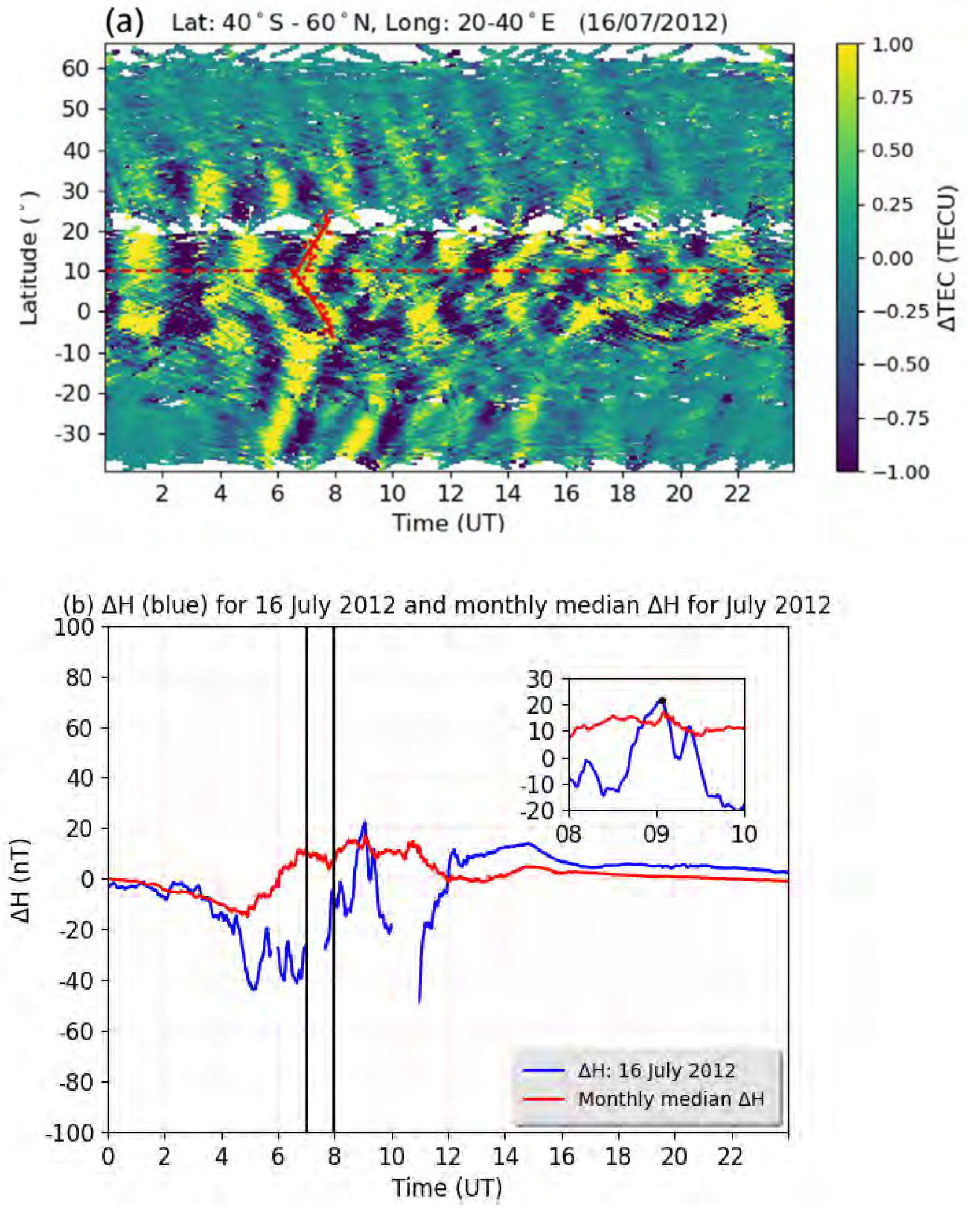

Figure 6.9: Variation of ΔTEC (TECU) over the Africa-European sector, ΔH (nT) for July 16, 2012 and corresponding monthly median ΔH (nT) for July 2012. The blue curve represents the ΔH, whereas the red curve represents the monthly median ΔH.

recovery phases. This suggests that poleward TIDs are more likely to emerge during CME-driven storms and mostly occur during the recovery phase. CMEs are commonly observed during periods of high solar activity (Crooker *et al.*, 1997; Hargreaves, 1992; Gopalswamy, 2006). Figures 6.11 (b)-(c) show the diurnal horizontal velocities and periods for the main and recovery phases, respectively. The velocities and periods of the TIDs are plotted as blue dots and open black circles, respectively (Figures 6.11 (b)-(c)), while the dashed vertical black lines represent the local sunrise (07:00 LT) and sunset (18:00 LT). Poleward TIDs are observed in both phases between 04:00-15:30 UT (approximately 06:00-17:30 LT), particularly during the local daytime. Almost all poleward TIDs (with the exception of two cases) during the main phase of the geomagnetic storms were large-scale with horizontal velocities within the range of 250-503 m/s and periods within the range of 37 min- 2 h. Figure 6.11 (b) shows that, with the exception of two cases, the period values range from 30 min to 2 h. The period and horizontal velocity values in Figure 6.11 (c) range from 23 min to 2 h and 150 m/s to 390 m/s, respectively.

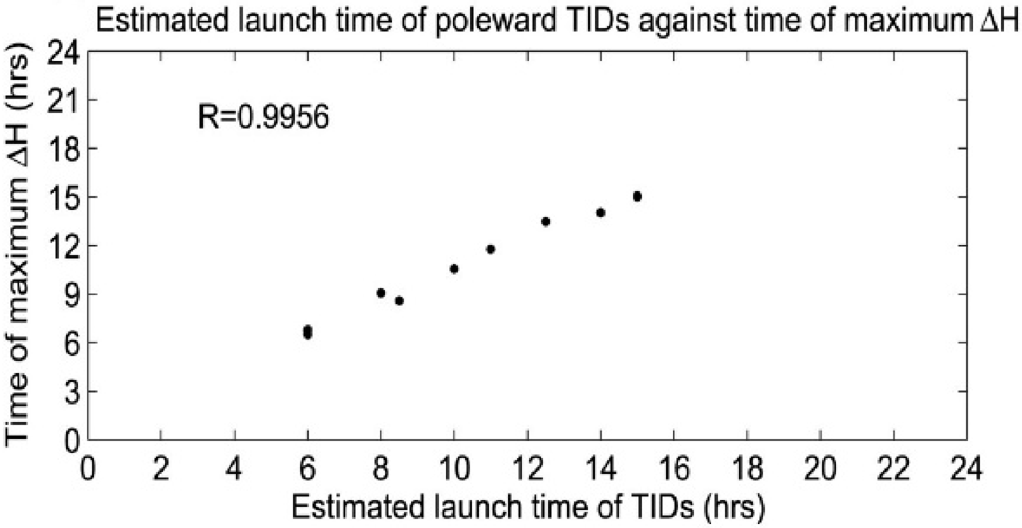

Figure 6.10: The relationship between maximum ΔH and estimated launch time of poleward TIDs (Habarulema, Thaganyana *et al.*, 2022).

Table 6.3: Properties of poleward TIDs launched from the geomagnetic equator over the African-European sector during the main phase of geomagnetic storms. 1^{st} column: storm periods; 2^{nd} column: dates of occurrence of poleward TIDs; 3^{rd} column: estimated times of occurrence of TIDs; 4^{th} column: southward and northward propagation of TIDs from geomagnetic equator, respectively; 5^{th} column: southward (S) and northward (N) progagation angles of the wavefront TIDs (clockwise from north); 6^{th} column: averaged meridional phase velocities (southward and northward) calculated by means of wave least-square fitting method; 7^{th} column: horizontal phase velocities c_H; 8^{th} column: the periods of TIDs; 9^{th} column: storm driver; 10^{th} column: minimum Dst value.

Storm period	Date and characteristics of poleward TIDs launched during the main phase of geomagnetic storms								
Date	Date	Time (UT)	TIDs Prop. Lat(°)$S \leftarrow Eq \rightarrow N$	Prop. Angle S(N)	Velocity (m/s)	c_H (m/s)	Period (min)	Cause of storm	Minimum Dst(nT)
14-16.02.2012	15.02.2012	10:30-11:30	$-18 \leftarrow 0 \rightarrow 5$	135 (45)	321.4 ± 44.9	227	52 ± 14	CME	-67 (15.02.2012)
07-12.03.2012	09.03.2012	06:00-07:00	$-10 \leftarrow 0 \rightarrow 9$	138 (37.1)	510.6 ± 14.3	379	74 ± 23	CME	-145 (09.03.2012)
		10:00-11:00	$-20 \leftarrow 0 \rightarrow 9$	155 (40.6)	499.2 ± 54.1	452	66 ± 10		
		14:00-15:00	$-40 \leftarrow 0 \rightarrow 8$	140 (33.1)	274.1 ± 11.3	210	41 ± 12		
15-19.07.2012	15.07.2012	06:00-07:00	$-25 \leftarrow 0 \rightarrow 9$	158.2 (50)	541.6 ± 44.7	503	63 ± 23	CME	-139 (15.07.2012)
09-11.07.2012	09.07.2012	06:00-07:00	$-25 \leftarrow 0 \rightarrow 9$	139 (51.2)	462.4 ± 55.3	349	28 ± 9	CME	-78 (09.07.2012)
02-05.09.2012	03.09.2012	08:30-10:00	$-20 \leftarrow 0 \rightarrow 12$	139 (41)	211.9 ± 40.1	150	23 ± 6	CME	-67 (03.09.2012)
01-04.03.2013	01.03.2013	13:15-14:00	$-20 \leftarrow 0 \rightarrow 9$	146.6 (46)	451.3 ± 18.7	377	71 ± 18	CIR	-55 (01.03.2013)
16-20.11.2014	16.11.2014	14:30-15:30	$-20 \leftarrow 0 \rightarrow 7$	150 (30.5)	348 ± 5	301	120 ± 7	CIR	-59 (16.11.2014)
26-27.12.2014	26.12.2014	10:00-11:00	$-28 \leftarrow 0 \rightarrow 10$	142 (40.3)	337.2 ± 19.4	266	58 ± 16	CIR	-57 (26.12.2014)
01-04.03.2015	01.03.2015	11:00-12:00	$-15 \leftarrow 0 \rightarrow 7$	140.5 (35)	405.9 ± 24.5	313	37 ± 8	CME	-55 (02.03.2015)
16-23.03.2015	17.03.2015	11:30-13:00	$-22 \leftarrow 0 \rightarrow 9$	155.5 (31.5)	498.5 ± 48.9	454	68 ± 15	CME	-222 (17.03.2015)
08-12.06.2015	08.06.2015	04:00-05:00	$-25 \leftarrow 0 \rightarrow 9$	145.3 (52.2)	304.7 ± 27.4	251	59 ± 11	CIR	-73 (08.06.2015)
23-30.06.2015	22.06.2015	04:00-05:00	$-25 \leftarrow 0 \rightarrow 8$	147.5 (47.1)	318.2 ± 66.1	268	112 ± 33	CME	-185 (23.06.2015)
02-03.02.2016	03.02.2016	08:00-09:00	$-10 \leftarrow 0 \rightarrow 7$	147 (37)	276.8 ± 45.5	232	23 ± 9	CIR	-52 (03.02.2016)

Table 6.4: Properties of poleward TIDs launched from the geomagnetic equator over the African-European sector during the recovery phase of geomagnetic storms. 1st column: storm periods; 2nd column: dates of occurrence of poleward TIDs; 3rd column: estimated time of occurrence of TIDs; 4th column: southward and northward propagation of TIDs from geomagnetic equator; 5th column: southward (S) and northward (N) progagation angle of wavefronts of the TIDs (clockwise from north); 6th column: averaged meridional phase velocities (northward and southward) calculated by means of the wave least-square fitting method; 7th column: horizontal phase velocities c_H; 8th column: the periods of TIDs; 9th column: storm driver; 10th column: minimum Dst value.

Storm period	Dates and characteristics of poleward TIDs launched during the recovery phase of geomagnetic storms								
Date	Date	Time (UT)	TIDs Prop. Lat(°)$S \leftarrow Eq \rightarrow N$	Prop. Angle S(N)	Velocity (m/s)	c_H (m/s)	Period (min)	Cause of storm	Minimum Dst(nT)
14-16.02.2012	16.02.2012	15.00-16:00	$-10 \leftarrow 0 \rightarrow 9$	125 (32)	267.4 ± 45.1	153	32 ± 12	CME	-67 (15.02.2012)
07-12.03.2012	11.03.2012	10:00-11:00	$-20 \leftarrow 0 \rightarrow 9$	140 (50)	310.5 ± 22.3	237	52 ± 17	CME	-145 (09.03.2012)
	15.03.2012	15:00-16:00	$-18 \leftarrow 0 \rightarrow 9$	125 (37)	290.5 ± 56.4	167	44 ± 17		
16-20.06.2012	18.06.2012	15:00-16:00	$-15 \leftarrow 0 \rightarrow 9$	145.5 (39)	190.3 ± 51.3	157	26 ± 8	CME	-86 (17.06.2012)
	19.06.2012	04:30-05:30	$-16 \leftarrow 0 \rightarrow 10$	141.5 (45)	325.6 ± 67.7	255	65 ± 15		
15-19.07.2012	16.07.2012	06:00-8:00	$-20 \leftarrow 0 \rightarrow 10$	145 (35)	380 ± 33.3	311	32 ± 11	CME	-139 (15.07.2012)
01-05.09.2012	05.09.2012	05:00-06:00	$-20 \leftarrow 0 \rightarrow 5$	145 (49.7)	199.5 ± 12.8	163	34 ± 18	CME	-67 (03.09.2012)
		07:00-08:00	$-20 \leftarrow 0 \rightarrow 10$	130 (48.5)	230.4 ± 81.2	148	25 ± 7		
08-15.10.2012	12.10.2012	12:00-13:00	$-20 \leftarrow 0 \rightarrow 20$	135 (36.3)	337.6 ± 35.5	239	62 ± 20	CME	-109 (09.10.2012)
	14.10.2012	12:30-13:30	$-22 \leftarrow 0 \rightarrow 22$	146.4 (36.4)	395.6 ± 82.4	330	55 ± 17		
		15:00-16:00	$-10 \leftarrow 0 \rightarrow 10$	158.8 (43.8)	288.6 ± 52.3	269	36 ± 15		
	15.10.2012	15:00-16:00	$-15 \leftarrow 0 \rightarrow 10$	156.8 (51.2)	410.6 ± 10.4	376	61 ± 22		
17-19.03.2013	19.03.2013	12:30-13:30	$-19 \leftarrow 0 \rightarrow 8$	140.3 (39)	265.7 ± 33.5	204	40 ± 15	CME	-132 (17.03.2013)
18-24.02.2014	20.02.2014	06:00-08:00	$-30 \leftarrow 0 \rightarrow 8$	148 (35.5)	360.1 ± 29.4	305	59 ± 6	CME	-119 (19.02.2014)
12-16.04.2014	14.04.2014	04:30-05:30	$-30 \leftarrow 0 \rightarrow 20$	144.5 (38)	221.5 ± 17.5	180	45 ± 12	CME	-88 (12.04.2014)
	16.04.2014	04:00-05:00	$-10 \leftarrow 0 \rightarrow 5$	135.5 (35.5)	328.4 ± 9.6	234	63 ± 9		
30.04.2014-01.05.2014	01.05.2014	04:30-05:30	$-32 \leftarrow 0 \rightarrow 9$	126.4 (36.4)	216.8 ± 24.9	129	47 ± 16	CME	-67 (30.04.2014)
27-29.10.2014	29.10.2014	14:30-15:30	$-20 \leftarrow 0 \rightarrow 10$	143.5 (39.2)	291.8 ± 64.4	235	38 ± 21	CIR	-57 (28.10.2015)
10-11.11.2014	11.10.2014	06:00-07:00	$-15 \leftarrow 0 \rightarrow 5$	140.3 (46.1)	215.1 ± 14.3	165	34 ± 10	CME	-67 (11.11.2014)
07-10.01.2015	08.01.2015	14:30-15:30	$-20 \leftarrow 0 \rightarrow 8$	133 (34.7)	241.6 ± 17.3	165	81 ± 24	CME	-99 (17.01.2015)
01-04.03.2015	02.03.2015	07:00-07:00	$-18 \leftarrow 0 \rightarrow 8$	125 (37.3)	302.5 ± 11.3	174	31 ± 5	CME	-55 (02.03.2015)
16-23.03.2015	18.03.2015	08:00-10:00	$-10 \leftarrow 0 \rightarrow 10$	150 (40.3)	246.1 ± 74.3	213	53 ± 10	CME	-222 (17.03.2015)
		12:00-13:00	$-25 \leftarrow 0 \rightarrow 9$	134.6 (34.6)	281.4 ± 26.3	198	43 ± 18		
08-12.06.2015	12.06.2015	04:00-05:00	$-20 \leftarrow 0 \rightarrow 8$	138.6 (40)	268.7 ± 37.3	202	33 ± 8	CIR	-73 (08.06.2015)
20-24.01.2015	24.01.2015	07:00-08:00	$-25 \leftarrow 0 \rightarrow 7$	130 (41.1)	349.6 ± 21.3	225	88 ± 20	CME	-104 (20.06.2015)

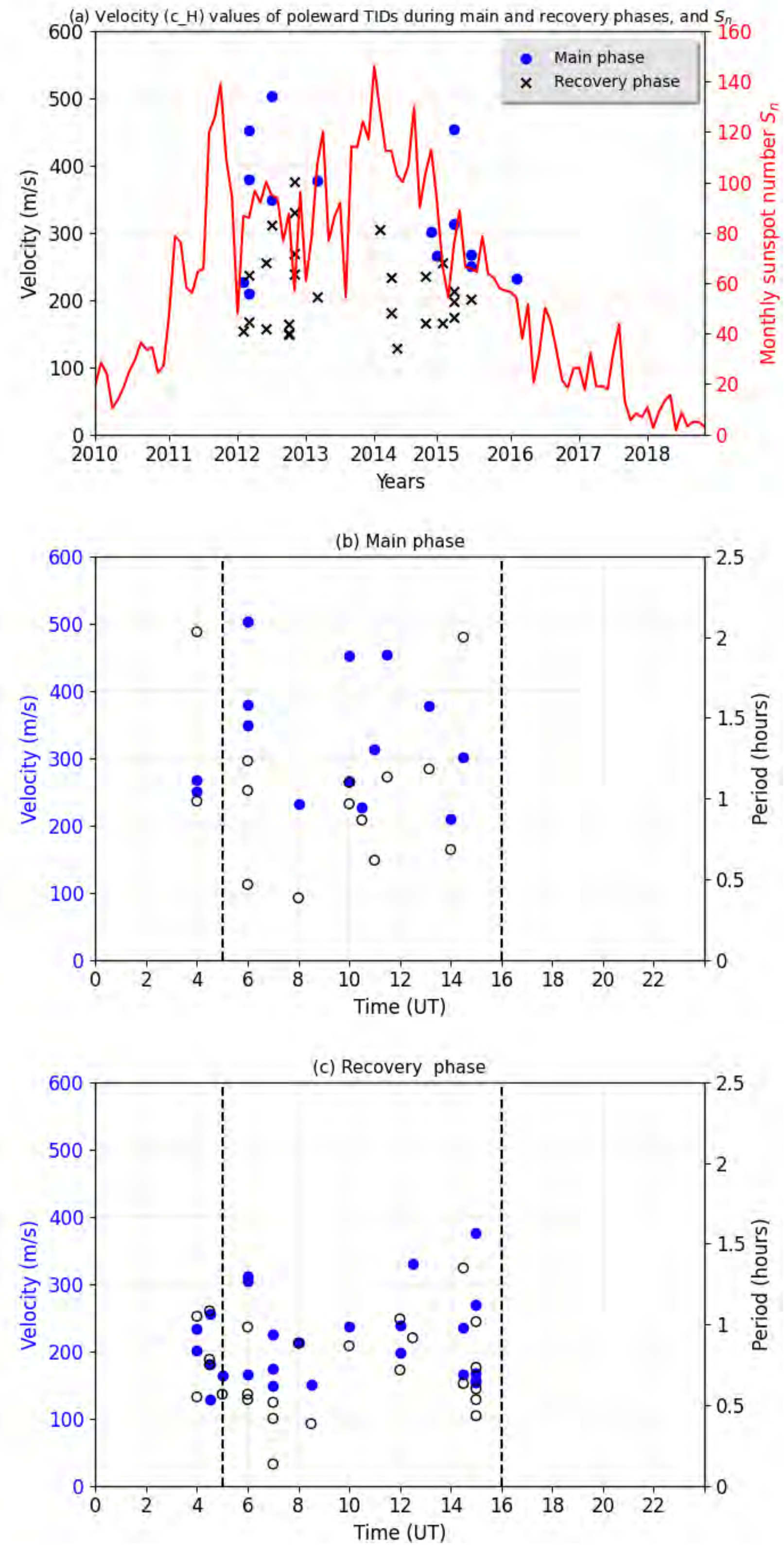

Figure 6.11: Results of the analysis of poleward TIDs during the main and recovery phases of geomagnetic storms that occurred over the African sector from 2010 to 2018. (a) A red curve line represents the monthly sunspot number S_n (`https://www.sidc.be/silso/monthlyssnplot`), whereas a blue dots and black crosses represents the horizontal velocity c_H during the main and recovery phases, respectively. (b)-(c) Blue dots represent the horizontal velocity c_H, and black open circles represents the periods of TIDs.

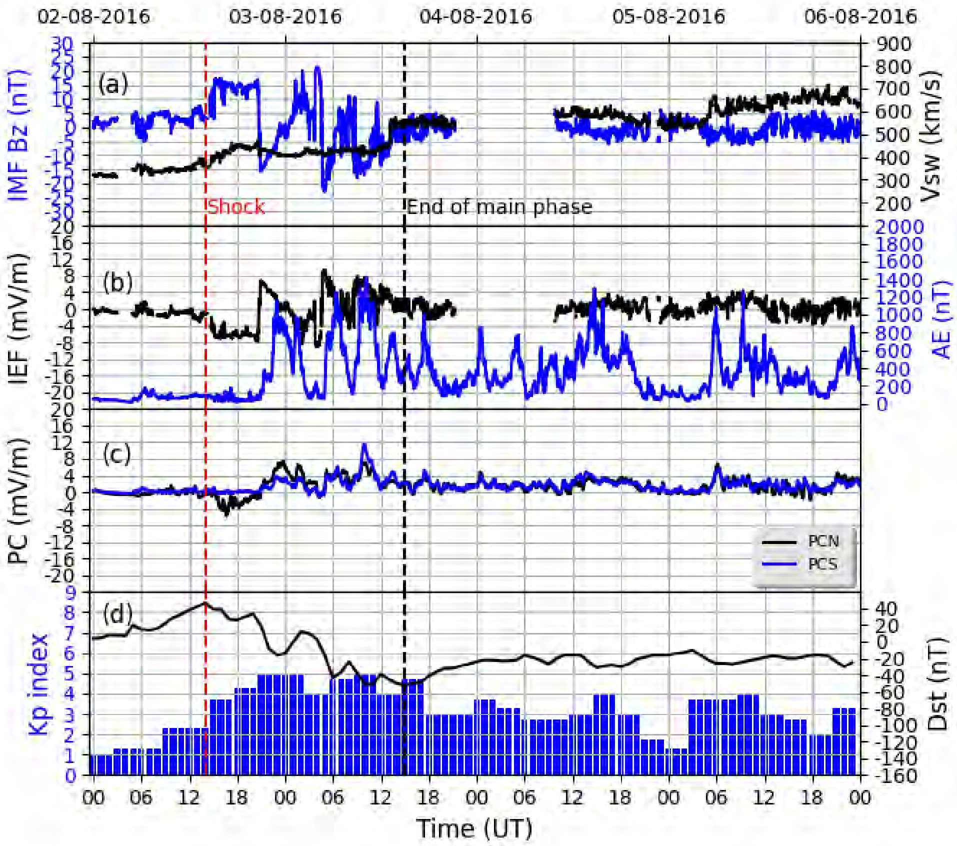

Figure 6.12: Variation of solar wind speed (V_{sw}, km/s), interplanetary magnetic field (Bz [nT]), interplanetary electric field (IEF [mV/m]), polar cap (PCN and PCS [mV/m]), Dst, Kp and AE index (nT) on 02-05 August 2016. Blue curve represents the IMF Bz, AE index, and PCS, while black curve represents the V_{sw}, IEF, PCN and Dst index. The blue bar graph represents the Kp index. The red vertical dash line indicates the arrival of the shock, and the black vertical dash line represents end of the main phase.

6.2.2 Storm-time poleward TIDs over the American sector

Analyses of poleward TIDs were also done for disturbed conditions during the period 2010-2018 over the American sector. An event during which poleward TIDs during disturbed conditions were identified over the American sector, occurred on 04 August 2016. The storm lasted from 02 August until 05 August 2016 (He *et al.*, 2021). Figure 6.12 shows variations of (a) IMF Bz (blue curve) and V_{sw} (black curve), (b) AE (blue curve) and IEF (black curve), (c) polar cap indices (PCN in black curve and PCS in blue), and (d) Dst (black curve) and Kp (blue bar) indices for 04 August 2016. The ACE satellite detected a shock at approximately 14:00 UT on 02 August 2016 (He *et al.*, 2021). V_{sw} increased from about 400 km/s to 565.1 km/s after the shock. The Kp index reached the value of 5 at 21:00 UT, and the Dst index reached a minimum of -52 nT at 15:00 UT on 03 August 2016. After the arrival of the shock, the IMF Bz changed from southward to northward, and remained northward for a period of 6 h, and abruptly moved in a southerly direction at about 20:00 UT. The

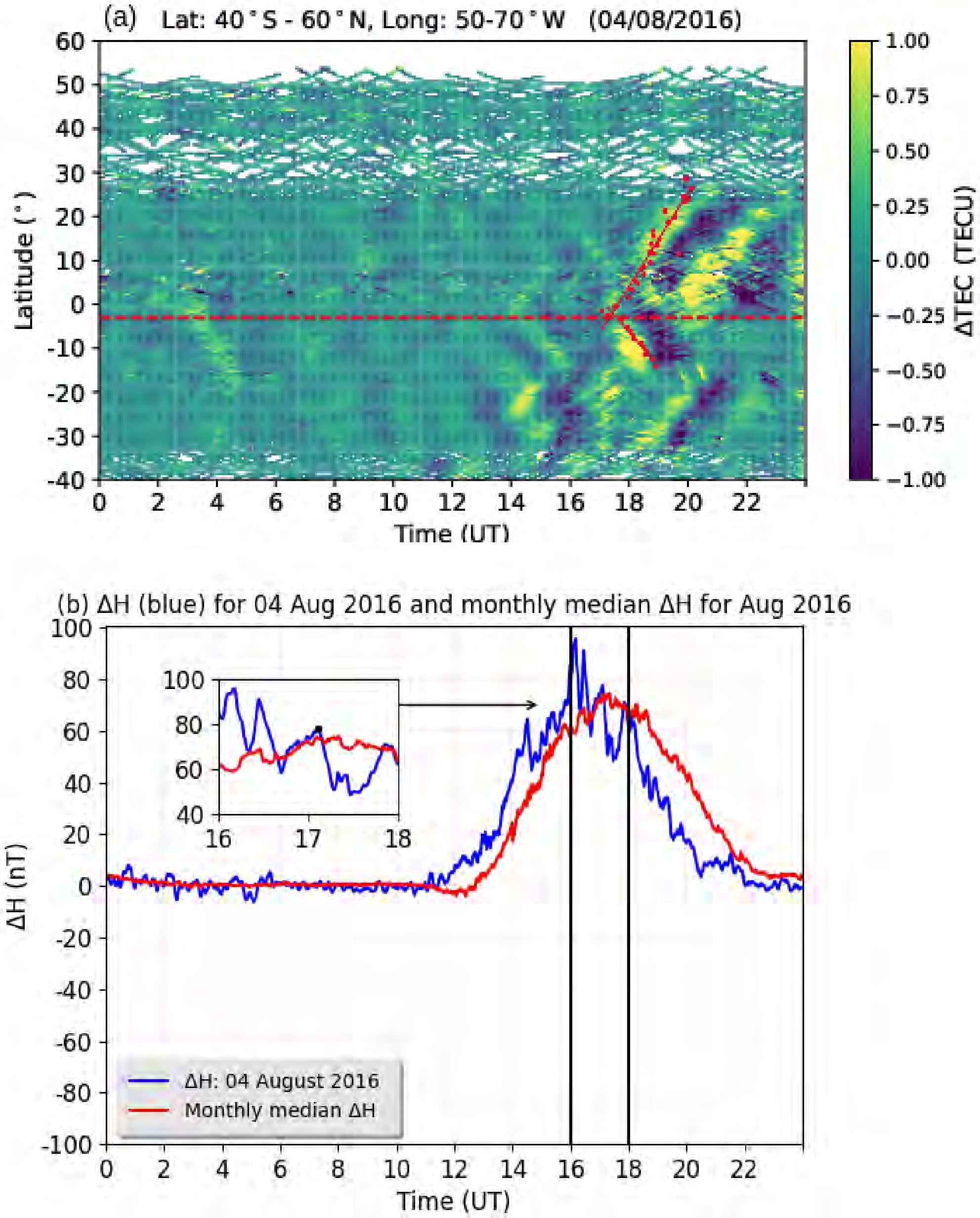

Figure 6.13: Variation of ΔTEC (TECU)over the American sector, ΔH (nT) for 04 August 2016 and corresponding monthly median ΔH (nT) for August 2016. The blue curve represents the ΔH, and the red curve represents the monthly median ΔH.

AE index increased abruptly to a maximum value of 1247 nT at 06:24 UT. The poleward TIDs were identified during the recovery phase of the geomagnetic storm on 04 August 2016. Figure 6.13 (a) shows the latitude-time plot of ΔTEC over the American sector within the latitudinal and longitudinal ranges of 40°S-60°N and 50°-70°W. As shown in Figure 6.13 (a), the poleward TIDs were observed at about 17:00 UT (13:00 LT). The pair of magnetometer locations within 50°-70°W are Alta Floresta, ALTA (9.9°S, 56.1°W, 0.8°N geomagnetic) and Cuiaba, CUIB (15.6°S, 56.1°W, 5.9°S geomagnetic). For 04 August 2016, ALTA-CUIB had missing EEJ data. The magnetometer data on which Figure 6.13 (b) is based, was provided by Jicamarca, JICA (11.8°S, 77.2°W; 0.8°N geomagnetic) and Piura, PIUR (5.2°S, 80.6°W; 6.8°N geomagnetic). The two vertical black lines in Figure 6.13 (b), indicates that the ΔH values were above the monthly median ΔH values. The IMF Bz was already moving in a southward direction within the range of -0.5 nT to -6 nT throughout the existence of poleward TIDs. It is thus possible that eastward PPEFs from high-latitudes could have contributed to the enhanced eastward electric field (EEJ) during local daytime, and which could have resulted in the launching of the poleward TIDs observed between 17:00 UT and 18:00 UT on 04 August 2016.

The correlation between maximum ΔH and estimated time occurrence of poleward TIDs (derived the fitted red line) was computed using different pairs of magnetometers within the American sector. The pairs of magnetometers that were used are ALTA-CUIB, Belem station (BELM 1.45°S, 48.5°W, 1.05°S geomagnetic) and Petrolina station (PETR (9.5°S, 40.5°W, 6.95°S geomagnetic), and JICA-PIUR, depending on availability of EEJ data. Figure 6.14 shows the scatter plot of approximate times that poleward TIDs occurred and the corresponding time of maximum ΔH within that time period. The black dots in Figure 6.14 represent ΔH data over ALTA-CUIB and BELM-PETR for 2017 cases. The red crosses represent ΔH data over JICA-PIUR. Where EEJ data was available for the American sector, ΔH was above the monthly median ΔH values, with a correlation close to one.

Table 6.5 shows all characteristics of poleward TIDs launched from the geomagnetic equator over the American sector during the main and recovery phases of geomagnetic storms. Figure 6.15 summarises the results of Table 6.5. The storm-induced poleward TIDs emerging from the equatorial regions are largely constrained within 30°N and 30°S around the geomagnetic equator over the American sector. The majority of poleward TIDs were launched during the CMEs driven storms. Figure 6.15 (a) shows the approximate times of the occurrence of poleward TIDs during different years as a function of the calculated horizontal velocity (c_H). The red curve represents the monthly sunspot number S_n. The poleward TIDs are mostly present during the descending phase of solar activity. The periods and horizontal velocities of TIDs ranged between 45 min-1.5 h and 180-296 m/s during the main phase (see Figure 6.15 (b)). During the recovery phase (Figure 6.15 (c)), the horizontal velocity and period ranged between 177-271 m/s and 40-1.5 h, respectively. With the exception of the case near the 07:00 LT line (Figure 6.15 (b)), three cases of poleward TIDs were observed over the American sector at night. There were fewer poleward TIDs over the American sector than over the African sector. There were approximately 12 and 40 cases of poleward TIDs were identified over the American and African sectors, respectively. It can thus be postulated that the eastward PPEF associated with a geomagnetic storm could increase the EEJ and contribute to the launch of poleward TIDs (Habarulema *et al.*, 2015, 2016; Ngwira *et al.*, 2019). Yizengaw *et al.* (2011) states that the E×B drift (EEJ) in the American sector is stronger

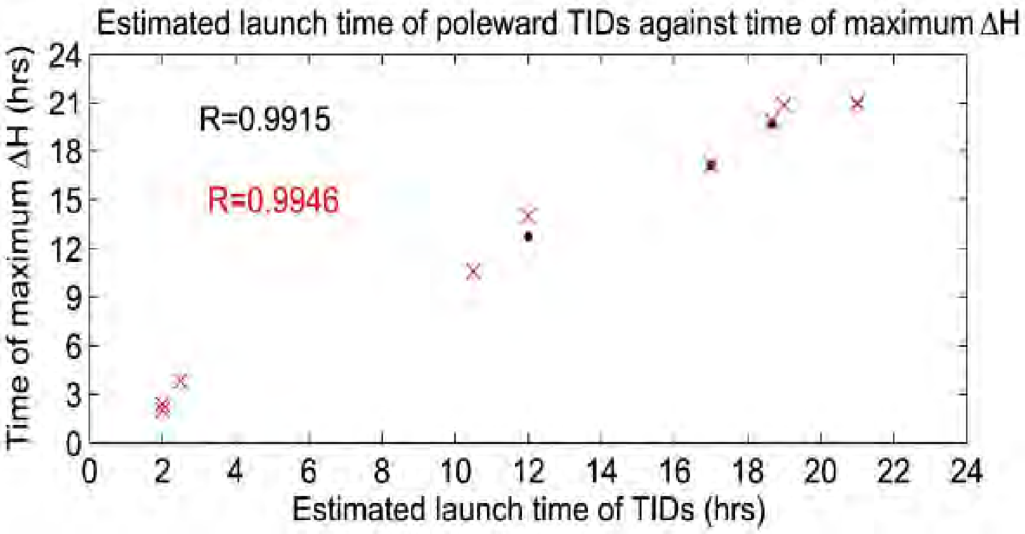

Figure 6.14: The relationship between maximum ΔH and estimated launch time of poleward TIDs. Data from two pairs of magnetometers was used, namely from ALTA-CUIB (black dots), BELM-PETR (black dots) and JICA-PIUR (red crosses)(Habarulema, Thaganyana *et al.*, 2022).

than that in the African sector at the same local time. This being so, one could have expected to see more poleward TIDs in the American sector than in the African-European sector. The reasons for this discrepancy were not established in this study and should be investigated more in the future.

Poleward TIDs experience energy dissipation as they propagate from their source. Ding *et al.* (2013) reported two cases of poleward TIDs during the recovery phase of a geomagnetic storm in southern China's low-latitude region. They discovered that poleward propagating large-scale TIDs have a narrower latitudinal range and a smaller amplitude. It was suggested that the large-scale TIDs, during the dissipation of some primary medium-scale TIDs from the lower atmosphere, could be a possible mechanism for poleward TIDs. The EEJ is one possible source of poleward travelling disturbances within the EIA region. It has been proposed and numerically demonstrated that changes in the EEJ can contribute to AGWs during disturbed conditions (e.g., Chimonas, 1969; Knudsen, 1969). Chimonas (1969) and Knudsen (1969) suggested that if the auroral electrojet (AE) generates TIDs, there is a possibility that the equatorial electrojet will act similarly. Knudsen (1969) pointed out that the amplitude of AGWs generated by EEJ dynamics is smaller than that of AGWs which emerge as a result of changes in the AE. As a result, it is difficult to observe and track the AGWs which originate from the low or equatorial latitudes. According to Habarulema *et al.* (2015, 2016), the enhanced eastward electric field may result in an increase in the Lorentz force, which renders coupling of neutrals to ionised components efficient for conditions responsible for launching poleward TIDs. This was reported in a study based on TEC observations of two geomagnetic storms on 09 March 2012, and 17 March 2015. Jonah *et al.* (2018) suggested that the source of poleward TID could be the result of deep convection induced by AGWs from tropospheric weather. Ngwira *et al.* (2019) demonstrated that the Thermosphere Ionosphere Electrodynamics General Circulation Model was unable to capture the existence of medium-scale TIDs of equatorial origin over Brazilian longitudes during the storm of 22-23 June 2015. The model captured only the equatorward large-scale TIDs. When compared to auroral regions, Lorentz coupling involving EEJ changes is less effective in launching AGWs resulting in TIDs in equatorial regions (e.g. Chimonas, 1969; Knudsen, 1969). During geomagnetic storms, other processes such as Lorentz forcing, particle precipitation, and Joule heating are more effective in high latitudes than in equatorial latitudes (Hunsucker, 1982; Hocke and Schlegel, 1996; Balthazor and Moffett, 1997; Borries *et al.*, 2016). The results of analyses of both the American and African-European sectors, show a clear one-to-one relationship between the launch of poleward TIDs from the geomagnetic equator and the enhancement of the EEJ. These findings imply that electrodynamics related to an increase in the eastward electric field and thus an increase in the vertical ExB drift play an important role in launching atmospheric gravity waves in equatorial latitudes, which are a likely source of the reported poleward TIDs. Because the ionosphere and thermosphere are influenced by both internal and external dynamical and electrodynamical sources, such as magnetospheric and disturbance dynamo electric field contributions, as well as global changes in the thermospheric neutral wind, it is difficult to isolate the dominant physical mechanism for each observation.

Table 6.5: Properties of poleward TIDs launched from the geomagnetic equator over the American sector during the main phase of geomagnetic storms. 1^{st} column: storm periods; 2^{nd} column: dates of occurrence of poleward TIDs; 3^{rd} column: estimated times of occurrence of TIDs; 4^{th} column: northward and southward propagation of TIDs from geomagnetic equator; 5^{th} column: southward (N) and northward (S) progagation angles of wavefronts of the TIDs (clockwise from north); 6^{th} column: average meridional phase velocities (southward and northward) caculated by means of the wave least-square fitting method; 7^{th} column: horizontal phase velocities c_H; 8^{th} column: the periods of TIDs; 9^{th} column: storm driver; 10^{th} column: minimum Dst value.

Storm period	Dates and characteristics poleward TIDs launched during the main phase of geomagnetic storms								
Date	Date	Time (UT)	TIDs Prop. Lat(°)$S \leftarrow Eq \rightarrow N$	Prop. Angle S (N)	Velocity (m/s)	c_H (m/s)	Period (min)	Cause of storm	Minimum Dst(nT)
07-12.03.2012	09.03.2012	12:00-12:00	$-25 \leftarrow 0 \rightarrow 20$	147 (45)	350 ± 44.7	294	90 ± 23	CME	-145 (09.03.2012)
15-18.10.2013	15.07.2013	06:00-07:00	$-30 \leftarrow 0 \rightarrow 25$	155 (43.5)	211.9 ± 15.3	192	65 ± 9	CME	-72 (15.07.2013)
02-03.10.2013	02.10.2013	21:00-22:00	$-20 \leftarrow 0 \rightarrow 25$	142 (36)	240.4 ± 55.3	189	28 ± 9	CME	-122 (09.10.2013)
02-04.04.2016	02.04.2016	03:00-03:50	$-25 \leftarrow 0 \rightarrow 30$	135 (46)	309.6 ± 13.1	219	88 ± 20	CIR	-59 (02.04.2016)
07-09.04.2016	07.04.2016	03.00-03:51	$-20 \leftarrow 0 \rightarrow 25$	139 (38)	297 ± 55	224	60 ± 12	CIR	-62 (07.04.2016)
29-30.09.2016	29.09.2016	11:00-12:00	$-30 \leftarrow 0 \rightarrow 15$	149 (41)	345.2 ± 12.5	296	50 ± 9	CME	-66 (29.09.2016)
29-30.10.2016	29.10.2016	12:00-12:55	$-20 \leftarrow 0 \rightarrow 13$	130 (50)	344.5 ± 13.5	221	80 ± 9	CME	-64 (29.10.2016)
Dates and characteristics of poleward TIDs launched during the recovery phase of geomagnetic storms									
Date	Date	Time (UT)	TIDs Prop. Lat(°)$S \leftarrow Eq \rightarrow N$	Prop. Angle S(N)	Velocity (m/s)	c_H (m/s)	Period (min)	Cause of storm	Minimum Dst(nT)
07-09.03.2016	08.03.2016	02:30-03:00	$-30 \leftarrow 0 \rightarrow 30$	145 (40)	300 ± 45.5	245	45 ± 16	CME	-52 (03.02.2016)
03-05.08.2016	04.08.2016	08:00-09:00	$-10 \leftarrow 0 \rightarrow 30$	135.5 (32)	2250 ± 15.1	178	40 ± 11	CME	-52 (03.02.2016)
26-28.10.2016	27.10.2016	21:00-21:50	$-30 \leftarrow 0 \rightarrow 30$	140 (36)	334.2 ± 15.5	258	80 ± 9	CIR	-51 (27.10.2016)
01-05.03.2017	02.03.2017	17:00-17:44	$-30 \leftarrow 0 \rightarrow 30$	132 (34)	281.5 ± 16.1	188	50 ± 9	CIR	-61 (01.03.2017)
16-20.07.2017	17.07.2017	18:00-18:50	$-30 \leftarrow 0 \rightarrow 30$	160 (44)	288.8 ± 15.5	271	70 ± 9	CME	-72 (16.07.2017)

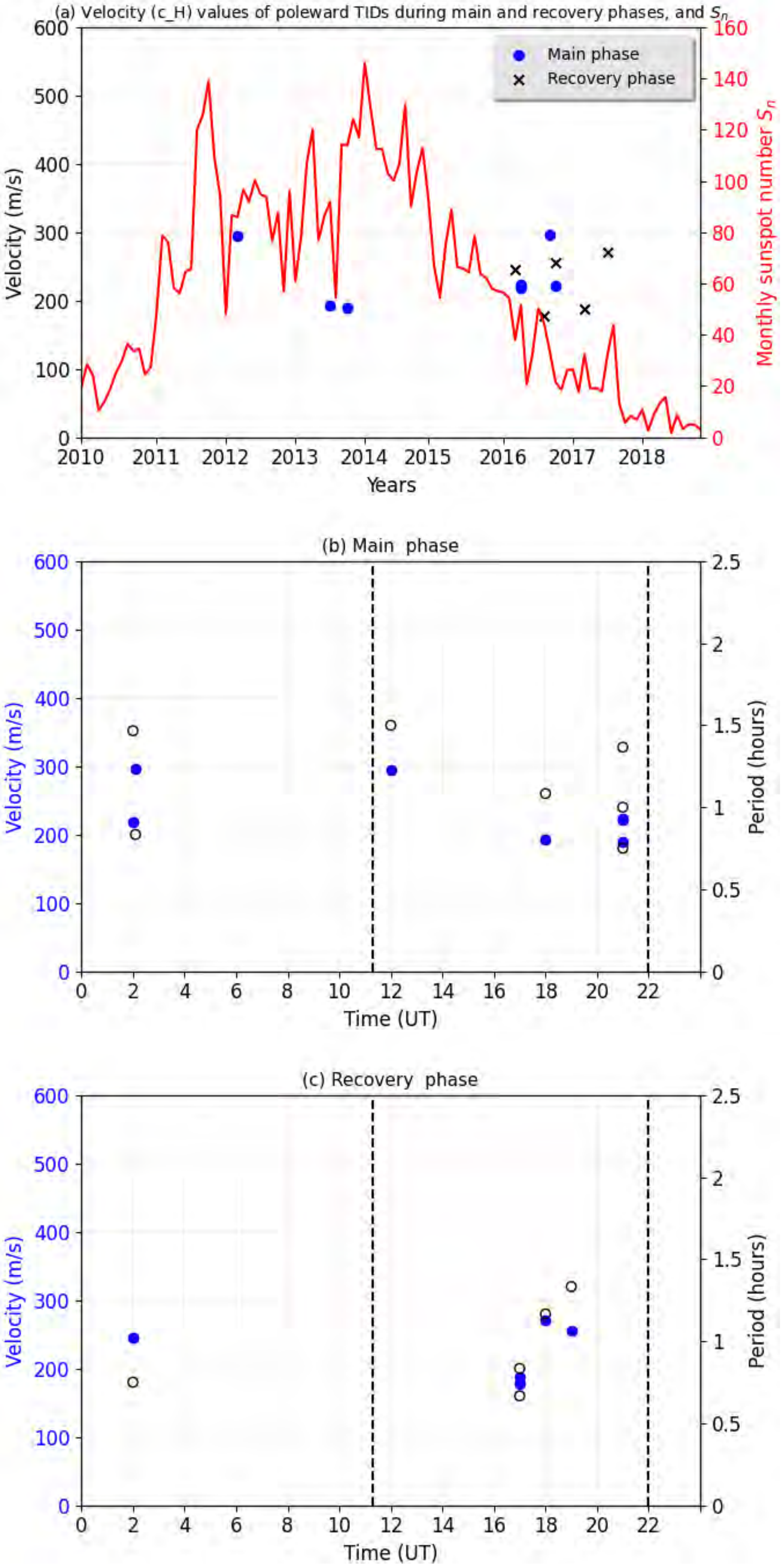

Figure 6.15: Results of the statistical analysis of poleward TIDs during the main and recovery phases of geomagnetic storms that occurred over the American sector from 2010 to 2018. (a) The red curve represents the monthly sunspot number S_n, and the blue dots and black crosses represent the horizontal velocity c_H during the main and recovery phases, respectively. (b)-(c) Blue dots represent the horizontal velocity c_H, and the black open cycles represent the periods of TIDs.

6.3 Summary

This chapter described a long-term statistical study of poleward TIDs over the African-European and American sectors. This study was conducted for geomagnetically quiet and disturbed conditions over the period 2010 to 2018. Geomagnetically disturbed conditions were defined as meeting the criteria Kp $>$ 4 and Dst $\leq$ -50 nT. For each month during the study period, the four quietest days (maximum Kp $<$ 3) were identified in the data from the World Data Center for Geomagnetism, Kyoto. TIDs were identified in GNSS TEC derived data. The conclusion was that for both disturbed and quiet conditions, the African-European sector had more poleward TIDs than the American sector. The majority of the poleward TIDs occurred primarily during the local daytime. The meridional velocities and periods of the TIDs were in the range of 210-299 m/s and 39-70 minutes over African-European and American sectors during quiet conditions, respectively. Most of the poleward TIDs during quiet conditions were medium-scale TIDs. Almost all poleward TIDs (with the exception of two cases) during the main phase of geomagnetic storms in the African-European sector were large-scale with horizontal velocities and periods ranging between 250-503 m/s and 30 min to 2 hours. During the recovery phase, poleward TIDs were of medium-scale. Poleward TIDs presented mostly during the recovery phase. Surprisingly, the majority of poleward TIDs over the American sector occurred during a storm's main phase, in contrast to the African sector, where the number of poleward TIDs was larger during the recovery phase. Where magnetometer data was available, the majority of the cases during quiet and disturbed conditions could be linked to changes in ionospheric electrodynamics, specifically the enhancement of the equatorial electrojet, although there were some cases that could not explained by the variation of the EEJ.

Chapter 7

Conclusions and Future work

The primary goal of this research was to do a long-term statistical study of TIDs originating in the low- and high-latitudes origin over the American and African-European sectors. Poleward TIDs were studied for both quiet and disturbed conditions, whereas equatorward TIDs were only studied in quiet conditions. This research covered the period between 2010 and 2018. Geomagnetically disturbed conditions were defined as those with Kp $>$ 4 and Dst $\leq$ -50 nT were used. The four quietest days (maximum Kp $<$ 3) for each month of the study period were identified in the data from the World Data Center for Geomagnetism in Kyoto. TIDs were identified in data from the Global Navigation Satellite Systems (GNSS).

This study presents observations of equatorward medium- to large-scale TIDs, possibly launched in the polar region, and crossing the geomagnetic equator to the opposite hemisphere over the African-European and American sectors during quiet conditions. For the American sector, two cases of equatorward propagating medium-scale TIDs were identified. Seven transhemispheric TIDs were identified, with five originating in the southern and the rest in northern wintertime hemisphere over the African-European sector (Thaganyana *et al.*, 2022). The meridional phase velocities, periods and meridional wavelengths of the TIDs were in the range of 270-322 m/s, 48-80 min and 802-1296 km, respectively. The ranges of the horizontal propagation velocity and horizontal wavelengths were c_H=120-274 m/s and λ_H=379-1104 km, respectively. These properties characterise medium- to large-scale TIDs (Hunsucker, 1982; Hocke and Schlegel, 1996; Katamzi-Joseph *et al.*, 2019). The observed TIDs originated from the wintertime hemisphere and propagated to the summertime hemisphere. TIDs were more often launched in the high-latitude of the southern winter hemisphere than in the high-latitude northern winter hemisphere for the African-European sector. For the American sector, TIDs were only launched in the southern winter hemisphere. Earlier modelling results (e.g. Vadas and Becker, 2019; Vadas *et al.*, 2019; Becker and Vadas, 2020), suggest that the sources of these medium- to large-scale TIDs are likely tertiary GWs from the dissipation of secondary GWs, and excited by the local body force created by breaking mountain waves.

This study established that poleward TIDs, during geomagnetically quiet conditions over the African and American sectors, occur mainly during local daytime. The African-European sector had more poleward TIDs than the American sector. The meridional propagation velocities and periods of the TIDs were in the range of 210-299 m/s and 39-70 min over both the African-European and American sectors. Overall, during quiet conditions, the ionospheric changes associated with forces from the lower atmosphere such as fronts, convection systems, and sudden stratospheric warmings (Kazimirovsky and KoKouRov, 1991; Anderson and Araujo-Pradere, 2010; Goncharenko *et al.*, 2010; Chau *et al.*, 2012; Huang *et al.*, 2020), may play a critical role in launching AGWs in the equatorial latitudes. The latter may be among the likely sources of the reported poleward TIDs. However, the exact mechanisms responsible for launching poleward TIDs from the low/equatorial latitudes were been established in this study and therefore remain a subject for future investigation.

During geomagnetic storms, poleward TIDs occurred primarily during local daytime over the African-European and American sectors. Fewer poleward TIDs were identified over the American sector than over the African-European sector. In total, 12 and 40 poleward TIDs were identified in the American and African-European sectors, respectively, for geomagnetic storms which occurred between 2010 and 2018. Almost all poleward TIDs (with the exception of two cases) during the main phase of geomagnetic storms were large-scale with horizontal velocities and periods ranging between 250-503 m/s and 30 min to 2 hours over the African-European sector. During the main phase, poleward TIDs as a result of CMEs and CIRs driven storms accounted for 66.7 % and 33.3 %, respectively. Poleward TIDs were identified mostly during the recovery phase. Poleward TIDs in the recovery phase were of medium-scale. During the recovery phase, poleward TIDs as a result of CMEs accounted for 92 % and CIRs for 8 %. This suggests that poleward TIDs are more likely to be present during CME-driven storms and mostly occur during the recovery phase.

For the American sector, poleward TIDs occurred primarily during local daytime hours. Four poleward TIDs occurred during nighttime hours. The periods and horizontal velocities of TIDs ranged between 45 min-1.5 h and 180-296 m/s during the main phase. During the recovery phase, the horizontal velocities and periods range between 177-271 m/s and 40-1.5 h, respectively. The majority of poleward TIDs over the American sector occurred during the storm's main phase, as opposed to the African-European sector, in which a significant number of poleward TIDs occurred during the recovery phase. The majority of poleward TIDs were launched during the CMEs driven storms.The storm-induced poleward TIDs emerging from the equatorial regions were largely contained within the boundaries of 10°N and 25°S, and 30°N and 30°S over the African-European sector and American sectors, respectively. However, in the northern hemisphere of the African-European sector (10°-25°N) has significant data gaps and it was thus not possible to determine the exact latitudinal coverage of these poleward TIDs for this region. Overall, electrodynamics relating to the enhanced eastward electric field, and hence an increase in the EEJ (ΔH) played a crucial role in launching atmospheric gravity waves in the equatorial latitudes that were a likely source of the reported poleward TIDs.

7.1 Future work

The study was mainly conducted by visually inspecting generated 2-D ΔTEC maps to identify TIDs. It would be beneficial to automate this process in order to make it easier to do long-term statistical analyses that cover more than one solar cycle. According to this study, the African sector has more poleward TIDs than the American sector during both quiet and disturbed conditions. The reasons for this difference were not established in this study and should be investigated. While observations of poleward TIDs during storm-time conditions have been largely associated with electrodynamic changes specifically related to an increase in the equatorial electric field, thus enhancing the vertical E×B drift (Habarulema *et al.*, 2015, 2016, 2022), the causes of TIDs in absence of storms is completely unknown at this stage. This is an important observation which requires further observational and theoretical study. Ngwira *et al.* (2019) attempted to model the poleward TIDs of equatorial origin in the storm of 22-23 June 2015 over the Brazilian longitudes by means of the Thermosphere Ionosphere Electrodynamics General Circulation Model. The model captured only the equatorward large-scale TIDs. There is a need to model these poleward TIDs of equatorial origin during for quiet and disturbed conditions.

References

Aa, E., Zou, S., Erickson, P. J., Zhang, S.-R. and Liu, S. 2020. Statistical analysis of the main ionospheric trough using Swarm in situ measurements. *Journal of Geophysical Research: Space Physics*, 125(3): e2019JA027583. doi: https://doi.org/10.1029/2019JA027583.

Abdu, M., Sobral, J., Nelson, O. and Batista, I. 1985. Solar cycle related range type spread-f occurrence characteristics over equatorial and low latitude stations in brazil. *Journal of Atmospheric and Terrestrial Physics*, 47(8-10): 901–905. doi: https://doi.org/10.1016/0021-9169(85)90065-0.

Afraimovich, E., Edemskiy, I., Voeykov, S., Yasyukevich, Y. V. and Zhivetiev, I. 2009*a*. The first GPS-TEC imaging of the space structure of MS wave packets excited by the solar terminator. *Annales Geophysicae*, 27(4): 1521–1525. doi: https://doi.org/10.5194/angeo-27-1521-2009.

Afraimovich, E., Edemskiy, I., Voeykov, S., Yasyukevich, Y. V. and Zhivetiev, I. 2009*b*. Spatio-temporal structure of the wave packets generated by the solar terminator. *Advances in Space Research*, 44(7): 824–835. doi: https://doi.org/10.1016/j.asr.2009.05.017.

Afraimovich, E., Perevalova, N. and Voyeikov, S. 2003. Traveling wave packets of total electron content disturbances as deduced from global GPS network data. *Journal of Atmospheric and Solar-Terrestrial Physics*, 65(11-13): 1245–1262. doi: https://doi.org/10.1016/j.jastp.2003.08.007.

Afraimovich, E., Terekhov, A., Udodov, M. Y. and Fridman, S. 1992. Refraction distortions of transionospheric radio signals caused by changes in a regular ionosphere and by travelling ionospheric disturbances. *Journal of Atmospheric and Terrestrial Physics*, 54(7-8): 1013–1020. doi: https://doi.org/10.1016/0021-9169(92)90068-V.

Afraimovich, E., Voeykov, S., Perevalova, N. and Ratovsky, K. 2008. Large-scale traveling ionospheric disturbances of auroral origin according to the data of the GPS network and ionosondes. *Advances in Space Research*, 42(7): 1213–1217. doi: https://doi.org/10.1016/j.asr.2007.11.023.

Ahmed, M., Sagalyn, R., Wildman, P. and Burke, W. 1979. Topside ionospheric trough morphology: Occurrence frequency and diurnal, seasonal, and altitude variations. *Journal of Geophysical Research: Space Physics*, 84(A2): 489–498. doi: https://doi.org/10.1029/JA084iA02p00489.

Akasofu, S.-I. 1981. Energy coupling between the solar wind and the magnetosphere. *Space Science Reviews*, 28(2): 121–190.

Alex, S., Roy, M. and Rastogi, R. 1987. The effect of counter electrojet on the plasma distribution of the topside ionosphere. *Geophysical Research Letters*, 14(7): 693–695. doi: https://doi.org/10.1029/GL014i007p00693.

Alexander, M. 2003. Gravity wave fluxes. *Encyclopedia of Atmospheric Sciences, Academic Press*, pp. 1699–1705. doi: https://doi.org/10.1016/B0-12-227090-8/00309-2.

Alexander, M. J. and Teitelbaum, H. 2007. Observation and analysis of a large amplitude mountain wave event over the Antarctic peninsula. *Journal of Geophysical Research: Atmospheres*, 112(D21). doi: https://doi.org/10.1029/2006JD008368.

Alexander, M. J. and Teitelbaum, H. 2011. Three-dimensional properties of Andes mountain waves observed by satellite: A case study. *Journal of Geophysical Research: Atmospheres*, 116(D23). doi: https://doi.org/10.1029/2011JD016151.

Anderson, D. 1973. A theoretical study of the ionospheric F region equatorial anomaly—I. Theory. *Planetary and Space Science*, 21(3): 409–419. doi: https://doi.org/10.1016/0032-0633(73)90040-8.

Anderson, D., Anghel, A., Yumoto, K., Ishitsuka, M. and Kudeki, E. 2002. Estimating daytime vertical ExB drift velocities in the equatorial F-region using ground-based magnetometer observations. *Geophysical Research Letters*, 29(12): 37–1–37–4. doi: https://doi.org/10.1029/2001GL014562.

Anderson, D. and Araujo-Pradere, E. A. 2010. Sudden stratospheric warming event signatures in daytime exb drift velocities in the peruvian and philippine longitude sectors for january 2003 and 2004. *Journal of Geophysical Research: Space Physics*, 115(A8). doi: https://doi.org/10.1029/2010JA015337.

Anderson, P., Heelis, R. and Hanson, W. 1991. The ionospheric signatures of rapid subauroral ion drifts. *Journal of Geophysical Research: Space Physics*, 96(A4): 5785–5792. doi: https://doi.org/10.1029/90JA02651.

Andrews, D. G. 2010. *An introduction to atmospheric physics*. Cambridge: Cambridge University Press.

Appleton, E. V. 1946. Two anomalies in the ionosphere. *Nature*, 157(3995): 691–691.

Araujo-Pradere, E. 2005. GPS-derived total electron content response for the Bastille Day magnetic storm of 2000 at a low mid-latitude station. *Geofísica Internacional*, 44(2): 211–218.

Atilaw, T. Y., Stephenson, J. A. and Katamzi-Joseph, Z. T. 2021. Multitaper analysis of an MSTID event above Antarctica on 17 March 2013. *Polar Science*, 28: 100643. doi: https://doi.org/10.1016/j.polar.2021.100643.

Atiq, M. 2018. Historical review of ionosphere in perspective of sources of ionization and radio waves propagation. *Research & Reviews: Journal of Space Science & Technology*, 7(2): 28–39. doi: http://sciencejournals.stmjournals.in/index.php/RRJoSST/article/view/1218.

Aumann, H. H., Broberg, S., Elliott, D., Gaiser, S. and Gregorich, D. 2006. Three years of Atmospheric Infrared Sounder radiometric calibration validation using sea surface temperatures. *Journal of Geophysical Research: Atmospheres*, 111(D16). doi: https://doi.org/10.1029/2005JD006822.

Aumann, H. H., Chahine, M. T., Gautier, C., Goldberg, M. D., Kalnay, E., McMillin, L. M. *et al.*, 2003. AIRS/AMSU/HSB on the Aqua mission: Design, science objectives, data products, and processing systems. *IEEE Transactions on Geoscience and Remote Sensing*, 41(2): 253–264. doi: 10.1109/TGRS.2002.808356.

Azeem, I. 2021. Spectral asymmetry of near-concentric traveling ionospheric disturbances due to Doppler-shifted atmospheric gravity waves. *Frontiers in Astronomy and Space Sciences*, 8: 690480. doi: https://doi.org/10.3389/fspas.2021.690480.

Azeem, I., Yue, J., Hoffmann, L., Miller, S. D., Straka III, W. C. and Crowley, G. 2015. Multisensor profiling of a concentric gravity wave event propagating from the troposphere to the ionosphere. *Geophysical Research Letters*, 42(19): 7874–7880. doi: https://doi.org/10.1002/2015GL065903.

Azpilicueta, F., Brunini, C. and Radicella, S. 2012. Semi-annual anomaly and annual asymmetry on TOPEX TEC during a full solar cycle. *Geodesy for Planet Earth*, pp. 769–774. doi: 10.1007/978-3-642-20338-1_96.

Bacmeister, J. T. and Schoeberl, M. R. 1989. Breakdown of vertically propagating two-dimensional gravity waves forced by orography. *Journal of Atmospheric Sciences*, 46(14): 2109–2134. doi: https://doi.org/10.1175/1520-0469(1989)046<2109:BOVPTD>2.0.CO;2.

Bagiya, M. S., Hazarika, R., Laskar, F. I., Sunda, S., Gurubaran, S., Chakrabarty, D., Bhuyan, P., Sridharan, R., Veenadhari, B. and Pallamraju, D. 2014. Effects of prolonged southward interplanetary magnetic field on low-latitude ionospheric electron density. *Journal of Geophysical Research: Space Physics*, 119(7): 5764–5776. doi: https://doi.org/10.1002/2014JA020156.

Bagiya, M. S., Iyer, K., Joshi, H., Thampi, S. V., Tsugawa, T., Ravindran, S., Sridharan, R. and Pathan, B. 2011. Low-latitude ionospheric-thermospheric response to storm time electrodynamical coupling between high and low latitudes. *Journal of Geophysical Research: Space Physics*, 116(A1). doi: https://doi.org/10.1029/2010JA015845.

Baker, D., Kanekal, S., Hoxie, V., Henderson, M., Li, X., Spence, H. E., Elkington, S., Friedel, R., Goldstein, J., Hudson, M. *et al.*, 2013. A long-lived relativistic electron storage ring embedded in Earth's outer Van Allen belt. *Science*, 340(6129): 186–190. doi: 10.1126/science.1233518.

Balachandran, N. K. 1980. Gravity waves from thunderstorms. *Monthly Weather Review*, 108(6): 804–816. doi: https://doi.org/10.1175/1520-0493(1980)108<0804:GWFT>2.0.CO;2.

Balan, N., Jayachandran, B., Nair, R. B., Namboothiri, S., Bailey, G. and Rao, P. 1992. HF Doppler observations of vector plasma drifts in the evening F-region at the magnetic equator. *Journal of Atmospheric and Terrestrial Physics*, 54(11-12): 1545–1554. doi: https://doi.org/10.1016/0021-9169(92)90162-E.

Balan, N., Liu, L. and Le, H. 2018. A brief review of equatorial ionization anomaly and ionospheric irregularities. *Earth and Planetary Physics*, 2(4): 257–275. doi: https://doi.org/10.26464/epp2018025.

Balan, N., Otsuka, Y., Fukao, S., Abdu, M. and Bailey, G. 2000. Annual variations of the ionosphere: A review based on MU radar observations. *Advances in Space Research*, 25(1): 153–162. doi: https://doi.org/10.1016/S0273-1177(99)00913-8.

Balan, N., Shiokawa, K., Otsuka, Y., Kikuchi, T., Vijaya Lekshmi, D., Kawamura, S., Yamamoto, M. and Bailey, G. 2010. A physical mechanism of positive ionospheric storms at low latitudes and midlatitudes. *Journal of Geophysical Research: Space Physics*, 115(A2): A02304. doi: https://doi.org/10.1029/2009JA014515.

Balan, N., Shiokawa, K., Otsuka, Y., Watanabe, S. and Bailey, G. 2009. Super plasma fountain and equatorial ionization anomaly during penetration electric field. *Journal of Geophysical Research: Space Physics*, 114(A3). doi: https://doi.org/10.1029/2008JA013768.

Balan, N., Souza, J. and Bailey, G. 2018. Recent developments in the understanding of equatorial ionization anomaly: A review. *Journal of Atmospheric and Solar-Terrestrial Physics*, 171: 3–11. doi: https://doi.org/10.1016/j.jastp.2017.06.020.

Balogh, A., Gosling, J., Jokipii, J., Kallenbach, R. and Kunow, H. 2000. *Corotating Interaction Regions: Proceedings of an ISSI Workshop 6-13 June 1998, Bern, Switzerland.* Vol. 7, Kluwer Academic Publishers.

Balthazor, R. and Moffett, R. 1997. A study of atmospheric gravity waves and travelling ionospheric disturbances at equatorial latitudes. *Annales Geophysicae*, 15(8): 1048–1056. doi: https://doi.org/10.1007/s00585-997-1048-4.

Bani Shahabadi, M., Huang, Y., Garand, L., Heilliette, S. and Yang, P. 2016. Validation of a weather forecast model at radiance level against satellite observations allowing quantification of temperature, humidity, and cloud-related biases. *Journal of Advances in Modeling Earth Systems*, 8(3): 1453–1467. doi: https://doi.org/10.1002/2016MS000751.

Bartels, J., Heck, N. and Johnston, H. 1939. The three-hour-range index measuring geomagnetic activity. *Terrestrial Magnetism and Atmospheric Electricity*, 44(4): 411–454. doi: https://doi.org/10.1029/TE044i004p00411.

Basu, S., Basu, S., Valladares, C., Yeh, H.-C., Su, S.-Y., MacKenzie, E., Sultan, P., Aarons, J., Rich, F., Doherty, P. *et al.*, 2001. Ionospheric effects of major magnetic storms during the International Space Weather Period of September and October 1999: GPS observations, VHF/UHF scintillations, and in situ density structures at middle and equatorial latitudes. *Journal of Geophysical Research: Space Physics*, 106(A12): 30389–30413. doi: https://doi.org/10.1029/2001JA001116.

Basu, S., Groves, K., Basu, S. and Sultan, P. 2002. Specification and forecasting of scintillations in communication/navigation links: Current status and future plans. *Journal of Atmospheric and Solar-Terrestrial Physics*, 64(16): 1745–1754. doi: https://doi.org/10.1016/S1364-6826(02)00124-4.

Basu, S., MacKenzie, E. and Basu, S. 1988. Ionospheric constraints on VHF/UHF communications links during solar maximum and minimum periods. *Radio Science*, 23(03): 363–378. doi: 10.1029/RS023i003p00363.

Becker, E. and Vadas, S. L. 2020. Explicit global simulation of gravity waves in the thermosphere. *Journal of Geophysical Research: Space Physics*, 125(10): e2020JA028034. doi: https://doi.org/10.1029/2020JA028034.

Beer, T. 1974. *Atmospheric waves*. New York: John Wiley.

Berger, T., Holzinger, M., Sutton, E. and Thayer, J. 2020. Flying through uncertainty. *Space Weather*, 18(1): e2019SW002373. doi: https://doi.org/10.1029/2019SW002373.

Blanc, M. and Richmond, A. 1980. The ionospheric disturbance dynamo. *Journal of Geophysical Research: Space Physics*, 85(A4): 1669–1686. doi: https://doi.org/10.1029/JA085iA04p01669.

Bland, E. C., Heino, E., Kosch, M. J. and Partamies, N. 2018. SuperDARN radar-derived HF radio attenuation during the September 2017 solar proton events. *Space Weather*, 16(10): 1455–1469. doi: https://doi.org/10.1029/2018SW001916.

Booker, J. R. and Bretherton, F. P. 1967. The critical layer for internal gravity waves in a shear flow. *Journal of Fluid Mechanics*, 27(3): 513–539. doi: https://doi.org/10.1017/S0022112067000515.

Borovsky, J. E. and Denton, M. H. 2006. Differences between CME-driven storms and CIR-driven storms. *Journal of Geophysical Research: Space Physics*, 111(A7). doi: 10.1029/2005JA011447.

Borries, C., Mahrous, A. M., Ellahouny, N. M. and Badeke, R. 2016. Multiple ionospheric perturbations during the Saint Patrick's Day storm 2015 in the European-African sector. *Journal of Geophysical Research: Space Physics*, 121(11): 11–333. doi: https://doi.org/10.1002/2016JA023178.

Boška, J. and Šauli, P. 2001. Observations of gravity waves of meteorological origin in the F-region ionosphere. *Physics and Chemistry of the Earth, Part C: Solar, Terrestrial & Planetary Science*, 26(6): 425–428. doi: https://doi.org/10.1016/S1464-1917(01)00024-1.

Bowman, G. 1990. A review of some recent work on mid-latitude spread-F occurrence as detected by ionosondes. *Journal of Geomagnetism and Geoelectricity*, 42(2): 109–138. doi: https://doi.org/10.5636/jgg.42.109.

Bravo, M., Benavente, R., Foppiano, A., Urra, B. and Ovalle, E. 2022. Traveling ionospheric disturbances observed over South America after lithospheric events: 2010–2020. *Journal of Geophysical Research: Space Physics*, 127(4): e2021JA030060. doi: https://doi.org/10.1029/2021JA030060.

Bruinsma, S. L. and Forbes, J. M. 2008. Medium-to large-scale density variability as observed by CHAMP. *Space Weather*, 6(8): 1–9. doi: https://doi.org/10.1029/2008SW000411.

Cai, X., Burns, A. G., Wang, W., Qian, L., Pedatella, N., Coster, A., Zhang, S., Solomon, S. C., Eastes, R. W., Daniell, R. E. *et al.*, 2021. Variations in thermosphere composition and ionosphere total electron content under "geomagnetically quiet" conditions at solar-minimum. *Geophysical Research Letters*, 48(11): e2021GL093300. doi: https://doi.org/10.1029/2021GL093300.

Campbell, W. H. 1997. *Introduction to geomagnetic fields.* Cambridge: Cambridge University Press.

Campbell, W. H. 2001. *Earth magnetism: a guided tour through magnetic fields.* San Diego: Academic Press.

Chahine, M. T., Pagano, T. S., Aumann, H. H., Atlas, R. *et al.*, 2006. AIRS: Improving weather forecasting and providing new data on greenhouse gases. *Bulletin of the American Meteorological Society*, 87(7): 911–926. doi: https://doi.org/10.1175/BAMS-87-7-911.

Charron, M. and Brunet, G. 1999. Gravity wave diagnosis using empirical normal modes. *Journal of the Atmospheric Sciences*, 56(15): 2706–2727. doi: https://doi.org/10.1175/1520-0469(1999)056<2706:GWDUEN>2.0.CO;2.

Chau, J. L., Goncharenko, L. P., Fejer, B. G. and Liu, H.-L. 2012. Equatorial and low latitude ionospheric effects during sudden stratospheric warming events. *Space Science Reviews*, 168(1): 385–417. doi: https://doi.org/10.1007/s11214-011-9797-5.

Chen, G.-m., Xu, J., Wang, W. and Burns, A. G. 2014. A comparison of the effects of CIR- and CME-induced geomagnetic activity on thermospheric densities and spacecraft orbits: Statistical studies. *Journal of Geophysical Research: Space Physics*, 119(9): 7928–7939. doi: https://doi.org/10.1002/2014JA019831.

Chen, P., Yao, Y. and Yao, W. 2017. On the coseismic ionospheric disturbances after the Nepal Mw7. 8 earthquake on April 25, 2015 using GNSS observations. *Advances in Space Research*, 59(1): 103–113. doi: https://doi.org/10.1016/j.asr.2016.09.021.

Chimonas, G. 1969. The upper atmosphere in motion: The equatorial electrojet as a source of long period travelling ionospheric disturbances. *Geophysical Monograph Series*, 18: 698–706.

Chimonas, G. 1970. The equatorial electrojet as a source of long period travelling ionospheric disturbances. *Planetary and Space Science*, 18(4): 583–589. doi: https://doi.org/10.1016/0032-0633(70)90133-9.

Choi, B., Cho, J. and Lee, S. 2011. Estimation and analysis of GPS receiver differential code biases using KGN in Korean Peninsula. *Advances in Space Research*, 47(9): 1590–1599. doi: https://doi.org/10.1016/j.asr.2010.12.021.

Chum, J., Athieno, R., Baše, J., Burešová, D., Hruška, F., Laštovička, J., McKinnell, L. and Šindelářová, T. 2012. Statistical investigation of horizontal propagation of gravity waves in the ionosphere over Europe and South Africa. *Journal of Geophysical Research: Space Physics*, 117(A3). doi: https://doi.org/10.1029/2011JA017161.

Collis, P. and Häggström, I. 1988. Plasma convection and auroral precipitation processes associated with the main ionospheric trough at high latitudes. *Journal of Atmospheric and Terrestrial Physics*, 50(4-5): 389–404. doi: https://doi.org/10.1016/0021-9169(88)90024-4.

Crooker, N., Joselyn, J. A. and Feynman, J. 1997. *Coronal Mass Ejections*. Washington, D.C.:American Geophysical Union.

Crowley, G., Jones, T. and Dudeney, J. 1987. Comparison of short period TID morphologies in Antarctica during geomagnetically quiet and active intervals. *Journal of atmospheric and terrestrial physics*, 49(11-12): 1155–1162. doi: https://doi.org/10.1016/0021-9169(87)90098-5.

Cruz, J. C. and Trujillo, H. 1999. Design of a fourth harmonic fluxgate magnetometer. *Sensors and Actuators A: Physical*, 78(2-3): 71–73. doi: https://doi.org/10.1016/S0924-4247(99)00194-6.

Davies, K. 1990. *Ionospheric Radio*. London: The Institution of Engineering and Technology.

Davis, M. 1971. On polar substorms as the source of large-scale traveling ionospheric disturbances. *Journal of Geophysical Research*, 76(19): 4525–4533. doi: https://doi.org/10.1029/JA076i019p04525.

Davis, T. N. and Sugiura, M. 1966. Auroral electrojet activity index AE and its universal time variations. *Journal of Geophysical Research*, 71(3): 785–801. doi: https://doi.org/10.1029/JZ071i003p00785.

Ding, F., Wan, W., Li, Q., Zhang, R., Song, Q., Ning, B., Liu, L., Zhao, B. and Xiong, B. 2014. Comparative climatological study of large-scale traveling ionospheric disturbances over North America and China in 2011–2012. *Journal of Geophysical Research: Space Physics*, 119(1): 519–529. doi: https://doi.org/10.1002/2013JA019523.

Ding, F., Wan, W., Ning, B. and Wang, M. 2007. Large-scale traveling ionospheric disturbances observed by GPS total electron content during the magnetic storm of 29–30 October 2003. *Journal of Geophysical Research: Space Physics*, 112(A6). doi: https://doi.org/10.1029/2006JA012013.

Ding, F., Wan, W., Ning, B., Zhao, B., Li, Q., Wang, Y., Hu, L., Zhang, R. and Xiong, B. 2013. Observations of poleward-propagating large-scale traveling ionospheric disturbances in southern China. *Annales Geophysicae*, 31(2): 377–385. doi: https://doi.org/10.5194/angeo-31-377-2013.

Doyle, J. D., Shapiro, M. A., Jiang, Q. and Bartels, D. L. 2005. Large-amplitude mountain wave breaking over Greenland. *Journal of the Atmospheric Sciences*, 62(9): 3106–3126. doi: https://doi.org/10.1175/JAS3528.1.

Dubazane, M. B. and Habarulema, J. B. 2018. An empirical model of vertical plasma drift over the African sector. *Space Weather*, 16(6): 619–635. doi: https://doi.org/10.1029/2018SW001820.

Dugassa, T., Habarulema, J. B. and Nigussie, M. 2019. Longitudinal variability of occurrence of ionospheric irregularities over the American, African and Indian regions during geomagnetic storms. *Advances in Space Research*, 63(8): 2609–2622. doi: https://doi.org/10.1016/j.asr.2019.01.001.

Dugassa, T., Habarulema, J. B. and Nigussie, M. 2020. Equatorial and low-latitude ionospheric TEC response to CIR-driven geomagnetic storms at different longitude sectors. *Advances in Space Research*, 66(8): 1947–1966. doi: https://doi.org/10.1016/j.asr.2020.07.003.

Dunkerton, T. 2015. Gravity Waves: Buoyancy and Buoyancy Waves: Theory. in North, G.R., Pyle, J. and Zhang F. (eds.). *Encyclopedia of Atmospheric Sciences: Second Edition*, 160–163. doi: https://doi.org/10.1016/b978-0-12-382225-3.00022-0.

Eastes, R., Solomon, S., Daniell, R., Anderson, D., Burns, A., England, S., Martinis, C. and McClintock, W. 2019. Global-scale observations of the equatorial ionization anomaly. *Geophysical Research Letters*, 46(16): 9318–9326. doi: https://doi.org/10.1029/2019GL084199.

Echer, E., Gonzalez, W. and Tsurutani, B. 2011. Statistical studies of geomagnetic storms with peak Dst ≤ -50 nT from 1957 to 2008. *Journal of Atmospheric and Solar-Terrestrial Physics*, 73(11-12): 1454–1459.

Eckermann, S., Hoffmann, L., Höpfner, M., Wu, D. and Alexander, M. 2009. Antarctic NAT PSC belt of June 2003: Observational validation of the mountain wave seeding hypothesis. *Geophysical Research Letters*, 36(2). doi: https://doi.org/10.1029/2008GL036629.

El-Rabbany, A. 2002. *Introduction to GPS: The Global Positioning System*. Artech House.

Elliott, H. A., Jahn, J.-M. and McComas, D. J. 2013. The Kp index and solar wind speed relationship: Insights for improving space weather forecasts. *Space Weather*, 11(6): 339–349. doi: https://doi.org/10.1002/swe.20053.

Ern, M., Hoffmann, L. and Preusse, P. 2017. Directional gravity wave momentum fluxes in the stratosphere derived from high-resolution AIRS temperature data. *Geophysical Research Letters*, 44(1): 475–485. doi: https://doi.org/10.1002/2016GL072007.

Farge, M. 1992. Wavelet transforms and their applications to turbulence. *Annual Review of Fluid Mechanics*, 24(1): 395–458. doi: https://doi.org/10.1146/annurev.fl.24.010192.002143.

Farrell, J. and Barth, M. 1999. *The Global Positioning System and inertial navigation*. New York: Mcgraw-hill.

Fejer, B. G. 1991. Low latitude electrodynamic plasma drifts: A review. *Journal of Atmospheric and Terrestrial Physics*, 53(8): 677–693. doi: https://doi.org/10.1016/0021-9169(91)90121-M.

Fejer, B. G. 1997. The electrodynamics of the low-latitude ionosphere: Recent results and future challenges. *Journal of Atmospheric and Solar-Terrestrial Physics*, 59(13): 1465–1482. doi: https://doi.org/10.1016/S1364-6826(96)00149-6.

Fejer, B. G. 2011. Low latitude ionospheric electrodynamics. *Space Science Reviews*, 158(1): 145–166. doi: https://doi.org/10.1007/s11214-010-9690-7.

Fejer, B. G. and Scherliess, L. 1998. Mid- and low-latitude prompt-penetration ionospheric zonal plasma drifts. *Geophysical Research Letters*, 25(16): 3071–3074. doi: https://doi.org/10.1029/98GL02325.

Ferguson, M. 1997. *GPS land navigation: A complete guidebook for backcountry users of the NAVSTAR satellite system.* Boiso, ID: Glassgord Publishers.

Figueiredo, C., Wrasse, C., Takahashi, H., Otsuka, Y., Shiokawa, K. and Barros, D. 2017. Large-scale traveling ionospheric disturbances observed by GPS dTEC maps over North and South America on Saint Patrick's Day storm in 2015. *Journal of Geophysical Research: Space Physics*, 122(4): 4755–4763. doi: https://doi.org/10.1002/2016JA023417.

Foster, J. and Burke, W. 2002. SAPS: A new categorization for sub-auroral electric fields. *Eos, Transactions American Geophysical Union*, 83(36): 393–394. doi: https://doi.org/10.1029/2002EO000289.

Francis, S. H. 1974. A theory of medium-scale traveling ionospheric disturbances. *Journal of Geophysical Research*, 79(34): 5245–5260. doi: https://doi.org/10.1029/JA079i034p05245.

Frissell, N. A., Baker, J. B., Ruohoniemi, J. M., Greenwald, R. A., Gerrard, A. J., Miller, E. S. and West, M. L. 2016. Sources and characteristics of medium-scale traveling ionospheric disturbances observed by high-frequency radars in the North American sector. *Journal of Geophysical Research: Space Physics*, 121(4): 3722–3739. doi: https://doi.org/10.1002/2015JA022168.

Fritts, D. 2015. Middle Atmosphere: Gravity Waves, in North, G.R., Pyle, J. and Zhang, F. (eds.). *Encyclopedia of Atmospheric Sciences. Second Edition. Elsevier*, pp. 1308–1314.

Fritts, D. C. and Vanzandt, T. E. 1993. Spectral estimates of gravity wave energy and momentum fluxes. Part I: Energy dissipation, acceleration, and constraints. *Journal of Atmospheric Sciences*, 50(22): 3685–3694. doi: https://doi.org/10.1175/1520-0469(1985)042<0549:FOHACD>2.0.CO;2.

Fukushima, D., Shiokawa, K., Otsuka, Y. and Ogawa, T. 2012. Observation of equatorial nighttime medium-scale traveling ionospheric disturbances in 630-nm airglow images over 7 years. *Journal of Geophysical Research: Space Physics*, 117(A10). doi: https://doi.org/10.1029/2012JA017758.

Fuller-Rowell, T., Codrescu, M., Fejer, B. G., Borer, W., Marcos, F. and Anderson, D. 1997. Dynamics of the low-latitude thermosphere: Quiet and disturbed conditions. *Journal of Atmospheric and Solar-Terrestrial Physics*, 59(13): 1533–1540. doi: https://doi.org/10.1016/S1364-6826(96)00154-X.

Fuller-Rowell, T., Codrescu, M., Moffett, R. and Quegan, S. 1994. Response of the thermosphere and ionosphere to geomagnetic storms. *Journal of Geophysical Research: Space Physics*, 99(A3): 3893–3914. doi: https://doi.org/10.1029/93JA02015.

Gao, Y., Liu, Z. *et al.*, 2002. Precise ionosphere modeling using regional GPS network data. *Journal of Global Positioning Systems*, 1(3): 18–24.

Gil, A., Modzelewska, R., Moskwa, S., Siluszyk, A., Siluszyk, M., Wawrzynczak, A., Pozoga, M. and Tomasik, L. 2020. The solar event of 14–15 July 2012 and its geoeffectiveness. *Solar Physics*, 295(10): 1–16. doi: https://doi.org/10.1007/s11207-020-01703-2.

Goncharenko, L., Chau, J., Liu, H.-L. and Coster, A. 2010. Unexpected connections between the stratosphere and ionosphere. *Geophysical Research Letters*, 37(10). doi: https://doi.org/10.1029/2010GL043125.

Gonzalez, W. D., Tsurutani, B. T. and Clúa de Gonzalez, A. L. 1999. Interplanetary origin of geomagnetic storms. *Space Science Reviews*, 88(3): 529–562.

Gonzalez, W., Joselyn, J.-A., Kamide, Y., Kroehl, H. W., Rostoker, G., Tsurutani, B. and Vasyliunas, V. 1994. What is a geomagnetic storm? *Journal of Geophysical Research: Space Physics*, 99(A4): 5771–5792. doi: https://doi.org/10.1029/93JA02867.

Gopalswamy, N. 2006. Consequences of coronal mass ejections in the heliosphere. *Sun and Geosphere*, 1(2): 5–12.

Grocott, A., Hosokawa, K., Ishida, T., Lester, M., Milan, S., Freeman, M., Sato, N. and Yukimatu, A. 2013. Characteristics of medium-scale traveling ionospheric disturbances observed near the Antarctic Peninsula by HF radar. *Journal of Geophysical Research: Space Physics*, 118(9): 5830–5841. doi: https://doi.org/10.1002/jgra.50515.

Habarulema, J. B., Katamzi, Z. T. and McKinnell, L.-A. 2013. Estimating the propagation characteristics of large-scale traveling ionospheric disturbances using ground-based and satellite data. *Journal of Geophysical Research: Space Physics*, 118(12): 7768–7782. doi: https://doi.org/10.1002/2013JA018997.

Habarulema, J. B., Katamzi, Z. T. and Yizengaw, E. 2015. First observations of poleward large-scale traveling ionospheric disturbances over the African sector during geomagnetic storm conditions. *Journal of Geophysical Research: Space Physics*, 120(8): 6914–6929. doi: https://doi.org/10.1002/2015JA021066.

Habarulema, J. B., Katamzi, Z. T., Yizengaw, E., Yamazaki, Y. and Seemala, G. 2016. Simultaneous storm time equatorward and poleward large-scale TIDs on a global scale. *Geophysical Research Letters*, 43(13): 6678–6686. doi: https://doi.org/10.1002/2016GL069740.

Habarulema, J. B., Lefebvre, G., Moldwin, M. B., Katamzi-Joseph, Z. T. and Yizengaw, E. 2019. Counter-electrojet occurrence as observed from C/NOFS satellite and ground-based magnetometer data over the African and American sectors. *Space Weather*, 17(7): 1090–1104. doi: https://doi.org/10.1029/2019SW002236.

Habarulema, J. B., Thaganyana, G. P., Katamzi-Joseph, Z. T., Yizengaw, E., Moldwin, M. B. and Ngwira, C. M. 2022. A statistical study of poleward traveling ionospheric disturbances over the African and American sectors during geomagnetic storms. *Journal of Geophysical Research: Space Physics*, 127(4): e2021JA030162. doi: https://doi.org/10.1029/2021JA030162.

Habarulema, J. B., Yizengaw, E., Katamzi-Joseph, Z. T., Moldwin, M. B. and Buchert, S. 2018. Storm time global observations of large-scale TIDs from ground-based and in situ satellite measurements. *Journal of Geophysical Research: Space Physics*, 123(1): 711–724. doi: https://doi.org/10.1002/2017JA024510.

Hajkowicz, L. and Hunsucker, R. 1987. A simultaneous observation of large-scale periodic TIDs in both hemispheres following an onset of auroral disturbances. *Planetary and Space Science*, 35(6): 785–791. doi: https://doi.org/10.1016/0032-0633(87)90038-9.

Handzo, R., Forbes, J. and Reinisch, B. 2014. Ionospheric electron density response to solar flares as viewed by digisondes. *Space Weather*, 12(4): 205–216. doi: https://doi.org/10.1002/2013SW001020.

Hargreaves, J. K. 1992. *The solar-terrestrial environment: an introduction to geospace - the science of the terrestrial upper atmosphere, ionosphere, and magnetosphere.* Cambridge: Cambridge University Press.

Hari, S. and Murthy, B. K. 1995. Seasonal variations of equatorial night-time thermospheric meridional winds. *Journal of Atmospheric and Terrestrial Physics*, 57(11): 1241–1246. doi: https://doi.org/10.1016/0021-9169(95)00007-O.

Haridas, M. M., Rao, P., Rao, K. S. and Sudhakar, P. 2018. Studies of forest fire induced changes in atmosphere over Uttarakhand, India, using space based observations and model simulations. *Current Science*, 114(12): 2504–2512. doi: https://www.jstor.org/stable/26495763.

He, J., Jin, Y., Xiao, F., He, Z., Yang, C., Xie, Y., He, Q., Wang, C., Shang, X., Liu, S. *et al.*, 2021. The influence of various frequency chorus waves on electron dynamics in radiation belts. *Science China Technological Sciences*, 64(4): 890–897. doi: https://doi.org/10.1007/s11431-020-1750-6.

Heale, C. J., Bossert, K., Vadas, S., Hoffmann, L., Dörnbrack, A., Stober, G., Snively, J. and Jacobi, C. 2020. Secondary gravity waves generated by breaking mountain waves over Europe. *Journal of Geophysical Research: Atmospheres*, 125(5): e2019JD031662. doi: https://doi.org/10.1029/2019JD031662.

Hedin, A. and Mayr, H. 1987. Characteristics of wavelike fluctuations in Dynamics Explorer neutral composition data. *Journal of Geophysical Research: Space Physics*, 92(A10): 11159–11172. doi: https://doi.org/10.1029/JA092iA10p11159.

Heelis, R. 2004. Electrodynamics in the low and middle latitude ionosphere: A tutorial. *Journal of Atmospheric and Solar-Terrestrial Physics*, 66(10): 825–838. doi: https://doi.org/10.1016/j.jastp.2004.01.034.

Heelis, R., Kendall, P., Moffett, R., Windle, D. and Rishbeth, H. 1974. Electrical coupling of the E-and F-regions and its effect on F-region drifts and winds. *Planetary and Space Science*, 22(5): 743–756. doi: https://doi.org/10.1016/0032-0633(74)90144-5.

Hernández-Pajares, M., Juan, J. M. and Sanz, J. 2006. Medium-scale traveling ionospheric disturbances affecting GPS measurements: Spatial and temporal analysis. *Journal of Geophysical Research: Space Physics*, 111(A7). doi: https://doi.org/10.1029/2005JA011474.

Hess, P. and Zhang, J. 2014. Stereoscopic study of the kinematic evolution of a coronal mass ejection and its driven shock from the Sun to the Earth and the prediction of their arrival times. *The Astrophysical Journal*, 792(1): 49. doi: 10.1088/0004-637X/792/1/49.

Hines, C. 1967. On the nature of traveling ionospheric disturbances launched by low-altitude nuclear explosions. *Journal of Geophysical Research*, 72(7): 1877–1882. doi: https://doi.org/10.1029/JZ072i007p01877.

Hines, C. O. 1960. Internal atmospheric gravity waves at ionospheric heights. *Canadian Journal of Physics*, 38(11): 1441–1481. doi: https://doi.org/10.1029/GM018p0248.

Hocke, K. and Schlegel, K. 1996. A review of atmospheric gravity waves and travelling ionospheric disturbances: 1982–1995. *Annales Geophysicae*, 14(9): 917. doi: 10.1007/s00585-996-0917-6.

Hoffmann, L. and Alexander, M. 2009. Retrieval of stratospheric temperatures from Atmospheric Infrared Sounder radiance measurements for gravity wave studies. *Journal of Geophysical Research: Atmospheres*, 114(D7). doi: https://doi.org/10.1029/2008JD011241.

Hoffmann, L., Alexander, M. J., Clerbaux, C., Grimsdell, A. W., Meyer, C. I., Rößler, T. and Tournier, B. 2014. Intercomparison of stratospheric gravity wave observations with AIRS and IASI. *Atmospheric Measurement Techniques*, 7(12): 4517–4537. doi: https://doi.org/10.5194/amt-7-4517-2014.

Hoffmann, L., Grimsdell, A. W. and Alexander, M. J. 2016. Stratospheric gravity waves at Southern Hemisphere orographic hotspots: 2003–2014 AIRS/Aqua observations. *Atmospheric Chemistry and Physics*, 16(14): 9381–9397. doi: https://doi.org/10.5194/acp-16-9381-2016.

Hoffmann, L., Spang, R., Orr, A., Alexander, M. J., Holt, L. A. and Stein, O. 2017. A decadal satellite record of gravity wave activity in the lower stratosphere to study polar stratospheric cloud formation. *Atmospheric Chemistry and Physics*, 17(4): 2901–2920. doi: https://doi.org/10.5194/acp-17-2901-2017.

Hoffmann, L., Xue, X. and Alexander, M. 2013. A global view of stratospheric gravity wave hotspots located with Atmospheric Infrared Sounder observations. *Journal of Geophysical Research: Atmospheres*, 118(2): 416–434. doi: https://doi.org/10.1029/2012JD018658.

Hofmann-Wellenhof, B., Lichtenegger, H. and Collins, J. 1992. *GPS theory and practice.* New York: Spring Wien.

Holton, J. R., Curry, J. A. and Pyle, J. A. 2003. *Encyclopedia of Atmospheric Sciences.* Vol. 3, New York: Academic Press.

Hooke, W. H. 1970. The ionospheric response to internal gravity waves: 1. The F2 region response. *Journal of Geophysical Research*, 75(28): 5535–5544. doi: https://doi.org/10.1029/JA075i028p05535.

Horne, R., Glauert, S., Meredith, N., Boscher, D., Maget, V., Heynderickx, D. and Pitchford, D. 2013. Space weather impacts on satellites and forecasting the Earth's electron radiation belts with SPACECAST. *Space Weather*, 11(4): 169–186. doi: https://doi.org/10.1002/swe.20023.

Huang, C. 2013. Disturbance dynamo electric fields in response to geomagnetic storms occurring at different universal times. *Journal of Geophysical Research: Space Physics*, 118(1): 496–501. doi: https://doi.org/10.1029/2012JA018118.

Huang, C.-S., Foster, J. C. and Kelley, M. C. 2005. Long-duration penetration of the interplanetary electric field to the low-latitude ionosphere during the main phase of magnetic storms. *Journal of Geophysical Research: Space Physics*, 110(A11). doi: https://doi.org/10.1029/2005JA011202.

Huang, F., Lei, J., Zhang, R., Li, N., Gu, S., Yu, Y., Liu, L., Owolabi, C., Ning, B., Li, G. *et al.*, 2020. Prominent daytime TEC enhancements under the quiescent condition of January 2017. *Geophysical Research Letters*, 47(14): e2020GL088398. doi: https://doi.org/10.1029/2020GL088398.

Huba, J., Joyce, G., Sazykin, S., Wolf, R. and Spiro, R. 2005. Simulation study of penetration electric field effects on the low-to mid-latitude ionosphere. *Geophysical Research Letters*, 32(23). doi: https://doi.org/10.1029/2005GL024162.

Huber, P. 1981. *Robust Statistics.* New York: John Wiley.

Hunsucker, R. D. 1982. Atmospheric gravity waves generated in the high-latitude ionosphere: A review. *Reviews of Geophysics*, 20(2): 293–315. doi: https://doi.org/10.1029/RG020i002p00293.

Hunsucker, R. D. and Hargreaves, J. K. 2007. *The high-latitude ionosphere and its effects on radio propagation.* Cambridge: Cambridge University Press.

Huttunen, K. E. J., Koskinen, H. E. and Schwenn, R. 2002. Variability of magnetospheric storms driven by different solar wind perturbations. *Journal of Geophysical Research: Space Physics*, 107(A7): SMP–20. doi: https://doi.org/10.1029/2001JA900171.

Ibrahim, C., Chane-Ming, F., Barthe, C. and Kuleshov, Y. 2010. Diagnosis of tropical cyclone activity through gravity wave energy density in the southwest Indian Ocean. *Geophysical Research Letters*, 37(9). doi: 10.1029/2010GL042938.

Immel, T., Sagawa, E., England, S., Henderson, S., Hagan, M., Mende, S., Frey, H., Swenson, C. and Paxton, L. 2006. Control of equatorial ionospheric morphology by atmospheric tides. *Geophysical Research Letters*, 33(15). doi: https://doi.org/10.1029/2006GL026161.

Ishida, T., Ogawa, Y., Kadokura, A., Hiraki, Y. and Häggström, I. 2014. Seasonal variation and solar activity dependence of the quiet-time ionospheric trough. *Journal of Geophysical Research: Space Physics*, 119(8): 6774–6783. doi: https://doi.org/10.1002/2014JA019996.

Iyemori, T. 1990. Storm-time magnetospheric currents inferred from mid-latitude geomagnetic field variations. *Journal of Geomagnetism and Geoelectricity*, 42(11): 1249–1265. doi: https://doi.org/10.5636/jgg.42.1249.

Iyemori, T. and Rao, D. 1996. Decay of the Dst field of geomagnetic disturbance after substorm onset and its implication to storm-substorm relation. *Annales Geophysicae*, . doi: https://doi.org/10.1007/s00585-996-0608-3.

Jiao, Y., Morton, Y. T., Taylor, S. and Pelgrum, W. 2013. Characterization of high-latitude ionospheric scintillation of GPS signals. *Radio Science*, 48(6): 698–708. doi: 10.1002/2013RS005259.

Jonah, O., Coster, A., Zhang, S., Goncharenko, L., Erickson, P., de Paula, E. and Kherani, E. 2018. TID observations and source analysis during the 2017 Memorial Day weekend geomagnetic storm over North America. *Journal of Geophysical Research: Space Physics*, 123(10): 8749–8765. doi: https://doi.org/10.1029/2018JA025367.

JPL 2021. AIRS: Atmospheric Infrared Sounder. *Jet Propulsion Laboratory*, .
URL: *https://airs.jpl.nasa.gov/data/guides-docs/*

Kalikhman, A. 1980. Medium-scale travelling ionospheric disturbances and thermospheric winds in the F-region. *Journal of Atmospheric and Terrestrial physics*, 42(8): 697–703. doi: https://doi.org/10.1016/0021-9169(80)90053-7.

Kamide, Y. and Maltsev, Y. P. 2007. Geomagnetic Storms, in Kamide, Y. and Maltsev, Y.P. *Handbook of Solar-Terrestrial Environment*, pp. 355–374.

Kan, J. and Lee, L. 1979. Energy coupling function and solar wind-magnetosphere dynamo. *Geophysical Research Letters*, 6(7): 577–580. doi: https://doi.org/10.1029/GL006i007p005.

Karpachev, A. and Afonin, V. 1998. Ionospheric trough observation probability dependence on the season, local time, longitude and magnetic activity level. *Geomagnetizm i Aehronomiya*, 38(3): 79–91.

Karpachev, A., Klimenko, M., Klimenko, V. and Pustovalova, L. 2016. Empirical model of the main ionospheric trough for the nighttime winter conditions. *Journal of Atmospheric and Solar-Terrestrial Physics*, 146: 149–159. doi: https://doi.org/10.1016/j.jastp.2016.05.008.

Karpachev, A. T., Klimenko, M. V., Klimenko, V. V., Chirik, N. V., Zhbankov, G. A. and Pustovalova, L. V. 2022. Satellite model of foF2 in winter high-latitude ionosphere describing the trough structure. *Advances in Space Research*, 69(1): 2–15. doi: https://doi.org/10.1016/j.asr.2021.07.014.

Katamzi-Joseph, Z., Grawe, M., Makela, J., Habarulema, J., Martinis, C. and Baumgardner, J. 2022. First results on characteristics of nighttime MSTIDs observed over South Africa: Influence of thermospheric wind and sporadic E. *Journal of Geophysical Research: Space Physics*, 127(11): e2022JA030375. doi: https://doi.org/10.1029/2022JA030375.

Katamzi-Joseph, Z. T., Aruliah, A. L., Oksavik, K., Habarulema, J. B., Kauristie, K. and Kosch, M. J. 2019. Multi-instrument observations of large-scale atmospheric gravity waves/traveling ionospheric disturbances associated with enhanced auroral activity over Svalbard. *Advances in Space Research*, 63(1): 270–281. doi: https://doi.org/10.1016/j.asr.2018.08.042.

Katamzi, Z., Smith, N., Mitchell, C., Spalla, P. and Materassi, M. 2012. Statistical analysis of travelling ionospheric disturbances using TEC observations from geostationary satellites. *Journal of Atmospheric and Solar-Terrestrial Physics*, 74: 64–80. doi: https://doi.org/10.1016/j.jastp.2011.10.006.

Katamzi, Z. T. and Habarulema, J. B. 2014. Traveling ionospheric disturbances observed at South African midlatitudes during the 29–31 October 2003 geomagnetically disturbed period. *Advances in Space Research*, 53(1): 48–62. doi: https://doi.org/10.1016/j.asr.2013.10.019.

Kazimirovsky, E. S. and KoKouRov, V. D. 1991. The tropospheric and stratospheric effects in the ionosphere. *Journal of Geomagnetism and Geoelectricity*, 43(Supplement1): 551–562. doi: https://doi.org/10.5636/jgg.43.Supplement1551.

Keesee, A. M. and Scime, E. E. 2015. Database of ion temperature maps during geomagnetic storms. *Earth and Space Science*, 2(2): 39–46. doi: https://doi.org/10.1002/2014EA000061.

Kelley, M. C. 2009. *The Earth's ionosphere: plasma physics and electrodynamics*. Academic Press.

Kelley, M. C., Vlasov, M. N., Foster, J. C. and Coster, A. J. 2004. A quantitative explanation for the phenomenon known as storm-enhanced density. *Geophysical Research Letters*, 31(19). doi: https://doi.org/10.1029/2004GL020875.

Kersley, L., Pryse, S. and Wheadon, N. 1988. Amplitude and phase scintillation at high latitudes over northern Europe. *Radio Science*, 23(03): 320–330. doi: 10.1029/RS023i003p00320.

Kikuchi, T. and Hashimoto, K. K. 2016. Transmission of the electric fields to the low latitude ionosphere in the magnetosphere-ionosphere current circuit. *Geoscience Letters*, 3(1): 1–11. doi: 10.1186/s40562-016-0035-6.

Kikuchi, T., Hashimoto, K. K. and Nozaki, K. 2008. Penetration of magnetospheric electric fields to the equator during a geomagnetic storm. *Journal of Geophysical Research: Space Physics*, 113(A6). doi: https://doi.org/10.1029/2007JA012628.

Kirtskhalia, V. G. 2012. Speed of sound in atmosphere of the Earth. *Open Journal of Acoustics*, 2(2): 80–85. doi: http://dx.doi.org/10.4236/oja.2012.22009.

Kivi, R., Dörnbrack, A., Sprenger, M. and Vömel, H. 2020. Far-ranging impact of mountain waves excited over Greenland on stratospheric dehydration and rehydration. *Journal of Geophysical Research: Atmospheres*, 125(18): e2020JD033055. doi: https://doi.org/10.1029/2020JD033055.

Klobuchar, J. A. 1987. Ionospheric time-delay algorithm for single-frequency GPS users. *IEEE Transactions on Aerospace and Electronic Systems*, AES-23(3): 325–331. doi: https://doi.org/10.1029/JZ070i005p01254.

Knudsen, W. 1969. Neutral atmosphere wave generation by the equatorial electrojet. *Journal of Geophysical Research: Space Physics*, 74(16).

Knudsen, W. 1974. Magnetospheric convection and the high-latitude F2 ionosphere. *Journal of Geophysical Research*, 79(7): 1046–1055. doi: https://doi.org/10.1029/JA079i007p01046.

Kogure, M., Yue, J., Nakamura, T., Hoffmann, L., Vadas, S. L., Tomikawa, Y. *et al.*, 2020. First direct observational evidence for secondary gravity waves generated by mountain waves over the Andes. *Geophysical Research Letters*, 47(17): e2020GL088845. doi: https://doi.org/10.1029/2020GL088845.

Kotake, N., Otsuka, Y., Ogawa, T., Tsugawa, T. and Saito, A. 2007. Statistical study of medium-scale traveling ionospheric disturbances observed with the GPS networks in southern California. *Earth, Planets and Space*, 59(2): 95–102. doi: 10.1186/BF03352681.

Kozlovsky, A., Turunen, T. and Ulich, T. 2013. Rapid-run ionosonde observations of traveling ionospheric disturbances in the auroral ionosphere. *Journal of Geophysical Research: Space Physics*, 118(8): 5265–5276. doi: https://doi.org/10.1002/jgra.50474.

Kuai, J., Liu, L., Lei, J., Liu, J., Zhao, B., Chen, Y., Le, H., Wang, Y. and Hu, L. 2017. Regional differences of the ionospheric response to the July 2012 geomagnetic storm. *Journal of Geophysical Research: Space Physics*, 122(4): 4654–4668. doi: https://doi.org/10.1002/2016JA023844.

Kuai, J., Liu, L., Liu, J., Zhao, B., Chen, Y., Le, H. and Wan, W. 2015. The long-duration positive storm effects in the equatorial ionosphere over Jicamarca. *Journal of Geophysical Research: Space Physics*, 120(2): 1311–1324. doi: https://doi.org/10.1002/2014JA020552.

Kuai, J., Wang, K., Zhong, J., Wan, X., Huang, F., Sun, H., Chen, J., Song, X. and Han, H. 2022. Analysis of the Ionospheric Irregularities and Phase Scintillation at Low and Middle Latitudes Based on Swarm Observations. *Remote Sensing*, 14(19): 4780. doi: https://doi.org/10.3390/rs14194780.

Kumar, S. and Moore, K. B. 2002. The evolution of global positioning system (GPS) technology. *Journal of Science Education and Technology*, 11(1): 59–80. doi: https://doi.org/10.1023/A:1013999415003.

Lei, J., Burns, A. G., Tsugawa, T., Wang, W., Solomon, S. C. and Wiltberger, M. 2008. Observations and simulations of quasiperiodic ionospheric oscillations and large-scale traveling ionospheric disturbances during the December 2006 geomagnetic storm. *Journal of Geophysical Research: Space Physics*, 113(A6). doi: 10.1029/2007JA012807.

Leick, A., Rapoport, L. and Tatarnikov, D. 2015. *GPS satellite surveying. 4th ed.* Hoboken, NJ: Wiley.

Leutbecher, M. and Volkert, H. 2000. The propagation of mountain waves into the stratosphere: Quantitative evaluation of three-dimensional simulations. *Journal of the Atmospheric Sciences*, 57(18): 3090–3108. doi: https://doi.org/10.1175/1520-0469(2000)057<3090:TPOMWI>2.0.CO;2.

Leys, C., Ley, C., Klein, O., Bernard, P. and Licata, L. 2013. Detecting outliers: Do not use standard deviation around the mean, use absolute deviation around the median. *Journal of Experimental Social Psychology*, 49(4): 764–766. doi: https://doi.org/10.1016/j.jesp.2013.03.013.

Lin, C., Richmond, A., Heelis, R., Bailey, G., Lu, G., Liu, J.-Y., Yeh, H. and Su, S.-Y. 2005. Theoretical study of the low-and midlatitude ionospheric electron density enhancement during the October 2003 superstorm: Relative importance of the neutral wind and the electric field. *Journal of Geophysical Research: Space Physics*, 110(A12). doi: https://doi.org/10.1029/2005JA011304.

Liu, J., Liu, L., Nakamura, T., Zhao, B., Ning, B. and Yoshikawa, A. 2014. A case study of ionospheric storm effects during long-lasting southward IMF Bz-driven geomagnetic storm. *Journal of Geophysical Research: Space Physics*, 119(9): 7716–7731. doi: https://doi.org/10.1002/2014JA020273.

Liu, J., Zhang, D.-H., Coster, A. J., Zhang, S.-R., Ma, G.-Y., Hao, Y.-Q. and Xiao, Z. 2019. A case study of the large-scale traveling ionospheric disturbances in the eastern Asian sector during the 2015 St. Patrick's Day geomagnetic storm. *Annales Geophysicae*, 37(4): 673–687. doi: https://doi.org/10.5194/angeo-37-673-2019.

Liu, K., Li, G., Ning, B., Hu, L. and Li, H. 2015. Statistical characteristics of low-latitude ionospheric scintillation over China. *Advances in Space Research*, 55(5): 1356–1365. doi: https://doi.org/10.1016/j.asr.2014.12.001.

Liu, L., Wan, W., Chen, Y. and Le, H. 2011. Solar activity effects of the ionosphere: A brief review. *Chinese Science Bulletin*, 56(12): 1202–1211. doi: 10.1007/s11434-010-4226-9.

Liu, L., Zhao, B., Wan, W., Ning, B., Zhang, M.-L. and He, M. 2009. Seasonal variations of the ionospheric electron densities retrieved from Constellation Observing System for Meteorology, Ionosphere, and Climate mission radio occultation measurements. *Journal of Geophysical Research: Space Physics*, 114(A2). doi: https://doi.org/10.1029/2008JA013819.

Loewe, C. and Prölss, G. 1997. Classification and mean behavior of magnetic storms. *Journal of Geophysical Research: Space Physics*, 102(A7): 14209–14213.

Lubyk, K., Hoque, M. M. and Stolle, C. 2022. Evaluation of the Mid-Latitude Ionospheric trough Using GRACE Data. *Remote Sensing*, 14(17): 4384. doi: https://doi.org/10.3390/rs14174384.

MacDougall, J., Abdu, M., Batista, I., Fagundes, P., Sahai, Y. and Jayachandran, P. 2009. On the production of traveling ionospheric disturbances by atmospheric gravity waves. *Journal of Amospheric and Solar-Terrestrial Physics*, 71(17-18): 2013–2016. doi: https://doi.org/10.1016/j.jastp.2009.09.006.

Macleod, M. A. 1966. Sporadic E theory. I. Collision-geomagnetic equilibrium. *Journal of Atmospheric Sciences*, 23(1): 96–109. doi: https://doi.org/10.1175/1520-0469(1966)023<0096:SETICG>2.0.CO;2.

Mallat, S. 1999. *A wavelet tour of signal processing.* Elsevier.

Mannucci, A., Tsurutani, B., Iijima, B., Komjathy, A., Saito, A., Gonzalez, W., Guarnieri, F., Kozyra, J. and Skoug, R. 2005. Dayside global ionospheric response to the major interplanetary events of October 29–30, 2003 "Halloween Storms". *Geophysical Research Letters*, 32(12). doi: https://doi.org/10.1029/2004GL021467.

Marriott, R., Richmond, A. and Venkateswaran, S. 1979. The quiet-time equatorial electrojet and counter-electrojet. *Journal of Geomagnetism and Geoelectricity*, 31(3): 311–340. doi: https://doi.org/10.5636/jgg.31.311.

Matamba, T. M. and Habarulema, J. B. 2018. Ionospheric responses to CME-and CIR-driven geomagnetic storms along 30 E–40 E over the African sector from 2001 to 2015. *Space Weather*, 16(5): 538–556. doi: https://doi.org/10.1029/2017SW001754.

Materassi, M. and Mitchell, C. N. 2007. Wavelet analysis of GPS amplitude scintillation: A case study. *Radio Science*, 42(01): 1–10. doi: https://doi.org/10.1029/2005RS003415.

Matzka, J., Stolle, C., Yamazaki, Y., Bronkalla, O. and Morschhauser, A. 2021. The geomagnetic Kp index and derived indices of geomagnetic activity. *Space Weather*, 19(5): e2020SW002641. doi: https://doi.org/10.1029/2020SW002641.

Maynard, N. and Chen, A. 1975. Isolated cold plasma regions: Observations and their relation to possible production mechanisms. *Journal of Geophysical Research*, 80(7): 1009–1013. doi: https://doi.org/10.1029/JA080i007p01009.

Mayr, H. G., Talaat, E. R. and Wolven, B. C. 2013. Global propagation of gravity waves generated with the whole atmosphere transfer function model. *Journal of Atmospheric and Solar-Terrestrial Physics*, 104: 7–17. doi: https://doi.org/10.1016/j.jastp.2013.08.001.

Mayr, H., Harris, I. and Dube, M. 1990. Polar thermospheric Joule heating, and redistribution of recombination energy in the upper mesosphere. *Journal of atmospheric and terrestrial physics*, 52(2): 103–112. doi: https://doi.org/10.1016/0021-9169(90)90072-U.

Mayr, H., Harris, I., Herrero, F. and Pesnell, W. 1991. Transfer Function Model (TFM) and gravity waves. *Journal of Geomagnetism and Geoelectricity*, 43(1): 525–536. doi: https://doi.org/10.5636/jgg.43.1525.

Mayr, H., Harris, I., Varosi, F. and Herrero, F. 1984. Global excitation of wave phenomena in a dissipative multiconstituent medium: 1. Transfer function of the Earth's thermosphere. *Journal of Geophysical Research: Space Physics*, 89(A12): 10929–10959. doi: https://doi.org/10.1029/JA089iA12p10929.

McNamara, L. F. 1991. *The ionosphere: communications, surveillance, and direction finding.* Malabar, FL:Krieger Publishing.

McRae, W. M. and Thomson, N. R. 2004. Solar flare induced ionospheric D-region enhancements from VLF phase and amplitude observations. *Journal of Atmospheric and Solar-Terrestrial Physics*, 66(1): 77–87. doi: https://doi.org/10.1016/j.jastp.2003.09.009.

Menvielle, M. and Berthelier, A. 1991. The K-derived planetary indices: Description and availability. *Reviews of Geophysics*, 29(3): 415–432. doi: https://doi.org/10.1029/91RG00994.

Miller, J. 1991. Reaction time analysis with outlier exclusion: Bias varies with sample size. *The Quarterly Journal of Experimental Psychology*, 43(4): 907–912. doi: https://doi.org/10.1080/14640749108400962.

Mishin, E., Burke, W., Huang, C. and Rich, F. 2003. Electromagnetic wave structures within subauroral polarization streams. *Journal of Geophysical Research: Space Physics*, 108(A8). doi: https://doi.org/10.1029/2002JA009793.

Misra, P. and Enge, P. 2006. *Global Positioning System, Signals, Measurements, and Performance.* Ganga-Jumuna Press, P.O. Box 692 Lincoln, Massachusetts 01773.

Mitra, A. P. 1974. *Ionospheric effects of solar flares.* Dordrecht: Springer.

Moffett, R. and Quegan, S. 1983. The mid-latitude trough in the electron concentration of the ionospheric F-layer: a review of observations and modelling. *Journal of Atmospheric and Terrestrial Physics*, 45(5): 315–343. doi: https://doi.org/10.1016/S0021-9169(83)80038-5.

Moldwin, M. 2008. *An introduction to space weather.* Cambridge: Cambridge University Press.

Muella, M., Kherani, E. d., De Paula, E., Cerruti, A., Kintner, P., Kantor, I., Mitchell, C., Batista, I. and Abdu, M. 2010. Scintillation-producing Fresnel-scale irregularities associated with the regions of steepest TEC gradients adjacent to the equatorial ionization anomaly. *Journal of Geophysical Research: Space Physics*, 115(A3). doi: https://doi.org/10.1029/2009JA014788.

Mukherjee, S., Sarkar, S., Purohit, P. and Gwal, A. 2010. Seasonal variation of total electron content at crest of equatorial anomaly station during low solar activity conditions. *Advances in Space Research*, 46(3): 291–295. doi: https://doi.org/10.1016/j.asr.2010.03.024.

Mulla, A., Baviskar, J., Baviskar, A. and Bhovad, A. 2015. GPS assisted Standard Positioning Service for navigation and tracking: Review & implementation. *in International Conference on Pervasive Computing (ICPC), PUne, India, 8-10 January 2015. IEEE*, pp. 1–6. doi: 10.1109/PERVASIVE.2015.7087165.

Nair, R. B., Balan, N., Bailey, G. and Rao, P. 1992. Spectra of the ac electric fields in the post-sunset F-region at the magnetic equator. *Planetary and Space Science*, 40(5): 655–662. doi: https://doi.org/10.1016/0032-0633(92)90006-A.

Nakamura, M., Yoneda, A., Oda, M. and Tsubouchi, K. 2015. Statistical analysis of extreme auroral electrojet indices. *Earth, Planets and Space*, 67(1): 1–8. doi: 10.1186/s40623-015-0321-0.

Nappo, C. J. 2013. *An introduction to atmospheric gravity waves.* Academic press.

Nastrom, G. D. and Fritts, D. C. 1992. Sources of mesoscale variability of gravity waves. Part I: Topographic excitation. *Journal of the Atmospheric Sciences*, 49(2): 101–110. doi: 10.1175/1520-0469(1992)049<0101:SOMVOG>2.0.CO;2.

Ngwira, C. M., Habarulema, J.-B., Astafyeva, E., Yizengaw, E., Jonah, O. F., Crowley, G. *et al.*, 2019. Dynamic response of ionospheric plasma density to the geomagnetic storm of 22-23 June 2015. *Journal of Geophysical Research: Space Physics*, 124(8): 7123–7139. doi: https://doi.org/10.1029/2018JA026172.

Ngwira, C. M., McKinnell, L.-A., Cilliers, P. J. and Yizengaw, E. 2012. An investigation of ionospheric disturbances over South Africa during the magnetic storm on 15 May 2005. *Advances in Space Research*, 49(2): 327–335. doi: https://doi.org/10.1016/j.asr.2011.09.035.

Nicolls, M. J. and Heinselman, C. J. 2007. Three-dimensional measurements of traveling ionospheric disturbances with the Poker Flat Incoherent Scatter Radar. *Geophysical Research Letters*, 34(21). doi: https://doi.org/10.1029/2007GL031506.

Nicolls, M., Vadas, S., Meriwether, J., Conde, M. and Hampton, D. 2012. The phases and amplitudes of gravity waves propagating and dissipating in the thermosphere: Application to measurements over Alaska. *Journal of Geophysical Research: Space Physics*, 117(A5). doi: 10.1029/2011JA017426.

Nishida, A. 1968. Coherence of geomagnetic DP 2 fluctuations with interplanetary magnetic variations. *Journal of Geophysical Research*, 73(17): 5549–5559. doi: https://doi.org/10.1029/JA073i017p05549.

Nishioka, M., Saito, A. and Tsugawa, T. 2009. Super-medium-scale traveling ionospheric disturbance observed at midlatitude during the geomagnetic storm on 10 November 2004. *Journal of Geophysical Research: Space Physics*, 114(A7). doi: https://doi.org/10.1029/2008JA013581.

Nitta, N. V., Mulligan, T., Kilpua, E. K., Lynch, B. J., Mierla, M., O'Kane, J., Pagano, P., Palmerio, E., Pomoell, J., Richardson, I. G. *et al.*, 2021. Understanding the origins of problem geomagnetic storms associated with "stealth" coronal mass ejections. *Space Science Reviews*, 217(8): 1–53. doi: https://doi.org/10.1007/s11214-021-00857-0.

Oinats, A. V., Kurkin, V. I. and Nishitani, N. 2015. Statistical study of medium-scale traveling ionospheric disturbances using SuperDARN Hokkaido ground backscatter data for 2011. *Earth, Planets and Space*, 67(1): 1–9. doi: 10.1186/s40623-015-0192-4.

Olafsson, H. and Agústsson, H. 2009. Gravity wave breaking in easterly flow over Greenland and associated low level barrier-and reverse tip-jets. *Meteorology and Atmospheric Physics*, 104(3): 191–197.

Olifer, L., Mann, I. R., Morley, S. K., Ozeke, L. G. and Choi, D. 2018. On the role of last closed drift shell dynamics in driving fast losses and Van Allen radiation belt extinction. *Journal of Geophysical Research: Space Physics*, 123(5): 3692–3703. doi: https://doi.org/10.1029/2018JA025190.

Otsuka, Y., Kotake, N., Shiokawa, K., Ogawa, T., Tsugawa, T. and Saito, A. 2011. Statistical study of medium-scale traveling ionospheric disturbances observed with a GPS receiver network in Japan, in Abdu, M.A. and Pancheva, D. (eds.). *Aeronomy of the Earth's Atmosphere and Ionosphere. Dordrecht: Springer*, pp. 291–299. doi: 10.1007/978-94-007-0326-121.

Otsuka, Y., Shiokawa, K., Ogawa, T. and Wilkinson, P. 2004. Geomagnetic conjugate observations of medium-scale traveling ionospheric disturbances at midlatitude using all-sky airglow imagers. *Geophysical Research Letters*, 31(15). doi: 10.1029/2004GL020262, 2004.

Otsuka, Y., Suzuki, K., Nakagawa, S., Nishioka, M., Shiokawa, K. and Tsugawa, a. 2013. GPS observations of medium-scale traveling ionospheric disturbances over Europe. *Annales Geophysicae*, 31(2): 163–172. doi: https://doi.org/10.5194/angeo-31-163-2013.

Panasenko, S. V., Otsuka, Y., Van de Kamp, M., Chernogor, L. F., Shinbori, A., Tsugawa, T. and Nishioka, M. 2019. Observation and characterization of traveling ionospheric disturbances induced by solar eclipse of 20 March 2015 using incoherent scatter radars and GPS networks. *Journal of Atmospheric and Solar-Terrestrial Physics*, 191: 105051. doi: https://doi.org/10.1016/j.jastp.2019.05.015.

Parkinson, W. D. 1983. *Introduction to geomagnetism.* Scottish Academic Press.

Patel, N. C., Karia, S. P., Pathak, K. N. *et al.*, 2017. GPS-TEC variation during low to high solar activity period (2010-2014) under the northern crest of Indian equatorial ionization anomaly region. *Positioning*, 8(02): 13. doi: 10.4236/pos.2017.82002.

Phiri, T.-J. 2013. Correlation between SQUID and fluxgate magnetometer data for geomagnetic storms. *Unpublished Master's thesis. Stellenbosch: Stellenbosch University*, .

Pi, X., Oveisgharan, S., Tymofyeyeva, E., Fattahi, H., Rosen, P. and Akopian, V. 2021. Measuring small- and medium-scale TEC spatial variations and irregularities from ground-based GNSS observations. *in Proceedings of the 2021 International Technical Meeting of The Institute of Navigation*, pp. 648–655. doi: https://doi.org/10.33012/2021.17856.

Pignalberi, A., Habarulema, J. B., Pezzopane, M. and Rizzi, R. 2019. On the development of a method for updating an empirical climatological ionospheric model by means of assimilated vTEC measurements from a GNSS receiver network. *Space Weather*, 17(7): 1131–1164. doi: https://doi.org/10.1029/2019SW002185.

Pimenta, A., Kelley, M., Sahai, Y., Bittencourt, J. and Fagundes, P. 2008. Thermospheric dark band structures observed in all-sky OI 630 nm emission images over the Brazilian low-latitude sector. *Journal of Geophysical Research: Space Physics*, 113(A1). doi: https://doi.org/10.1029/2007JA012444.

Prata, A. T. 2017. *Active and Passive Satellite Remote Sensing of Volcanic Clouds.*

Primdahl, F. 1979. The fluxgate magnetometer. *Journal of Physics E: Scientific Instruments*, 12(4): 241. doi: 10.1088/0022-3735/12/4/001.

Rastogi, R. 1975. On the simultaneous existence of eastward and westward flowing equatorial electrojet currents. *Proceedings of the Indian Academy of Sciences-Section A*, 81(2): 80–92. doi: https://doi.org/10.1007/BF03051175.

Rastogi, R. and Klobuchar, J. 1990. Ionospheric electron content within the equatorial F2 layer anomaly belt. *Journal of Geophysical Research: Space Physics*, 95(A11): 19045–19052. doi: https://doi.org/10.1029/JA095iA11p19045.

Rauber, R. and Ramamurthy, M. 2015. Mesoscale meteorology: Cloud and precipitation bands. *Encyclopedia of Atmospheric Sciences: Second Edition*, pp. 323–330.

Richardson, I. G. 2018. Solar wind stream interaction regions throughout the heliosphere. *Living Reviews in Solar Physics*, 15(1): 1–95.

Richardson, I. G. and Cane, H. V. 2010. Near-Earth interplanetary coronal mass ejections during solar cycle 23 (1996–2009): Catalog and summary of properties. *Solar Physics*, 264(1): 189–237.

Richmond, A. 1973. Equatorial electrojet—I. Development of a model including winds and instabilities. *Journal of Atmospheric and Terrestrial physics*, 35(6): 1083–1103. doi: https://doi.org/10.1016/0021-9169(73)90007-X.

Richmond, A. 1978. Gravity wave generation, propagation, and dissipation in the thermosphere. *Journal of Geophysical Research: Space Physics*, 83(A9): 4131–4145. doi: https://doi.org/10.1029/JA083iA09p04131.

Richmond, A., Ridley, E. and Roble, R. 1992. A thermosphere/ionosphere general circulation model with coupled electrodynamics. *Geophysical Research Letters*, 19(6): 601–604. doi: https://doi.org/10.1029/92GL00401.

Richmond, A. and Thayer, J. 2000. Ionospheric electrodynamics: A tutorial. *Magnetospheric Current Systems*, 118: 131–146.

Ripka, P. 1992. Review of fluxgate sensors. *Sensors and Actuators A: Physical*, 33(3): 129–141. doi: https://doi.org/10.1016/0924-4247(92)80159-Z.

Ripka, P. 2001. *Magnetic Sensors and Magnetometers.* Artech House.

Rishbeth, H. and Garriott, O. K. 1969. *Introduction to Ionospheric Physics.* Elsevier.

Rishbeth, H., Müller-Wodarg, I., Zou, L., Fuller-Rowell, T., Millward, G., Moffett, R., Idenden, D. and Aylward, A. 2000. Annual and semiannual variations in the ionospheric F2-layer: II. Physical discussion. *Annales Geophysicae*, 18(8): 945–956.

Rodger, A., Moffett, R. and Quegan, S. 1992. The role of ion drift in the formation of ionisation troughs in the mid-and high-latitude ionosphere—A review. *Journal of Atmospheric and Terrestrial Physics*, 54(1): 1–30. doi: https://doi.org/10.1016/0021-9169(92)90082-V.

Rodger, A. S., Brace, L., Hoegy, W. and Winningham, J. 1986. The poleward edge of the mid-latitude trough—its formation, orientation and dynamics. *Journal of Atmospheric and Terrestrial Physics*, 48(8): 715–728. doi: https://doi.org/10.1016/0021-9169(86)90021-8.

Rostoker, G. 1972. Geomagnetic indices. *Reviews of Geophysics*, 10(4): 935–950. doi: https://doi.org/10.1029/RG010i004p00935.

Rousseeuw, P. J. and Croux, C. 1993. Alternatives to the median absolute deviation. *Journal of the American Statistical Association*, 88(424): 1273–1283. doi: 10.1080/01621459.1993.10476408.

Sabzehee, F., Farzaneh, S., Sharifi, M. A. and Akhoondzadeh, M. 2018. TEC regional modeling and prediction using ANN method and single frequency receiver over Iran. *Annals of Geophysics*, 61(1): GM103–GM103. doi: 10.4401/ag-7297.

Saha, K. 2008. *The Earth's atmosphere: Its physics and dynamics.* Springer.

Saito, A., Fukao, S. and Miyazaki, S. 1998. High resolution mapping of TEC perturbations with the GSI GPS network over Japan. *Geophysical Research Letters*, 25(16): 3079–3082. doi: https://doi.org/10.1029/98GL52361.

Sastri, J. H. 1990. Equatorial anomaly in F-region—a review. *Indian Journal of Radio and Space Physics*, 19: 225–240.

Sastri, J. H. 1995. Short-period (5-33 min) variations in vertical drift of F-region plasma near the magnetic equator. *Journal of Geomagnetism and Geoelectricity*, 47(11): 1215–1222. doi: https://doi.org/10.5636/jgg.47.1215.

Satomura, T. and Sato, K. 1999. Secondary generation of gravity waves associated with the breaking of mountain waves. *Journal of the Atmospheric Sciences*, 56(22): 3847–3858. doi: https://doi.org/10.1175/1520-0469(1999)056<3847:SGOGWA>2.0.CO;2.

Savastano, G., Komjathy, A., Verkhoglyadova, O., Mazzoni, A., Crespi, M., Wei, Y. and Mannucci, A. J. 2017. Real-time detection of tsunami ionospheric disturbances with a stand-alone GNSS receiver: A preliminary feasibility demonstration. *Scientific Reports*, 7(1): 1–10. doi: 10.1038/srep46607.

Schunk, R. and Nagy, A. 2009. *Ionospheres: physics, plasma physics, and chemistry.* Cambridge university press.

Secan, J., Bussey, R., Fremouw, E. and Basu, S. 1997. High-latitude upgrade to the wideband ionospheric scintillation model. *Radio Science*, 32(4): 1567–1574. doi: https://doi.org/10.1029/97RS00453.

Seemala, G. and Valladares, C. 2011. Statistics of total electron content depletions observed over the South American continent for the year 2008. *Radio Science*, 46(5): 1–14. doi: https://doi.org/10.1029/2011RS004722.

Shiokawa, K., Otsuka, Y. and Ogawa, T. 2009. Propagation characteristics of nighttime mesospheric and thermospheric waves observed by optical mesosphere thermosphere imagers at middle and low latitudes. *Earth, Planets and Space*, 61(4): 479–491. doi: https://doi.org/10.1186/BF03353165.

Shiokawa, K., Otsuka, Y., Ogawa, T., Balan, N., Igarashi, K., Ridley, A., Knipp, D., Saito, A. and Yumoto, K. 2002. A large-scale traveling ionospheric disturbance during the magnetic storm of 15 September 1999. *Journal of Geophysical Research: Space Physics*, 107(A6): SIA–5.

Silwal, A., Gautam, S., Poudel, P., Karki, M., Adhikari, B., Chapagain, N., Mishra, R., Ghimire, B. and Migoya-Orue, Y. 2021. Global positioning system observations of ionospheric total electron content variations during the 15th January 2010 and 21st June 2020 solar eclipse. *Radio Science*, 56(5): 1–20. doi: 10.1029/2020RS007215.

Smith, W. L., Woolf, H. M. and Fleming, H. E. 1972. Retrieval of atmospheric temperature profiles from satellite measurements for dynamical forecasting. *Journal of Applied Meteorology and Climatology*, 11(1): 113–122. doi: https://doi.org/10.1175/1520-0450(1972)011<0113:ROATPF>2.0.CO;2.

Somsikov, V. 2011. Solar terminator and dynamic phenomena in the atmosphere: A review. *Geomagnetism and Aeronomy*, 51(6): 707–719. doi: 10.1134/S0016793211060168.

Somsikov, V. and Ganguly, B. 1995. On the formation of atmospheric inhomogeneities in the solar terminator region. *Journal of Atmospheric and Terrestrial Physics*, 57(12): 1513–1523. doi: https://doi.org/10.1016/0021-9169(95)00014-S.

Somsikov, V. and Trotskii, B. 1975. Generation of disturbances in the atmosphere during the passage of the solar terminator through it. *Geomagnetism and Aeronomy. (USSR)(Engl. Transl.);(United States)*, 15(5). doi: https://www.osti.gov/biblio/7265156.

Spiro, R., Heelis, R. and Hanson, W. 1979. Rapid subauroral ion drifts observed by Atmosphere Explorer C. *Geophysical Research Letters*, 6(8): 657–660. doi: https://doi.org/10.1029/GL006i008p00657.

Stauning, P. 2013. The polar cap index: A critical review of methods and a new approach. *Journal of Geophysical Research: Space Physics*, 118(8): 5021–5038. doi: https://doi.org/10.1002/jgra.50462.

Stauning, P. 2020. The polar cap (PC) index: invalid index series and a different approach. *Space Weather*, 18(10): e2020SW002442. doi: https://doi.org/10.1029/2020SW002442.

Subbarao, K. and Murthy, B. K. 1994. Post-sunset F-region vertical velocity variations at magnetic equator. *Journal of Atmospheric and Terrestrial Physics*, 56(1): 59–65. doi: https://doi.org/10.1016/0021-9169(94)90176-7.

Sugiura, M. and Kamei, T. 1991. Equatorial Dst index 1957–1986. *International Association of Geomagnetism and Aeronomy (IAGA) Bulletin*, 40: 17–38.

Sugiura, M. and Poros, D. 1971. *Hourly values of equatorial Dst for years 1957 to 1970, Rep. X-645-71-278.* Greenbelt, MD: NASA, Goddard Space Flight Center.

Taylor Jr, H., Grebowsky, J. and Chen, A. 1975. Ion composition irregularities and ionosphere-plasmasphere coupling: Observations of a high latitude ion trough. *Journal of Atmospheric and Terrestrial Physics*, 37(4): 613–623. doi: https://doi.org/10.1016/0021-9169(75)90056-2.

Temmer, M. 2016. Kinematical properties of coronal mass ejections. *Astronomical Notes*, 337(10): 1010–1015. doi: https://doi.org/10.1002/asna.201612425.

Thaganyana, G. P., Habarulema, J. B., Ngwira, C. and Azeem, I. 2022. Equatorward medium to large-scale traveling ionospheric disturbances of high latitude origin during quiet conditions. *Journal of Geophysical Research: Space Physics*, 127(3): e2021JA029558. doi: https://doi.org/10.1029/2021JA029558.

Themens, D. R., Watson, C., Žagar, N., Vasylkevych, S., Elvidge, S., McCaffrey, A., Prikryl, P., Reid, B., Wood, A. and Jayachandran, P. 2022. Global propagation of ionospheric disturbances associated with the 2022 Tonga volcanic eruption. *Geophysical Research Letters*, 49(7): e2022GL098158. doi: https://doi.org/10.1029/2022GL098158.

Thomas, L. 1996. The coupling of the lower ionosphere with the mesosphere and lower thermosphere, in Kohl, H., Ruster, R., Schlegel, K. (eds.). *Modern Ionospheric Science*, pp. 67–101.

Thompson, A. R., Moran, J. M. and Swenson, G. W. 2017. *Interferometry and Synthesis in Radio Astronomy*. Springer Nature.

Titheridge, J. 1995. Winds in the ionosphere—A review. *Journal of Atmospheric and Terrestrial Physics*, 57(14): 1681–1714. doi: https://doi.org/10.1016/0021-9169(95)00091-F.

Torr, M. R. and Torr, D. 1973. The seasonal behaviour of the F2-layer of the ionosphere. *Journal of Atmospheric and Terrestrial Physics*, 35(12): 2237–2251. doi: https://doi.org/10.1016/0021-9169(73)90140-2.

Torrence, C. and Compo, G. P. 1998. A practical guide to wavelet analysis. *Bulletin of the American Meteorological Society*, 79(1): 61–78. doi: https://doi.org/10.1175/1520-0477(1998)079<0061:APGTWA>2.0.CO;2.

Troshichev, O., Andrezen, V., Vennerstrøm, S. and Friis-Christensen, E. 1988. Magnetic activity in the polar cap—A new index. *Planetary and Space Science*, 36(11): 1095–1102. doi: https://doi.org/10.1016/0032-0633(88)90063-3.

Troshichev, O., Janzhura, A. and Stauning, P. 2006. Unified PCN and PCS indices: Method of calculation, physical sense, and dependence on the IMF azimuthal and northward components. *Journal of Geophysical Research: Space Physics*, 111(A5). doi: https://doi.org/10.1029/2005JA011402.

Tsugawa, T., Saito, A. and Otsuka, Y. 2004. A statistical study of large-scale traveling ionospheric disturbances using the GPS network in Japan. *Journal of Geophysical Research: Space Physics*, 109(A6). doi: https://doi.org/10.1029/2003JA010302.

Tsurutani, B. T. 2001. The interplanetary causes of magnetic storms, substorms and geomagnetic quiet, edited by ia daglis. *Dordrecht: Springer*, 38: 103–130.

Tsurutani, B. T., Gonzalez, W. D., Gonzalez, A. L., Guarnieri, F. L., Gopalswamy, N., Grande, M., Kamide, Y., Kasahara, Y., Lu, G., Mann, I. *et al.*, 2006. Corotating solar wind streams and recurrent geomagnetic activity: A review. *Journal of Geophysical Research: Space Physics*, 111(A7). doi: https://doi.org/10.1029/2005JA011273.

Tsurutani, T., Gonzalez, W., Yohsuke, K. and Arballo, J. 1997. *Magnetic Storms*. Washington, DC: American Geophysical Union.

Turner, N. E., Cramer, W. D., Earles, S. K. and Emery, B. A. 2009. Geoefficiency and energy partitioning in CIR-driven and CME-driven storms. *Journal of Atmospheric and Solar-Terrestrial Physics*, 71(10-11): 1023–1031. doi: https://doi.org/10.1016/j.jastp.2009.02.005.

U.S.Army 1996. Navstar GPS - user equipment introduction. *Unpublished U.S. Government report*, .

Uwamahoro, J. C., Giday, N. M., Habarulema, J. B., Katamzi-Joseph, Z. T. and Seemala, G. K. 2018. Reconstruction of storm-time total electron content using ionospheric tomography and artificial neural networks: A comparative study over the African region. *Radio Science*, 53(11): 1328–1345. doi: 10.1029/2017RS006499.

Vadas, S. L. 2007. Horizontal and vertical propagation and dissipation of gravity waves in the thermosphere from lower atmospheric and thermospheric sources. *Journal of Geophysical Research: Space Physics*, 112(A6). doi: https://doi.org/10.1029/2006JA011845.

Vadas, S. L. and Becker, E. 2018. Numerical modeling of the excitation, propagation, and dissipation of primary and secondary gravity waves during wintertime at McMurdo Station in the Antarctic. *Journal of Geophysical Research: Atmospheres*, 123(17): 9326–9369. doi: https://doi.org/10.1029/2017JD027974.

Vadas, S. L. and Becker, E. 2019. Numerical modeling of the generation of tertiary gravity waves in the mesosphere and thermosphere during strong mountain wave events over the Southern Andes. *Journal of Geophysical Research: Space Physics*, 124(9): 7687–7718. doi: https://doi.org/10.1029/2019JA026694.

Vadas, S. L. and Crowley, G. 2010. Sources of the traveling ionospheric disturbances observed by the ionospheric TIDDBIT sounder near Wallops Island on 30 October 2007. *Journal of Geophysical Research: Space Physics*, 115(A7). doi: https://doi.org/10.1029/2009JA015053.

Vadas, S. L. and Liu, H.-l. 2009. Generation of large-scale gravity waves and neutral winds in the thermosphere from the dissipation of convectively generated gravity waves. *Journal of Geophysical Research: Space Physics*, 114(A10). doi: https://doi.org/10.1029/2009JA014108.

Vadas, S. L. and Liu, H.-L. 2013. Numerical modeling of the large-scale neutral and plasma responses to the body forces created by the dissipation of gravity waves from 6 h of deep convection in Brazil. *Journal of Geophysical Research: Space Physics*, 118(5): 2593–2617. doi: https://doi.org/10.1002/jgra.50249.

Vadas, S. L., Liu, H.-L. and Lieberman, R. 2014. Numerical modeling of the global changes to the thermosphere and ionosphere from the dissipation of gravity waves from deep convection. *Journal of Geophysical Research: Space Physics*, 119(9): 7762–7793. doi: https://doi.org/10.1002/2014JA020280.

Vadas, S. L., Taylor, M. J., Pautet, P.-D., Stamus, P., Fritts, D. C., Liu, H.-L., Sao Sabbas, F., Rampinelli, V., Batista, P. and Takahashi, H. 2009. Convection: the likely source of the medium-scale gravity waves observed in the OH airglow layer near Brasilia, Brazil, during the SpreadFEx campaign. *Annales Geophysicae*, 27(1): 231–259. doi: https://doi.org/10.5194/angeo-27-231-2009.

Vadas, S. L., Xu, S., Yue, J., Bossert, K., Becker, E. and Baumgarten, G. 2019. Characteristics of the quiet-time hot spot gravity waves observed by GOCE over the Southern Andes on 5 July 2010. *Journal of Geophysical Research: Space Physics*, 124(8): 7034–7061. doi: https://doi.org/10.1029/2019JA026693.

Vadas, S. L., Zhao, J., Chu, X. and Becker, E. 2018. The excitation of secondary gravity waves from local body forces: Theory and observation. *Journal of Geophysical Research: Atmospheres*, 123(17): 9296–9325. doi: https://doi.org/10.1029/2017JD027970.

Valladares, C. and Hei, M. A. 2012. Measurement of the characteristics of TIDs using small and regional networks of GPS receivers during the campaign of 17–30 July of 2008. *International Journal of Geophysics*, 2012: 548784. doi: doi:10.1155/2012/548784.

Valladares, C., Villalobos, J., Hei, M., Sheehan, R., Basu, S., MacKenzie, E. *et al.*, 2009. Simultaneous observation of traveling ionospheric disturbances in the Northern and Southern Hemispheres. *Annales Geophysicae*, 27(4): 1501–1508. doi: https://doi.org/10.5194/angeo-27-1501-2009.

Voiculescu, M., Nygrén, T., Aikio, A. and Kuula, R. 2010. An olden but golden EISCAT observation of a quiet-time ionospheric trough. *Journal of Geophysical Research: Space Physics*, 115(A10). doi: https://doi.org/10.1029/2010JA015557.

Voiculescu, M., Nygrén, T., Aikio, A., Vanhamäki, H. and Pierrard, V. 2016. Postmidnight ionospheric troughs in summer at high latitudes. *Journal of Geophysical Research: Space Physics*, 121(12): 12–171. doi: https://doi.org/10.1002/2016JA023360.

Waldock, J. and Jones, T. 1986. Hf doppler observations of medium-scale travelling ionospheric disturbances at mid-latitudes. *Journal of atmospheric and terrestrial physics*, 48(3): 245–260. doi: https://doi.org/10.1016/0021-9169(86)90099-1.

Walker, S., Kadirkamanathan, V. and Pokhotelov, O. 2013. Changes in the ultra-low frequency wave field during the precursor phase to the Sichuan earthquake: DEMETER observations. , 31(9): 1597–1603. doi: https://doi.org/10.5194/angeo-31-1597-2013.

Wan, W., Yuan, H., Ning, B., Liang, J. and Ding, F. 1998. Traveling ionospheric disturbances associated with the tropospheric vortexes around Qinghai-Tibet Plateau. *Geophysical Research Letters*, 25(20): 3775–3778. doi: https://doi.org/10.1029/1998GL900030.

Wanliss, J. A. and Showalter, K. M. 2006. High-resolution global storm index: Dst versus SYM-H. *Journal of Geophysical Research: Space Physics*, 111(A2). doi: https://doi.org/10.1029/2005JA011034.

Webb, D. F. 1991. The solar cycle variation of the rates of CMEs and related activity. *Advances in Space Research*, 11(1): 37–40. doi: https://doi.org/10.1016/0273-1177(91)90086-Y.

Wei, Y., Zhao, B., Li, G. and Wan, W. 2015. Electric field penetration into Earth's ionosphere: A brief review for 2000–2013. *Science Bulletin*, 60(8): 748–761. doi: https://doi.org/10.1007/s11434-015-0749-4.

Wright, C. J., Hindley, N. P., Moss, A. C. and Mitchell, N. J. 2016. Multi-instrument gravity-wave measurements over Tierra del Fuego and the Drake Passage–Part 1: Potential energies and vertical wavelengths from AIRS, COSMIC, HIRDLS, MLS-Aura, SAAMER, SABER and radiosondes. *Atmospheric Measurement Techniques*, 9(3): 877–908. doi: https://doi.org/10.5194/amt-9-877-2016.

Wu, D. L., Preusse, P., Eckermann, S. D., Jiang, J. H., de la Torre Juarez, M., Coy, L. and Wang, D. Y. 2006. Remote sounding of atmospheric gravity waves with satellite limb and nadir techniques. *Advances in Space Research*, 37(12): 2269–2277. doi: https://doi.org/10.1016/j.asr.2005.07.031.

Xiong, C., Stolle, C. and Lühr, H. 2016. The Swarm satellite loss of GPS signal and its relation to ionospheric plasma irregularities. *Space Weather*, 14(8): 563–577. doi: https://doi.org/10.1002/2016SW001439.

Xiong, C., Stolle, C. and Park, J. 2018. Climatology of GPS signal loss observed by Swarm satellites. , 36(2): 679–693. doi: https://doi.org/10.5194/angeo-36-679-2018.

Xu, G. and Xu, Y. 2016. *GPS: Theory, Algorithms and Applications*. Springer.

Yiğit, E., Knížová, P. K., Georgieva, K. and Ward, W. 2016. A review of vertical coupling in the Atmosphere–Ionosphere system: Effects of waves, sudden stratospheric warmings, space weather, and of solar activity. *Journal of Atmospheric and Solar-Terrestrial Physics*, 141: 1–12. doi: https://doi.org/10.1016/j.jastp.2016.02.011.

Yiğit, E. and Medvedev, A. S. 2009. Heating and cooling of the thermosphere by internal gravity waves. *Geophysical Research Letters*, 36(14). doi: https://doi.org/10.1029/2009GL038507.

Yizengaw, E. and Moldwin, M. B. 2005. The altitude extension of the mid-latitude trough and its correlation with plasmapause position. *Geophysical Research Letters*, 32(9). doi: https://doi.org/10.1029/2005GL022854.

Yizengaw, E., Moldwin, M., Mebrahtu, A., Damtie, B., Zesta, E., Valladares, C. and Doherty, P. 2011. Comparison of storm time equatorial ionospheric electrodynamics in the african and american sectors. *Journal of Atmospheric and Solar-Terrestrial Physics*, 73(1): 156–163. doi: https://doi.org/10.1016/j.jastp.2010.08.008.

Yizengaw, E., Zesta, E., Moldwin, M., Damtie, B., Mebrahtu, A., Valladares, C. and Pfaff, R. 2012. Longitudinal differences of ionospheric vertical density distribution and equatorial electrodynamics. *Journal of Geophysical Research: Space Physics*, 117(A7). doi: https://doi.org/10.1029/2011JA017454.

Zhang, J., Howard, K. and Gourley, J. 2005. Constructing three-dimensional multiple-radar reflectivity mosaics: Examples of convective storms and stratiform rain echoes. *Journal of Atmospheric and Oceanic Technology*, 22(1): 30–42. doi: https://doi.org/10.1175/JTECH-1689.1.

Zhang, S.-R. and Holt, J. M. 2008. Ionospheric variability from an incoherent scatter radar long-duration experiment at Millstone Hill. *Journal of Geophysical Research: Space Physics*, 113(A3). doi: https://doi.org/10.1029/2007JA012639.

Zhou, Y.-L., Lühr, H., Xu, H.-w. and Alken, P. 2018. Comprehensive analysis of the counter equatorial electrojet: Average properties as deduced from CHAMP observations. *Journal of Geophysical Research: Space Physics*, 123(6): 5159–5181. doi: https://doi.org/10.1029/2018JA025526.

Zolesi, B. and Cander, L. R. 2014. *Ionospheric Prediction and Forecasting*. Springer.